
Comparing real and synthetic observations of protostellar disks

Joaquin Zamponi



München 2023

Comparing real and synthetic observations of protostellar disks

Joaquin Zamponi

Dissertation
der Fakultät für Physik
der Ludwig-Maximilians-Universität
München

vorgelegt von
Joaquin Zamponi
aus Temuco, Chile

München, den 06.06.2023

Erstgutachter: Prof. Dr. Paola Caselli

Zweitgutachter: Prof. Dr. Tilman Birnstiel

Tag der mündlichen Prüfung: 18.07.2023

*Quién sabe y alguien nos ve igual como aquí vemos
Hormiguitas, que se están riendo al ver lo mal que actuamos
Hermano, la tierra es un grano, o quizás medio grano
De algún desierto en donde habitamos*

- Canserbero

Contents

Zusammenfassung	xiii
Abstract	xiv
1 Introduction	1
1.1 The interstellar medium and star formation	1
1.1.1 Molecular clouds, filaments and cores	3
1.1.2 Cloud stability and fragmentation	6
1.2 Low-mass star formation	13
1.2.1 Prestellar collapse	13
1.2.2 Protostar formation	14
1.2.3 Protostellar disk formation	15
1.3 Radiative transfer	20
1.3.1 Basic concepts	20
1.3.2 The equation of radiative transfer	20
1.3.3 Radiative transfer on dusty media	21
1.3.4 Dust opacity	24
1.3.5 Polarization by dust alignment and scattering	25
1.4 The Class 0 protostellar system IRAS 16293-2422	28
1.5 Contents of this thesis	30
2 IRAS 16293-2422 B hosts a hot and gravitationally unstable disk	31
2.1 Introduction	32
2.2 Observations	33
2.2.1 Data and Imaging	33
2.2.2 Results	34
2.3 Protostellar disk simulations	36
2.3.1 Simulations of disk formation and evolution	36
2.4 Radiative transfer	40
2.4.1 Dust grain size distribution and composition	41
2.4.2 Dust temperature distributions	42
2.4.3 ALMA synthetic observations	45
2.5 Comparison with observations	47

2.5.1	Brightness profiles	47
2.5.2	Synthetic maps and spectral index of the gravitationally unstable model	48
2.6	Discussion	50
2.6.1	Are early disks hotter towards the midplane?	50
2.6.2	Are self-gravitating disks at the origin of some hot corinos?	52
2.6.3	Radiative heating under different assumptions	54
2.6.4	Comparison to more evolved gravitationally unstable disks	55
2.6.5	The origin of the observed asymmetry	55
2.6.6	Mass estimates under the optically thin approximation	57
2.7	Conclusions	57
3	Dust grain sizes and polarization in IRAS 16293B	61
3.1	Introduction	62
3.1.1	Previous observations towards the class 0 disk IRAS 16293 B	63
3.2	Observations	64
3.2.1	ALMA & VLA archival data	64
3.2.2	VLA Band Ka & Ku observations	64
3.3	Disk and dust model	65
3.3.1	Protostellar disk model	65
3.3.2	The Synthesizer: from simulations to synthetic observations	66
3.3.3	Grain sizes	68
3.3.4	Composition	68
3.3.5	Polarization by dust self-scattering	70
3.3.6	Synthetic observations	71
3.4	Results	72
3.4.1	Effects of different maximum grain sizes on the Stokes I fluxes	72
3.4.2	Effect of carbon sublimation within the soot line	73
3.4.3	Variation of the spectral index	76
3.4.4	Polarization by self-scattering	77
3.5	Discussion	81
3.5.1	Grain growth in Class 0 disks	81
3.5.2	Grain growth within the soot-line	82
3.5.3	If not self-scattering, what is the polarization mechanism in IRAS 16293B?	84
3.6	Conclusions	85
4	The Synthesizer: synthetic observations from the command line	87
4.1	Introduction	87
4.1.1	What is a synthetic observation?	87
4.2	The code	88
4.2.1	Requirements	90
4.2.2	Installation	90
4.2.3	Running the code	91
4.3	Modules	92

4.3.1	Gridding (<code>--grid</code>)	92
4.3.2	Dust Opacity (<code>--opacity</code>)	96
4.3.3	Radiative Transfer (<code>--raytrace</code>)	103
4.3.4	Synthetic Observation (<code>--synobs</code>)	104
4.4	Science cases	108
4.4.1	Data visualization	111
4.5	Current and future code features	112
5	Summary and future	119
5.1	Work summary	119
5.2	Future research	121
5.2.1	Model ALMA polarization with models of magnetic grain alignment . .	122
5.2.2	Investigating the origin of hot dust spots in a young binary system	123
A	Complementary Material for Chapter 2	125
A.1	Spectral index	125
A.2	Spectral index for the MHD disk model	126
A.3	Toomre Q parameter for both disk models	126
B	Complementary Material for Chapter 3	129
B.1	The DustMixer: a command-line tool to generate dust opacities	129
B.2	Polarization models by self-scattering for an edge-on hot disk	130
	Acknowledgements	145

List of Figures

1.1	Example of a filamentary Infrared Dark Cloud	5
1.2	Derivation of prestellar core density profiles	7
1.3	Numerical simulation of first core formation	16
1.4	Close surroundings of a newly born protostar	17
1.5	Spectral classification of protostars	19
1.6	Dust opacities for interstellar silicate dust	25
1.7	Polarization of light by magnetic grain alignment	27
1.8	Polarization vectors for different Q and U stokes components	28
1.9	The Class 0 Protostar IRAS 16293-2422 B observed with ALMA	30
2.1	ALMA observations of IRAS 16293-2422 B	36
2.2	Gas density and temperature of the MHD disk model	38
2.3	Gas density and temperature of the RHD disk model	39
2.4	Dust opacities for different grain sizes	43
2.5	Radially averaged midplane dust temperatures from both disk models	46
2.6	Comparison of brightness temperature profiles of all synthetic and real observations	49
2.7	Synthetic observations of the RHD disk model	50
2.8	Dust temperature distribution of the RHD disk model at the $\tau = 1$ surface	52
2.9	3D rendering of the dust temperature distribution of the RHD disk model	53
2.10	Spectral index map of the RHD disk model	56
2.11	Ratio of the observational mass estimates over the original disk mass	58
3.1	ALMA and JVLA observations of IRAS 16293-2422 B	66
3.2	Gas density and temperature of the disk model	67
3.3	Dust opacities for different grain sizes and compositions	70
3.4	Comparison of brightness temperature profiles of all synthetic and real observations	74
3.5	Optical depth profiles for all synthetic models	75
3.6	Spectral indices for observations and models with and without C-sublimation	77
3.7	Polarized radiative transfer models produced by self-scattering	79
3.8	Polarized ALMA and JVLA synthetic observations of the self-scattering models	80
3.9	Models accounting for grain growth within the sootline	83
4.1	All the steps involved in a synthetic observations	89

4.2	Analytical model of a Prestellar Core	93
4.3	Analytical model of a gapped protoplanetary disk	93
4.4	Analytical vector field models	94
4.5	Interpolation of SPH particles onto a Cartesian grid	96
4.6	How to calculate opacities	100
4.7	Radiative transfer images created by the Synthesizer	104
4.8	Diagnostic plots from simobserve and tclean	109
4.9	AREPO simulation post-processed using the Synthesizer	111
4.10	Models of magnetic grain alignment in G31.41+031 using the Synthesizer	112
4.11	3D rendering of the $\tau = 1$ surface	113
5.1	Science idea for future research 1	123
5.2	Science idea for future research 2	124
A.1	Synthetic observations of the MHD disk model	126
A.2	Toomre parameter Q from both disk models	127
B.1	Radiative transfer models of self-scattering for an edge-on disk	130

List of Tables

1.1	Physical properties of interstellar environments	2
3.1	Dust opacities for two different silicate-carbon mixtures	71
4.1	List of possible command line argument for the Synthesizer	116
4.2	Continuation of Table 4.1	117

Zusammenfassung

Die entstehenden Scheiben- und Hüllenstrukturen um Protosterne spielen eine entscheidende Rolle im Prozess der Stern- und Planetenbildung. ALMA enthüllt nie dagewesene Details der Hüllen-, Scheiben- und Ausfluss Strukturen von Hüllen im nahen protoplanetaren Systeme, denn es fehlt eine konsistente Interpretation dieser Beobachtungen. Stattdessen werden oft stark vereinfachte Modelle verwendet, um die beobachteten Merkmale zu beschreiben. In diesem Projekt wollen wir realistischere synthetische Beobachtungen des entstehenden Scheiben- und Hüllensystems mit Hilfe bestehender Ausstrahlung und nicht-idealer magnetohydrodynamischen Simulationen des protoplanetaren Kollapses und der Scheibenbildung zeigen, und gegen realistischere millimeter Beobachtungen vergleichen. Das Hauptziel des Projekts ist es eine facettenreiche Interpretation der aktuellen Kontinuums- und Polarisationsbeobachtungen der protoplanetaren Quellen in ihren frühesten Stadien zu liefern, und realistischere Einschränkungen für das Staubwachstum in den frühen protoplanetaren Scheiben zu bieten

Abstract

Nascent envelope disk structures around protostars play a crucial role in the process of star and planet formation. As ALMA reveals unprecedented details of the envelope, disk, and outflow structures in nearby protostellar systems, a consistent interpretation for these observations remains absent, instead, highly simplified models are often adopted to partially fit the observed features. In this project, we aim to generate more realistic synthetic observations of the nascent protostellar disk and envelope system, using existing radiation and non-ideal magnetohydrodynamic simulations of protostellar collapse and disk formation. The main goal of the project is to provide multi-facet interpretation of the current continuum and polarization observations of protostellar sources at their earliest stages, and offer more realistic constraints on the dust growth in the early protoplanetary disks.

Chapter 1

Introduction

1.1 The interstellar medium and star formation

Naked-eye observations of the sky have told us many things about the universe. They tell us that there are objects floating in space, orbiting each other and leading to the formation of larger objects. They tell us about the presence of planets, of comets, of stars and even galaxies. When you look out on a dark night, the sky looks so big and full of astronomical objects and colors, and yet the space between the stars seems to be apparently empty. To study the largest and earliest structures of the universe, we study the galaxies that formed them. To study the galaxies and their dynamics, we study the stars that formed them. To study the stars and what formed them, we need to focus on this apparently empty space between them. This colorful and beautiful space in between is called, the Interstellar Medium (ISM), and all the answers to how stars form reside in it. The ISM is primarily composed of gas. The density and composition of the gas vary significantly across different regions of the ISM. It consists of several distinct components, including atomic hydrogen (HI), ionized hydrogen (HII), molecular hydrogen (H₂), a mixture of molecules, atoms, and ions. Another component of the ISM is interstellar dust. These are tiny ($\lesssim 1 \mu\text{m}$) solid particles consisting of carbon, silicon, and various heavy elements. Dust particles play a crucial role in absorbing, scattering, and emitting light from the newly born stars, affecting the overall appearance of astronomical objects. The interstellar medium exists in a wide range of physical conditions, from diffuse, low-density regions to dense molecular clouds. These clouds range from a few parsec (pc) to hundreds of pc and serve as the birthplaces of new stars. Under the influence of gravity and various other physical processes, these molecular clouds fragment and form local overdensities. These overdensities can undergo gravitational collapse and lead to the formation of protostellar cores and subsequent star formation. The interplay between stars and the ISM is dynamic and complex. Stellar processes, such as stellar winds, supernova explosions, and radiation, can inject energy, momentum, and newly synthesized elements into the surrounding interstellar medium, influencing its properties and triggering subsequent star formation. Conversely, the formation and evolution of stars can also profoundly impact the ISM through the injection of stellar feedback and the dispersal of material into the galactic environment. Observational studies of the interstellar medium rely on various techniques spanning a

wide range of wavelengths, including radio, infrared, optical, and X-ray observations. These observations provide insights into the physical conditions, composition, and kinematics of the ISM, helping astronomers unravel the intricate processes occurring within this dynamic medium.

The ISM can be divided into different phases according to their temperature and density, such as, the Cold Neutral Medium (CNM), the Warm Neutral Medium (WNM), the Warm Ionized Medium (WIM), the HII regions, the Coronal gas and the dense molecular gas. The interstellar matter can be either found in a gaseous state, e.g., atoms, ions and molecules or in a solid state, e.g., dust grains. The existence of both states of the matter is what sets the place for the formation and evolution of further species that would not be created otherwise (e.g., H_2) as well as the subsequent star formation. Table 1.1 lists the main physical properties of every phase of the ISM.

Table 1.1: Physical properties for different interstellar environments. Table data reproduced from Tielens (2010) and Smith et al. (2013).

Environment	Temperature (K)	Number density (cm^{-3})	Filling factor (%)	Total mass ($\times 10^9 M_\odot$)	Scale height (pc)	Surface density $M_\odot \text{pc}^{-2}$
Coronal gas	$10^{5.5}-10^7$	0.004	50	–	3000	0.3
Warm ionized medium	$\sim 10^4$	0.3	25	1.0	900	1.1
Warm neutral medium	~ 5000	0.6	30	2.8	220	1.5
Cold neutral medium	40-100	30	1.0	2.2	94	2.3
Molecular gas	6-50	10^3-10^6	0.05	1.3	75	1.0
HII regions	10^4	10^2-10^4	0.01	0.05	70	0.05

In this thesis, we focus on the molecular gas phase of the ISM. This is characterized by low temperatures (6-50 K) and high number densities (10^4-10^6cm^{-3}), where gas particles are mostly in the form of molecules instead of free floating atoms. These clouds are the coldest regions of the interstellar medium and they are essential for the evolution of the Galaxy and the Universe, as they play the role of nurseries for new stars. When these clouds become dynamically and thermally unstable, they become filamentary and fragment (see section 1.1.2). Small substructures within these filaments become bounded objects and begin to contract gravitationally. As the collapse goes on, their central densities increase significantly and lead to the formation of dense objects known as protostars (see 1.2.2) surrounded by a rotationally supported disk, known as a protostellar disk (see 1.2.3). This disk does later get thinner and ringed, clears out its small particles and leave only newly born planets orbiting the new star. The protostar stars to burn deuterium in its core and then enter their main-sequence life stage, to become an actual star.

Interstellar dust is the only part of the ISM material in solid form. Its presence in the ISM is essential, because it sets the place for the formation of molecules that could not be formed in space otherwise. The most relevant molecule for star formation is H_2 . The formation of H_2 primarily occurs on the surfaces of dust grains, which act as catalytic sites for the reaction. The process begins with the adsorption of atomic hydrogen (H) onto the grain surface, followed by its diffusion and accumulation in the grain's icy mantles. Once a sufficient concentration of

H atoms is reached, they can undergo surface reactions, involving quantum tunneling, to form H_2 molecules. The energy released during this exothermic process contributes to heating the surrounding environment which release molecules back to the gas phase. Once H_2 is back in the gas-phase, a small part of the H_2 content gets ionized by the external cosmic-rays, creating H_2^+ . After rapid encounters of H_2^+ with the remaining neutral H_2 , they form H_3^+ . This essential ion easily donates one of the constituent protons (H^+) to heavier atoms already found in atomic form such as C and O (after the dissociation fronts of photodissociation regions). These protons released after the formation of H_3^+ combine with C atoms to form CH^+ , which subsequently interacts two times more with H_3^+ to form CH_3^+ . When Oxygen comes into play with this newly formed CH_3^+ , they create the HCO^+ molecule, which then dissociatively recombines with free electrons to form CO (Yamamoto 2017). CO is one of the most abundant species found in the gas-phase, after H_2 . Because of its high abundance and very high dipole moment, it is used to trace the invisible H_2 mass distribution (at low temperatures; $T \lesssim 100$ K) via the CO-to- H_2 conversion factor (Bolatto et al. 2013). CO rotational line emission, along with atomic line cooling (e.g., from CII), is the responsible mechanism to efficiently cool down the cloud to a few tens of a Kelvin, lowering the contribution of thermal against gravitational pressure and favouring the occurrence of fragmentation and the formation of denser objects.

1.1.1 Molecular clouds, filaments and cores

Giant Molecular Clouds

The galactic disk is filled with mixture of two fluids that are gravitationally coupled: the interstellar matter and the stars. At galactic scales, the interstellar fluid is represented by the neutral atomic gas (HI) disk, which, driven by the galactic rotation, may lead to instabilities. The stability for this rotating disk is given by the disk's Toomre Q parameter (Toomre 1964)

$$Q = \frac{c_s \kappa}{\pi G \Sigma}. \quad (1.1)$$

where c_s is the gas sound speed, κ is the epicyclic frequency (equal to the angular velocity Ω in a Keplerian disc) and Σ is the gas surface density. c_s represents the thermal pressure contribution to the equilibrium, κ or Ω represent the rotational support component and Σ the gravitational pull. The Toomre parameter is indicative of whether the disk will remain rotationally supported or if self-gravity terms will dominate and form substructures. However, even in an smooth and unfragmented rotating disk, where the Toomre stability criterion is met for the global disk, local instabilities may be produced given its differential rotation. These instabilities are defined by the *Parker instability* (Parker 1966), which is a variant of the Rayleigh-Taylor instability that arises in a disk supported against gravity by the gas pressure, the galactic magnetic field and cosmic rays. A description of the Parker instability is beyond the scope of the present introduction, even though we regard it as the responsible mechanism for the formation of Giant HII structures (Mouschovias 1974; Draine 2011; Lequeux 2005). Giant Molecular Clouds (GMCs) are formed efficiently in the arms of spiral galaxies, where density waves have already created large HI clouds. GMC formation occurs when the density of an HI structure reaches a threshold

that allows the formation of H_2 on dust grain surfaces. This typically happens after the cloud achieves high column densities, shielding it from external UV radiation (Snow & McCall 2006; Lequeux 2005). Alternatively, GMCs can also form through inelastic collisions between HI clouds, which decrease their velocity dispersions and enable gravitational collapse to overcome outward radiation pressure. In this scenario, the presence of magnetic fields can either facilitate rapid fragmentation or promote the coalescence of initial HI clouds by mixing and interconnecting their magnetic fields. The coalescence pathway is favored in the spiral arms, supported by the presence of large-scale magnetic fields (Davis & Greenstein 1951) and leading to the formation of GMCs with masses ranging from 10^2 - $10^7 M_\odot$, which subsequently collapse into dense molecular clouds within a timescale comparable to the collision time between the initial clouds (Elmegreen 1989). These GMCs exhibit filamentary subunits of similar length scales that converge at specific angles, giving rise to the formation of Massive Dense Cores (MDCs) through fragmentation (see Fig. 1.1; Motte et al. 2018) and low-mass cores along the filaments. Since these core are dusty, once they become denser than the parent filament, they also become opaque to background starlight and start to look dark for an external observer at optical wavelength. The optically invisible clouds are then traced from their infrared emission. The subset of dark clouds that are highly massive and obscured, even at infrared light, receive the name of Infrared Dark Clouds (IRDCs) and form at the converging point of multiple filaments. These regions are then observed at submillimeter wavelength and represent the likely birthplaces of massive stars due to their large mass reservoir.

Filaments and dark clouds

Dark clouds, which serve as the structural subunits of Giant Molecular Clouds, were initially proposed to have a filamentary structure by (Barnard 1907), inspired by Herschel's observation of dark patches in the sky towards ρ Ophiucus. This filamentary nature has been more recently examined and refined by (Myers 2009). These filaments often exhibit lengths similar to that of the underlying GMC, as observed in regions like Taurus and Ophiucus. Furthermore, there are companion filaments with comparable scales that tend to align parallel to each other and converge at specific angles, creating what is known as a "hub" (Myers 2009; see Figure 1.1). This filamentary structure appears to be an inherent characteristic of the cloud itself, rather than a consequence of internal evolutionary processes like star formation, which tends to inherit the distribution of its parent filaments (see Hartmann (2002), for a study of Taurus). The coherent spatial and velocity fields observed in Ophiucus, as documented by Loren (1989), further support this notion.

Dark clouds exhibit a hierarchical structure characterized by the presence of nested subunits. This mass distribution discontinuity has been classified by Williams et al. (2000), who introduced a rough categorization of mass units including clouds, clumps, and cores. *Giant Clouds* (e.g., GMCs), represent the primary structures that naturally develops filamentary gas on parsec scales. These filaments contain denser embedded *clumps* with masses ranging from 50 to $500 M_\odot$ and radii between 0.3 and 3 pc. Within these clumps, smaller self-gravitating structures with single-peak density profiles, known as *cores*, can be found. These cores have the potential to undergo further fragmentation, as demonstrated by numerical MHD simulations magnetized

collapsing cores, either in isolated environments (Myers et al. 2013; Seifried & Walch 2015; Körtgen et al. 2017) or even when embedded within oscillating and disrupted filaments (Körtgen et al. 2018). Observational evidence also supports the occurrence of core fragmentation. One example is found within the Taurus molecular cloud, where (Kraus et al. 2011) have shown that the cloud harbors numerous binary systems. (Reipurth et al. 2014) have later suggested that these binaries are likely formed via core fragmentation. Another case is the observed quadrupole pre- and protostellar system with a wide separation of even up to 1000 au but dynamically bound (Pineda et al. 2015). This system is suggested to have been formed out of the fragmentation of its filament/core on scales of about 5000 au. However, it is crucial to be cautious when claiming fragmentation, considering that limited resolution and filtering of large scale emission in interferometric observations may lead to artifacts that resemble artificial fragmentation. This issue was addressed through a comparative analysis of real ALMA and synthetic observations carried out by Caselli et al. (2019), focused on the core center of the prestellar core L1544. Their high-resolution observations revealed the presence of previously unseen substructures within the flat central "kernel" of the core. Their analysis shows that such small structures are indeed smaller than their corresponding Jeans lengths and not in the process of contraction. They show that such observed bumps are the result of interferometric filtering instead of the detection of new sources.

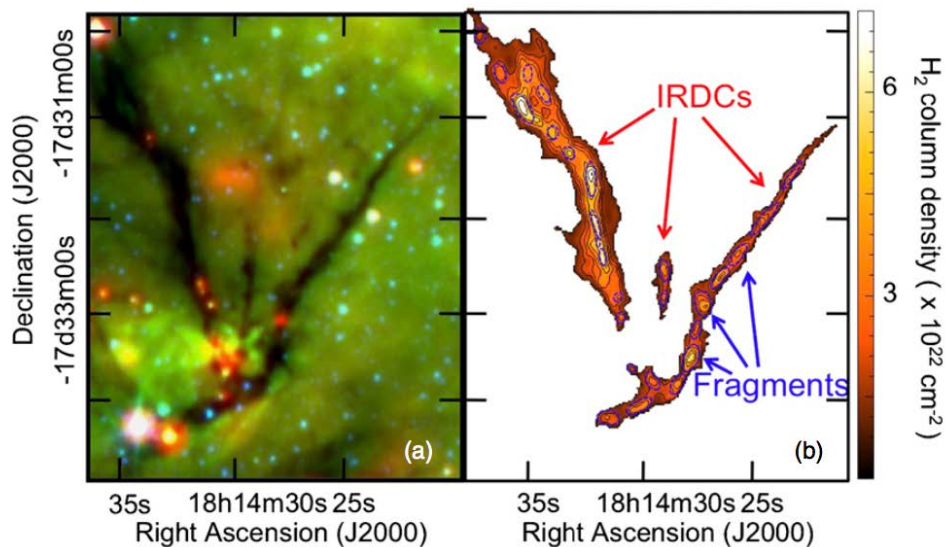


Figure 1.1: Filamentary Infrared Dark Clouds (IRDCs) converging at a common hub and fragmenting into dense cores. On the left, the cloud is seen in extinction against the infrared dust continuum at $3.6 \mu\text{m}$ (blue), $8 \mu\text{m}$ (green) and $24 \mu\text{m}$ (red) by the Spitzer telescope's composite image. On the right, H₂ column density map reconstructed from the $8 \mu\text{m}$ extinction map. Image taken from Motte et al. (2018).

Starless and prestellar cores

As described in the previous section and originally introduced by Larson (1969), a *core* refers to a self-gravitating object that forms within a clump (Draine 2011). If it undergoes collapse, the core can gather surrounding gas through infalling gas motions. Cores typically exhibit a density profile that reaches its peak around 10^4 - 10^5 cm^{-3} or higher. Their masses range from approximately 0.5 - $5 M_{\odot}$ for low-mass cores, and can extend even higher, reaching around $100 M_{\odot}$ for high-mass cores.

In simple terms, *starless cores* are a class of cores without any embedded objects like protostars. Their future regarding gravitational collapse is uncertain. They might either disperse and merge back with the surrounding clump gas or contract and collapse after accumulating enough material from the parent cloud. This outcome depends on their dynamic state, which is determined by the virial parameter and the magnetic field they are surrounded by (see section 1.1.2). On the other hand, *prestellar cores* refer to a specific subset of starless cores that exhibit signs of eventual star formation. These cores have already become gravitationally unstable and are undergoing isothermal collapse, similar to that of a Bonnor-Ebert sphere (see section 1.2.1). These are isothermal spheres characterized by a centrally flat density profile that steeply declines (following an inverse square law) towards the edges (see 1.2).

Low-mass cores refer to cores that contain masses comparable to or slightly larger than that of the sun. These cores have the ability to form only low-mass stars. They are quiescent in their interiors, with gas temperatures of around 10 or 15 K and sonic motions. High-mass starless cores are those containing masses higher than $10 M_{\odot}$ and usually found at larger distances (>1 kpc) than for low-mass stars. Massive cores are also associated with a tendency to have warmer temperatures and supersonic flows. Finding such massive cores presents a harder challenge than for the low-mass counterparts, specially because of the large distances and high optical depth within hubs (the most likely birthplaces of massive stars). Additionally, massive stars are short-lived stars that tend to rapidly contaminate their birthplace with stellar winds and supernova explosions, making it difficult to observe their formation.

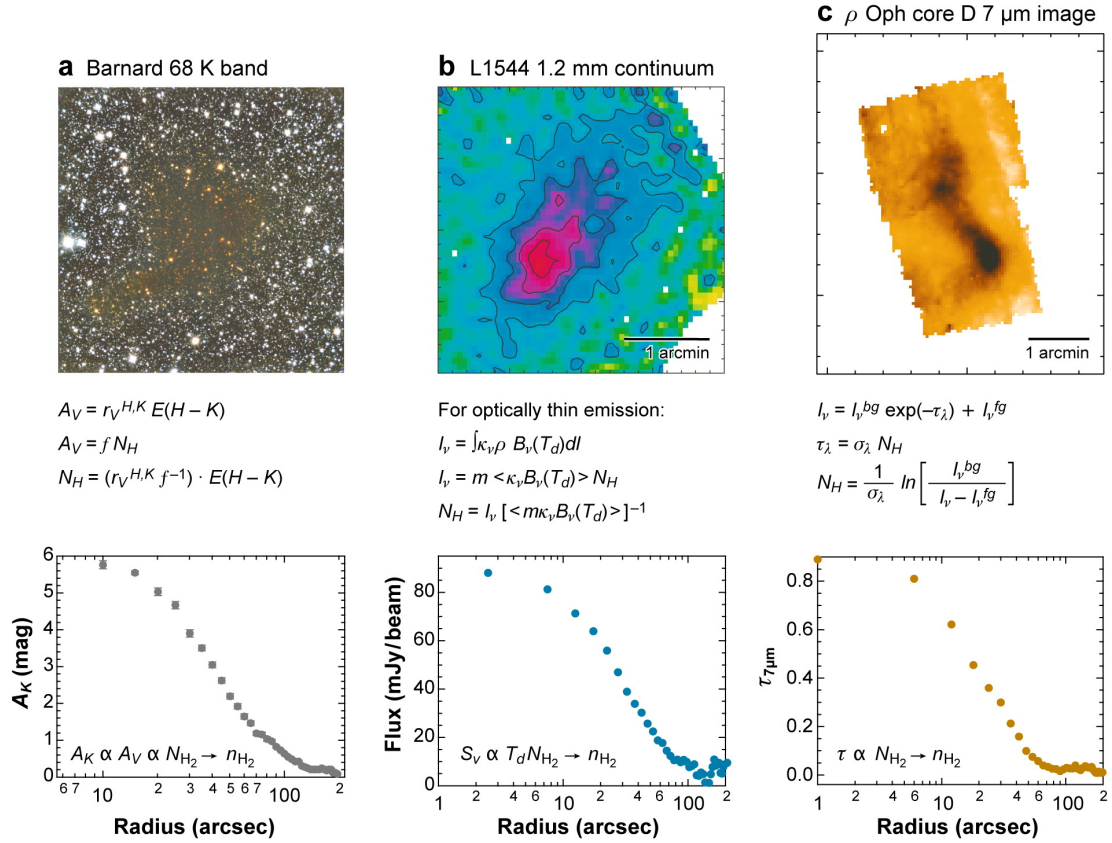
1.1.2 Cloud stability and fragmentation

The virial theorem

In this section, I provide an insight to the theoretical framework upon which star formation has been built. This is, the virial theorem for spherically symmetric objects, and states what are the conditions for cloud equilibrium or cloud instability. We start from the magneto-hydrodynamics (MHD) equations for molecular clouds on scales where viscosity and resistivity can be neglected. we begin with the two fundamental equations, the continuity equation (mass conservation) and the momentum equation:

$$\frac{\partial \rho}{\partial t} = -\nabla \cdot (\rho \mathbf{v}), \quad (1.2)$$

$$\frac{\partial \rho \mathbf{v}}{\partial t} = -\nabla \cdot (\rho \mathbf{v} \mathbf{v}) - \nabla \mathbf{P} + \frac{1}{4\pi} (\nabla \times \mathbf{B}) \times \mathbf{B} - \rho \nabla \phi, \quad (1.3)$$



 Bergin EA, Tafalla M. 2007. Annu. Rev. Astron. Astrophys. 45:339–96

Figure 1.2: Derivation of density profiles for prestellar cores using three different methods. In panel (a), the Barnard 68 cold dark cloud is observed in the K-band, and the equations used to determine the extinction distribution are shown, along with the corresponding results (Alves et al. 2001). Panel (b) presents the L1544 dark cloud, where a dense core is highlighted in the 1.2-mm continuum map, and the equations and results of the flux estimation are provided (Ward-Thompson et al. 1999). Panel (c) showcases the ρ Oph dark cloud, with a dense core detected against the bright background of PAHs, and the equations and results of the opacity estimations are presented (Bacmann et al. 2000). This image is taken from Bergin & Tafalla (2007).

where ρ is the gas density, \mathbf{v} is the gas velocity, \mathbf{P} is the pressure in the cloud, \mathbf{B} is the magnetic field and ϕ is the gravitational potential, so that $-\rho \nabla \phi$ represents the gravitational force per unit volume. The fluid pressure tensor $\mathbf{\Pi}$ and the Maxwell stress tensor \mathbf{T}_M can be defined as

$$\mathbf{\Pi} = \rho \mathbf{v} \mathbf{v} + \mathbf{P} \mathbf{I} \quad (1.4)$$

$$\mathbf{T}_M = \frac{1}{4\pi} \left(\mathbf{B} \mathbf{B} - \frac{B^2}{2} \mathbf{I} \right), \quad (1.5)$$

with \mathbf{I} is the identity tensor. If we now rewrite (1.4) and (1.5) in tensor form, we get

$$\Pi_{ij} = \rho v_i v_j + P \delta_{ij} \quad (1.6)$$

$$(\mathbf{T}_M)_{ij} = \frac{1}{4\pi} \left(B_i B_j - \frac{1}{2} B_k B_k \delta_{ij} \right), \quad (1.7)$$

which we use to rewrite equation (1.3),

$$\frac{\partial \rho \mathbf{v}}{\partial t} = -\nabla \cdot (\mathbf{\Pi} - \mathbf{T}_M) - \rho \nabla \phi \quad (1.8)$$

by using $\nabla \cdot \mathbf{T}_M = 1/(4\pi)(\nabla \times \mathbf{B}) \times \mathbf{B}$ and $(\nabla \times \mathbf{B}) \times \mathbf{B} = \nabla \cdot (\mathbf{B}\mathbf{B} - B^2/2)$. Let us now consider a spherical cloud of gas encompassing a volume V and a surface S . For such a cloud, the moment of inertia (i.e., the mass distribution) will be given by

$$I = \int_V \rho r^2 dV. \quad (1.9)$$

To study the temporal evolution of the overall mass distribution, we will assume that mass changes within the cloud can be neglected. Thus, we take the time derivative of I

$$\frac{dI}{dt} = \int_V \frac{\partial \rho}{\partial t} r^2 dV,$$

we apply the continuity equation (1.2)

$$\dot{I} = - \int_V \nabla \cdot (\rho \mathbf{v}) r^2 dV$$

and we bring r^2 into the divergence to then use the divergence theorem

$$\begin{aligned} \dot{I} &= - \int_V \nabla \cdot (\rho \mathbf{v} r^2) dV + 2 \int_V \rho \mathbf{v} \cdot \mathbf{r} dV \\ &= - \int_S (\rho \mathbf{v} r^2) \cdot d\mathbf{S} + 2 \int_V \rho \mathbf{v} \cdot \mathbf{r} dV. \end{aligned}$$

Let us now take the time derivative of I once more, and multiply it by $\frac{1}{2}$

$$\begin{aligned} \frac{1}{2} \ddot{I} &= -\frac{1}{2} \int_S r^2 \frac{\partial}{\partial t} (\rho \mathbf{v}) \cdot d\mathbf{S} + \int_V \frac{\partial}{\partial t} (\rho \mathbf{v}) \cdot \mathbf{r} dV, \\ &= -\frac{1}{2} \frac{d}{dt} \int_S r^2 (\rho \mathbf{v}) \cdot d\mathbf{S} - \int_V \mathbf{r} \cdot [\nabla \cdot (\mathbf{\Pi} - \mathbf{T}_M) + \rho \nabla \phi] dV. \end{aligned} \quad (1.10)$$

For the right-hand-side volume integral we have replaced $\frac{\partial}{\partial t} (\rho \mathbf{v})$ using (1.8). Now we can decompose the volume integral of the gradient of a function as the difference between the surface integral of the function and the volume integral of the "trace" of the function, as

$$\int_V \mathbf{r} \cdot \nabla \cdot (\mathbf{\Pi} - \mathbf{T}_M) dV = \int_S \mathbf{r} \cdot (\mathbf{\Pi} - \mathbf{T}_M) \cdot d\mathbf{S} - \int_V \text{Tr}(\mathbf{\Pi} - \mathbf{T}_M) dV, \quad (1.11)$$

here Tr is called the trace operator. From equations 1.4 and 1.5, the trace of $\mathbf{\Pi}$ and \mathbf{T}_M are

$$\begin{aligned}\text{Tr}(\mathbf{\Pi}) &= 3P + \rho v^2, \\ \text{Tr}(\mathbf{T}_M) &= -\frac{B^2}{8\pi}.\end{aligned}$$

Applying now these two expressions to the volume integral of (1.10), we get the general form of the virial theorem

$$\frac{1}{2}\ddot{I} = 2(\mathcal{T} - \mathcal{T}_S) + \mathcal{B} + \mathcal{W} - \frac{1}{2} \frac{d}{dt} \int_S (\rho \mathbf{v} r^2) \cdot d\mathbf{S}, \quad (1.12)$$

Let's go over every term on this last equation.

$$\mathcal{T} = \int_V \left(\frac{1}{2} \rho v^2 + \frac{3}{2} P \right) dV = \frac{3}{2} M \sigma^2 \quad (1.13)$$

is the sum of the kinetic and the thermal energy of the cloud, with σ being the velocity dispersion,

$$\mathcal{T}_S = \int_S \mathbf{r} \cdot \mathbf{\Pi} \cdot d\mathbf{S} = 4\pi R^3 P_S \quad (1.14)$$

is the pressure on the surface of the cloud,

$$\mathcal{B} = \frac{1}{8\pi} \int_V B^2 dV - \int_S \mathbf{r} \cdot \mathbf{T}_M \cdot d\mathbf{S} \quad (1.15)$$

is the magnetic pressure inside the cloud, providing support against collapse, minus the magnetic pressure in the surface, attempting to compress the cloud, and

$$\mathcal{W} = - \int_V \rho \mathbf{r} \cdot \nabla \phi dV = -a \frac{GM^2}{R} \quad (1.16)$$

is the gravitational energy of the cloud. In this last term, a a constant of order unity and depends on the internal density distribution. Finally, the rightmost term in (1.12) accounts variations in the momentum flux across the surface of the cloud. If we neglect the divergence of momentum through the clouds surface, and consider a magnetic field fixed at B_0 , we can reduce the general form of the virial theorem to

$$\frac{1}{2}\ddot{I} = 2(\mathcal{T} - \mathcal{T}_S) + \mathcal{B} + \mathcal{W}, \quad (1.17)$$

where

$$\mathcal{T}_S = \int_S r P dS \quad (1.18)$$

$$\mathcal{B} = \frac{1}{8\pi} \int_V (B^2 - B_0^2) dV. \quad (1.19)$$

The fundamental statement of the virial theorem lies on the integrated form of the acceleration, \ddot{I} , and can be interpreted as follows

- $\ddot{I} < 0$: Contraction terms dominate (surface pressure and gravity) and the cloud accelerates inward, i.e., contracts,
- $\ddot{I} > 0$: Expansion terms dominate (thermal pressure and magnetic support) and the cloud accelerates outward, i.e., expands,
- $\ddot{I} = 0$: the cloud is said to be in *virial equilibrium*.

Furthermore, for the particular case of a system in virial equilibrium and with negligible surface and magnetic forces, we can write $2\mathcal{T} = -\mathcal{W}$. We can use this to characterize the state of the cloud with the ratio of both components, as

$$\alpha_{\text{vir}} = \frac{2\mathcal{T}}{|\mathcal{W}|}. \quad (1.20)$$

This characteristic ratio is known as the *virial parameter* or *virial ratio* of a cloud (Bertoldi & McKee 1992; McKee et al. 1993). Analogous to what we did with the values of \ddot{I} , we distinguish three main cloud states from the virial parameter

- If $\alpha_{\text{vir}} > 1$, then $\ddot{I} > 0$ and the cloud is likely to expand. The system said to be *supervirial*,
- if $\alpha_{\text{vir}} < 1$, then $\ddot{I} < 0$ and the cloud is likely to collapse. The system said to be *subvirial*,
- if $\alpha_{\text{vir}} = 1$, then $\ddot{I} = 0$ and the cloud is said to be in virial equilibrium.

The Jeans instability

Additional conditions for the stability of a cloud against fragmentation have been proposed in the past and commonly used in astronomy. Jeans (1902) studied the effects of the growth of perturbations in the fluid properties of a gas cloud. He did so by linearly-perturbing the gas motion equations (1.2) and (1.3). For this, one needs to consider small variations of every quantity involved in the equations. We do so accounting for first-order approximations only, and the terms for the density, pressure, velocity and gravitational potential for a uniform, infinite and isothermal medium at rest, read as follows

$$\rho = \rho_0 + \epsilon\rho_1, \quad (1.21)$$

$$\mathbf{v} = \epsilon\mathbf{v}_1, \quad (1.22)$$

$$P = P_0 + \epsilon P_1, = c_s^2(\rho_0 + \epsilon\rho_1) \quad (1.23)$$

$$\phi = \phi_0 + \epsilon\phi_1. \quad (1.24)$$

In the expression for P , $c_s^2 = P_0/\rho_0$ and $\epsilon \ll 1$ is the very small normalized perturbation. Jeans (1902) modelled such perturbations as a sum of Fourier components for a single Fourier mode of the form $\rho_1 = \rho_a e^{i(kx - \omega t)}$. Converting the expressions for every term ρ , \mathbf{v} , P and ϕ into Fourier modes, we can obtain the following *dispersion relation* (i.e., the relation between the spatial and

frequency properties of a system modelled as a wave, see Jeans 1902, Krumholz 2015 or Stahler & Palla 2004 for details on the derivation)

$$w = \sqrt{c_s^2 k^2 - 4\pi G \rho_0}, \quad (1.25)$$

with w and k the temporal and spatial frequency of the plane perturbation wave, respectively. This relation means that in the case of a short spatial range, or large spatial frequency, k is large and terms inside the square root $c_s^2 k^2 - 4\pi G \rho_0 > 0$. This implies that w is a real number and the exponential perturbations do not grow ($|e^{i(kx-wt)}| < 1$). On the other hand, in the case of large spatial range perturbations, or small spatial frequency perturbations, $c_s^2 k^2 - 4\pi G \rho_0 < 0$ and w becomes imaginary, leading $|e^{i(kx-wt)}|$ to either decay towards zero or to grow infinitely large in time. The latter case, represents the *Jeans instability* and states that if the density of a cloud faces very tiny deviations with respect to the background values, at a sufficiently large spatial scale (interpreted as a wavelength) it will eventually grow large.

Similar to the case of \ddot{I} and α_{vir} , the dispersion relation provides a threshold for stability at $w = 0$. This means that

$$k_J = \sqrt{\frac{4\pi G \rho_0}{c_s^2}},$$

is the spatial frequency for stability. We can convert this wavenumber into a wavelength, or physical scale

$$\lambda_J = \frac{2\pi}{k_J} = \sqrt{\frac{\pi c_s^2}{G \rho_0}}. \quad (1.26)$$

This scale receives the name of *Jeans length*. Moreover, we can derive the mass associated to this stability length as

$$M_J = \frac{\rho \lambda^3}{8}, \quad (1.27)$$

which receives the name of *Jeans Mass*. The Jeans mass sets the mass above which gravitational collapse is triggered. Analogously, the Jeans length is the threshold radius over which a sphere of fixed mass would undergo collapse. The Jeans length has been found to be smaller than the characteristic scales of most GMCs, suggesting that the Jeans instability mechanism is the most likely scenario for GMCs to initiate collapse. This criterion can also be applied at smaller scales to determine whether collapse is occurring in fragmented clumps within dark clouds. Furthermore, within the context of GMCs, where the length scale of perturbations matches the scale of the cloud, we can approximate $w \approx \pm i \sqrt{4\pi G \rho}$. Considering the negative root (representing the growing perturbation), we find that

$$\rho \approx e^{\sqrt{4\pi G \rho_0} t}.$$

Now, we can solve for t to find the characteristic time for a pressureless cloud to undergo gravitational collapse. This would be

$$t_{\text{ff}} = \sqrt{\frac{3\pi}{32G\rho_0}}, \quad (1.28)$$

and is known as the *free-fall* time.

The role of magnetic fields

The previous derivations of the virial theorem have so far neglected the effects of the magnetic field support, however, they do play an important role on the stability of a cloud (Parker 1966). To understand its contribution, we start by considering a cloud threaded by a two component magnetic field, an internal uniform magnetic field of strength B and a considerably weaker external magnetic field of uniform strength B_0 . These are the two components of the magnetic tensor expressed in (1.15). The strong field inside the cloud and the magnetic pressure in the surface can be approximated to

$$\frac{1}{8\pi} \int_V B^2 dV \approx \frac{B^2 R^3}{6}, \quad \int_S \mathbf{x} \cdot \mathbf{T}_M \cdot d\mathbf{S} = \int_S \frac{B_0^2}{8\pi} \mathbf{x} \cdot d\mathbf{S} \approx \frac{B_0^2 R_0^3}{6}, \quad (1.29)$$

respectively. We now equate the magnetic field going through the cloud to the one crossing the surface of the cloud as $\Phi_B = \pi B R^2 = \pi B_0 R_0^2$. Now we express the magnetic tensor (1.15) as

$$\mathcal{B} \approx \frac{B^2 R^3}{6} - \frac{B_0^2 R_0^3}{6} = \frac{1}{6\pi^2} \left(\frac{\Phi_B^2}{R} - \frac{\Phi_B^2}{R_0} \right) \approx \frac{\Phi_B^2}{6\pi^2 R}, \quad (1.30)$$

We notice that \mathcal{B} falls to zero when R_0 extends to infinity. We can now compare the magnetic and gravitational (1.16) contribution of both virial terms

$$\mathcal{B} + \mathcal{W} = \frac{\Phi_B^2}{6\pi^2 R} - \frac{3GM^2}{5R} = \frac{3G}{5R} (M_\Phi^2 - M^2), \quad (1.31)$$

and solve for M_Φ ,

$$M_\Phi = \sqrt{\frac{5}{2}} \left(\frac{\Phi_B}{3\pi\sqrt{G}} \right) \approx \frac{\Phi_B}{2\pi\sqrt{G}}. \quad (1.32)$$

This mass represents a *magnetic critical mass*, yet another characteristic ratio for cloud stability. The cloud's behaviour set with this threshold mass can be summarized as follows,

- If $M > M_\Phi$, then $\mathcal{B} + \mathcal{W} < 0$, the magnetic force is incapable to halt the gravitational contraction,
- if $M < M_\Phi$, then $\mathcal{B} + \mathcal{W} > 0$, the magnetic force overcomes the gravitational contraction and attempts to stabilize the cloud,
- if $M = M_\Phi$, then $\mathcal{B} + \mathcal{W} = 0$, both magnetic and gravitational forces are in equilibrium.

A corollary characteristic ratio can be derived from this magnetic critical mass, that is more commonly used in observational studies of prestellar cores. This is known as the *mass-to-flux ratio* μ

$$\mu_{\text{crit}} = \left(\frac{M}{\Phi} \right)_{\text{crit}} = \frac{1}{2\pi\sqrt{G}}, \quad (1.33)$$

whose classification can be listed as

- if $\mu / \mu_{\text{crit}} > 1$, the cloud is said to be *supercritical*,
- if $\mu / \mu_{\text{crit}} < 1$, the cloud is said to be *subcritical*,
- if $\mu / \mu_{\text{crit}} = 1$, the cloud is in equilibrium.

As a final note, we can see from equation (1.31) that since $\mathcal{B} + \mathcal{W} \propto R^{-1}$, this sum grows as the cloud compresses, making the magnetic support eventually large enough to halt the collapse. This statement remain always true within the framework of ideal-MHD, whose main assumption is that of *flux-freezing*. Flux-freezing means that the neutrals and ions of the gas (either atomic or molecular) are collisionally coupled and therefore they follow a common fluid dynamics, with negligible velocity drift. The decoupling of ions and neutrals, namely, a ion-neutral drift, occurs in the dense inner regions of dense cores with low ionization fraction and receives the name of *ambipolar diffusion*. Ambipolar diffusion breaks the flux-freezing assumption and allows for a cloud to start in a subcritical state and become supercritical, leading to its collapse.

1.2 Low-mass star formation

1.2.1 Prestellar collapse

Once a dense core becomes unstable and undergo collapse, it initiates the prestellar phase. The theoretical description of prestellar collapse is based on the seminal work of Bonnor (1956) and Ebert (1955), derived from the hydrostatic equilibrium of an isothermal sphere supported by internal thermal pressure and bounded by an external pressure on its surface P_S . The condition for the virial equilibrium of such an object (retrieving equations 1.13, 1.14 and 1.16; with $a = 3/5$) is

$$0 = 2(\mathcal{T} - \mathcal{T}_S) + \mathcal{W} \quad (1.34)$$

$$= 3Mc_s^2 - 8\pi R^3 P_S - \frac{3GM^2}{5R} \quad (1.35)$$

from where we can solve for the surface pressure P_S ,

$$P_S = \frac{3Mc_s^2}{8\pi} \left[\frac{1}{R^3} - \left(\frac{GM}{5c_s^2} \right) \frac{1}{R^4} \right]. \quad (1.36)$$

The radial dependency of this pressure is two-fold, the R^{-3} and $-R^{-4}$ terms dominate at large and small values of R , respectively. To find the radius at which the pressure is maximum between these two terms, we derive P_S

$$\frac{dP_S}{dR} = \frac{3Mc_s^2}{8\pi} \left[\left(\frac{4GM}{5c_s^2} - \frac{3}{R^4} \right) \frac{1}{R^5} \right], \quad (1.37)$$

we set it to zero and we solve for R

$$R_{\text{BE}} = \frac{4GM}{15c_s^2}. \quad (1.38)$$

This R_{BE} is then the maximum radius for a sphere of uniform density to be in virial equilibrium and receives the name of *Bonnor-Ebert radius*. The pressure of the cloud at this radius is

$$P_S \approx 1.57 \frac{c_s^8}{G^3 M^2}.$$

We can also solve for the mass that a spherical gas cloud with thermal pressure P_S can hold to remain in hydrostatic equilibrium, namely, the *Bonnor-Ebert mass*

$$M_{\text{BE}} = 1.18 \frac{v_T^4}{\sqrt{P_S G^3}}, \quad (1.39)$$

where $v_T = \sqrt{kT/\mu m_{\text{H}}}$ is the isothermal sound speed and μ the molecular mass. The radial density profile of such sphere is given by

$$\rho(r) = \frac{c_s^2}{2\pi G r^2}. \quad (1.40)$$

This density distribution resembles that of a Plummer sphere but has a smoother central part, so-called plateau or kernel (see 1.2 for such observational signatures).

1.2.2 Protostar formation

Once a prestellar core becomes supercritical and the thermal pressure is low enough to allow gravitational collapse to go on, the gas starts to fall inward having non-zero angular momentum. The infalling trajectories happen preferentially along the magnetic field lines, on the scales where the flux-freezing assumption holds. Rotation and flux-freezing lead to the pinching of magnetic field lines in the regions closer to the rotation plane. Ambipolar diffusion lets some material to leak through towards the center of the core, creating a steadily increasing radial density contrast. The conservation of angular momentum from the parent cloud, makes this infalling and rotating material to form a circumstellar disk around the central high density. The prestellar collapse phase has so far proceeded almost isothermally, thanks to the efficient thermal cooling of the optically thin material. The rapid central density increase quickly becomes opaque to its own thermal radiation and turns the collapse into an adiabatic process. Further compression increases the central temperature of the molecular hydrogen and so does the outward thermal pressure. This enhanced pressure decelerates the infalling material up to the point of reaching hydrostatic equilibrium. This short-lived hydrostatic structure is known as the *first core*. The remaining infalling material that sits right outside the optically thick surface, can still radiate infrared thermal emission, making this stage potentially observable. However, the energy loss from this outer layer further enhances compression, and makes the core to stop expanding and rather to shrink. The mass of the core at this point is about $5 \times 10^{-2} M_{\odot}$ and ~ 5 AU in radius (Stahler & Palla 2004). Fig. 1.3 show snapshots of 3D non-ideal MHD simulations that follow the prestellar collapse and protostar formation. In the upper panel of the figure it can be seen how a flattened rotating hydrostatic structure is formed from an initially rotating collapsing core. The gas within

the core remains molecular up to this point but quickly increase in temperature (≥ 850 K). The addition of mass and shrinking of the core easily raises the temperature to above 2000 K and triggers collisional dissociation of H_2 and converts the innermost gas into atomic hydrogen. This process repeats and extends inside-out, converting most of the inner hydrogen from molecular to atomic. This process cannot extend infinitely without becoming gravitationally unstable (Stahler & Palla 2004), and that is indeed what happens. The core then undergoes a *second collapse*, marking the end of the first core phase, and giving birth to a newly born protostar. This new protostar has a radius of a few solar radii, a mass of $\sim 0.1 M_\odot$ and a mean internal temperature of 10^5 K.

As the protostar increase its central temperature and density it begins to burn deuterium, turning the central hydrostatic sphere into a fully convective core (see Fig. 1.4) and entering the pre-main-sequence phase. The gas that keeps falling from the outer envelope falls now at free-fall speed, which is much larger than the local sound speed, and generates an accretion shock front around the protostar's surface (see Fig. 1.4). The free-falling gas landing on the accretion front converts all its kinetical energy into radiation, namely, into accretion luminosity. This is, at this radial scale, the main source of luminosity from the protostar, even above the contributions from nuclear burning and quasi-static contraction of the interior. This optical radiation is nevertheless absorbed by an optically thick spherical photosphere of accumulated infalling dust, and makes the protostar invisible to an external infrared observer (see Fig. 1.4). The inner layers of the optically heated dust can easily overcome the grain's sublimation temperature and evaporate some of the solid material, creating a opacity gap (see Fig. 1.4). The external layers of the dusty envelope can instead survive as solid grains and re-emit the optical radiation in the form of infrared emission. This form of protostellar infrared emission represents the main observable property of the protostar formation process.

1.2.3 Protostellar disk formation

Formation and evolution of an accretion disk

The contracting core does not only collapse radially under gravitational pull. The reality is that all dense cores inherit some degree of rotation from their parent filaments and molecular clouds. The conservation of this angular momentum along the the collapse leads to the formation of a rotating disk around the central protostar. Gas parcels with low initial specific angular momentum will probably be deposited on the surface of the protostar, whereas those with the largest specific angular momentum can spiral inwards, miss the protostar and land at a radius far from the center. The particle with the maximum specific angular momentum will land the farthest from the protostar and will define the radius of the newly born disk. This is known as the *centrifugal radius* and defined the actual radius of the disk under the consideration of only rotational and gravitational forces. For every spiraling particle, at least one analogous gas parcel at the other hemisphere of the cloud will mirror such trajectory and collide with the other at the midplane (Stahler & Palla 2004). Such an accretion happens at supersonic speed and develops an accretion surface in the ever growing outer layer of the disk. Accretion onto the protostar is thought to be episodic with evidence of this found in jets and outflows showing knots and bullets

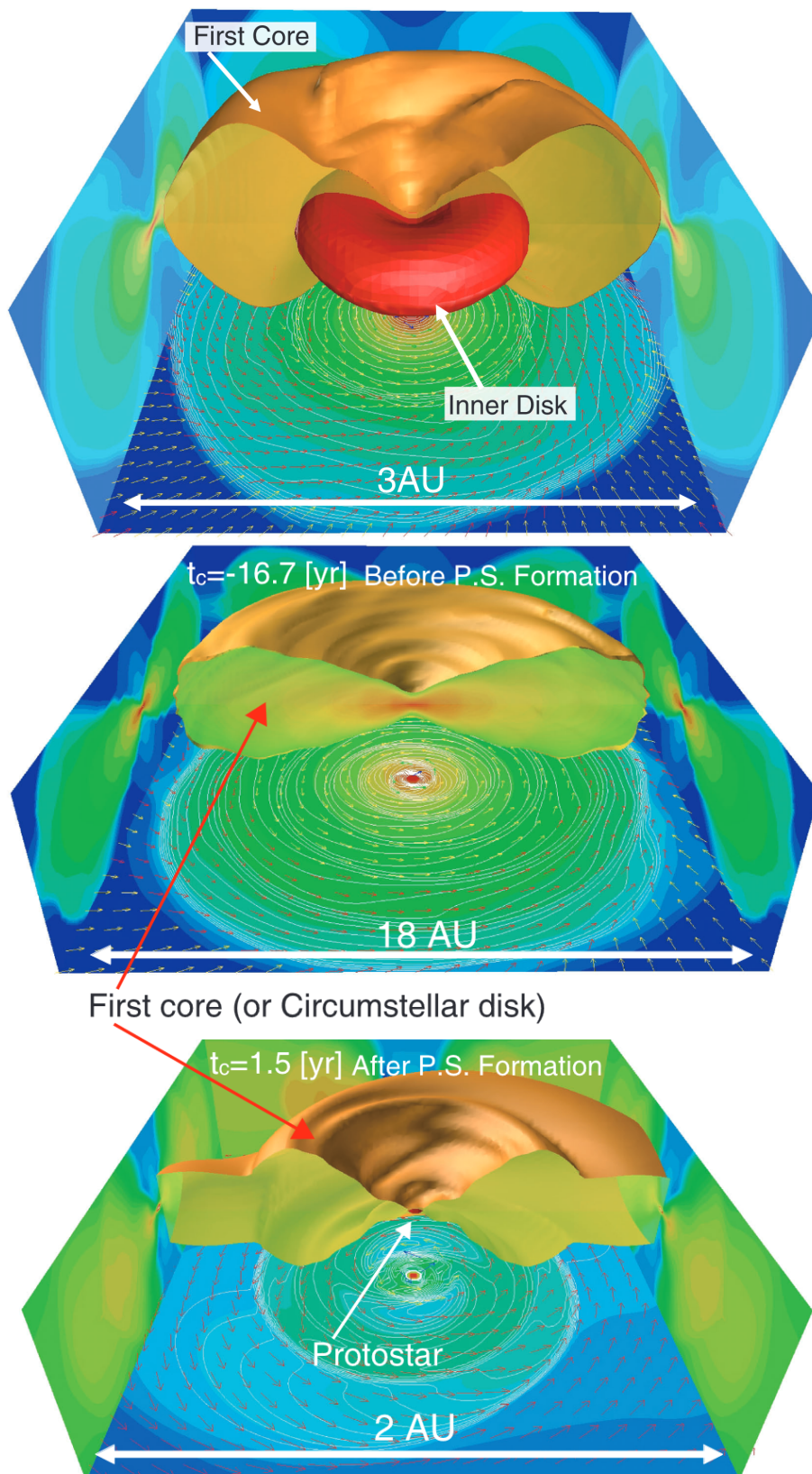


Figure 1.3: 3D non ideal-MHD simulations of first core and circumstellar disk formation (Machida et al. 2011). Upper panel shows a first core and an inner rotating disk formed from the collapse of a magnetized rotating core 1.6 yrs after protostar formation. Central and bottom panels show timeframes before and after protostar formation, with the 2D disk and protostar density projected at the bottom of the scene.

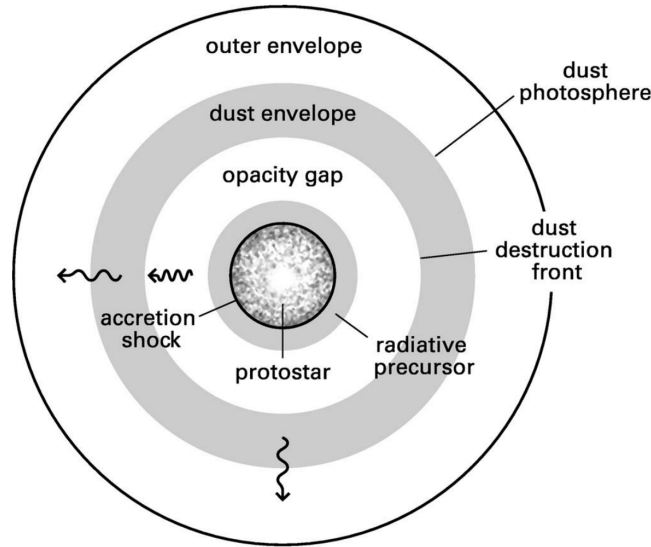


Figure 1.4: Close surroundings of a newly born protostar and its various fronts of accretion and obscuration from infalling material. The main protostar luminosity comes from free-falling envelope gas that converts all its kinetic energy into thermal radiation after it lands on the stellar surface, though this is invisible to an external observer. The observed protostellar infrared flux comes from the warm dust envelope that is heated by the accretion luminosity (Stahler & Palla 2004).

(Plunkett et al. 2015). This accretion of material from the envelope has been recently observed to be asymmetric and not necessarily smooth (see Fig. 1.5), consistent with predictions from numerical simulations that introduce asymmetries in the natal core due to turbulence (Seifried & Walch 2015; Kuffmeier et al. 2018, 2021). These portions of gas that feed the disk have been labelled *streamers* and have been the target source of many recent observations (Pineda et al. 2020; Valdivia-Mena et al. 2022; Garufi et al. 2022; Pineda et al. 2022).

After a million years, envelope accretion onto the disk diminishes and the inner disk becomes rotationally supported. If the mass accretion from the envelope overcomes the accretion onto the protostar, the disk accumulates mass. If the disk mass grows large enough to make self-gravity overcome the rotational stability then the disk becomes gravitationally unstable (Kratte & Lodato 2016). Such a stability condition is characterized by the already introduced Toomre Q parameter (see equation 1.1). Stability criteria states that $Q \lesssim 1.7$ indicates local gravitational instability (Durisen et al. 2007). Gravitational instability (GI) results in local overdensities across the disk becoming gravitationally bound and decoupled from the rest of the disk. This decoupling does not imply that the disk disrupts globally. It still keeps rotating but fragmented. Common substructures found on gravitationally unstable disks are in the form of two or more spiral arms (Dong et al. 2016). In Chapter 3 we discuss on the idea that the young protostellar disk in IRAS 16293-2422 B, classified as a Class 0 (see below) is undergoing GI and potentially contains two unresolved spiral arms. The large mass required to develop GI means that dissipation processes driven by the accretion heat the disk as the mass flows inward. Such a massive and optically thick

disk cools down very inefficiently (Rafikov 2009; Kratter et al. 2008; Rafikov 2015). This heating source can result in very high gas midplane temperatures ($\gtrsim 500$ K). This high temperatures make the dusty disk look brighter than as it would only by protostellar heating.

Observational evolutionary stages of protostars and disks

The dusty envelope of the central protostar and its circumstellar disk become bright in the infrared regime. The spectrum of such radiation is now the combination of two black-body components, the protostar and the disk. The protostar is initially hidden and only the disk is visible. As the system evolves and the envelope fades, the protostar becomes more visible and the disk optically thinner, varying their single contributions to the Spectral Energy Distribution (SED). This time variation of the SED allows to classify protostars and Young Stellar Objects (YSOs) according to their formation stage, using the slope of the spectrum at the points where both black-body are expected to peak (Lada 1987). This is quantified with the spectral index

$$\alpha = \frac{d \log(\lambda F_\lambda)}{d \log \lambda} \quad (1.41)$$

or $\nu F_\nu \propto \nu^{-\alpha}$. Due to the IR absorption from the ground, two atmospheric windows are commonly used to compute the spectral index: the $2.2\mu\text{m}$ (*K* band) and the $10\mu\text{m}$ (*N* band). For these two, α is obtained as

$$\alpha_{K,N} = \frac{\log(\lambda F_\lambda)_{10\mu\text{m}} - \log(\lambda F_\lambda)_{2.2\mu\text{m}}}{\log(10/2.2)}, \quad (1.42)$$

and the classification, also depicted in figure 1.5, goes as follows:

- **Class 0:** are protostars highly obscured, with a spectrum peaking at $100\mu\text{m}$. At this stage, the protostars are invisible at $2.2\mu\text{m}$ and suffer from deep absorption at $10\mu\text{m}$ by cold dust. Thus, to distinguish them from first cores and Class I object, people classified them as sources with a ratio of submillimeter ($\lambda \gtrsim 350\mu\text{m}$) over bolometric (namely, black-body) luminosity $L_{\text{submm}}/L_{\text{bol}}$ greater than 0.5% (Dunham et al. 2014). Class 0 protostars are also characterized by the low black-body temperatures of their warm dust, above 20 and below 70 K (Chen et al. 1995), with little to no contribution from the protostar. Signatures of infall are detected by means of asymmetric molecular line spectra (e.g., Pineda et al. 2012). Typical lifetimes of Class 0 and I objects is around $<5 \times 10^5$ yr (Dunham et al. 2014), measured after the onset of prestellar collapse.
- **Class I:** are source whose spectral index is positive and larger than 0.3 (between $-0.3 \leq \alpha_{K,N} < 0.3$ they receive the name of Flat-SED Greene et al. 1994). This means that the emission at $10\mu\text{m}$ is stronger than at $2.2\mu\text{m}$. The blackbody temperature of Class I objects is lower than 650 K (Chen et al. 1995), a combination of warm dust and the now slightly visible protostar. Class 0 and Class I protostars are episodically fed by asymmetric infalling streamers from the parent cloud (Pineda et al. 2022).
- **Class II:** are sources with a spectral index $-1.6 < \alpha_{K,N} < 0.3$ (Dunham et al. 2014) and a blackbody temperature between 650 and 2800 K (Chen et al. 1995). The Class II YSOs

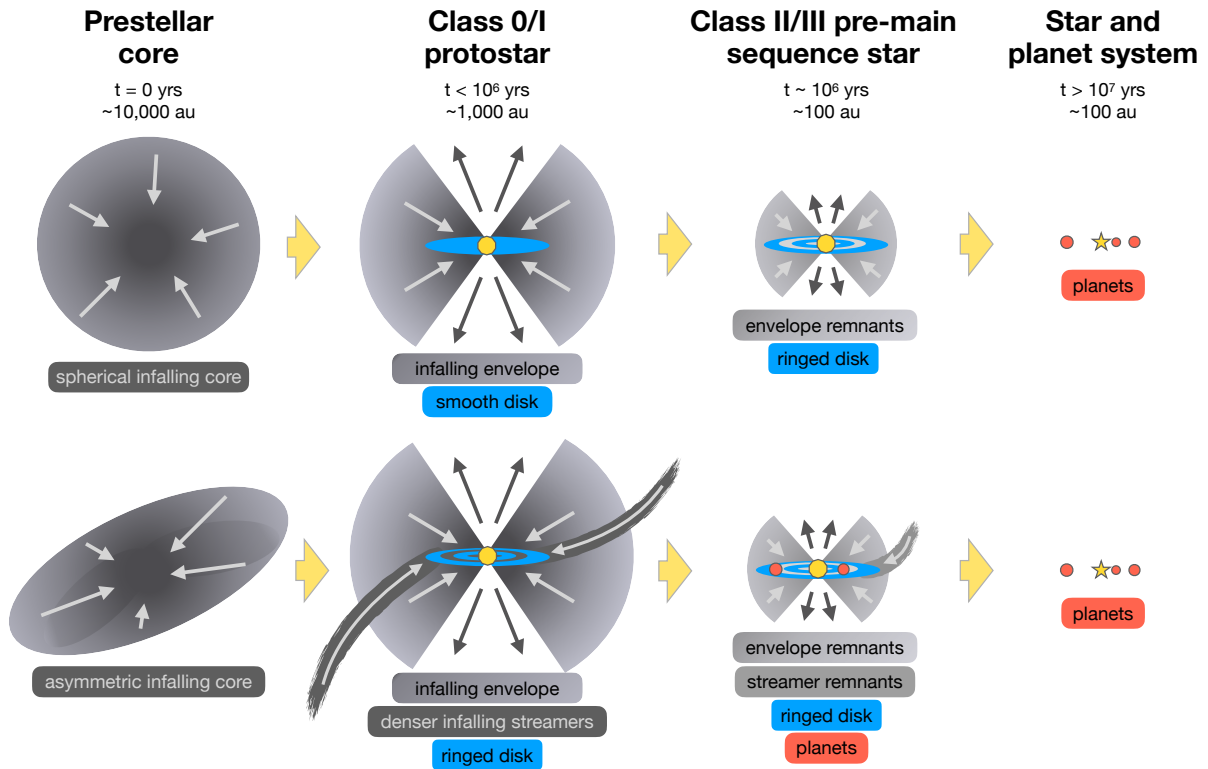


Figure 1.5: Previous (upper row) and revisited (bottom row) schematic of the protostar, protostellar and protoplanetary disk formation process. Classifications are based on the slope of the spectral energy distribution (spectral index) between two infrared wavelengths, 2.2 and $10\ \mu\text{m}$. The revisited frame of evolution suggests the presence of previously unseen streamers feeding the disk asymmetrically with material from the envelope. Image obtained from Pineda et al. (2022) and Segura-Cox (in prep.).

represent the well-known T Tauri stars, i.e., stars already in the pre-main sequence but still experiencing gravitational contraction and accretion from the disk. Their typical lifetimes of the order of 10^6 yr. In Class II disks, asymmetric streamers are still a source of cloud accretion but at a much lower rate than in earlier stages (Pineda et al. 2022).

- **Class III:** are sources with a spectral index $\alpha_{K,N} < -1.6$ and a blackbody temperature above 2700 K (Chen et al. 1995), since almost all the contribution to the bolometric temperature comes from the star. Class III protostars are also T Tauri stars that undergo gravitational contraction but with virtually no residual accretion. These objects are close to their final mass.

1.3 Radiative transfer

1.3.1 Basic concepts

The theory of radiative transfer deals with the propagation of electromagnetic radiation through a medium. The way to quantify this radiation depends on, from where do we observe it and in what units do we want to express it. In order to understand the following sections, a few basic concepts related to radiative transfer need to be introduced. First and foremost, luminosity. The luminosity L is the amount of energy radiated by an object per unit time and in all directions. The Stefan-Boltzmann law states that the luminosity of black-body at temperature T is $L \propto \sigma T^4$, with σ the Stefan-Boltzmann constant. When we attempt to observe such an object, we cannot get the energy radiated in all directions, but only that traversing a given surface area element. The amount of luminosity going through an element of area dA is called *flux*, and falls from the true luminosity as the fourth power of the distance d to the object, i.e., $F = L/4\pi d^2$. The flux that we receive in a given direction, confined by a solid angle $d\Omega = \sin\theta d\theta d\phi$ (with θ and ϕ the inclination from the zenith and the azimuthal angle from the source projected direction, respectively), within a finite frequency interval $d\nu$, is given by

$$dI_\nu = B_\nu \cos\theta d\Omega dA d\nu \quad (1.43)$$

and receives the name of *intensity*. The final relevant quantity to introduce, specially for the radiative transfer modelling detailed in Chapters 2 and 3, is called *brightness temperature* T_b . The brightness temperature is the temperature associated to a black-body that emits the same amount of energy as our observed system, and can be derived from the Plank's function or, more specifically to this thesis, from the Rayleigh-Jeans approximation of this function, valid within the radio wavelength regime. Solving for the temperature from the Rayleigh-Jeans approximation we get

$$T_b = \frac{\lambda^2}{2k_B\Omega} F \quad (1.44)$$

with k_B the Boltzmann constant and λ the wavelength of observation.

1.3.2 The equation of radiative transfer

The stationary radiation field traversing an absorbing and emitting medium is described by the specific intensity $I_\nu(x, n, \nu)$, where x represents a point in space within the medium and n represents a unit vector indicating the direction of propagation and wavelength. The propagation of radiation along its path can be described by the radiative transfer equation (RTE), and received the form,

$$\frac{dI_\nu}{ds} = -\kappa_\nu \rho I_\nu + j_\nu, \quad (1.45)$$

with s the direction of propagation. This equation can be more conveniently put in terms of the optical depth of the line-of-sight, as

$$\frac{dI_\nu}{d\tau_\nu} = S - I_\nu, \quad (1.46)$$

with \mathcal{S} known as the source function $\mathcal{S} = j_\nu/\kappa_\nu$. For a medium in Local Thermodynamic Equilibrium (LTE), each point of the system can be modelled as a black-body with local temperature T , whose source function equals the Planck's function, i.e.,

$$\mathcal{S} = \frac{j_\nu}{\kappa_\nu} = B_\nu(T). \quad (1.47)$$

This equation received the name of *Kirchoff's law* and is also conveniently expressed as $j_\nu = \kappa_\nu B_\nu(T)$. To find a general solution to the RTE, we need the source function not to depend on the incident intensity. Under this assumption, the a general solution to the RTE gets the form

$$I_\nu = \int_{-\infty}^s j_\nu(s) e^{-\tau(s_1, s_2)} ds, \quad (1.48)$$

where

$$\tau(s_1, s_2) = \int_{s_1}^{s_2} \kappa(s) \rho(s) ds, \quad (1.49)$$

is the optical depth along the direction of propagation.

We can interpret the general solution of the RTE as the following: the intensity of a light ray in s , is the result of the accumulated emission along every single point of propagation, exponentially attenuated by the factor of absorption towards the observer $e^{-\tau}$. This is indeed a formal and simplistic solution to the RTE, because in general the source function does depend on the matter properties (density, temperature and composition), and this properties can indeed be affected by the intensity itself. This simplistic scenario also assumes that all radiation is transported along a line and does not deflect or *scatter* into random directions. Realistic modelling of radiative transfer must indeed account for both absorbing and scattering processes. However, both processes are indeed different in nature (stochastic and non-stochastic) and need to be numerically modelled separately (i.e., raytracing vs monte-carlo; see section 1.3.3).

1.3.3 Radiative transfer on dusty media

Obtaining a general analytical solution to RTE by propagating rays in three dimensions, is not possible for realistic non-symmetric geometries and high model resolutions. Because of this, multiple radiative transfer code have been written (e.g., POLARIS Reissl et al. 2016, RADMC3D Dullemond et al. 2012, LIME Brinch & Hogerheijde 2010, RADEX van der Tak et al. 2007), focused on parallelizing the propagation of independent rays towards a common observer. Raytracing codes discretize the three spatial coordinates, the two propagation coordinates, wavelength intervals, also the dust and molecular properties, if included. The non-dust 3D-RT problem then becomes a 6D integro-differential problem that requires high amounts of computational resources (Steinacker et al. 2013). The main difference in numerical applications for solving RT on dusty media, lies on whether the energy is being propagated along a line or if it is being randomly scattered. Both of these cases should in principle always be combined to retrieve the true net flux (scattered plus thermal) but should be computed separately. The two numerical approaches for calculating thermal and scattered emission are ray-tracing and Monte-Carlo, respectively.

The Ray Tracing approach

The ray tracing (RayT) method propagates electromagnetic waves through a simulated medium with varying properties. The core function of RayT is to solve the first-order differential radiative transfer equation (1.45), for a given model grid cell and along a given direction. Every model cell is associated with a mass density ρ_0 , an absorption coefficient κ_0 , and an emission coefficient j_0 . All assumed to be constant within one cell. The intensity $I_\nu(s + \Delta s)$ (with Δs the cell length, i.e., the local spatial resolution) can be estimated by evolving $I_\nu(s)$ using the general solution to the RTE (equation 1.48) as

$$I_\nu(s + \Delta s) = I_\nu(s) e^{-\tau_0} + \frac{j_0 \Delta s}{\tau_0} (1 - e^{-\tau_0}), \quad (1.50)$$

with $\tau_0 = \kappa_0 \rho_0 \Delta s$. The propagation of this ray through several grid cells is the actual numerical challenge of a radiative transfer code, and it is commonly addressed as an iterative process of the three following items:

1. First, the code tries to find what cells are being hit by the incoming ray. This might be trivial for fixed resolution grids, but not for adaptive grids, commonly used in high-performance hydro codes. Some of these nested grids are often stored as a cell-tree (OctTree) and then calculations for the neighbour-search are required.
2. The code then calculates the points of intersection with the cell borders and split the ray into more rays if necessary, with every ray implying a new full solution to the RTE.
3. The code finally uses equation (1.50) to solve and update the intensity value at every cell along the ray, until it reaches the observer plane at the edge of the grid, and stores the final intensity generated by the model.

The Monte Carlo approach

The Monte Carlo method (MC) is a probabilistic technique that, when applied to the 3D-RT problem, chooses the resulting direction of a photon package, after interaction with matter, based on the random sampling of a physically-motivated Probability Distribution Function (PDF). It has been applied in astrophysics and to study the radiation transport in interstellar clouds since many decades (e.g., Mattila 1970; Roark et al. 1974), and has become the most widely used method in RT simulations used to calculate radiative temperature distributions. This method is not exactly "better" than raytracing, but does offer high efficiency when the photon propagation in many directions, as a 3D model for instance. Propagating rays along every single possible light cone is an extremely large and inefficient task. This is where Monte-carlo comes in handy. Scattering is for instance a multi-direction process and is indeed the main reason to consider Monte-carlo methods. The stochasticism lies in randomly sampling the outgoing direction of a scattered photon from the scattering phase function (see section 4.3.2 for details). This allows for faster absorption and reemission of photons instead of following every single photon package until it extincts or escape the grid. This also allow for the parallelization of the problem, since

every scattering event is treated independent of each other. Monte-carlo is used to simulate the radiation field as a flow made of a finite number of photon packages. The method assume that radiating sources are included within our outside the grid and launch a finite number of photons, all scattered separately, letting every package to either deposit energy on a cell or pass through it based on its albedo (i.e., the ratio of the absorption over scattering opacity).

The POLARIS and RADMC3D code

Within the plethora of publicly available radiative codes, such as RADEX (van der Tak et al. 2007), LIME (Brinch & Hogerheijde 2010), DUSTPOL (Padovani et al. 2012), HYPERION (Robitaille 2011), TORUS (Harries et al. 2019), MCFOST (Pinte et al. 2006), among others, in this work we have made use of the codes POLARIS (Reissl et al. 2016) and RADMC3D (Dullemond et al. 2012).

POLARIS, used in Chapter 2, is a high-performance line- and continuum- radiative transfer code designed to calculate polarized fluxes from analytical models and full 3D hydrodynamic simulations, with a special focus on the effects of dust grain alignment. POLARIS offers treatment for a wide variety of grain alignment paradigms, both internal and external. POLARIS allows to model imperfect internal alignment, imperfect Davis-Greenstein alignment, "Gold" magneto-mechanical alignment and radiative torque alignment. Details on some of these alignment mechanisms are given in section 1.3.5. POLARIS does also offer the possibility to model the effects of polarization by light scattering on spherical particles. Thanks to its nice memory-usage efficiency, thread parallelization and adaptability to different MHD codes, POLARIS has been used for modelling a wide range of astrophysical contexts. From extragalactic galactic scales (Mushtaq et al. 2023), to the ISM (Ponnada et al. 2022), and filaments (Le Gouellec et al. 2023), prestellar cores (Zamponi et al. 2022), protostellar envelopes (Valdivia et al. 2019, 2022), cores (Le Gouellec et al. 2020) and disks (Zamponi et al. 2021; Kuffmeier et al. 2021), multiple protostellar systems (Kuffmeier et al. 2020a), protoplanetary disks (Brunngräber & Wolf 2018, 2020, 2021; Habart et al. 2021; Devinat et al. 2022) and circumplanetary disks (Lietzow & Wolf 2023).

RADMC3D, used in Chapter 3, is a versatile software package designed to perform radiative transfer calculations in a wide range of astrophysical contexts. This includes different source geometries, either in 1D, 2D or 3D setups. Its primary focus is on continuum radiative transfer within dusty media, although it also incorporates modules for gas line transfer. RADMC3D is being particularly useful in modelling the different stages of the star formation process, such as prestellar cores (Scibelli et al. 2023; Jiao et al. 2023; Jensen et al. 2023), protostellar (first) cores (Duan et al. 2023), protostellar envelopes (Miotello et al. 2014; Agurto-Gangas et al. 2019) and disks (Zamponi et al. Submitted) and protoplanetary disks (e.g., Dullemond et al. 2007; Kataoka et al. 2015; Ballering & Eisner 2019; Cieza et al. 2017; Ueda et al. 2023, and references therein). The code does not treat gas photoionization or chemistry to estimate the gas temperature, but allows to calculate dust temperature distributions from radiative equilibrium and to derive a gas temperature from them if needed. The key advantage of RADMC3D lies in its adaptability regarding the spatial arrangement of models and its general file format flexibility. It allow users to create custom models or to utilize parameterized dust and/or gas density distributions, as

well as import such distributions from hydrodynamic simulations. Its flexibility and ease of use motivated the creation of the automation tool for the generation of synthetic observations introduced in this work, and described in detail in chapter 4.

1.3.4 Dust opacity

The key quantity involved in the general solution of the radiative transfer equation (1.49) is the optical depth τ , which in turn depends on the surface density $\int \rho dz$ of the medium along the direction of propagation and the opacity of the medium κ_ν . The opacity of a medium depends entirely on its composition and size. The opacity basically quantifies how efficiently will a particle of a given surface area transmit (absorb) or refract (scatter) the light that is shed on it. In radiative transfer theory, scattering and absorption are the two physical events that describe in full the microscopic interaction of light and matter. Each of them both have an efficiency, or more precisely, an opacity, associated to them and receive the name of the *scattering* and *absorption opacities*, κ_{sca} and κ_{abs} , respectively. The scattering opacity determines the probability for a photon to either not interact or to be absorbed and instantaneously re-emitted in a new random direction, facing a change in wavelength but no loss of energy. This probability is quantified from the normalized ratio $\kappa_{\text{sca}}/(\kappa_{\text{sca}} + \kappa_{\text{abs}})$ and is called *albedo*. On the other hand, the absorption opacity quantifies the efficiency of thermal absorption to incident radiation. Because the photon-matter interaction can happen in two different ways, the true opacity used to solve the radiative transfer equation needs to account for both scattering and absorption. This quantity receives the name of *extinction opacity* $\kappa_{\text{ext}} = \kappa_{\text{sca}} + \kappa_{\text{abs}}$.

At the temperatures found in molecular clouds ($\lesssim 500$ K), the main source of opacity is interstellar dust. The calculation of opacity tables over a range of wavelengths for a dust population depends on its composition and size distribution. Details on how to obtain dust opacities from optical laboratory measurements of different materials (silicate, carbonaceous, water, etc.) are given in full detail in section 4.3.2. In this section, the aim is to highlight the relevance of dust grain structures and sizes on their resultant opacities. Several works in the past have focused on generating opacity models for typical interstellar dust (e.g., Mathis et al. 1977; Draine & Lee 1984; Draine & Malhotra 1993; Ossenkopf & Henning 1994; Pollack et al. 1994; Jager et al. 1998; Draine 2003a,b; Zubko et al. 2004), and used them to fit the recovered interstellar medium spectral energy distribution. The canonical interstellar dust composition is a mixture of a silicate and carbonaceous (either in graphitic or amorphous material) solid core, coated by an icy layer of water or organics ice. Several works have used a common solid mass share between silicates and carbon of 62.5% and 37.5%, respectively. This is indeed the fiducial composition we use in this work.

The size distribution of interstellar grains was initially suggested by Mathis et al. (1977) and quickly became a reference standard for future modelling. They fitted different dust models to the micrometric interstellar extinction curve, and found that the distribution of grain sizes follow a power-law of the form $f(a) \propto a^{-3.5}$, with a representing the radius of a spherical grain, within $a_{\text{min}} = 5$ nm and $a_{\text{max}} = 0.25$ μm (see Fig. 1.6). However, dust grains are expected to grow in size within the densest regions of the ISM. Details on how this is done in the context of this thesis are given in Chapter 3 and discussed in section 3.5.1.

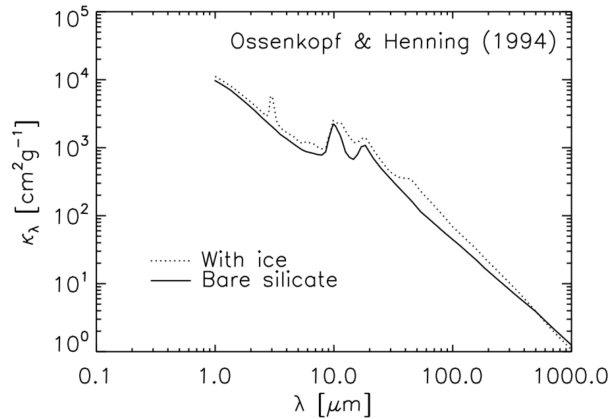


Figure 1.6: Extinction dust opacities for interstellar silicate dust. The opacities were calculated by Ossenkopf & Henning (1994) from models of dust coagulation in protostellar cores. Image obtained from lecture notes on Radiative Transfer (Dullemond, C.P.).

1.3.5 Polarization by dust alignment and scattering

Dust grain alignment

Polarization observations allow to estimate dust grain properties. Light can be either emitted linearly polarized directly from the grains or it can get polarized when traversing a dusty medium. Both cases produce different levels of polarization and different patterns of polarization. Let us first discuss the cases of polarized light generated by dust particles. The first, and most commonly studied, polarization mechanism, is the case of light emitted by elongated dust grains that are aligned with a given underlying vector field. For a net effect to be observable, all grains must have their angular momentum aligned in space, and this angular momentum must be aligned with one of their main axes (e. g., with their moment of inertia). The second condition is called *internal alignment*, and even though it is very poorly observationally constrained (Andersson et al. 2015), theoretical studies suggest that this can be achieved in the ISM by relaxation via the Barnett effect (Purcell 1979). In the context that all elongated grains in an ensemble align either of their axes to an underlying field, three main alignment paradigms can be distinguished: paramagnetic relaxation (Davis & Greenstein 1951), mechanical alignment (Gold 1952) and radiative alignment (Dolginov & Mitrofanov 1976) (see also Lazarian 2003, Andersson et al. 2015, Reissl et al. 2016 or Hoang et al. 2022 for clear and complete reviews on grain alignment mechanism). In the context of paramagnetic relaxation, spinning grains are expected to preferentially dissipate their components of the angular momentum that are perpendicular to the field lines and will tend to align their spin with the field, if the relaxation time is shorter than the randomization due to gas-dust collisions. The second case refers to the gas pressure exerted on the grain's surface in the presence of a gas-dust velocity drift. This pressure forces the angular momentum of the grain to align perpendicular to the differential gas-dust flow (Gold 1952; Dolginov & Mitrofanov 1976; Lazarian 1994; Lazarian & Hoang 2007b; Hoang et al. 2018; Kataoka et al. 2019). The third paradigm refers to the effect of radiation on the surface of non-spherical grains. In this case, the

different scattering cross-sections of both axes interact differently with the right- and left-handed polarization components of the incident light and lead to the generation of a net radiative torque that makes the grain spin. (Dolginov & Mitrofanov 1976) predicted that such a spinning charged particle will develop a magnetic momentum, via the Barnett effect, and will eventually undergo paramagnetic relaxation and align with the magnetic field. This theory of alignment receives the name of Radiative Torque Alignment (RAT) and it was theoretically introduced by Dolginov & Mitrofanov (1976). It has later been revisited and applied to several astrophysical contexts Draine & Weingartner (1997); Lazarian & Hoang (2007a); Reissl et al. (2016); Kataoka et al. (2017); Tazaki et al. (2017); Reissl et al. (2022). Polarization observations indicate that indeed RAT seems to be the most likely mechanism aligning grains in the ISM (Andersson et al. 2015). The first and third alignment mechanisms result in the alignment of the grain's long axis perpendicular to the magnetic field. The light emitted by a group of elongated grains will have a net polarization excess along the grain's long axis, which in the case of paramagnetic relaxation or RAT will produce polarization vectors perpendicular to the magnetic field (see right-hand-side illustration in Fig. 1.7). This picture holds as long as we are sure that the light we receive is optically thin thermal emission generated by the dust grains. On the other hand, if the light we receive is instead produced by a background source and absorbed by foreground aligned grains then the observed polarization pattern is exactly the opposite (see left-hand-side illustration in Fig. 1.7). In this case, the background optically thick source (i.e., a star or a massive protostellar disk) emits unpolarized light that gets absorbed preferentially along the grain's long axis and results in a polarization excess parallel to the field lines. This is also commonly referred to as *dichroic extinction* (Wood 1997). Such alignment mechanisms have been commonly used in the literature to derive the ISM magnetic field direction on the plane-of-the-sky (Planck Collaboration et al. 2020) and also within prestellar and protostellar cores (Hull et al. 2013; Segura-Cox et al. 2015; Maury et al. 2018; Sadavoy et al. 2019; Hull et al. 2020; Ko et al. 2020; Liu 2021; Lee et al. 2021) and protoplanetary disks (Stephens et al. 2013, 2014; Alves et al. 2018; Cox et al. 2018).

Dust self-scattering

Another polarization mechanism, not associated with elongated grains or grain alignment, is that produced by light-scattering and represents one of the main science cases of chapter 3. Scattering is by nature a light polarization phenomenon. After a scattering event the wavelength and polarization status of the outgoing photon is altered. The net polarization produced from scattered light is associated to the dust spatial distribution and not to any underlying vector field. The amount of polarization by scattering is highly wavelength and grain size dependant, and it peaks within the Mie regime, i.e., the regime where the grain size is comparable to the wavelength (further details about dust scattering and polarization are later given in section 4.3.2 and the description given here is limited to observational signatures only). Because of this, dust polarization observations have been used in the past to reconstruct the shape of the outer flared layers of protoplanetary disks from the scattering of optical stellar flux by nanometric dust (Avenhaus et al. 2018; Garufi et al. 2019). In the context of sub- and millimetric emission from protostellar disks, relevant to this work, the scattered light observed is not originated from the protostar but

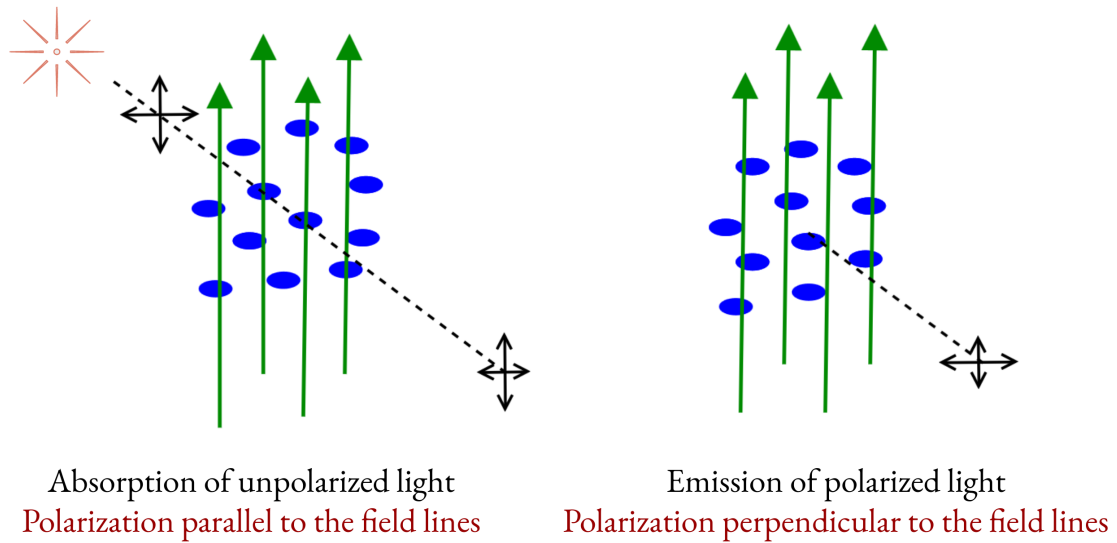


Figure 1.7: Polarization of light produced by the alignment of elongated dust grains with the magnetic field. Observed light will be polarized parallel or perpendicular to the field lines when observed either in absorption (left) or emission (right), respectively.

the thermal emission of the dust itself. This type of scattering received the name of *self-scattering* and has been used to model the polarization in galactic (Wood 1997) and circumstellar (Kataoka et al. 2015) disks. The relevance of self-scattering being the responsible mechanism for the observed polarization lies in its grain size dependence. Since its polarization fraction is maximum at $\lambda = 2\pi a_{\max}$, constraining multiwavelength-polarization in disks can be used as a proxy to estimate grain sizes (Sadavoy et al. 2018; Stephens et al. 2017; Ohashi et al. 2020). Unlike ISM and dense core environments, self-scattering has been suggested to be the responsible mechanism for the observed polarization towards some Class 0/I (Cox et al. 2018; Lee et al. 2021) and more evolved Class II disks (Kataoka et al. 2016a; Stephens et al. 2017; Hull et al. 2018; Bacciotti et al. 2018; Dent et al. 2019). This is in part due to the fact that circumstellar disks represent the site of dust coagulation and growth to produce such significant polarization fractions.

Stokes vector and polarization vector

Information about the polarization state of a photon package is described by a 4-component vector called, the Stokes vector S . The four components of this vector are I , Q , U and V . $I \geq \sqrt{Q^2 + U^2 + V^2}$ represent the intensity of light, regardless of its polarization E-vector. Q and U hold information about the linear polarization of the photon, i.e., they describe the direction of the E-vector. V holds information about circular polarization. In this thesis we deal only with the I , Q and U Stokes components of linear polarization. Q and U can take positive and negative values, and it's the combination of both components what give rise to the observed polarization patterns (either azimuthal, radial, uniform, etc.). Fig. 1.8 illustrates the simplest cases of uniform polarization for reference. More complex patterns can be later seen in Fig. 3.7. These patterns

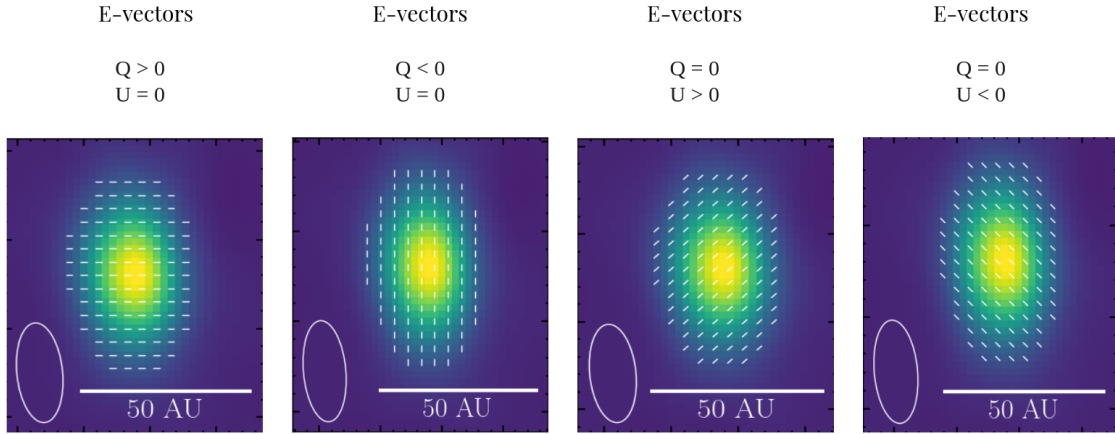


Figure 1.8: Polarization vector angles for different Q and U Stokes components, following the standard for the polarization ellipse from Rybicki & Lightman (1979). More sophisticated patterns can be seen in Fig. 3.7.

are derived from the vector angles via

$$P_{\text{ang}} = \frac{1}{2} \tan^{-1} \left(\frac{U}{Q} \right). \quad (1.51)$$

The length of the vectors commonly quantifies the intensity of the polarized light

$$PI = \sqrt{Q^2 + U^2}, \quad (1.52)$$

but is done as a normalized quantity known as the *polarization fraction*

$$P_{\text{frac}} = \frac{\sqrt{Q^2 + U^2}}{I}. \quad (1.53)$$

This is the key quantity used in Chapter 3 to assess whether the polarization observed towards the Class 0 protostar IRAS 16293-2422 B can be explained by self-scattering polarization or not.

1.4 The Class 0 protostellar system IRAS 16293-2422

IRAS 16293-2422 is a well studied Class 0 protostar located in the star-forming region ρ -Ophiuchi, inside the dark cloud L1689N, at a distance of 141 pc (Dzib et al. 2018). It is suggested to be very young, less than 10^4 yr old (Andre et al. 1993), and its being subject of many astrochemical studies because of its rich chemical variety (Blake et al. 1994; van Dishoeck et al. 1995; Ceccarelli et al. 1998, 2000; Schöier et al. 2002; Cazaux et al. 2003; Crimier et al. 2010; Jørgensen et al. 2011, 2016; Pineda et al. 2015; Oya et al. 2016; Jacobsen et al. 2018; van der Wiel et al. 2019; Hernández-Gómez et al. 2019b; Coutens et al. 2020; Ferrer Asensio et al. 2023). It was indeed the first source proposed to be a hot corino, based on the detection of multiple

complex organic molecules (Blake et al. 1994; van Dishoeck et al. 1995; Ceccarelli et al. 1998). Both its very young age and highly rich chemistry make it one of the most interesting sources of study, because it represents the initial physical and chemical conditions for star and planet formation. The source is in fact a triple protostellar system, composed of sources A1, A2 in the south, and northern companion B, with B being located ~ 700 au away from A1 and A2 (see Fig. 1.9). Several studies in the past have studied the nature of the two southern protobinaries A1 and A2 (Wootten 1989; Oya et al. 2015, 2016; Maureira et al. 2020, 2022). In this work, the focus is on characterizing the northern source B. Previous line and continuum studies (Rodríguez et al. 2005; Hernández-Gómez et al. 2019a; Pineda et al. 2012) have suggested that source B is a young protostar surrounded by very dense and optically thick protostellar disk, almost in face-on orientation (Pineda et al. 2015), and with no unambiguous signs of substructures being formed (Rodríguez et al. 2005). Recent high resolution ALMA observations (see Fig. 1.9) followed by radiative transfer modelling, presented in Zamponi et al. (2021), suggested that this protostellar disk is hot, with temperatures raising towards the midplane and reaching values above 400 K. The disk is also shown to be massive, with a disk mass tentatively around $0.3 M_{\odot}$ leading to optically depths of above 100. A dust model with a mixture of silicates and graphites with maximum grain sizes of at least $10 \mu\text{m}$ was able to reproduce the continuum observations of this disk. The full details of this analysis are presented in Chapter 2. The follow up study presented in Zamponi et al. (Submitted) and detailed in Chapter 3 suggests that grains can even be larger, up to $1000 \mu\text{m}$ with possibly enhanced grain growth in the innermost regions.

IRAS 16293-2422 B has also been targeted in polarization studies. The first SMA observations from Rao et al. (2009) and Rao et al. (2014) at $0.87 \mu\text{m}$, reported around 1.5% of polarization fraction with an azimuthal vector pattern distributed around the central protostar. These $0.6''$ (85 au) observations could be contaminated by envelope emission. This "envelope" emission refers to the material surrounding the disk including the bridge structure connecting the northern and southern protostars (Jørgensen et al. 2016; Maureira et al. 2020), shown also in Fig. 1.9. More recently, Liu et al. (2018b) presented new JVLA polarization observations at 7 mm with 1.5 times better resolution. These observations resolved down to the central 50 au and reported a similar azimuthal vector pattern with polarization levels of $\lesssim 2\%$. At the same time, the survey of 1.3 mm polarization observations towards Class 0 protostars in ρ -Ophiucus, carried out by Sadavoy et al. (2019) at a 2 times better resolution ($0.2''$; 30 au), found polarization signatures associated to self-scattering in inner regions of most of their sources. The polarization in the disk of IRAS 16293 B was found to be azimuthal, similar to the SMA and VLA observations, however the authors associated the vector distribution to polarized self-scattering from an optically thick face-on disk, based on the models from Yang et al. (2017). The connection of a similar polarization pattern between 1.3 mm and 7 mm, being produced by self-scattering, implies that grains can have sizes between $200\text{-}2000 \mu\text{m}$. Having significant growth in a protostar less than 10^4 yr old, would imply that grain sizes pivotal to planet formation could already be present in the Class 0 stage. The open question of whether self-scattering can indeed explain the observed polarization in IRAS 16293 B and set such grain size constraints, is indeed the science goal of the project presented in Chapter 3.

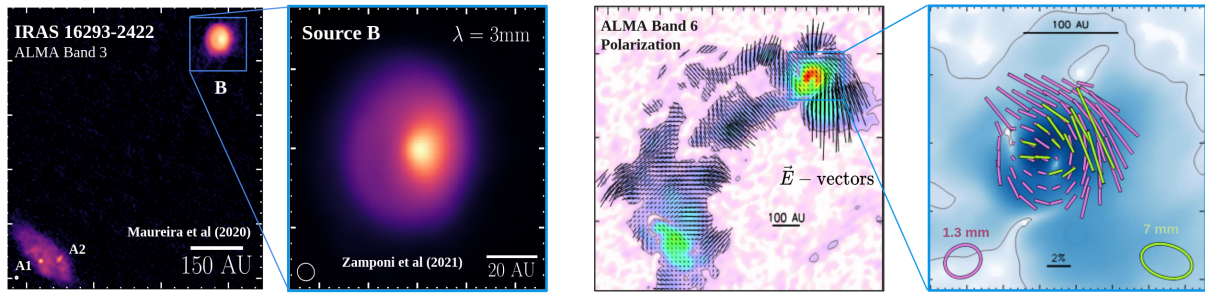


Figure 1.9: The Class 0 Protostar IRAS 16293-2422 B observed with ALMA. First and second panel, from left to right, show high-resolution continuum observation as presented by Maureira et al. (2020) and Zamponi et al. (2021). Third and fourth panel show the polarized emission detected by Sadavoy et al. (2018) along with 7 mm JVLA data from Liu et al. (2018b).

1.5 Contents of this thesis

In this chapter, I have introduced all the theoretical framework on which the following chapters are based: interstellar gas and its dust content, cloud instabilities and the subsequent formation of stars surrounded by dusty disks, the importance of dust opacities and finally, how to use light polarization as a proxy for dust properties.

Below I briefly summarize the contents of the following chapters:

Chapter 2: ALMA high-resolution (~ 6 au) observations and radiative transfer modelling of MHD simulations of the Class 0 protostar IRAS 16293-2422 B.

Chapter 3: Follow-up study from Chapter 2, including multiwavelength (1.3, 3, 7, 9 & 18 mm) continuum and polarization observations to provide grain size constraints on IRAS 16293 B. This is compared to independent grain size constraints from models of dust self-scattering.

Chapter 4: Presentation of a newly developed tool to generate synthetic observations of MHD simulations directly from the command line, including the effects of polarization by alignment and scattering and also of different dust composition and sizes.

Chapter 5: Summary of the entire document, followed by a personal look to the future, about the new questions left open after carrying out this thesis, and how to possibly answer them.

Chapter 2

The young protostellar disk in IRAS 16293-2422 B is hot and shows signatures of gravitational instability

The contents of this chapter were published in the *Monthly Notices of the Royal Astronomical Society* Journal. Credit: Zamponi et al., MNRAS, 508, 2583-2599, 2021.

Abstract

Deeply embedded protostars are actively fed from their surrounding envelopes through their protostellar disk. The physical structure of such early disks might be different from that of more evolved sources due to the active accretion. We present 1.3 and 3 mm ALMA continuum observations at resolutions of 6.5 au and 12 au respectively, towards the Class 0 source IRAS 16293-2422 B. The resolved brightness temperatures appear remarkably high, with $T_b > 100$ K within ~ 30 au and T_b peak over 400 K at 3 mm. Both wavelengths show a lopsided emission with a spectral index reaching values less than 2 in the central ~ 20 au region. We compare these observations with a series of radiative transfer calculations and synthetic observations of magnetohydrodynamic and radiation hydrodynamic protostellar disk models formed after the collapse of a dense core. Based on our results, we argue that the gas kinematics within the disk may play a more significant role in heating the disk than the protostellar radiation. In particular, our radiation hydrodynamic simulation of disk formation, including heating sources associated with gravitational instabilities, is able to generate the temperatures necessary to explain the high fluxes observed in IRAS 16293B. Besides, the low spectral index values are naturally reproduced by the high optical depth and high inner temperatures of the protostellar disk models. The high temperatures in IRAS 16293B imply that volatile species are mostly in the gas phase, suggesting that a self-gravitating disk could be at the origin of a hot corino.

2.1 Introduction

In the earliest stages of star formation, the Class 0 stage Andre et al. (2000), the protostellar envelope still contains a significant fraction of the total mass of the system. The protostellar disk is continuously fed by the surrounding envelope and it may become gravitationally unstable depending on environmental conditions at the start of the pre-stellar core collapse (e.g. Zhao et al. 2018). Large streamers of molecular material from the outer envelope and surrounding cloud can also contribute to the disk mass growth (Dullemond et al. 2019; Akiyama et al. 2019; Pineda et al. 2020; Kuffmeier et al. 2020b). Gravitationally unstable disks can fragment, enabling the formation of giant planets (Boss 2009; Vorobyov & Basu 2010; Machida et al. 2011) and develop spiral arms where gas compression and shocks locally heat the gas and dust to values well above those predicted by irradiated viscously evolving disks (e.g. Boley & Durisen 2008; Dong et al. 2016). The chemical composition of the disk is heavily affected by gravitational instabilities (GI) (e.g. Ilee et al. 2011, 2017). Moreover, their relatively large masses and surface mass densities of gravitationally unstable disks imply large opacities of their dust emission at millimeter and sub-millimeter wavelengths, thus hindering total mass measurements (e.g. Evans et al. 2017; Galván-Madrid et al. 2018; Li et al. 2017) and making molecular line observations difficult to probe their full structure (Evans et al. 2019).

So far, there is no clear evidence of a gravitational unstable disk among Class 0 sources, with the possible exception of the disk around the triple protostar system L1448 IRS3B (Tobin et al. 2016), but this disk is highly perturbed by the presence of multiple sources which can induce tidal forces and instabilities mimicking original GIs. To make progress in this field and unveil a gravitationally unstable disk at the earliest stages of star formation, one needs high sensitivity and high angular resolution observations of a bright Class 0 source and state-of-the art numerical simulations of disk formation which can then be compared in detail with observations.

Located in the star-forming region ρ -Ophiuchi, inside the dark cloud L1689N and at a distance of 141 pc (Dzib et al. 2018), IRAS16293-2422 is a well studied Young Stellar Object (YSO) classified as a Class 0 source with less than 10^4 yr (Andre et al. 1993), and represents one of the very early stages of low-mass star formation. It was the first source identified as a hot corino (Blake et al. 1994; van Dishoeck et al. 1995) based on the detection of Complex Organic Molecules (COMs) in the source, which was later supported by follow up studies (Ceccarelli et al. 1998, 2000; Schöier et al. 2002; Crimier et al. 2010; Pineda et al. 2012; Jørgensen et al. 2011, 2016; Oya et al. 2016; Jacobsen et al. 2018; van der Wiel et al. 2019). Higher resolution observations revealed that IRAS16293-2422 is in fact a triple system, composed of sources A1 and A2, separated by 54 au from each other (Maureira et al. 2020) and source B, 738 au (5"; Wootten 1989) away from source A. Due to this larger separation, tidal truncation between the three protostars is discarded and therefore source B is considered to have evolved as an isolated source (Rodríguez et al. 2005). It was initially proposed to be either an evolved T Tauri star (Stark et al. 2004; Takakuwa et al. 2007) or a very young object (Chandler et al. 2005), however, Chandler et al. (2005) suggested that source B has large scale infalls based on SO line emission. Pineda et al. (2012) confirmed the infall of an inner envelope, with mass accretion rates of $4.5 \times 10^{-5} M_{\odot} \text{yr}^{-1}$, based on ALMA detections of inverse P-Cygni profiles in $\text{CH}_3\text{OCHO-E}$, $\text{CH}_3\text{OCHO-E-A}$ and H_2CCO , ruling out the possibility of it being a T Tauri star. The interpre-

tations of infall from these profiles was also suggested by Jørgensen et al. (2012) and Zapata et al. (2013). Unlike the A1 and A2 protostars, source B has not shown clear signs of outflow launching, explained by the lack of free-free emission at low frequencies (Chandler et al. 2005; Rodríguez et al. 2005; Loinard et al. 2007; Rao et al. 2009; Liu et al. 2018b; Hernández-Gómez et al. 2019a) and also based on molecular lines (Loinard et al. 2002; van der Wiel et al. 2019).

The possibility of source B being gravitationally unstable in the outer part of its disk was also proposed by Rodríguez et al. (2005) and discussed by Kratter & Lodato (2016). The disk around source B must be highly dense and massive ($\gtrsim 0.2 M_{\odot}$; Rao et al. 2009; Pineda et al. 2012) to produce gravitational instabilities. After comparing high sensitivity interferometric data with MHD and RHD star formation simulations, we demonstrate here that indeed the physical structure (in particular the temperature) of the IRAS16293-2422 B disk resembles that of a self-gravitating disk.

This paper is organized as follows: in section 2.2 we provide details on the data observation and reduction, followed by our results from the ALMA observations, in section 2.3 we describe the numerical simulations used to compare against our ALMA observations, in section 2.4 we outline the post-processing scheme done with radiative transfer calculations, in section 2.5 we compare our synthetic observations to the real data, then we discuss about possible interpretations for the features observed in section 2.6 and finally, we present our conclusion in section 2.7.

2.2 Observations

2.2.1 Data and Imaging

Observations of IRAS 1629-2422 were taken in band 3 and band 6 with ALMA (project IDs: 2017.1.01247.S and 2016.1.00457.S, respectively). The band 3 observations were taken on October 8 and 12, 2017 in the most extended Cycle 5 configuration with a baseline range of 41.4 m–16.2 km and a maximum recoverable scale of $\sim 0.5''$ (or 70 au). The single spectral window for the band 3 continuum used in this work has a bandwidth of 2 GHz divided into 128 channels and centered at 99.988 GHz. The band 6 observations were taken during 2017 August 21. The baselines range between 21 and 3697 m, with a maximum recoverable scale of $\sim 0.6''$ (or 85 au). The spectral setup consisted of four spectral windows centered at a frequency of 240.3 GHz, 240.5 GHz, 224.7 GHz, 222.9 GHz, with a channel width of 61.0 kHz, 15.3 kHz, 30.5 kHz, 488.3 kHz and bandwidth of 0.23 GHz, 0.06 GHz, 0.11 GHz, 0.94 GHz, respectively. To create the continuum image we carefully check each spectral window and flag the lines. The resulting bandwidth for the band 6 continuum is 0.12 GHz with most of the channels coming from the spectral window centered at 222.9 GHz. Both, the band 3 and band 6 continuum data has been previously published in Maureira et al. (2020) and Oya & Yamamoto (2020), respectively.

For band 3, the procedure for the calibration of the continuum data (including phase and amplitude self-calibration) as well as the imaging are detailed in Maureira et al. (2020). In summary, when imaging the continuum we iteratively performed phase-only self-calibration with a minimum solution interval of 9 seconds. Afterwards we performed two amplitude self-calibration iterations, with a minimum solution interval of 60 seconds. The final continuum dataset after

phase+amplitude self-calibration was imaged using the `tclean` task from the Common Astronomy Software Applications (CASA; v5.6.2) with the multiscale deconvolver (Cornwell 2008; Rau & Cornwell 2011) and a robust parameter of 0.5. The beam size, beam position angle (P.A.) and noise of the continuum image are $0.048'' \times 0.046''$ (6.5 au), 79.3° and $15 \mu\text{Jy beam}^{-1}$, respectively. This image was used when analyzing the band 3 data alone, while a new additional map was done for producing a spectral index map (see below). For band 6, we performed iteratively phase-only self-calibration with a minimum solution interval of `solint='int'` or 4 seconds. Afterwards we performed one amplitude self-calibration, with `solint='inf'` (two solutions, one for each track). For the process of self-calibration of the final image we selected visibilities with a minimum baseline of 120 klambda, in order to avoid missing flux artifacts, but also because shorter baselines are not covered by the band 3 observations with which we want to compare for our analysis.

The continuum image for band 6 and an additional continuum image for band 3 with matching uv -range were created using `tclean`. This additional image of the band 3 data with matching uv -range was done with the goal of producing a spectral index map. We use multiscale, a robust parameter of 0 and a uv -range parameter of 120-2670 $k\lambda$ (overlapping baselines) for both datasets. A reference frequency of 223 GHz and 100 GHz was set for the band 6 and band 3 observations, respectively. The resultant beam size, P.A. and rms of the band 3 observations correspond to $0.062'' \times 0.050''$, 41.7° and $17 \mu\text{Jy beam}^{-1}$, respectively. Similarly, for the band 6 observations these values are $0.114'' \times 0.069''$, -88.2° and $104 \mu\text{Jy beam}^{-1}$, respectively. This study focuses on source B, corresponding to the single northern source of the IRAS 16293-2422 triple system. The corresponding maps for the southern pair (A1 and A2), as well as further details of the imaging in both bands, are presented by Maureira et al. (2022).

2.2.2 Results

Continuum observations at 1.3 and 3 mm

The continuum observations obtained with ALMA toward source B are shown in Fig. 2.1 at $\lambda = 1.3$ and 3 mm. The structure seen at 3 mm has a radius of ~ 46 au, measured along the major axis of a contour at 5σ . This size is consistent with the reported typical sizes of embedded disks (Segura-Cox et al. 2018; Maury et al. 2019; Tobin et al. 2020) and also consistent with previous observations of this source (Rodríguez et al. 2005; Oya et al. 2018).

Interestingly, both wavelengths show the emission peak clearly shifted to the West of the center of the overall structure. At a first glance, this shift could imply a possible inclination of the disk or the presence of a real asymmetry in density and/or temperature. The aspect ratio of the disk is ~ 0.95 (derived from the east-west over north-south extensions of source B outlined by a contour at 5σ). The ratio was measured in the the optically thinner 3 mm image which, under the assumption of a circular disk, suggests a moderate inclination of $\sim 18^\circ$. If the disk were instead highly inclined, it would be expected that the peak would be more centered when seen at longer wavelengths. However, hints of a shift were also seen in high-resolution VLA continuum observations at 42 GHz reported by Rodríguez et al. (2005) and Hernández-Gómez et al. (2019a), unlike what is seen in the case of the highly inclined disk in HH212 (Lin et al.

2021). Furthermore, the line emission from complex organic molecules from the ALMA-PILS survey also appears to show a peak shifted to the west (Calcutt et al. 2018b,a; Manigand et al. 2020, 2021). Likewise, the source does not show a significant gradient indicative of rotation in previous ALMA line observations from 100 au down to 70 au scales. Instead, the kinematics is consistent with mostly infall motions (Pineda et al. 2012; Zapata et al. 2013; Oya et al. 2018) in a system with a face-on disk. All the above evidence suggests that there might be a real asymmetry present in the temperature and/or density structure of source B, instead of being a product of optical depth and inclination.

The brightness temperatures and rms uncertainties in the position of the peak are $T_b^{1.3\text{mm}} = 287 \pm 0.3$ K and $T_b^{3\text{mm}} = 470 \pm 1$ K, with the 3mm one remaining higher than the 1.3mm even after smoothing the 3mm observations to match the beam of the 1.3mm observations ($T_{b,\text{smooth}}^{3\text{mm}} = 364 \pm 0.4$ K). This same trend, of higher brightness temperature for longer wavelengths, is also consistent with recent VLA observations at 41 GHz (7 mm) and 33 GHz (9 mm) in Hernández-Gómez et al. (2019a), which had a comparable resolution to our observations. They measured a peak brightness of $T_b^{7\text{mm}} = 870$ K and $T_b^{9\text{mm}} = 700$ K. Additionally, they reported ALMA observations at 700 GHz that have a brightness temperature of $T_b^{1\text{mm}} = 185$ K. This trend is consistent with self-obscuration of inner hot material due to high optical depth, a scenario that we investigate in Section 2.5.2 and discuss in Section 2.6.1.

Spectral index

We derived the spectral index α between our ALMA observations at 1.3 and 3 mm using equation A.1. For this, we use maps imaged using the same uv -range (Section 2.2.1) and smoothing afterwards to match beams. The results are shown on the rightmost panel of Fig. 2.1. Black contours are placed at $\alpha=1.7, 2$ and 3 , inside-out. A clear decrease of spectral index is observed towards the center, ranging from 3 to values as low as 1.7 . The middle contour, at $\alpha=2$, shows an elongated shape. A similarly low α was measured in the center by Loinard et al. (2007) and it was suggested to be due to a modest thermal jet. However, Hernández-Gómez et al. (2019a) compiled integrated fluxes using SMA, VLA and ALMA observations ranging from 3 to 700 GHz and found no evidence of free-free emission. The SED was well fitted with a single spectral index of $\alpha = 2.28 \pm 0.02$, in agreement with optically thick thermal dust emission at all wavelengths.

Spectral indices close to and lower than 2 have also been reported toward other sources, such as those in the PROSAC survey of Class 0/I protostars (Jørgensen et al. 2007, 2009) and also toward the Class I source WL12 (Miotello et al. 2014). More recently, Lin et al. (2021) presented a map of the spectral index between ALMA bands 3, 6 and 7 towards the embedded edge-on disk around the Class 0 protostar HH212. The spectral index reaches values as low as ~ 1.5 within the central ~ 50 ($\alpha_{\text{band } 3,6}$) and 80 au ($\alpha_{\text{band } 6,7}$). The observations were well reproduced by considering a temperature gradient increasing toward the inner regions of the disk, which under optically thick conditions, results in self-obscuration of the inner hot regions and thus in low spectral indexes, as also suggested by Li et al. (2017) and Galván-Madrid et al. (2018). In section 2.6.1, we discuss further the origin of the low spectral index in source B, based on comparison with protostellar disk models formed from the collapse of a dense core.

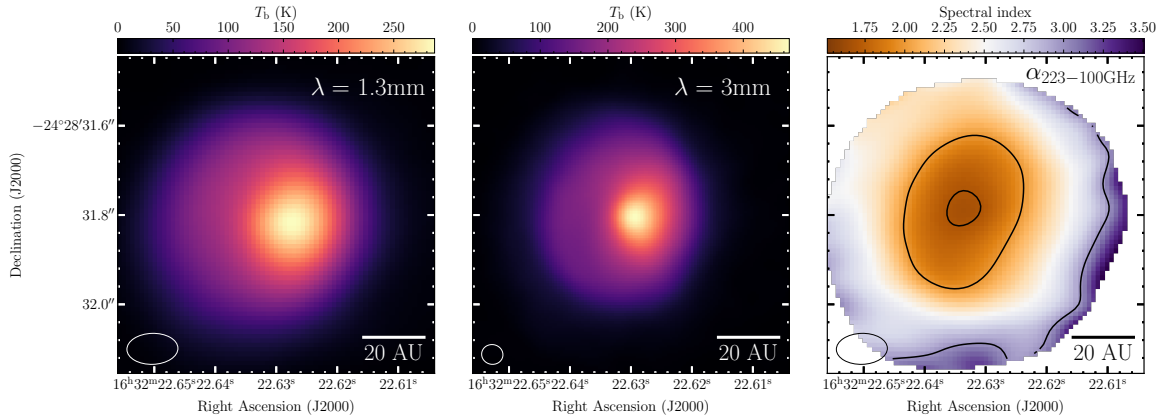


Figure 2.1: ALMA observations of IRAS16293-2422B. The left and central panels show the brightness temperatures observed at 1.3 mm (100 GHz; band 6) and 3 mm (223 GHz; band 3), respectively. The observation at 3 mm report brighter emission than at 1.3 mm, with a peak value of $T_b \sim 470$ K and $T_b \sim 290$ K, respectively. Both images indicate the presence of a resolved brightness asymmetry in the source. The rightmost panel shows the spectral index calculated between the two wavelengths (as described in Appendix A.1), for which the 3 mm image was smoothed to match the 1.3 mm beam. Contours for the spectral index map are shown at 1.7, 2 and 3, inside-out. The synthesized beams are $0.114'' \times 0.069''$ and $0.048'' \times 0.046''$ at 1.3 and 3 mm (see bottom left corners).

2.3 Protostellar disk simulations

2.3.1 Simulations of disk formation and evolution

non-ideal MHD disk model

In this work we have post-processed 3D non-ideal magnetohydrodynamic (MHD) simulations of protostellar disk formation presented in Zhao et al. (2018), using the code ZeusTW (Krasnopolsky et al. 2010). They employed a spherical grid that is non-uniform along the radial axis, to provide high resolution in the inner regions of the grid. The grid boundary has a 2 au radius and a 6684 au outer radius. All gas that flows into this 2 au central cell is considered to be accreted by the protostar. No additional sink particles were included in the simulations. These simulations start from the cloud core scale and evolve up to ~ 20 kyr after the formation of a rotationally supported disk, during which ambipolar diffusion plays the dominant role. We have selected the model *2.4Slw-trMRN* from Table 1 in Zhao et al. (2018). This core is initialized as an isolated isothermal sphere of uniform density ($\rho_0 = 4.77 \times 10^{-19}$ g cm $^{-3}$), with core radius $R_c = 6684$ au, core mass $M_c = 1 M_\odot$ and a constant temperature of 10 K. Assuming a mean molecular mass of $\mu = 2.36$ amu, the gas number density for molecular hydrogen correspond to $n(H_2) = 1.2 \times 10^5$ cm $^{-3}$. The core initially rotates as a solid body with angular speed $\omega_0 = 10^{-13}$ s $^{-1}$, which leads to a rotational to gravitational energy ratio of $\beta_{\text{rot}} = 0.025$. The core is magnetized and the initial magnetic field is uniformly distributed, along the rotation axis, hav-

ing a constant strength of $B_0 = 4.25 \times 10^{-5}$ G, which corresponds to a dimensionless mass-to-flux ratio of $\lambda = 2.4$.

The selected simulation model shows a relatively compact disk of ~ 50 au in diameter, without obvious spiral structures, due to the strong magnetic field and slow rotation of the initial core. We selected the timestep at which the disk mass was the highest ($0.09 M_\odot$). The disk is only marginally gravitationally unstable (see Fig. A.2) and relatively smooth, although at earlier times developing transient spiral arms. This snapshot represents a state ~ 144 kyr after the beginning of the core collapse and ~ 22.34 kyr after the formation of a first core (Larson 1969). Face-on and edge-on slices of the gas density and gas temperature distributions of the MHD disk model are shown in Fig. 2.2.

Starting from the inner boundary, the radial density distribution on the midplane goes as follows: the maximum is reached at the inner boundary region of 2-3 au with a density of 4.5×10^{-11} g cm $^{-3}$ ($n_{\text{gas}} = 1.14 \times 10^{13}$ cm $^{-3}$). The density remains roughly constant up to 7 au and then falls as a power-law of $r^{-2.8}$ until the disk's outer edge at 25 au. The overall density distribution is rather smooth across the entire disk with no signs of fragmentation. The vertical density distribution shown in the edge-on view of Fig. 2.2, indicates the presence of a midplane much denser than the outer layers, especially within the inner 7 au and a scale height of $\lesssim 5$ au.

The initial stages of the collapse proceeded isothermally at 10 K and then followed an adiabatic equation of state (EOS; see Appendix A in Zhao et al. 2018) after a density threshold of 10^{-13} g cm $^{-3}$ was reached. The gas temperature is then obtained from a barotropic EOS with an adiabatic index of 5/3 (up to 10^{-11} g cm $^{-3}$) and therefore follows always the density distribution. The edge-on view of the temperature (see lower-right panel in Fig.2.2) shows a gradient from the outer layers toward the midplane. In this warm midplane, the hottest regions are at $T \sim 190$ K and lie within the densest 7 au radius.

The edge-on view of the disk also show bipolar outflows and accreting flows from the parent dense core.

RHD gravitationally unstable disk model

We also model the formation of a disk in which temperature evolution is followed self-consistently along with the hydrodynamics. For this, we utilise the smoothed particle hydrodynamics (SPH) code sphNG (Bate et al. 1995) including the hybrid grey radiation transfer scheme of Forgan et al. (2009) to perform radiation hydrodynamic (RHD) simulations. In this case, material is able to exchange energy via flux-limited diffusion (see e.g. Bodenheimer et al. 1990; Whitehouse & Bate 2004) and the gas is able to cool radiatively according to its local optical depth (estimated from the local gravitational potential, see Stamatellos et al. 2007). We note that this approach does not consider any magnetohydrodynamic processes.

We follow the evolution of a spherical, isothermal cloud of mass $1 M_\odot$ and radius 2000 au using 5×10^5 SPH particles with a background temperature of 5 K. After approximately 17 kyr, a rotating disk is formed at the centre of the cloud. For the rest of this work, we consider the disk physical structure at 18.2 kyr of evolution, approximately 1000 yr after the disk first forms. At this point, the mass of the disk is $0.3 M_\odot$ and the sink particle close to the center of the disk has a mass of $0.2 M_\odot$. The disk is gravitationally unstable, with a Toomre Q parameter (Toomre 1964)

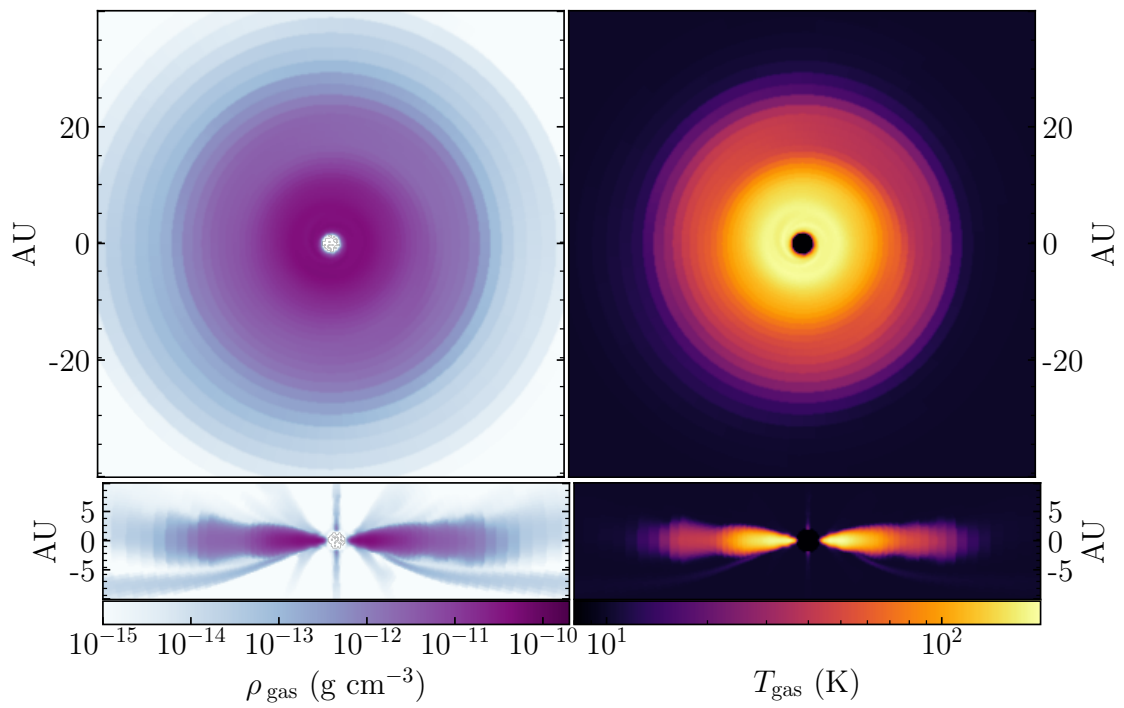


Figure 2.2: Face- and edge-on slices of the gas density (left column) and gas temperature (right column) distributions for the MHD disk model from Zhao et al. (2018), as described in section 2.3.1.

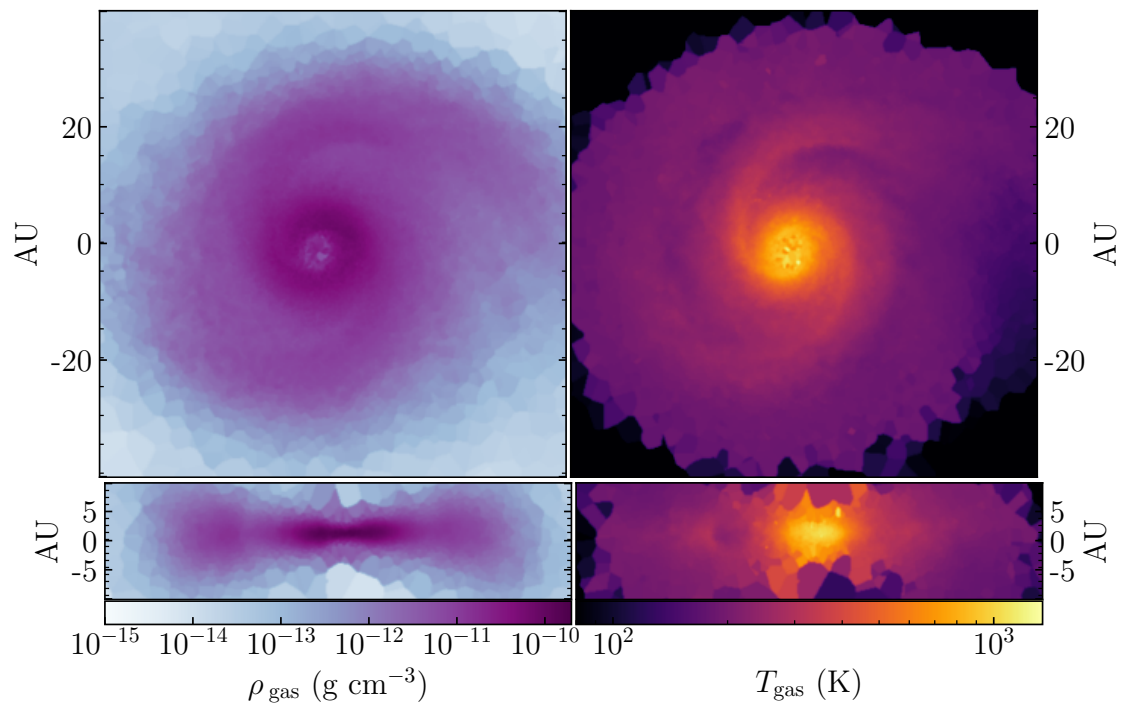


Figure 2.3: Face- and edge-on slices of the gas density (left column) and gas temperature (right column) distributions for the RHD the gravitationally unstable model, as described in section 2.3.1.

below 1.7 (the critical value for non-axisymmetric perturbations; Durisen et al. 2007) at radii larger than 7 au and a minimum value of ~ 1.4 at approximately 20 au (see Fig. A.2). While the disk does not undergo fragmentation during the period of time that we simulate, it does exhibit significant non-axisymmetric structures in the form of two spiral arms within the disk. Face-on and edge-on slices of the gas density and gas temperature distributions of the RHD disk model are shown in Fig. 2.3.

The radial dependence of gas density is similar to that of the MHD model: it reaches a maximum value of $5 \times 10^{-11} \text{ g cm}^{-3}$ at around 4 au, then stays roughly constant until 7 au, where it starts to decrease as $r^{-2.6}$ until ~ 40 au. Between 3 and 13 au both models have very similar density values and profiles. Beyond this region, the RHD model is denser than the MHD model by a factor of ~ 2.5 . Additionally, the density in the RHD disk model is not as smoothly distributed as in the MHD case, even when the two are marginally gravitationally unstable, since the spiral arms are more than twice as dense as the rest of the disk.

Since the RHD model includes a radiation transfer scheme, the temperature evolution is not only dependant on the hydrodynamics but also on the local radiation field. As a result, the coupling between the temperature and density is not as tight as in the MHD model. The disk temperature is the highest ($T \gtrsim 700 \text{ K}$) within the inner $\lesssim 5$ au, peaking at the very center with values of around 1000 K. However, the temperature at the center can be affected by artificial viscosity present in SPH simulations in regions of very high density, as those in the central few au (Bate et al. 1995; Forgan et al. 2009). For this reason, when comparing with the observations, we do not focus on the values reached in the very central region which we conservatively consider to be within 10 au. Beyond 10-15 and up to around 30 au, the overall temperature distribution follows that of the density, with temperature contrasts of 1.5-2 between the spiral arms ($\lesssim 500 \text{ K}$) and the rest of the disk. These outer regions are much hotter ($\sim 200 \text{ K}$) than the MHD disk model ($\sim 50 \text{ K}$) by a factor of about 4. The adiabatic equations of state of both models are very similar, but the treatment of the heating and cooling used in this model self-consistently produces higher temperatures at radii of 10-25 au. This is possibly due to a combination of the high gas densities and kinematics processes that lead to additional compression/shock heating.

The vertical temperature structure follows a similar gradient to that of the MHD model, increasing from the outer layers to the midplane.

2.4 Radiative transfer

We have post-processed the disk models previously introduced, by performing radiative transfer (RT) calculations on their density structures, with the publicly available code POLARIS¹ (v4.06) (Reissl et al. 2016). We use as input the density, velocity and magnetic field distributions at the timesteps of interest. We also consider the gas temperature from the simulations whose effects will be discussed below.

POLARIS is a parallelized full radiative transfer code written in C++. It allows to generate 3D dust temperature distributions from a density model, by propagating photons through the

¹<http://www1.astrophysik.uni-kiel.de/~polaris>

grid with a Monte Carlo (MC) approach, providing also a variety of radiating sources and grain alignment theories. It also allows to generate ideal intensity and polarization maps by ray-tracing the emission produced from the entered density and temperature distributions, assuming a certain dust composition, range of grain sizes and grain aspect ratios.

To facilitate the direct comparison between numerical simulations and real observations, POLARIS supports user-defined input grids, which could be converted from the snapshot of a full 3D-MHD code. In this work we have converted the models from Zhao et al. (2018) (see section 2.3.1) in spherical grid structure into the POLARIS spherical grid format and publicly released the code used for the task². For the RHD model (see section 2.3.1), the conversion was done from a non grid-based SPH data into a POLARIS Voronoi mesh format, mapping each SPH particle into one cell.

2.4.1 Dust grain size distribution and composition

Both the generation of dust temperature fields and the ray-tracing of the dust continuum emission depend strongly on the dust opacity. This wavelength-dependent opacity is determined by the composition of the dust mixture and the distribution of grain sizes. The dust component included in our setup is a mixture of spherical silicates and graphites, meant to resemble the dust composition in the interstellar medium (Mathis et al. 1977) and in protostellar cores (Ossenkopf & Henning 1994). The mixture contains a 62.5% (mass fraction) of silicates and a 37.5% of graphites. This mixture has been commonly used in previous work using POLARIS and at similar stages of star-formation (Reissl et al. 2016; Valdivia et al. 2019; Brunngräber & Wolf 2018; Kuffmeier et al. 2020b; Brunngräber & Wolf 2020). As the temperatures in the disk are mainly above the sublimation temperature of interstellar ices, no ice component has been included in the dust model. The graphite component follows the 2/3 - 1/3 relation for cross sections perpendicular and parallel to the incident electric field (Draine & Malhotra 1993). This means that 37.5% of the graphite is split into 25% and 12.5% of the perpendicular and parallel components, respectively. The densities of the silicates and graphites are 3.5 g cm^{-3} and 2.2 g cm^{-3} , respectively, leading to a mixture density of 2.896 g cm^{-3} . For all radiative transfer calculations, we have assumed a gas-to-dust mass ratio of 100.

The dust opacity is calculated from the refractive indices (a.k.a., dielectric constants) using the Wolf & Voshchinnikov approach (Wolf & Voshchinnikov 2004), which is in turn an implementation of the commonly used Bohren & Huffman approach (Bohren & Huffman 1983) optimized for large size parameters ($x = 2\pi a/\lambda$). We have used the refractive indices for astronomical silicates and graphites from the POLARIS repository, which are based on Draine & Lee (1984), Laor & Draine (1993) and Weingartner & Draine (2001).

POLARIS performs no mixing between the refractive indices of the two dust components (e.g., Bruggeman or Maxwell-Garnet mixing, see Ossenkopf 1991), rather it lets the two species coexist in every cell and compute the total opacity as a sum of single opacities weighted by the mass fraction (see e.g., Das et al. 2010) and removes them from the cell if the dust temperature ever exceeds the sublimation temperature of the material. The sublimation temperatures of

²<https://github.com/jzamponi/zeus2polaris>

silicates and graphites are 1200 and 2100 K, respectively.

The sizes of the dust grains follow a power-law distribution $N(a) \propto a^{-q}$, with $q = 3.5$, distributed among 200 logarithmically spaced size bins and 200 logarithmically spaced wavelengths. We chose a minimum grain size of $a_{\min} = 0.1 \mu\text{m}$, based on the value used in the disk simulations from Zhao et al. (2018) analyzed here and also consistent with recent simulations of grain growth in dense cores, showing that the population of very small grains is rapidly lost as they are swept out by larger grains (Silsbee et al. 2020). This parameter was kept fixed since it has been shown that variations in the lower limit of the grain size distribution do not produce significant effects on the sub-millimeter and millimeter opacities (Woitke et al. 2016). The maximum grain size (a_{\max}), on the other hand, directly affects the slope of the opacity curve (known as the opacity index β) at sub-millimeter and millimeter wavelengths. The opacity distributions generated by this mixture are shown in Fig. 2.4 for different a_{\max} .

Scattering opacities are commonly assumed to be negligible at long wavelengths. This is also consistent with our results for the dust opacity as long as the $a_{\max} \leq 100 \mu\text{m}$. In this work we have assumed $a_{\max} = 10 \mu\text{m}$. This results in the flux from the disks being mainly produced by thermal emission.

Since the focus of this study is not to constrain the grain sizes but to test if any of the presented numerical models can be a good fit to the new high-resolution observations of source B, we did not explore all the parameter space for a_{\max} , which would be analyzed in a future work. Considering that there is no unambiguous evidence of large grains at the early Class 0 protostellar stage, as a first step we consider only grains with $a_{\max} \leq 10 \mu\text{m}$. This choice also results in most of the continuum emission coming from thermal dust emission, since the opacity of scattering is very low compared to that of absorption. The dominance of absorption opacities in the millimeter wavelengths is relevant for understanding the flux distributions, however, for the calculation of temperature distributions, the full extinction opacity (scattering plus absorption) at all wavelengths was used.

Finally, the extinction dust opacities used in this study are $\kappa_{\text{ext}}^{1.3 \text{ mm}} = 1.50 \text{ cm}^2 \text{ g}^{-1}$ and $\kappa_{\text{ext}}^{3 \text{ mm}} = 0.58 \text{ cm}^2 \text{ g}^{-1}$, as shown in Fig. 2.4.

2.4.2 Dust temperature distributions

Dust temperatures from stellar radiation

We have generated 3D distributions of the dust temperature for both disk models, by heating the dust with the radiation from a central star. We first consider the dust temperature generated only from stellar radiation, with no inclusion of the gas temperature from the numerical simulations (shown in Fig. 2.2 and 2.3). For this, we placed a point source in the center of the grid, radiating as a black-body (i.e., a protostar) with $R_{\text{star}} = 3 R_{\odot}$ and effective temperature $T_{\text{eff}} = 4000 \text{ K}$. This results in a luminosity of $L_{\text{star}} = 2.1 L_{\odot}$, split among 10^8 photons (N_{ph}). These stellar parameters are similar to the findings obtained by Jacobsen et al. (2018) using radiative transfer modelling of both protostellar sources (A and B) in IRAS16293-2422. They constrained the individual luminosities to $L_{\text{A}} = 18 L_{\odot}$ and $L_{\text{B}} \leq 3 L_{\odot}$ for A and B, respectively.

Photon packages are emitted from the source with a certain energy and per unit time $\dot{E} =$

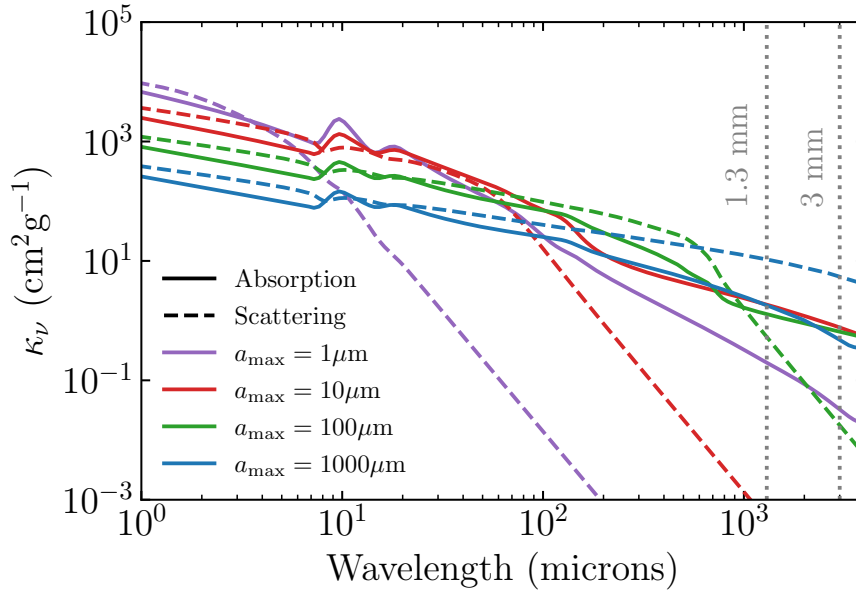


Figure 2.4: Absorption (solid lines) and scattering (dashed lines) opacities (in units of cm^2 per gram of dust) for dust grains of silicate plus graphite composition. All opacities were obtained assuming a grain size distribution with $q = 3.5$ and a minimum grain size of $0.1 \mu\text{m}$. Dotted vertical lines at 1.3 and 3 mm indicate the wavelengths of interest in the present study.

$L_{\text{star}}/N_{\text{ph}}$, wavelength, polarization state and a random direction. Along every direction, the probability for photon-dust interaction in an absorbing medium ($I_{\nu} = I_0 e^{-\tau}$, with τ the optical depth) is ruled by $p(\tau)d\tau = e^{-\tau}d\tau$, which integrated and normalized can be expressed as $z = 1 - e^{-\tau}$, or $\tau = -\ln(1-z)$, with $0 \leq z < 1$ a random number generated by a Monte-Carlo (MC) sampler. This statistical optical depth (τ_{MC}) is accumulated along the path length, and leads to a photon-dust interaction when the condition $\tau_{\text{MC}} > \tau_{\text{dust}}$ is met, where $\tau_{\text{dust}} = \int \kappa_{\text{ext}} \rho_{\text{dust}} ds$. Photon-dust encounters can be of absorbing or scattering nature. Upon every encounter, dust grains are assumed to absorb the incident photon energy and immediately re-emit a new photon as a black-body radiator. The temperature associated to this radiation is considered the dust temperature. Once the first photon finishes traversing the grid, another one is launched. This process is repeated iteratively until all photons have escaped the grid and the temperature distribution found at this stage is the resultant dust temperature field. Dust heating simulations in POLARIS base the absorption interaction on the scheme of continuous absorption (Lucy 1999) and instantaneous re-emission from Bjorkman & Wood (2001). in which the wavelength after interaction is sampled from

$$z = \frac{\int_{\lambda}^{\lambda+d\lambda} \kappa_{\text{abs}} \frac{d}{dT} B_{\lambda}(T_{\text{dust}}) d\lambda}{\int_{\lambda_{\text{min}}}^{\lambda_{\text{max}}} \kappa_{\text{abs}} \frac{d}{dT} B_{\lambda}(T_{\text{dust}}) d\lambda}, \quad (2.1)$$

with $0 \leq z < 1$ and λ sampled from 200 logarithmically spaced bins between $0.1 \mu\text{m}$ and 1 cm. Absorbing interactions change the wavelength of the outgoing photon, while for scattering

interactions, emitted photons change only their direction but not their wavelength. The outgoing direction is found by randomly sampling the scattering phase function. In this work we have used the Henyey-Greenstein phase function (Henyey & Greenstein 1941), $g = \langle \cos(\theta) \rangle$, which is fully determined by the g parameter ($-1 \leq g \leq 1$), with $g = -1$ and $g = 1$ representing backward and forward scattering, respectively.

Figure 2.5 shows the radially averaged midplane dust temperatures for both disk models. The temperature generated by star heating is only relevant within the very central zones in both cases, because the densities in the disks shield the outer regions from stellar radiation. In the MHD case, radiative heating overcomes the gas heating only up to 2 au outside the inner boundary and falls below ~ 60 K at larger radii. In the RHD case, it slightly overcomes the gas temperature at sub-au scales and then rapidly falls to a few K at 6 au, showing no contribution to the overall temperature field. We have also tested whether these results are dependent or not on the value of the opacities used and found that they hold (i.e., the disk does not heat up significantly beyond a radius of 10 au) even when increasing or decreasing the opacity by an order of magnitude. More details on such tests are described in section 2.6.3.

Dust temperatures combining stellar radiation and MHD/RHD gas temperatures

In this section, we consider both the gas temperature obtained from the heating mechanisms present in the MHD and RHD simulations T_{gas} (see section 2.3), and also the dust temperature provided by radiative dust heating T_{rad} . POLARIS allows to combine these two temperatures in order to account for heating at all scales. We provide here a brief explanation of the combination process and refer the reader to Reissl et al. (2016) for further details. In the case of a model with non-zero initial temperature, as for instance, when providing the temperature from the gas, the energy of a cell is considered to be the sum of the energy produced by radiation and that associated to the gas temperature. To obtain the energy of the gas temperature, POLARIS compares the new cell energy to the emissivity produced by the gas temperature and solve for the energy offset. Once the energy information is updated, the dust temperature is recalculated accordingly.

The gas temperatures in the MHD simulations are given by the EOS while in the RHD simulation the gas is able to cool radiatively according to its local optical depth (Stamatellos et al. 2007) and exchange energy via flux-limited diffusion (Bodenheimer et al. 1990; Whitehouse & Bate 2004). The radially averaged profiles for the $T_{\text{dust}} = T_{\text{gas}}$ and T_{rad} , as well as for the $T_{\text{dust}} = T_{\text{gas}}$ only case for both disk models are shown in Fig. 2.5.

From this figure, we conclude that for the MHD model, radiation from the protostar dominates within the first 4 au, but beyond that radius the temperature from the EOS dominates up to around 18 au. At larger radii ($\gtrsim 20$ au) outside disk edge, the protostellar heating dominates again resulting in a fairly constant temperature of 40 K. On the other hand, for the RHD model the protostar radiation is not able to penetrate beyond 1 au due to the high optical depth. Therefore, the disk temperatures at the scales where the spiral arms are located are not dominated by protostellar heating. Instead, the high dust temperature here is a result of the high gas temperature, which is also higher than the one reached by the MHD model. The resultant high dust temperatures are due to the efficient thermal coupling at high densities. It is non-trivial to disentangle the sources of extra heating in the RHD model versus the MHD model because they can come

from different sources. For instance, the models were generated with a different numerical setup, i.e., SPH vs grid-based code, with and without magnetic fields or radiative transfer and slightly different initial conditions. As pointed out by Whitehouse & Bate (2006) the thermal evolution of different setups is expected to be different. Moreover, they also discuss that the use of an EOS can underestimate the temperature of the gas surrounding the central highest density. This was also recently demonstrated specifically for the case of a gravitationally unstable disk (Xu & Kunz 2021b). In addition, the spiral arms do add extra compression heating, responsible for the local temperature rise.

While a comparative modelling study to investigate this is beyond the scope of this work, we can still rule out some possible reasons for the different temperature. For instance, it is not due to the RHD having higher density than the MHD model since the models show different temperatures while covering a similar density range. Likewise, the thermal evolution of the central density of the RHD code (shown in Fig. 8 of Forgan et al. 2009) and of the MHD code (see Fig. A1 from Zhao et al. 2018) is comparable. Also it is not due to the RHD disk being more optically thick, as a setup fully based on a EOS (with no cooling) would represent an optically thick limit.

Based on this analysis, we conclude that an extra source of heating is needed to explain the high brightness temperatures observed and that gravitational instabilities in the disk provide a relatively simple explanation for it. As discussed in Xu & Kunz (2021b), the lower the Toomre Q parameter, the larger the accretion rates which naturally result in higher temperatures.

2.4.3 ALMA synthetic observations

The ideal intensity distributions produced by POLARIS, in units of Jy pixel^{-1} , needed to be post-processed assuming a certain observing setup and telescope, in order to properly compare them with real observations. Because our goal is to compare our results to ALMA observations, we performed the synthetic observations using CASA, which provides the right tools to simulate ALMA observations. We first adjusted the header of our images to match those from the data at 1.3 and 3 mm described in section 2.2.1. We then used the `simobserve` task to generate the complex visibilities and finally cleaned the images using the `tclean` task. The observing and imaging setups for each frequency are slightly different since the real data was observed in different occasions and with different setups.

Visibilities were first generated at the frequency of 223 GHz (1.3 mm; band 6), with a bandwidth of 0.12 GHz toward the sky coordinates 16 h 32 m 22.63 s -24 d 28 m 31.8 s and using the array configuration C43-7 from Cycle 4. Such a setup achieves a synthesized beam of $0.082'' \times 0.067''$. The total observing time was 1.25 hours. Images were cleaned in multi-frequency synthesis (mfs) mode, with a standard gridding and a multiscale deconvolver. The visibilities were cleaned interactively using a briggs weighting scheme with a robust parameter of 0. For the observations at 1.3 mm only, we narrowed the range of baselines (uv -range) from 120 to 2670 $k\lambda$. The 3 mm observations shared the same setup, except that they were centered at the frequency of 99.99 GHz (band 3) with a bandwidth of 2 GHz using the most compact array configuration C43-10 from Cycle 5. Such a setup achieves a synthesized beam of $0.042'' \times 0.039''$. Since the resolutions of the simulated observations are slightly higher than those

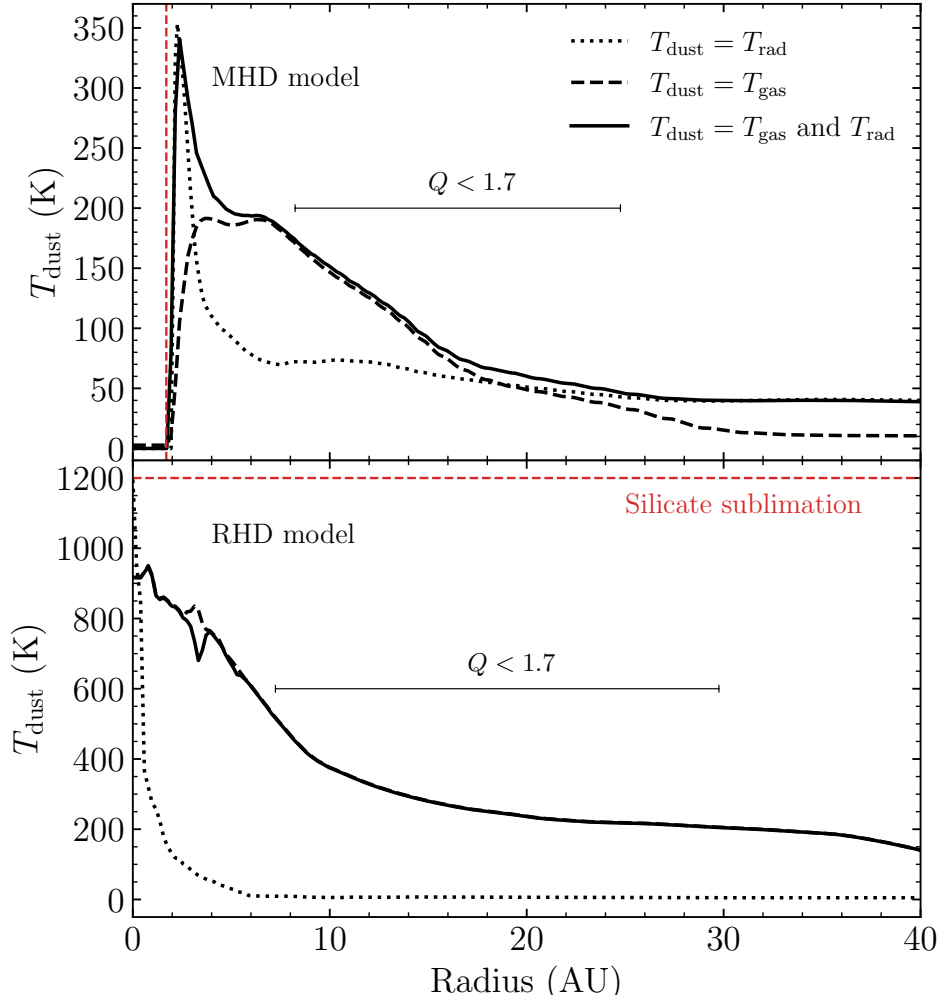


Figure 2.5: Radially averaged midplane dust temperatures. Temperatures are shown for the MHD disk formation model (top panel) and for the RHD gravitationally unstable disk (bottom panel). In both panels, the dotted line represents the dust temperature produced by radiative heating from the central source only, the dashed line represents the temperature assuming $T_{\text{dust}} = T_{\text{gas}}$, and the solid line represents a combination of both effects, as described in section 2.4.2. The red dashed line in the upper panel placed at 2 au, represents the inner boundary in the MHD model, and the red line in the lower panel represents an upper limit for the dust temperature set by the sublimation of silicates. The region where $Q < 1.7$ represents the extensions over which the disk is considered to be gravitationally unstable, as described in Appendix A.3.

of the real ALMA observations, all synthetic maps have been smoothed to match the respective resolution of the real observations.

2.5 Comparison with observations

2.5.1 Brightness profiles

Based on the intensity distributions generated by the radiative transfer calculations, we performed synthetic ALMA observations using the two disk models described in section 2.3 as sources. The observations were simulated with CASA (v5.6.2) following the procedure previously described in section 2.4.3. We analyzed the resulting images by generating cuts of the temperature brightness along the horizontal (east-west) axis and studied their similarities to the brightness profile from the real observations presented in section 2.2.2. The resulting profiles are shown in Fig. 2.6 at 1.3 (left column) and 3 mm (right column) for the MHD (upper panels) and RHD (lower panels) disk models. Profiles are shown for the real observation (semi-dotted black) and for different disk inclinations from 0 (face-on) to 40 degrees (rotated around the north-south direction) and assuming the opacity generated by a size distribution with $a_{\max} = 10\mu\text{m}$. The brightness temperatures are presented as a function of angular offset with respect to the peak emission, i.e., the zero offset corresponds to the peak in each image.

We have also tested the effects of a dust opacity with $a_{\max} = 1\mu\text{m}$ (i.e., $\kappa^{1.3\text{mm}} = 0.29\text{ cm}^2\text{ g}^{-1}$ and $\kappa^{3\text{mm}} = 0.05\text{ cm}^2\text{ g}^{-1}$), which is closer to ISM values (Mathis et al. 1977). However, the simulated emission with $a_{\max} = 1\mu\text{m}$ fails to reproduce the observed 3 mm fluxes at scales of ~ 20 au from the peak, by a factor of ~ 80 for the MHD model and ~ 5 for the RHD model. With this smaller a_{\max} , not only the fluxes are underestimated but also the disk looks much smaller and is incapable of reproducing brightness asymmetries with any of the two models. For this reason, the results presented hereafter, are all obtained assuming $a_{\max} = 10\mu\text{m}$.

Based on the analysis presented in section 2.4.2 and shown in Fig. 2.5, for our setup, the heating provided by protostellar radiation is only important when the gas temperature in the disk is relatively low ($T \sim 150$ K), as it is in the case of the MHD model. Therefore we consider both sources of heating (i.e., $T_{\text{dust}} = T_{\text{gas}} + T_{\text{rad}}$) when producing the synthetic emission maps of the MHD model. As the MHD model has a central hole (the inner boundary) with no temperature or density, we filled this hole before the ALMA simulations with a constant flux equal to the average values in the innermost ring (optically thick approximation). We note, however, that the angular extent of this hole is only 0.03 arcseconds and does not contribute significantly to the peak flux.

In the RHD model, the compression/shock heating overcomes radiative heating at almost all radii, and therefore, the results shown for the RHD model considered the dust temperature as provided by the **gas** temperature only ($T_{\text{dust}} = T_{\text{gas}}$). Regardless, the inclusion of the protostellar heating in this model would only change the fluxes of the peak, which we are not analyzing since the gas temperatures in this region can be overestimated due to the effect of the artificial viscosity (as explained in section 2.3.1).

Fig. 2.6 shows that the peak brightness generated by the MHD model underestimates the

values observed with ALMA by factors of 1.7 and 2, at 1.3 and 3 mm, respectively, when the disk is observed face-on.

We have also tested the effect of increasing the luminosity of the central protostar to 5 and 20 L_{\odot} , but this is still underestimating the fluxes even in the most luminous case, in agreement with the above-mentioned finding of rapid shielding from stellar flux at smaller radii. From all this parameter study, we conclude that the temperatures in the MHD disk are not capable of reproducing fluxes as high as those observed towards source B in these high-resolution observations, even when combining the temperature from both heating sources.

When considering both models beyond 10 au up to 40 au, the fluxes of the RHD model are much closer to the observed values than the case for the MHD disk. This is indeed the spatial scale at which the Toomre parameter is below 1.7 and the spiral arms are found in the RHD model. The fraction of underestimation from the MHD model at these scales (measured at a left-hand-side of the peak) is around 3 and 3.5 at 1.3 and 3 mm, respectively, while for the RHD model, the corresponding overestimation fractions are only 1.4 and 1.1 (measured at 0.14 arcseconds or ~ 20 au). As it can be seen, the match between simulated and real fluxes is better at the higher resolution observations, namely at 3 mm.

Our results also indicate the presence of asymmetric horizontal brightness profiles in the RHD disk model, similar to what is observed in Fig. 2.1, and follow a similar behavior to the left and right of the peak, i.e., a rapid decrease in intensity until 0.1" offset (14 au; $T_b \sim 180$ K) followed by a constant drop on the right and a two-phase drop (a.k.a, wing) on the left. Both features are best matched at the highest resolution observations taken at 3 mm. The asymmetric feature of the observations lies within offsets $\sim -0.07''$ and $-0.3''$. These are exactly the spatial scales at which the spiral arms are found in the RHD disk model (~ 10 -40 au; see Fig. 2.3), which supports that this type of asymmetry could be produced by the presence of spiral arms. However, this is only one possibility for the origin of the asymmetry and we acknowledge that other processes such as asymmetric accretion from the envelope onto the disk, based on the detection of infalling material (Pineda et al. 2012), may also be taking place. Further parameter space explorations are needed to rule-out any of the possible scenarios.

We also find that the more inclined disks produce lower fluxes than the face-on case. This can be explained by the higher optical depth obtained when the Line Of Sight (LOS) goes through more disk material, as it is the case for an inclined disk.

Since the RHD model, over scales of 10 to 40 au, appears to reproduce well the observed fluxes, we conclude that the high disk temperatures reached by the RHD gravitationally unstable model represent a good match to the ALMA observations of IRAS16293-2422 B. This suggests that the gas dynamics within the disk likely play a significant role in heating the disk.

2.5.2 Synthetic maps and spectral index of the RHD gravitationally unstable model

In this section, we present the synthetic observations at 1.3 and 3 mm along with its spectral index, for the best match to our observations, i.e., the RHD model. These results are shown in Fig. 2.7. We also provide the results for the MHD disk model in Appendix A.2. Similar to the real

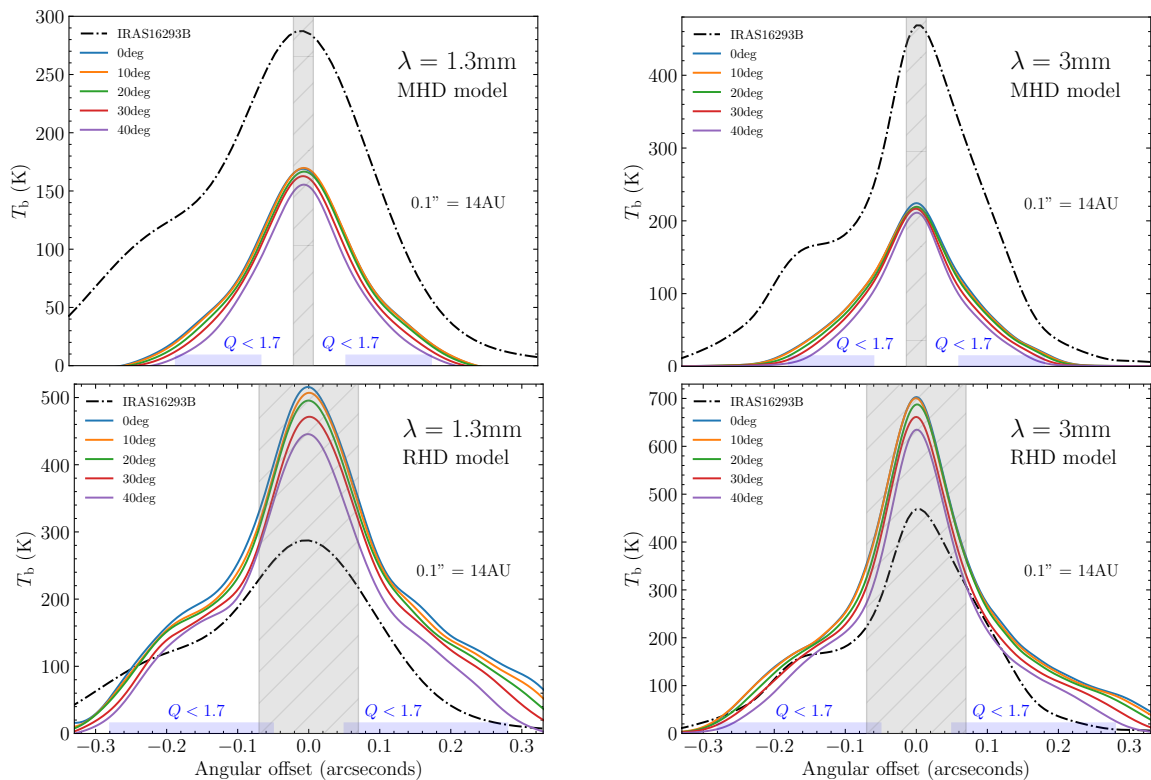


Figure 2.6: Horizontal cuts of brightness temperature distributions along the East-West direction and through the position of the peak flux. Top panels show the results at 1.3 and 3 mm, for the MHD model with $T_{\text{dust}} = T_{\text{gas}}$ and radiative heating. Lower panels show analogous results for the RHD model, where the disk temperature ($T_{\text{dust}} = T_{\text{gas}}$) is significantly higher and closer to the observed values. The grey shaded area in the MHD model represents the inner boundary of 2 au. The grey shaded region in the RHD model represents the inner 10 au in which the temperatures and therefore the fluxes can be overestimated by numerical high viscosity. The blue shaded region in all panels indicate the extensions over which the disk is considered to be gravitationally unstable, as described in Appendix A.3. The angular offset is measured with respect to the peak emission in each image.

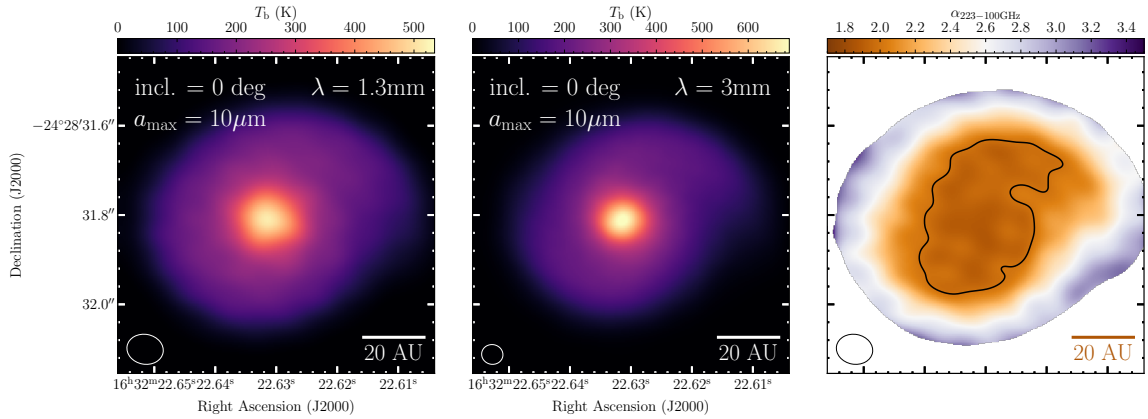


Figure 2.7: Synthetic brightness temperature maps at 1.3 and 3 mm along with the spectral index for the gravitationally unstable RHD model. The spectral index map reproduces well the trends seen in the observed map shown in Fig. 2.1. The contour for the spectral index indicates the $\alpha = 2$ region.

observations, the 3 mm map has been smoothed with the beam of the 1.3 mm observation before computing the spectral index. We present the results obtained by a dust grain size distribution with $a_{\text{max}} = 10 \mu\text{m}$ and for the face-on projection. At both wavelengths, the peak is approximately centered, although the extended structure is not circular or entirely symmetric. The substructures present in the disk, such as spiral arms (see Fig.2.3) are not clearly seen at 1.3 mm ($0.11'' \times 0.07''$ resolution), similar to the case with the real ALMA observations. On the other hand, the 3 mm observations, with their higher angular resolution and lower optical depth, display better the presence of spiral arms.

In analogy to Fig. 2.1, we present the derived spectral index between 1.3 and 3 mm (223 and 100 GHz) for the same disk model, with contours ranging from 3, 2 to 1.7. Our results indicate a drop to around $\alpha \lesssim 1.8$ at the very center of the source, similar to what is observed in the ALMA observations (see Fig. 2.1). This result is not only found in the case of the RHD disk model. In Fig. A.2 we show the results for the MHD disk model in a similar layout as Figs.2.1 and 2.7. The spectral index found in the MHD case is consistent with both the ALMA observations and the RHD model, with a tendency to decrease towards the center, reaching values as low as 1.7. In section 2.6.1 we discuss the origin of such a low α values in the observations and both models.

2.6 Discussion

2.6.1 Are early disks hotter towards the midplane?

The tendency for the spectral index α to decrease at the center of the disks found in the ALMA real and synthetic observations is an interesting observational feature that can provide us with information about the internal structure of early disks. The spectral index not only provides information on the slope of the SED but also indicates the presence of temperature gradients

along the LOS when the emission is optically thick. The dust opacity for a given grain size distribution follows a power-law function of wavelength and is therefore higher at 1.3 than at 3 mm. If the disk becomes optically thick along the LOS at both wavelengths, each wavelength will trace a different temperature layer within the disk, with the longer wavelength tracing the more deeply embedded layer. In the case of a positive temperature gradient towards the denser inner regions, which is the opposite of what's expected for more evolved passive disks (see e.g., Kenyon & Hartmann 1987; Chiang & Goldreich 1997; Armitage 2009, 2011; Dartois et al. 2003; Dullemond et al. 2007; Kama et al. 2009; Lizano et al. 2016; Tapia & Lizano 2017; Paneque-Carreño et al. 2021) where the dust temperature is mainly determined by radiative heating, lower frequency observations will trace hotter layers than higher frequency observations, leading to $\alpha \lesssim 2$ values, as described in Appendix A.1.

In principle, the brightness temperature resulting from our synthetic observations should trace the dust temperature of the layer within the disk at which the optical depth τ becomes unity (see also Evans et al. 2017). To prove our point, we show in Fig. 2.8 the 2D dust temperature distribution of the RHD disk at the $\tau = 1$ surface for both wavelengths, convolved with the corresponding beams of the ALMA observations. Such temperature structures match well those obtained from the radiative transfer calculations indicating that indeed both wavelengths trace two different temperature layers from different depths within the disk.

In Fig. 2.9 we present a 3D rendering of the dust temperature field of the RHD model, represented by the black-to-yellow colored isocontours and we include the $\tau = 1$ surfaces at 1.3 and 3 mm in green and blue, respectively. Assuming the observer is placed far above the top surface of the disk, this illustration shows the regions of the disk that the observations at 1.3 and 3 mm have access to. We obtain a similar result for the MHD model, which fluxes although too low for reproducing source B observations, can match observations towards other less luminous Class 0 disks. Hence, our results from these two models indicate that positive temperature gradients towards the inner denser regions in gravitationally unstable disks, can naturally explain the observations of low spectral index towards young disk sources, especially those with values below 2. These low spectral indices are usually interpreted as a sign of early grain growth, but early disks being warmer in their interior as compared with the later Class II disks is an alternative scenario, one that better matches with the theoretical predictions showed in this work. This scenario has also been suggested in previous works in which analytical temperature and density profiles were assumed (Galván-Madrid et al. 2018; Lin et al. 2021).

Recent constraints from molecular line observations have also shown that embedded disks are warmer than more evolved protoplanetary disks. For instance, the ^{13}CO and C^{18}O observations towards the nearly edge-on disk (85° ; Ohashi et al. 1997; Tobin et al. 2008; Oya et al. 2015) around the Class 0 protostar L1527, suggests that the midplane temperature is at least $\gtrsim 25$ K (van 't Hoff et al. 2018), which is contrary to the case of CO depletion in the midplane of Class II disks (Guilloteau et al. 2016; Dutrey et al. 2017). Warm disks have also been observed in several other disks in Taurus (van't Hoff et al. 2020).

The presence of a positive temperature gradient at small radii seems to be also the case in the evolved and gravitationally unstable (Dong et al. 2016) FU Ori disk (Lizano et al. 2016; Liu et al. 2019; Labdon et al. 2021). The high-resolution (0.1-10 au) observations reported by Liu et al. (2019) show the inner parts of the disk in FU Ori with temperatures above 700 K at radii

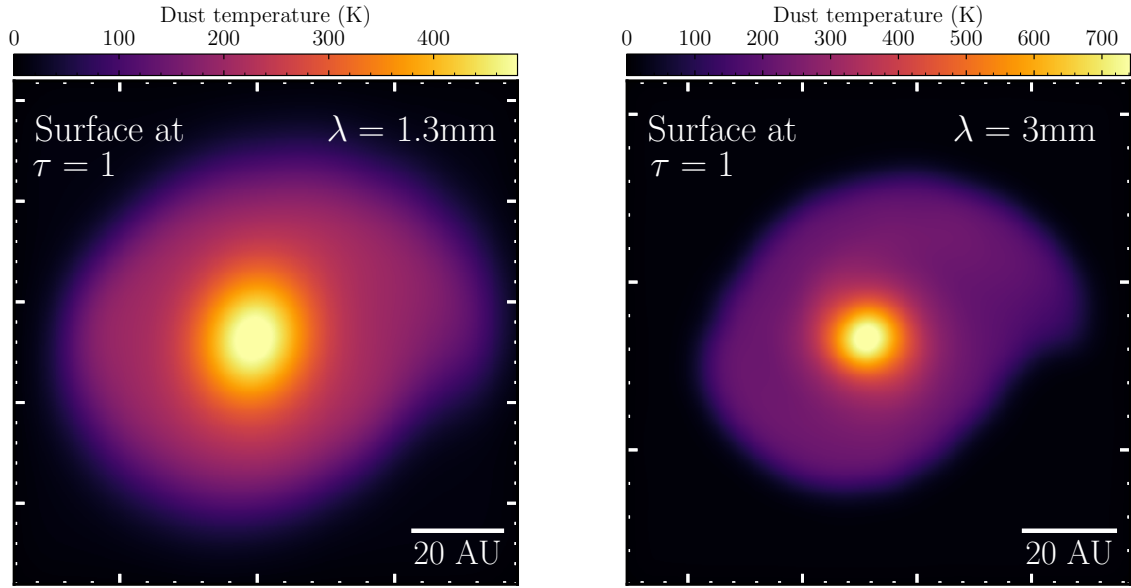


Figure 2.8: 2D face-on distribution of the dust temperature ($T_{\text{dust}} = T_{\text{gas}}$) from the RHD gravitationally unstable model, at the surface where the optical depth becomes unity. The temperature matches well the brightness temperature distributions shown in Fig. 2.7, demonstrating that the two wavelengths are indeed tracing different layers. A 3D view of such surfaces is shown in Fig. 2.9.

$\lesssim 3$ au. Their interpretation of the results suggests that the temperature in the inner 10 au is determined by the heating from gas kinematics and that radiative heating becomes important at larger radii, however, they acknowledge not having considered extra sources of heating (e.g., shocks and adiabatic compression) which could also dominate the viscosity as the main heating mechanism.

2.6.2 Are self-gravitating disks at the origin of some hot corinos?

The high temperatures (>100 K) of the IRAS 16293-2422 B disk implies that most of the volatile material in the dust icy mantles is thermally evaporated, including water and complex organic molecules accumulated during the prestellar phase. This process is likely at the origin of the rich chemistry observed by recent spectral line surveys (e.g. Jørgensen et al. 2018). It is then tempting to suggest that self-gravitating disks provide the conditions for the detections of the so-called ‘hot corinos’, hot regions nearby Class 0 sources, rich in complex organic molecules (e.g. Cazaux et al. 2003), since it has been shown that gravitational instabilities in a disk directly affects their chemical evolution (Ilee et al. 2011; Evans et al. 2015; Quénard et al. 2018). It is interesting to note that a self-gravitating disk with spiral arms has also been suggested to be present in the Class 0 hot corino HH 212 (Tobin et al. 2020; Lin et al. 2021; Lee et al. 2021). Additionally, another potentially gravitationally unstable disk in Orion A, HOPS-87 (Tobin et al. 2020) has been recently detected in methanol emission (Hsu et al. 2020), providing additional

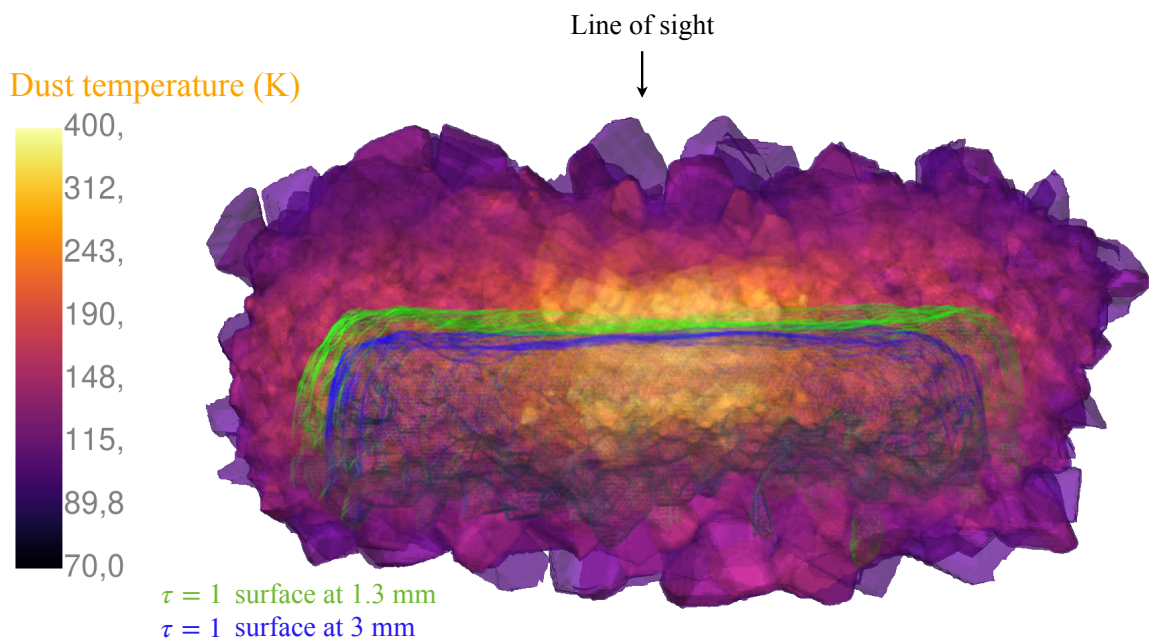


Figure 2.9: 3D rendering of the dust temperature ($T_{\text{dust}} = T_{\text{gas}}$) for the RHD disk model in edge-on projection. The green and blue surfaces represent the $\tau = 1$ layers at 1.3 and 3 mm, respectively. From the observer's point of view, the two optically thick surfaces lie at different depths within the disk and therefore trace dust layers at two distinct temperatures.

evidence for the presence of self-gravitating disks in hot corino sources. Studies similar to those presented here should be carried out in the currently known hot corinos to test our suggestion.

We finally note that within the central 20 au, in particular along the spiral arms of the self-gravitating disk where shocks are present (see Fig. 2.5), the temperature can exceed 300 K (as also found by Boley & Durisen 2008), allowing efficient sublimation of carbonaceous grains (e.g. van 't Hoff et al. 2020a). This is expected to affect the dust properties (as the important carbonaceous component will be locally depleted) as well as the gas phase chemical composition, due to the local increase of carbon atoms and hydrocarbons. This prediction could be tested with high angular resolution multiwavelength observations of the dust continuum emission (to measure possible opacity changes) as well as of C-bearing species (to measure possible increase of the C/O ratio at these locations) at low frequencies (to avoid dust opacity problems; e.g. De Simone et al. 2020).

2.6.3 Radiative heating under different assumptions

The complexity of a full 3D HD simulation requires that the inclusion of radiation transport should be somehow simplified as compared to a full 3D radiative transfer calculation like those performed with POLARIS. In particular, these two radiative transfer schemes differ in the frequency dependency of the opacities (Boley et al. 2006). The post-processing done in this paper is performed considering wavelength-dependent stellar fluxes and dust opacities. On the other hand, the RHD simulation makes use of a frequency-averaged opacity, the so-called Rosseland mean opacity, which changes to account for different temperature and density conditions (see Fig. 3 from Forgan et al. 2009).

In section 2.4.2 we discuss about the main heating mechanism determining the overall disk temperature in our MHD and RHD models. The results from the radiative equilibrium calculations suggest that protostellar radiation is not able to raise the disk temperature significantly beyond ~ 1 au and therefore the disk temperature is dominated by dynamical processes. However, here we want to check if these results also hold when assuming different opacities. In particular, constant opacities as those used in the RHD model. In order to test this effect, we ran radiative equilibrium calculations using roughly constant opacities between $0.5 \text{ cm}^2 \text{ g}^{-1}$ to $800 \text{ cm}^2 \text{ g}^{-1}$, which covers the opacities range used in the RHD model (Forgan et al. 2009), for temperatures less than 10^3 K. From these tests, we concluded that still protostellar heating alone is not sufficient to heat the disk to temperatures that can explain the observations. In addition, we performed these tests together with increasing the luminosity of the central source up to $20 L_{\odot}$ for the MHD disk, which is the less dense within the inner 5 au among the two models. We found that the temperature obtained from radiative heating alone, peaks at ~ 400 K within 1 au and falls rapidly to 150 K at 5 au, beyond which the profile closely follows that of the gas temperature (dashed curve from the upper panel in Fig. 2.5). This is obtained when using $20 L_{\odot}$ and $80 \text{ cm}^2 \text{ g}^{-1}$. This luminosity is close to the luminosity values inferred for the entire triple system IRAS 16293, and thus, represents an upper limit. As discussed in section 2.5.1, this temperature profile cannot explain the observations. Therefore, heating mechanisms due to dynamical processes are needed to explain the observations.

2.6.4 Comparison to spectral index in more evolved gravitationally unstable disks

Recently, the disk mass and millimetric spectral index for the Class II gravitationally unstable disk Elias 2-27 have been reported by Paneque-Carreño et al. (2021) and Veronesi et al. (2021). This protoplanetary disk shows spiral arms on $\gtrsim 200$ au scales, at which location the brightness temperature at 0.89, 1.3 and 3 mm is below 10 K, one order of magnitude lower than the observations of the Class 0 disk in this work. The derived disk mass is about $0.1 M_{\odot}$, this is factor of 3 lower than the RHD disk model presented in this work. The spectral index calculated using ALMA observations for Elias 2-27 at 0.89, 1.3 and 3 mm falls below 2.0 within $\lesssim 50$ au radius. As they also pointed out by the authors, such a low spectral index could be due to dust scattering effects (Liu 2019), but also due to relatively low dust temperature (Sierra & Lizano 2020). Alternatively, the heating mechanisms and the radiative transfer effects introduced in our present work may also partly contribute to that result as the inner region is expected to have higher densities. Given that Elias 2-27 is consistent with being gravitationally unstable, the gas kinematics may also play a non-negligible (e.g., as compared with protostellar irradiation) role heating the inner ~ 50 au of the disk, in particular, in the presence of spiral arms (c.f., Dong et al. 2016). As a demonstration, Fig. 2.10 shows the synthesized spectral index maps of our RHD model at the ordinary spatial resolution. It appears that the spectral indices can be low over a relatively spatially extended area, and are particularly low at the locations of the spiral arms. How important is this effect in Elias 2-27 can be discerned by constraining the dust brightness temperature and dust temperature with future high angular resolution and multi-frequency observations (e.g., including measurements at ~ 500 and ~ 700 GHz). The mechanisms we mentioned are not mutually exclusive. However, in the case that the low spectral indices are mainly due to low dust temperatures, the 0.89-1.3 mm spectral indices should be positively correlated with dust temperature and may not have a specific relation with the spiral structures. In the case that it is mainly due to non-radiative heating (e.g., compression or shocks), the 0.89-1.3 mm spectral index is expected to be anti-correlated with the dust temperature, and we should expect the spiral arms to be the local minimum of the 0.89-1.3 mm spectral indices.

2.6.5 The origin of the observed asymmetry

As discussed in Section 2.2.2, there is evidence also from continuum observations at $\sim 33 - 43$ GHz, molecular line distribution and kinematics showing that the asymmetry might be real and not a product of optical depth in a highly inclined disk (Rodríguez et al. 2005; Pineda et al. 2012; Zapata et al. 2013; Oya et al. 2018; Hernández-Gómez et al. 2019b).

Spiral arms are a natural feature in gravitationally unstable disks (Kratte & Lodato 2016). Depending on the physical conditions, they can be either symmetric or highly asymmetric structures. Regardless of their shape, a disk containing spiral arms will show brightness profiles that depart from a symmetric Gaussian profile, as the ones observed in Fig. 2.6. The exact shape of such a brightness profile depends strongly on the shape and position of the arms. Even if the arms are symmetric, they will not necessarily produce a flux pattern with symmetric wings around the peak, as we showed in the case of the RHD model in Fig. 2.6. Moreover, the position of the

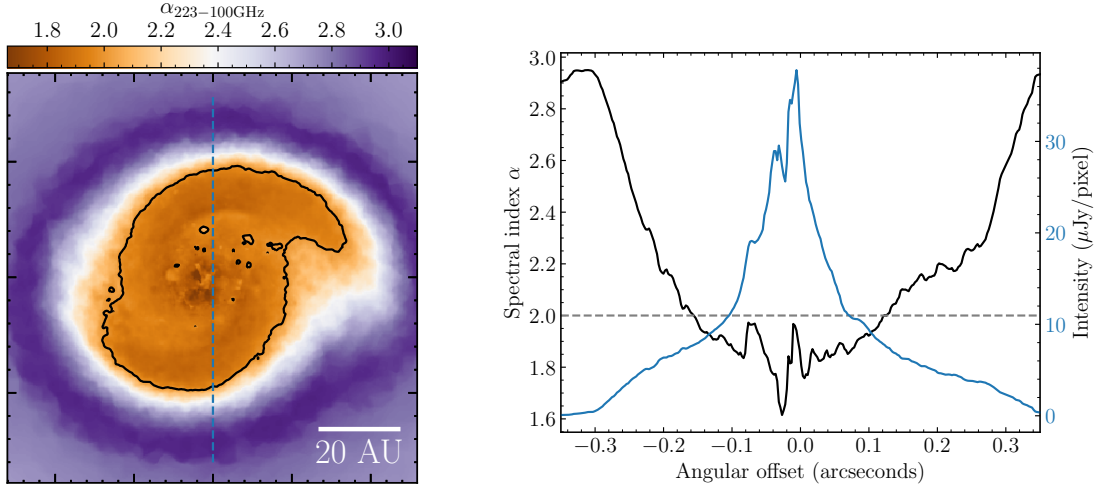


Figure 2.10: (top panel) Spectral index map for the RHD model disk shown in Fig. 2.7 before performing the ALMA simulation, i.e., at full spatial resolution. The black contour indicates the region with $\alpha = 2$ and the vertical dashed line indicates the cut region for the bottom panel. (bottom panel) The black line represents a vertical cut of the spectral index through the center of the image, for the face-on RHD model shown above, and the blue line represents the brightness distribution along the same cut for the 3 mm simulated observation, without convolution with the ALMA beam. The angular offset is measured with respect to the center of the map.

peak in a gravitationally unstable disk must not necessarily be centered within the disk. This shift of the peak from the center can arise by considering highly asymmetric spiral arms, unlike those shown by our RHD model. For instance, recent non-ideal MHD simulations presented by Coutens et al. (2020) showed a spiral arm pattern, produced by considering the collapse of a non-rotating $1 M_{\odot}$ core initialized with turbulence. Such an asymmetric structure, likely produced by the effect of the initial turbulent velocity field and magnetic field could explain the shift of the peak observed toward source B. This would also suggest that source B might have formed out of a core with initial turbulence or perturbation instead of solid-body rotation, which would be in agreement with the different orientations of the structures and rotation axes for sources A and B (Pineda et al. 2012; Maureira et al. 2020), similar to what has been suggested for other Class 0 multiple systems (Hara et al. 2021).

Another possibility not involving spiral arms would be that the position of the continuum is not tracing the position of the protostar. For instance, in the distribution of the spectral index shown in Fig. 2.1, the minimum value is fairly close to the center of the overall structure, while the peak of the dust continuum emission is not. This difference may be due to the continuum peak tracing instead the position of a hot structure close to the protostar and not the protostar itself, which would also be supported by the asymmetric distribution of the complex organic molecule emission (Calcutt et al. 2018b,a; Manigand et al. 2020, 2021). This asymmetry could also be associated with asymmetric accretion from the envelope onto the disk, based on the previous detection of infalling material in source B (Pineda et al. 2012; Zapata et al. 2013).

Follow-up observations with similarly high angular resolutions at longer wavelengths (e.g., VLA observations) would be helpful to further assess the origin of the asymmetry.

2.6.6 Mass estimates under the optically thin approximation

The masses of observed disks are generally calculated assuming that the dust emission is optically thin. However, as previously discussed, the model that best reproduces our observations is highly optically thick. Therefore, similar to the analysis done by Evans et al. (2017), we investigate here how much are the masses under- or overestimated in the case of embedded disks, when using this common approach.

The mass of a disk can be estimated from its flux density using the following equation (Hildebrand 1983):

$$M_{\text{disk}} = \frac{gS_{\nu}d^2}{\kappa_{\nu}B(T_{\text{dust}})}, \quad (2.2)$$

where S_{ν} is the flux, g is the gas-to-dust mass ratio of 100, d is the distance, $\kappa_{1.3\text{mm}} = 1.50 \text{ cm}^2 \text{ g}^{-1}$ and $\kappa_{3\text{mm}} = 0.58 \text{ cm}^2 \text{ g}^{-1}$ are the dust opacities and $B(T_{\text{dust}})$ is the Planck function for a given dust temperature T_{dust} . The fluxes of the RHD model integrated over a 5σ region are $S_{1.3\text{mm}} = 1.60 \text{ Jy}$ and $S_{3\text{mm}} = 0.29 \text{ Jy}$. Figure 2.11 shows the resultant masses as a fraction of the true mass ($0.3 M_{\odot}$) for temperatures from 30 K to 100 K. As the figure shows, although the disk temperatures are high, at least 100 K in the mid-plane (Fig. 2.5), when using the optically thin approximation at 1.3mm, the measured mass is closer to the real value for lower temperatures ($\sim 30 \text{ K}$). When assuming higher temperatures, the best estimates are obtained when using the 3 mm fluxes. For this particular disk model, using the 3 mm fluxes and a dust temperature of 55 K result in a more accurate estimate. This analysis shows that one can obtain a reasonable mass estimate under two erroneous assumptions (optically thin and low temperatures) due to the two effects canceling out each other. We caution the reader that the selection of this temperature works best for this particular model but it is not necessarily meant to be used for all kind of embedded disks.

2.7 Conclusions

In this work, we presented continuum ALMA observations at 1.3 and 3 mm towards the Class 0 protostar IRAS 16293-2422B with resolutions of 88 mas ($\sim 12 \text{ au}$) and 46 mas ($\sim 6.5 \text{ au}$), respectively. We analyzed profiles of brightness distribution and provide a spectral index map. We compared these with MHD and RHD numerical simulations of a gravitationally unstable disk with masses of 0.1 and $0.3 M_{\odot}$, respectively, both formed following the collapse of a dense core. Our results can be summarized as follows:

1. The peak brightness temperatures at 1.3 and 3 mm are 290 K and 470 K, respectively. Both peaks appear shifted to the west with respect to the center of the more extended emission which extends up to $r \sim 46 \text{ au}$ at 3mm. The spectral index decreases towards the center, starting from ~ 3 and reaching values less than 2 in the inner $\sim 20 \text{ au}$.

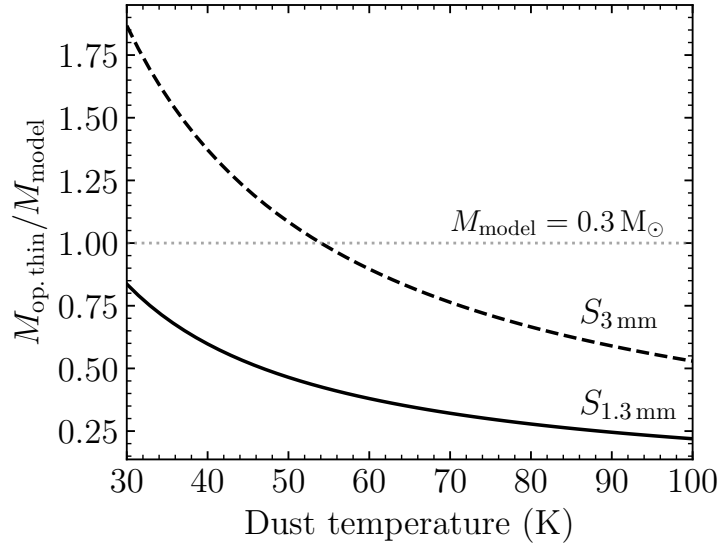


Figure 2.11: Ratio of the observational mass estimates over the original disk mass, for the RHD model. Masses are derived using equation 2.2 from the flux densities at 1.3 and 3 mm. The figure shows that the mass is best estimated for a dust temperature of 55 K with the less optically thick emission, i.e., at 3 mm.

2. We performed dust radiative transfer calculations and synthetic observations assuming maximum grain sizes of $a_{\max} = 1 \mu\text{m}$ and $10 \mu\text{m}$ for the two disk models. For these opacities, the albedo of the dust grains is very low and therefore the continuum flux arises mainly from thermal dust emission. The observed fluxes at both wavelengths can be better reproduced with the RHD disk assuming $a_{\max} = 10 \mu\text{m}$. This model has higher dust temperatures ranging from 200 K to 400 K across the disk midplane. These higher temperatures are naturally achieved by the numerical simulation that include radiative transfer coupled with additional heating from the compression triggered by the spiral arms.
3. Radiative heating from the central protostar alone is not able to heat up the dust beyond a few au from the central source and thus, cannot reproduce the high observed brightness temperatures (100 K to 200 K) between ~ 15 -30 au. These results still hold when increasing the luminosity of the central source or changing the dust opacities.
4. The presence of spiral arms in the RHD model leads to asymmetries in the brightness profiles beyond the peak. These asymmetries resemble the observed ones and thus we speculate spiral the structures could be present in this particular source.
5. Both disk models reproduce well the low spectral index values and its spatial distribution. This is because both disks are optically thick and show temperatures that are higher in the inner layers compared with the outer layers (i.e., self-obscuration). Thus, low spectral index values in embedded disks can naturally arise due to these disks being optically thick

and with an increasing temperature towards the inner layers (including the midplane) unlike the more evolved protoplanetary disks at comparable scales. This scenario does not require mm grain sizes or self-scattering effects.

The high temperatures present in the disk around source B allow to explain the large variety of complex organic molecules observed in the hot corino IRAS 16293-2422, as reported by recent spectral lines studies, such as the PILS survey. The possibility that these high temperatures are the consequence of gravitational instabilities, points to the idea that self-gravitating disks may provide the conditions for the detection of hot corinos in Class 0 sources. Thus, future observational and modelling studies targeting emission of COMs in gravitationally unstable disks may help to test this scenario.

Future high-resolution continuum observations at different wavelengths are needed to further investigate density and temperature substructures present in the disk. Similarly, future multi-wavelength high-resolution observations are necessary to investigate if the temperature and density distribution models presented in this work can also explain the fluxes and spectral index behavior for other embedded disks, providing important observational constraints to the physical structure of young protostellar disks.

Chapter 3

Exploring the dust grain size and polarization mechanism in IRAS 16293-2422 B

The content of this chapter was submitted to the *Astronomy & Astrophysics* journal. Credit: Zamponi et al. (submitted).

Abstract

Multiwavelength dust continuum and polarization observations arising from self-scattering have been used to investigate grain sizes in young disks. However, the likelihood of self-scattering being the polarization mechanism in embedded disks decreases for very highly optically thick disks and puts some of the size constraints from polarization on hold, particularly for the younger and more massive disks. The 1.3 mm polarized emission detected towards the hot ($\gtrsim 400$ K) Class 0 disk IRAS 16293-2422 B has been attributed to self-scattering, predicting bare grain sizes between 200-2000 μm . We aim to investigate the effects of changing the maximum grain sizes in the resultant continuum and continuum polarization fractions from self-scattering for a hot and massive Class 0 disk extracted from numerical simulations of prestellar core collapse and compare with IRAS 16293 B observations. We compared new and archival dust continuum and polarization observations at high-resolution between 1.3 and 18 mm to a set of synthetic models. We have developed a new public tool to automate this process called Synthesizer. It is an easy-to-use program to generate synthetic observations from numerical simulations. Optical depths are in the range 130 to 2 from 1.3 to 18 mm. Predictions from significant grain growth populations, including $a_{\text{max}} = 1000 \mu\text{m}$ are comparable to the observations from IRAS 16293 B at all observed wavelengths. The polarization fraction produced by self-scattering reaches a maximum of $\sim 0.1\%$ at 1.3 mm for a maximum grain size of 100 μm , which is an order of magnitude lower than that observed towards IRAS 16293 B. Significant grain growth could be present in the young Class 0 disk IRAS 16293 B, particularly in the inner hot region (< 10 au, $T > 300$ K) where refractory organics evaporate. The polarization produced by self-scattering

in our model is not high enough to explain the observations at 1.3 and 7 mm and that effects like dichroic extinction or polarization reversal of elongated aligned grains remain other possible but untested scenarios.

3.1 Introduction

Circumstellar disks, the sites of planet formation, are relatively well-studied in the more evolved Class II stage. However, in the earliest Class 0 phase, protostellar disks have only recently begun to be studied in detail (e.g., Maury et al. 2019; Segura-Cox et al. 2018; Tychoniec et al. 2020; Zamponi et al. 2021), and many of their properties such as mass, temperature and dust properties remain unknown, or highly debated. Since Class 0 protostellar disks set the initial conditions for planet formation, which could be underway already in the Class I phase (Sheehan & Eisner 2018; Segura-Cox et al. 2020), constraining the sizes of dust grains in disks at the earliest time possible is critical. This is usually done by constraining the variations of the spectral index at millimeter wavelengths, which can be related to the dust opacity index (Testi et al. 2014). In addition, polarization observations have proven to be a useful independent method to constrain the grain sizes in disks. This can be done if the origin of the polarized emission is self-scattering (Lazarian & Hoang 2007a,b; Kataoka et al. 2015; Andersson et al. 2015; Tazaki et al. 2017).

This mechanism refers to the polarization of the dust thermal emission scattered by the dust itself, and produces emission polarized to a few percent, at millimeter wavelengths for grain sizes in the micro- and millimeter range (Kataoka et al. 2017). The amount of polarization depends on the level of anisotropy of the radiation field generated by the self-scattered photons of the dust emission, which in turns depends on the inclination of the disk and the size of the scattering dust particles (Yang et al. 2016). The relation between the size of the dust grains and the maximum polarization fraction turns this polarized emission into a tool to estimate the level of grain growth at different evolution stages.

In the more evolved (Class II) protoplanetary disks, optical and near-infrared observations of scattered flux usually trace the emission from small dust grains that scatter off the protostellar flux in the upper layers of the disk (Avenhaus et al. 2018; Garufi et al. 2018, 2019, 2020). At millimeter wavelengths, the observed dust scattered emission is mainly originated from the dust thermal emission (Kataoka et al. 2015; Yang et al. 2016).

In this work we explore the effect of changing the maximum grain sizes in the resultant continuum and polarization fractions by dust self-scattering at millimeter wavelengths. We use a model produced by a radiation-hydrodynamic (RHD) numerical simulation of a prestellar core collapse. The disk formed is massive ($\sim 0.3 M_{\odot}$), hot (> 300 K, within 10 au), and optically thick at millimeter wavelengths. This disk model successfully reproduced Stokes I fluxes from ALMA ~ 6 -10 au resolution observations, at 1.3 mm and 3 mm, for the very young Class 0 disk IRAS 16293 B (Zamponi et al. 2021). Thus we also aim to test whether we can reproduce the fluxes and levels of polarization fraction observed in this source when the polarization is produced by self-scattering of spherical grains in the Mie regime. We expand on our previous exploration on grain sizes in this young disk (Zamponi et al. 2021) by showing the effects of varying the maximum grain size (a_{\max}) in the model from $10 \mu\text{m}$ to $1000 \mu\text{m}$. Furthermore, as the disk is

hot enough to evaporate solid organics, we show the effects of evaporating water and potentially some organics within the so-called sootline and having grain growth within this region, motivated by recent laboratory (Gundlach et al. 2018; Pillich et al. 2021) and observational (Liu et al. 2021) results.

This paper is structured as follows: in section 3.2 we provide details on the archival and new observational data used in this work, in section 3.3 we describe the dust model and polarization scheme used for the radiative transfer analysis, in section 3.4 we present the results of the assessment of grains sizes through the stokes I fluxes and our self-scattering models, in section 3.5 we discuss grain growth and possible mechanisms responsible for the observed polarization and other scenarios, and finally, in section 3.6 we present the conclusions of this work.

3.1.1 Previous observations towards the class 0 disk IRAS 16293 B

IRAS 16293-2422 B is a well studied Class 0 protostar located in the star-forming region ρ -Ophiuchi, and it is one of the closest and brightest protostars at a distance of 141 pc (Dzib et al. 2018). The disk around the protostar is hot ($T_b \gtrsim 400$ K) and massive, and likely subject to gravitational instabilities, as initially proposed by Rodríguez et al. (2005) and Dipierro et al. (2014), and recently confirmed by Zamponi et al. (2021). The source is very young ($<10^4$ yr, Andre et al. 1993) and its water snow line extends over a 20 au radius (Zamponi et al. 2021), making it an ideal laboratory to test the scenario proposed by recent laboratory experiments (Gundlach et al. 2018; Pillich et al. 2021; Li et al. 2021), that grain growth is boosted in dry conditions. The disk mass estimated by Zamponi et al. (2021) is $0.003 M_\odot$ in solid material, which would be 33 times higher than the minimum mass solar nebula of $30M_\oplus$ (in solids; Weidenschilling 1977; Andrews 2020). This implies that IRAS 16293B contains enough mass to form super-Earth planetesimals. Because of all these conditions, IRAS 16293B represents one of the ideal sites to probe grain growth at the earliest stages.

In the younger Class 0 disks, although polarization by self-scattering at millimeter wavelengths have also been proposed (e.g., Sadavoy et al. 2018; Tsukamoto et al. 2022), studies simulating the feasibility of this mechanism in more realistic young disk models, such as those formed out of the collapse of a core using 3D numerical simulations have not been done. This is particularly important since the physical properties of deeply embedded disks appear different in numerical simulations (e.g. Zamponi et al. 2021; Xu & Kunz 2021a,b; Bate 2022) as compared to widely used analytical models for Class II disks (Ballering & Eisner 2019).

In IRAS 16293-2422 B, polarized light was initially observed by Rao et al. (2009, 2014) with the SMA at $0.87 \mu\text{m}$, who detected polarization fractions of around $\sim 1.4\%$, distributed mostly azimuthally around the protostar location. The resolution of this detection was $0.6''$ (85 au) and likely traced envelope scales, which correspond to the bridge structure connecting the northern and southern protostars (Jørgensen et al. 2016; Maureira et al. 2020). Additional observations were presented by Liu et al. (2018b) with the VLA at 7 mm, and a 1.5 times better resolution. These observations resolved down to 50 au and found a similar polarization pattern and fraction ($\lesssim 2\%$). More recently, the survey of 1.3 mm polarization observations towards Class 0 protostars in ρ -Ophiucus, carried out by Sadavoy et al. (2019) at a 2 times better resolution ($0.2''$;

30 au), found polarization signatures associated to self-scattering in inner regions of most of their sources. The polarization in the disk of IRAS 16293 B was found to be azimuthal, similar to the SMA and VLA observations, however the authors associated the vector distribution to polarized self-scattering from an optically thick face-on disk, based on the models from Yang et al. (2017). The connection of a similar polarization pattern between 1.3 mm and 7 mm, being produced by self-scattering, implies that grains can have sizes between 200-2000 μm . In this work, we use a disk model from numerical simulations to test this hypothesis.

3.2 Observations

3.2.1 ALMA & VLA archival data

We have compiled archival multiwavelength polarization observations of IRAS 16293-2422 B at 1.3 mm (ALMA Band 6), 3 mm (ALMA Band 3) and 7 mm (JVLA Band Q). The 1.3 mm data used in this work is twofold. For the analysis presented in section 3.4.1 we used high-resolution Stokes I continuum images, with a resolution of $0.114'' \times 0.069''$ and a noise level of $104 \mu\text{Jy beam}^{-1}$ (0.3 K; see colorscale from leftmost panel in Fig. 3.1). For the analysis of polarized data, we used publicly available Stokes I, Q and U images by Sadavoy et al. (2018), each with a resolution of $0.18'' \times 0.09''$ and a noise level of $280 \mu\text{Jy beam}^{-1}$ (0.4 K), $25 \mu\text{Jy beam}^{-1}$ and $25 \mu\text{Jy beam}^{-1}$, respectively. Band 6 polarization vectors shown in Fig. 3.1 have been masked in regions where the stokes I flux is lower than $3\sigma_I$ and the polarized intensity is lower than $3\sigma_Q$. The 3 mm data we used is only available in stokes I, but presented the highest resolution image of IRAS 16293 B currently available, with a beam size of $0.048'' \times 0.046''$ and a noise level of $17 \mu\text{Jy beam}^{-1}$ (0.95 K). The data used at 7 mm contains full polarization information, with a resolution of $0.39'' \times 0.24''$ and a noise level of $35 \mu\text{Jy beam}^{-1}$ (0.25 K). Polarization vectors have been masked following the same criteria as for Band 6 observations.

We refer the reader to Zamponi et al. (2021) for more information about the high-resolution ALMA observations at bands 6 and 3 as well as their calibration and imaging. Similarly, we refer to Liu et al. (2018b) for the details on the observations, calibration and imaging of the polarized data at the JVLA band Q.

3.2.2 VLA Band Ka & Ku observations

We present JVLA standard continuum mode observations at Ka (9 mm) and Ku band (18 mm) toward IRAS 16293-2422 B, both in the A array configuration. Band Ka observations were carried out on March 07, 2022 (project code: 22A-322, PI: Zamponi). Band Ku observations were carried out on January 02, 04, and 05 2021 (project code: 20B-172, PI: Chia-Lin Ko). The pointing and phase referencing centers for our target source are R.A. = $16^{\text{h}}32^{\text{m}}22^{\text{s}}.610$ (J2000), decl. = $-24^{\circ}28'32''.61$ (J2000) for our Band Ka observations, and R.A. = $16^{\text{h}}32^{\text{m}}22^{\text{s}}.620$ (J2000), decl. = $-24^{\circ}28'32''.5$ (J2000) for Band Ku. We employed the 3 bit sampler in both observations.

For the band Ka observations, 24 antennas were used with a projected baseline range of 794-34.4 kilometers. Bandpass, phase and amplitude calibrators used were J1256-0547, J1625-

2527 & J1331+3030, respectively. We calibrated the data using the standard VLA Pipeline (v2021.2.0.128) using the Common Astronomy Software Applications (CASA; McMullin et al. 2007) package, release 6.2.1.7. The spectral configuration included 10 narrow (16 MHz) and 52 wide (128 MHz) spectral windows. We created our continuum image using wide windows only, with a total bandwidth of 7 GHz, centered at 33 GHz. We performed phase-only self-calibration iteratively in CASA. In each iteration the cleaning was done with the deconvolver `mtmfs`, a robust parameter of 0.5 and scales 0, 1 and 3 beams. The final image has a resolution of $0''.12 \times 0''.05$ (P.A. = -23.11°) and a noise level of $16 \mu\text{Jy beam}^{-1}$ (3 K)

For the band Ku observations, the absolute flux/passband and complex gain calibrators were 3C286 and J1625-2527. The projected baseline range is ~ 1.15 -36.50 kilometers. We manually followed the standard data calibration strategy using CASA (release 5.6.2). We utilized the built-in image model for 3C286 during the calibrations. After implementing the antenna position corrections, weather information, gain-elevation curve, and opacity model, we bootstrapped delay fitting and passband calibrations, and then performed complex gain calibration. We applied the absolute flux reference to our complex gain solutions, and then applied all derived solution tables to the target source. Finally, we based our observations on 3C286 to solve the cross-hand delay and absolute polarization position angles, and took J2355+4950 as a low polarization percentage calibrator when solving the leakage term (i.e., the D-term). We performed the zeroth order (i.e., `nterm=1`) multi-frequency synthesis imaging. The Briggs Robust=0 weighted image achieved a noise level of $47 \mu\text{Jy beam}^{-1}$ and a $0''.23 \times 0''.094$ (P.A. = 5.2°) synthesized beam.

Finally, since all the observations shown in Fig. 3.1 have been taken at different times, we have been corrected the images for the proper motion of the source calculated based on previous observations with the VLA (Hernández-Gómez et al. 2019a) and the 3 mm observations presented here. The applied correction is RA: -11.8 ± 0.3 mas/yr and DEC: -19.7 ± 1.3 mas/yr. We have aligned the observations to the observing time of the most recent band Ka observation (2022/03/07).

3.3 Disk and dust model

3.3.1 Protostellar disk model

To model the disk density and temperature structure of IRAS 16293-2422 B, we have used the numerical simulation of a hot and gravitationally unstable protostellar disk presented in Zamponi et al. (2021) and also shown in Fig. 3.2, which successfully reproduced the high continuum brightness temperatures ($T_b^{3\text{mm}} \gtrsim 400$ K) observed towards IRAS 16293B. The disk model represents a stage 18.2 kyr after the collapse of a $1 M_\odot$ spherical and isothermal cloud, simulated using the smoothed-particle-hydrodynamics (SPH) code `sphNG` (Bate et al. 1995) which included a radiation transport scheme, to account for cooling and heating processes along the temporal evolution. The mass in the disk at this point is $\sim 0.3 M_\odot$. The gas temperature is $\gtrsim 300$ K within the central 10 au and decreases to ~ 200 K at the scales where two roughly symmetric spiral arms have formed (10-30 au; see Fig. 3.2).

To generate our radiative transfer model, we have set the dust temperature to be equal to the

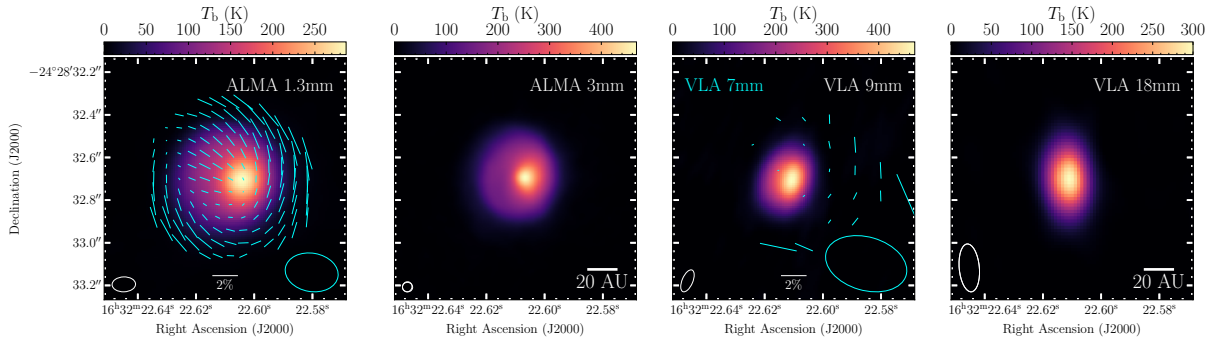


Figure 3.1: IRAS 16293-2422 B observed at ALMA bands 6 & 3 and VLA bands Q, Ka & Ku, from left to right. Cyan vectors represent polarization E-vectors (masked out below $3\sigma_1$ and $3\sigma_Q$) and the scalebar indicates a level of 2% polarization fraction. The continuum data at 1.3 and 3 mm was presented by Zamponi et al. (2021) and the 1.3 mm polarization observations were presented by Sadavoy et al. (2018). The polarized continuum observations at 7 mm were obtained from Liu et al. (2018b). 9 mm and 18 mm continuum observations are presented in this work for the first time. The angular resolution of the observations are: $0.114'' \times 0.069''$ at 1.3 mm ($0.18'' \times 0.09''$ for polarized data), $0.048'' \times 0.046''$ at 3 mm, $0.39'' \times 0.24''$ at 7 mm, $0.12'' \times 0.05''$ at 9 mm and $0.23'' \times 0.09''$ at 18 mm.

gas temperature from the RHD simulation. This is justified because of the high densities leading the dust to be coupled with the gas (see also Zamponi et al. 2021). We assume a gas to dust density ratio of 100. We have used the RADMC3D radiative transfer code (Dullemond et al. 2012) with a regular cartesian grid, generated by interpolating all particle positions. The particle interpolation and gridding was done through our new tool, called Synthesizer (see section 3.3.2), which automates the generation and execution of radiative transfer models from numerical simulations. The resulting dynamic range and spatial distribution of the gas density and temperature between our gridding scheme and that from Zamponi et al. (2021) are in very good agreement. The former gridding scheme used in Zamponi et al. (2021) consisted on a Voronoi tessellation of the particle locations which was supported in POLARIS (Reissl et al. 2016), but it is not yet fully supported in RADMC3D (beta feature).

3.3.2 The Synthesizer: from simulations to synthetic observations

In order to automate the comparison of observational data and simulation outputs, we have developed a new tool called SYNTHESIZER, which we have made publicly available¹ in the form of a python package. Synthesizer is a program to calculate synthetic images from either an analytical model or numerical simulations directly from the command-line. For SPH simulation, it interpolates the particle positions into a rectangular cartesian grid and then uses RADMC3D to do the Monte-Carlo and raytracing. Then it feeds the output image to CASA to generate a final

¹<https://github.com/jzamponi/synthesizer>

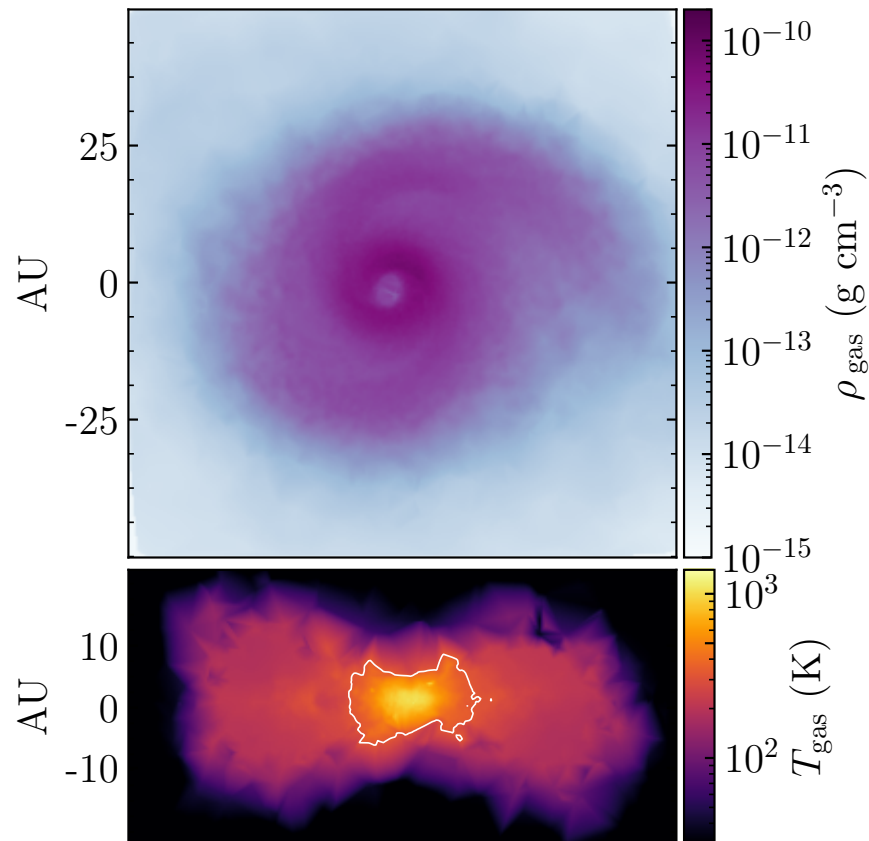


Figure 3.2: Face-on gas density (top) and edge-on temperature (bottom) distributions across the midplane of the protostellar disk model, that we used to model the emission of IRAS 16293-2422 B. The white contour in gas temperature represents the extension of the soot-line at 300 K. This model is presented in greater detail by Zamponi et al. (2021).

synthetic observation. Support for polarization models, either by scattering or grain alignment, is also included. Additionally, the SYNTHESIZER includes a module called the DUSTMIXER. This is a tool to generate dust opacity tables and full scattering matrices from the optical constants of a given material, all from the command-line. DUSTMIXER also allows to experiment with the mixing of different materials and different grain sizes. For further information about this dust module, see appendix B.1.

3.3.3 Grain sizes

In this work we have used a dust model similar to that used by Zamponi et al. (2021), corresponding to spherical grains with a minimum size of $0.1 \mu\text{m}$. This lower end of the size distribution is chosen based on the prediction for removal of very small grains during the stage of protostellar disk formation (Zhao et al. 2018; Silsbee et al. 2020). In this work we explore maximum grain sizes in IRAS 16293B by showing the effect of a_{max} on the resultant simulated fluxes. In Zamponi et al. (2021) we modelled the emission of IRAS16293B using a dust population with $a_{\text{max}} = 10 \mu\text{m}$ only, which successfully reproduced the observed brightness temperatures. The millimeter scattering opacities in that case are negligible (see Fig. 3.3). The results in Zamponi et al. (2021) demonstrated that the low ($< \sim 2$) 1.3-3mm spectral index observed in the IRAS 16293 B disk could be reproduced without the need for larger grains in which the scattering opacities are important. The reason for this was that the resultant disk from the numerical simulation is both hot towards the inner layers and optically thick at millimeter wavelengths, both necessary conditions to recover the low observed alpha (see Figure 9 in Zamponi et al. 2021). Here we extend the analysis by considering distributions with $a_{\text{max}} = 10, 100 \& 1000 \mu\text{m}$, and compare the resulting images to the observations presented in Fig. 3.1 (see section 3.4.1).

The dust opacities computed for different models are presented in Fig. 3.3 (silicates + graphites and silicates + graphites + organics). The figure shows three panels, one for each maximum grain size, and tabulated in Table 3.1 for the 4 observing wavelengths from Fig. 3.1. For each a_{max} , three different linestyles represent absorption, scattering and extinction opacities for a given composition (colored lines). When comparing the three panels, we can see at a glance the relation between the albedo ($\kappa_{\text{sca}}/\kappa_{\text{ext}}$) and the maximum grain size. The wavelength regime in which $\lambda \sim 2\pi a_{\text{max}}$ is also where the albedo is the highest. Because of this, the millimeter scattering opacities can vary by orders of magnitude for maximum grain sizes between 10 and $1000 \mu\text{m}$. These differences reflect also on the level of polarized scattered flux (produced by dust self-scattering) and turn it into a proxy of grain growth (Kataoka et al. 2016a,b; Yang et al. 2016; Stephens et al. 2017; Harris et al. 2018; Sadavoy et al. 2018; Ohashi et al. 2020; Lin et al. 2021).

3.3.4 Composition

Our fiducial dust mixture consists of 62.5% of astronomical silicates and 37.5% of graphite (Sil:Gra curve in Fig. 3.3). The optical constants² for both materials were obtained from Draine (2003a) and Draine (2003b), respectively. However, carbon-bearing species in the interstellar

²<https://github.com/jzamponi/synthesizer/tree/main/synthesizer/dustmixer/nk>

medium may be present in many forms and shapes, and may not necessarily be all crystallized as graphite. They can also be amorphous or ring-like (as in PAHs) carbonaceous. The predominant shape of carbonaceous material in space is hard to determine (Jager et al. 1998; Zubko et al. 2004; Birnstiel et al. 2018). According to Draine (2003a), molecules with sizes larger than $0.1 \mu\text{m}$ are likely to be crystallized. This is in fact the lower end of our size distribution (see section 3.3.3), hence, we assume graphite as a fiducial representation of the carbon budget in our dust model.

To consider the effects of carbon evaporation, we have also considered inclusions of refractory organics (Henning & Stognienko 1996) into the carbon mixture and studied the resulting differences in the overall opacity. Refractory organics have considerably lower sublimation temperature ($\sim 300 \text{ K}$, Jager et al. 1998; van 't Hoff et al. 2020b; Li et al. 2021) compared to that of graphite ($\sim 2100 \text{ K}$). Taking into account the lower sublimation temperatures of certain carbonaceous materials is important because they decrease the dust mass in hot regions and results in an overall decrease in the dust opacity. This sublimation zone within which the amount of carbon in the grains is reduced, also called "soot-line" (Kress et al. 2010; van 't Hoff et al. 2020b), is likely to be present in IRAS 16293B at a radius of $\sim 10 \text{ au}$, based on the high ($T_b \gtrsim 400 \text{ K}$) brightness temperatures observed (see Fig. 3.1). The spatial extension of this region in our disk model is illustrated by the white contour in the edge-on temperature projection in Fig. 3.2 which extends radially up to $\sim 10 \text{ au}$ and vertically to $\sim 8 \text{ au}$.

The difference between opacities with and without organics can be seen in Fig. 3.3. In the two compositions with carbon, the total carbon fraction of 37.5% is kept constant. For the one including refractory organics, we replaced 50% of the graphite by refractory organics, meaning, both have mass fractions of 18.75%. At millimeter wavelengths, the opacity of a dust population with a_{max} of 10 or $100 \mu\text{m}$ is largely dominated by graphite instead of silicate. When we compare the two different compositions, i.e., silicates-graphites versus silicates-graphites-organics, we see that a mixture with inclusions of organics has a lower opacity than a purely graphitic material. This is because the opacity of pure graphite is larger than that of pure organics and including organics into the mixture implies a partial removal of graphite, since our carbon budget is maintained constant³. When considering organics evaporation in our radiative transfer calculation we change the dust compositions accordingly. In regions where $T_{\text{dust}} < 300 \text{ K}$, the dust is a mixture of silicates, graphites and refractory organics, whereas in regions where $T_{\text{dust}} \geq 300 \text{ K}$ ($\sim 10 \text{ au}$ radius), we removed the organics from the mixture to mimic the sublimation of carbon and locally scaled down the dust-to-gas mass ratio by the corresponding mass-loss factor. Within the soot-line, the organics get sublimated and removed from the dust grains. This produces a reduction of the dust mass and opacity which results in a reduction of the optical depth.

Two major features can be concluded from Fig. 3.3: (I) for every a_{max} the difference in opacity between both compositions is very small, and (II) in the regime where $\lambda \sim 2\pi a_{\text{max}}$, i.e., where the albedo is maximum (Mie regime), the dust opacity is highly insensitive to variations in the dust composition. This means that observations of polarized emission produced by scattering

³We acknowledge that the presence of refractory organics in the icy mantles of dust grains should in principle not affect the content of core carbon (i.e., graphite) and that a proper sublimation model should evaporate the refractory carbon without affecting the graphitic core. However, the nature of the mixing process in our setup (see section 3.3.2), forces us to reduce the mass fractions of some materials to account for the inclusion of new others, while keeping the dust mass constant.

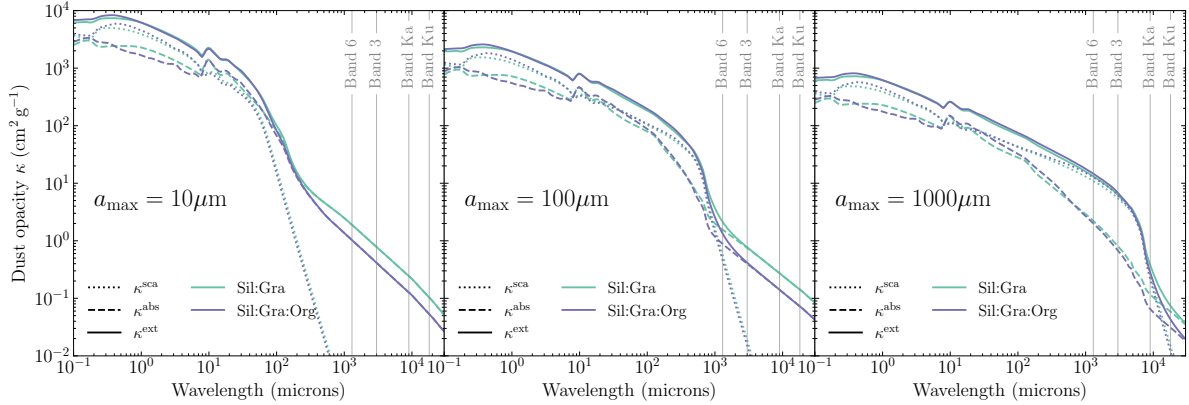


Figure 3.3: Dust opacities for different maximum grain sizes and compositions. The three panels show, from left to right, dust opacities for a maximum grain size of 10, 100 & 1000 μm , respectively. Each panel contains opacities generated for a mixture of silicates and graphite (0.625-0.375) and a mixture of silicates, graphites and refractory organics (0.627-0.300-0.075; 80% of organics). The gray curve on every panel indicates the albedo of the fiducial composition (silicates and graphites). Four vertical gray lines indicate the observing wavelengths used in this study, corresponding to the observations from Fig. 3.1. The exact opacity values used in this work are listed in Table 3.1, for different a_{max} and compositions, at all four wavelengths.

can serve as a tool to constrain grain sizes but not compositions. The small differences we find for different compositions are associated with the resulting extinction opacity and not with the polarization pattern or fraction. We acknowledge that in some cases, variations in the scattering polarization patterns can indeed be produced by different dust compositions, as it is shown by Yang & Li (2020). Their works shows that compositions like those from Kataoka et al. (2015) or Yang et al. (2016) can produce polarization reversal (i.e., 90 degrees rotation of the vector angles) when elongated millimetric grains are present.

3.3.5 Polarization by dust self-scattering

We have performed radiative transfer calculations in all four Stokes components (I, Q, U, V) using the radiative transfer code RADMC3D (Dullemond et al. 2012). To model the Stokes I fluxes produced by the model, we raytraced the dust thermal emission along the line-of-sight and included the emission scattered by the dust grains, both from stellar and dust thermal radiation. The dominant source of scattering at millimeter wavelengths is the scattered dust thermal emission, namely, self-scattering (Kataoka et al. 2015).

Scattering of light in dusty media is commonly modelled as a stochastic process of absorption and re-emission of light (Bjorkman & Wood 2001) by means of a Monte-Carlo (MC) simulation (Steinacker et al. 2013). The scattering event is modelled as the re-emission of an absorbed photon in a random direction. The likelihood for a given direction is not isotropically distributed, but rather follows the commonly used phase function from Henyey & Greenstein (1941). However,

a_{\max}	Mix	Band 6	Band 3	Band Ka	Band Ku
		1.3 mm	3 mm	9 mm	18 mm
10 μm	s-g	1.84	0.76	0.24	0.10
	s-g-o	0.52	0.20	0.06	0.02
100 μm	s-g	2.10	0.76	0.27	0.14
	s-g-o	0.86	0.20	0.06	0.03
1000 μm	s-g	13.19	6.22	0.38	0.07
	s-g-o	15.68	7.13	0.22	0.02

Table 3.1: Dust opacities (g cm^{-2}) used in this work, for different maximum grain sizes, different compositions and at four wavelengths. The two compositions are: silicate with graphite (s-g) with mass fractions 0.625 and 0.375, respectively, and silicate with graphite and refractory organics (s-g-o), with mass fractions 0.625, 0.1875 and 0.1875 (80% of carbon), respectively.

this kind of scattering model considers only information about the light intensity and not of the polarization state, i.e, stokes I only flux, without stokes Q and U. To calculate polarized flux, the scattering process has to be represented by a matrix rotation of all four Stokes components. This process is also called full Mie scattering (Mie 1908; Bohren & Huffman 1983; Wolf & Voshchinikov 2004) and is significantly more computationally expensive than the case for the Stokes I only. To ensure both approaches deliver similar Stokes I fluxes, we tested convergence of the scattering Monte-Carlo. The convergence was reached at about 10^{10} photons.

The information associated with linear polarization of light is stored in the Q and U components of the Stokes vector. We estimate the total linearly polarized intensity PI, polarization degree P_{frac} and polarization angle P_{angle} as

$$PI = \sqrt{Q^2 + U^2}, \quad (3.1)$$

$$P_{\text{frac}} = \frac{PI}{I}, \quad (3.2)$$

and

$$P_{\text{angle}} = \frac{1}{2} \arctan\left(\frac{U}{Q}\right), \quad (3.3)$$

respectively.

3.3.6 Synthetic observations

We post-processed the output from the radiative transfer model with a series of synthetic observations, using the observing setups of the ALMA and VLA observations shown in Fig. 3.1.

This step was performed using our newly developed tool Synthesizer (see section 3.3.2). The Synthesizer uses the CASA (v5.6.2) software and its SIMOBSERVE and TCLEAN tasks to produce a synthetic image from a model image, which we use as the output of RADMC3D. The CASA scripts for the setup at every band are available within the Synthesizer public repository⁴.

All synthetic maps include the thermal noise associated to the corresponding observing setup (time, bandwidth, cycle, etc.), and lead to noise levels comparable to the real observations. In regions of the images where Q and U are not well detected, equation (3.1) leads to a positive bias in the polarized intensity that must be removed (Simmons & Stewart 1985; Vaillancourt 2006). The polarized intensity must be then debiased by taking into consideration the thermal noise in the polarization map σ_{PI} as

$$PI = \sqrt{Q^2 + U^2 - \sigma_{PI}^2}, \quad (3.4)$$

where we assume that $\sigma_Q \sim \sigma_U \sim \sigma_{PI}$ (Vaillancourt 2006). When producing maps of polarized emission and polarization vectors from synthetic observations, we mask out the vectors at locations where $I/\sigma_I < 3$ and $PI/\sigma_{PI} < 3$, same as we did for the real observations in Fig. 3.1.

3.4 Results

3.4.1 Effects of different maximum grain sizes on the Stokes I fluxes

We start our analysis by producing synthetic observations of the Stokes I fluxes from our disk model at 4 different wavelengths: 1.3, 3, 9 & 18 mm, corresponding to the ALMA bands 6 & 3 and VLA bands Ka & Ku (Fig. 3.1). All Stokes I images and profiles presented in this paper represent net fluxes. This means thermal plus scattered flux. For each band we mimicked the observing setup of the real observations described in section 3.2 and presented in Fig. 3.1. We extracted a cut of the brightness temperature maps along the east-west axis and plotted it as a function of physical offset from the peak, as shown in Fig. 3.4. All brightness temperature cuts are taken along the position of the peak flux which correspond to offset zero in Fig. 3.4. The black line in Fig. 3.4 represents the observed source brightness, and the three different colored solid lines represent the models with different a_{max} . A black horizontal line in the upper right corner of each panel indicates the geometric mean between the major and minor axis of the beam. Dashed lines show models with carbon-sublimation (see section 3.4.2).

At each wavelength, the flux decreases with increasing a_{max} . This is because all the models are optically thick (see Fig. 3.5), and the larger the a_{max} the higher the optical depth. This effect, along with the decreasing temperature as a function of the scale height, leads to colder dust temperatures being traced by the larger a_{max} . For a_{max} 100 μm and 1000 μm the fluxes are further lowered from the dust temperature of the $\tau = 1$ layer due to a significant albedo (Birnstiel et al. 2018). This also explain why for a given a_{max} , the peak fluxes increase with wavelength as longer wavelength penetrate further within the disk where the temperatures are higher. We note that at 18 mm both the observed models and observations are affected by beam dilution.

⁴<https://github.com/jzamponi/synthesizer/tree/main/synthesizer/synobs/templates>

The net fluxes from both a_{\max} 10 and 100 μm are similar because they are completely determined by the extinction optical depth, which is similar between these two models (see Fig. 3.5). The difference between these two models lies on the albedo, which is higher for $a_{\max} = 100 \mu\text{m}$.

When comparing our models to the observations (black profile in Fig. 3.4), a similar trend is seen. This is a feature of a optically thick disks with a positive temperature gradient towards the center. Towards the center, the observed Class 0 disk fluxes lie between the models with $a_{\max} = 100 \mu\text{m}$ and 1000 μm , with differences between the observations and models within a factor of up to 2. On the outskirts, most models tend to overpredict fluxes up to a factor of 2 towards negative offsets and a factor of several for positive offsets. This east-west difference is because our disk model does not have such a marked east-west asymmetry as the one observed in IRAS 16293 B (see Fig. 3.1). Scenarios that can explain the observed asymmetry like the presence of asymmetric spiral arms or an off-center protostar were discussed in Zamponi et al. (2021). The comparison between models and observations suggest that grains could have grown significantly in this young Class 0 disk even up to millimeter grain sizes, provided that the vertical gradients of temperature and density are close to those in IRAS 16293 B.

3.4.2 Effect of carbon sublimation within the soot line

Because the observed brightness temperatures and model dust temperatures are high ($\gtrsim 400$ K), it might be that some of the dust materials get evaporated at these early stages. Silicate sublimation temperature is around 1200 K, and for graphite it is 2100 K. Both well above the central disk temperatures. However, carbon can also exist in non-graphitic forms, like amorphous carbon or Polycyclic Aromatic Hydrocarbons (PAHs) within ice layers. To study the scenario of dust containing refractory carbon that can sublimate at the observed disk temperatures, we also produced synthetic observations with a dust model that includes amorphous carbon. For this we use the optical constants from amorphous carbon (CHON) from Henning & Stognienko (1996) and set a sublimation temperature of 300 K. This temperature is based on the analysis presented by Li et al. (2021) who estimate a temperature range between 200 and 650 K from meteoritic constraints. This range was further narrowed to 300 K by van 't Hoff et al. (2020b) after analysing the relation between sublimation, gas temperature and pressure at hot-core conditions. The thermodynamic relations they used were derived from PAHs characterized in the lab (Goldfarb & Suuberg 2008; Siddiqi et al. 2009). In our disk model, the soot-line at 300 K covers the inner 10 au in radius and ~ 8 au in scale height (see Fig. 3.2). The extension of this region is also shown with a black scalebar at the bottom of Fig. 3.4. Further details on the dust composition and radiative transfer setup for the inclusion of amorphous carbon were described in section 3.3.4.

The resulting brightness temperature profiles for the case with carbon sublimation are also shown in Fig. 3.4 in the form of dashed lines. In the sublimation case the grain size remains homogeneous but the composition does not. Outside of the sootline, grains are composed by silicate, graphite and refractory organics (opacity given by the purple line of Fig. 3.3). Inside the sootline, amorphous carbon is removed and the composition is the fiducial silicate and graphite mixture (light-green line in Fig. 3.3), however, with a dust mass reduced by the factor of material sublimated. In Fig. 3.4 the dashed lines show the the case of 80% organics, meaning a dust

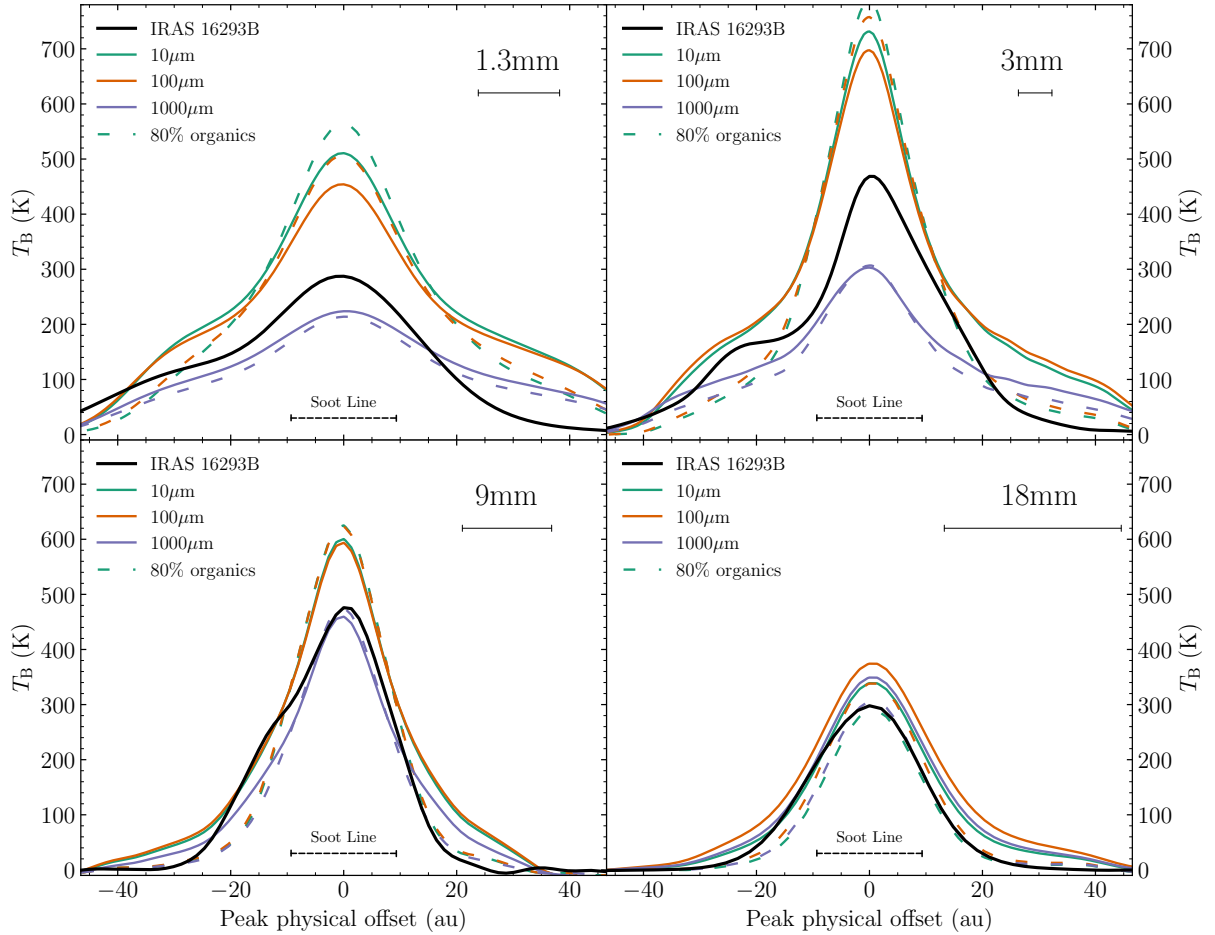


Figure 3.4: Cuts of the brightness temperature distribution along the east-west axis for real and synthetic observations at four wavelengths. The black solid line in each panel represents the ALMA and VLA observations shown in Fig. 3.1. Colored lines indicate models with different maximum dust grain size, taking values of $a_{\text{max}} = 10, 100 \text{ \& } 1000 \mu\text{m}$. We have included models accounting for the sublimation of 80% of the carbonaceous material, in the form of refractory organics. The sublimation zone extends over a 10 au radius where the gas temperature exceeds 300 K. The black line under every wavelength label, indicates the angular resolution.

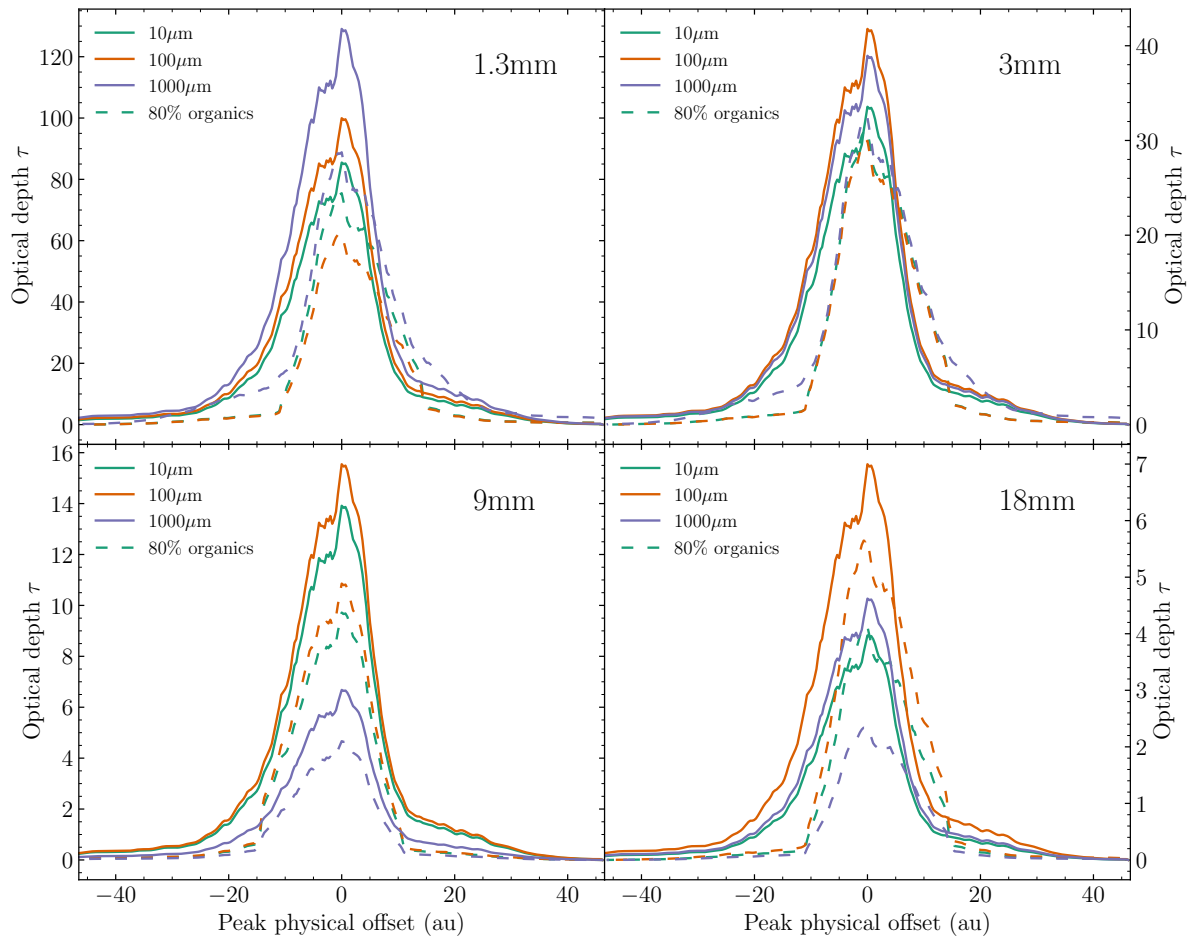


Figure 3.5: Similar to Fig. 3.4 but for the optical depth of every radiative transfer model at the ideal resolution, this is, at the resolution of the radiative transfer output before any beam convolution.

composition whose carbon budget was split between 20% of graphite and 80% of amorphous carbon, while keeping the carbon budget constant at 37.5%, i.e., with mass fractions of 0.675, 0.300 and 0.075 for silicate, graphite and amorphous carbon, respectively. We tried different percentages for organics but we show here the one with the most significant differences from our fiducial composition only.

The fluxes produced by sublimated grains are not significantly different to those without sublimation, regardless of the size and wavelength or particular amount of organics. As discussed in section 3.3.4, the sublimation has the effect of lowering the optical depth because of the mass reduction and the change in composition. This results in emission being produced by a slightly inner and hotter parcel of the disk, which leads to slightly higher fluxes towards the center than the fiducial model without organics evaporation. The difference in flux in the central region between models with and without evaporation is larger for the wavelengths with higher resolution observations.

Our results indicate that catching dust sublimation at a particular wavelength with continuum observations, even with very high-resolution is challenging. Future observations that can obtain molecular line emission from this region, can probe whether an active carbon-rich chemistry exists or not in this source (van 't Hoff et al. 2020b), providing independent robust constraints on the scenario of a sootline of about 10 au towards this Class 0 disk.

3.4.3 Variation of the spectral index

Another observable piece of comparison between observations and models is the spectral index α produced between 1.3 and 3 mm, for which there are higher resolution and deeper observations available. We computed the spectral index between 1.3 and 3 mm for all a_{\max} models and for several percentages of organics, 10%, 30%, 50% and 80%. We present in Fig. 3.6, our results for models with our fiducial composition, where carbon does not sublimate, and representative sublimation models with 50% and 80% of organics and sublimation temperature from 300 K.

Since the disk model is optically thick at 1.3 mm and 3 mm (see Fig. 3.5), the values of the spectral index will depend on the vertical distribution of temperature and opacity in the disk. The models in Fig. 3.6 have all the same temperature gradient but the opacity changes with a_{\max} and composition leading to the observed differences. The models with higher opacities towards the center show a more extended region with $\alpha < 2.5$ values.

An important feature observed in the IRAS 16293 B spectral index is that central values go as low as 1.7, this means, lower than the threshold of $\alpha = 2$ (indicated by the black contour in Fig. 3.6) indicating optically thick emission, first presented in Zamponi et al. (2021). The presence and extent of this feature in our models depend on having sufficient variations of temperature along the line of sight between the layers traced by the different wavelengths (with $T_{1.3\text{mm}} < T_{3\text{mm}}$). The larger the region for which these differences are present the more prominent and widespread this feature is. In the case of $100\mu\text{m}$ the feature is more prominent because of the higher optical depths while in the case of $1000\mu\text{m}$ sized grains with carbon sublimation, the feature is likely present because the reduced optical depth in the inner hot region allows flux to come from a region with a larger gradient in temperature than the same models with less amount of sublimation. Although none of our models reproduce the extent of this region, models with

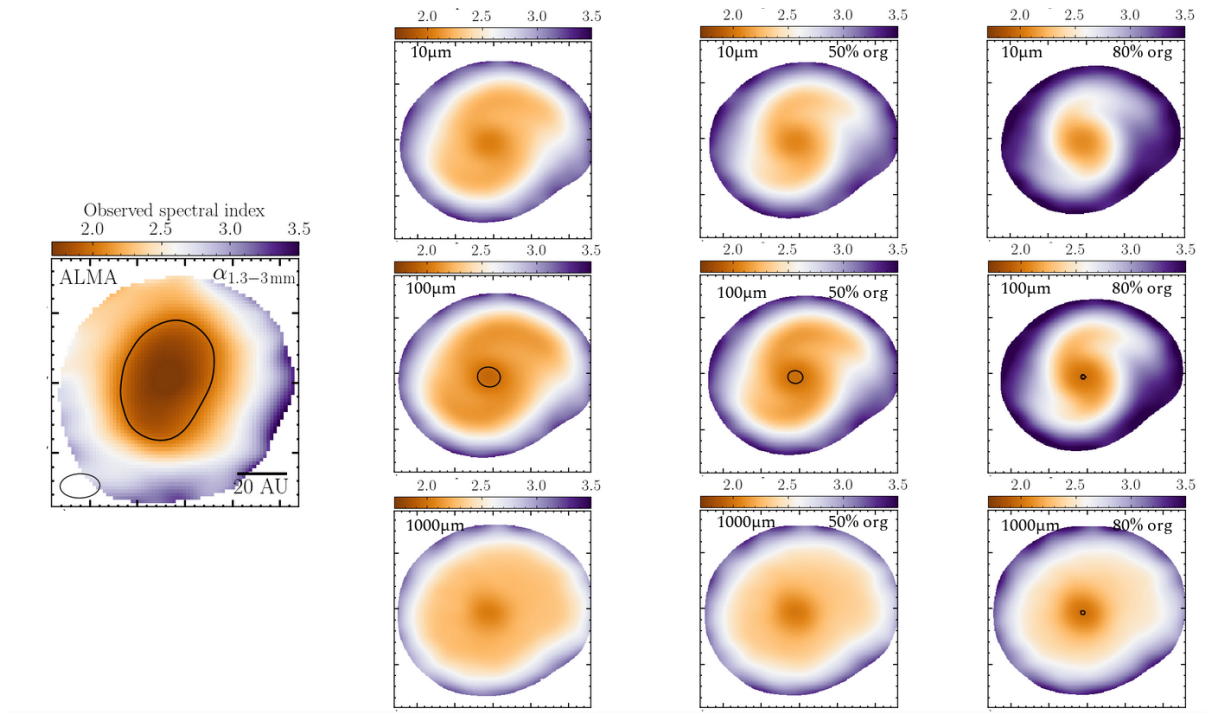


Figure 3.6: Spectral indexes for the real observation (left) and models (right). Models are shown for a_{\max} of 10 (top) and $100\mu\text{m}$ (center) and $1000\mu\text{m}$ (bottom). Columns represent the cases without sublimation and with 50% and 80% of carbon sublimation, from left to right, respectively. The black contour indicates $\alpha = 2$.

grain growth are able to reproduce small regions showing this feature (panels with $100\mu\text{m}$ or $1000\mu\text{m}$ considering carbon sublimation).

3.4.4 Polarization by self-scattering

Polarization observations towards embedded disks have been interpreted as caused by self-scattering, similar to that observed towards more evolved Class I sources (Kataoka et al. 2016a; Stephens et al. 2017; Lin et al. 2021). This interpretation is based on the morphology of the polarization observations. In this work, we test whether the disk model we use in this work, with a physical density and temperature structure representative of a Class 0 disk, can produce the few percent (2-4%) levels of polarization fractions as observed for IRAS 16293 B as well as other Class 0/I disk observations at millimeter wavelengths (Lee et al. 2021). We do so by generating radiative transfer models of polarization by scattering at 1.3 and 7 mm, meant to be compared with the available high-resolution polarization data shown in Fig. 3.1. Creating models of polarization by scattering requires the calculation of full Mie scattering (i.e., Monte-Carlo scattering in all four stokes components) and it's highly computationally expensive. Hence, we produced models for all three maximum grain sizes, using only our fiducial and homogeneous dust composition of silicates and graphites. Given that the albedo between the different compositions used in

this work are very similar, the results at each a_{\max} will not deviate significantly when considering the other compositions. Between the three models, the highest polarized intensity is produced by an a_{\max} of $100\ \mu\text{m}$, since the albedo of $10\ \mu\text{m}$ grains is negligible and the extinction opacity of $1000\ \mu\text{m}$ sized grains larger than for $100\ \mu\text{m}$ sized grains (see Table 3.1) and produces lower scattered flux. Unlike for a_{\max} 10 and $100\ \mu\text{m}$, the polarization fraction of millimetric grains is very similar at both 1.3 mm and 7 mm, both in polarization pattern and intensity (maximum $P_{\text{frac}} \sim 0.2\%$). This is because their albedo is almost constant at all millimetric wavelengths (see Fig. 3.3). The results of our self-scattering models are presented in Fig. 3.7 at the disk model's native resolution. We present the resulting Stokes I, Q and U fluxes, along with the polarization fraction (and polarization E-vectors overlaid) at both wavelengths. The resulting Stokes Q and U fluxes at 1.3 mm are extremely low. The polarization fraction in the model reaches around a tenth of percent ($P_{\text{frac}} \lesssim 0.1\%$) within the central 20 au where it shows an azimuthal polarization pattern for the E-vectors. This azimuthal distribution is expected from a centrally concentrated density distribution (Kataoka et al. 2015), in the spiral arms, the vectors become radial or rather perpendicular to these structures. These patterns are similar to those presented by Kataoka et al. (2015) for a ringed and lopsided disk. The fraction of polarization falls significantly at 7 mm as expected, since it is far from the $\lambda \sim 2\pi a_{\max}$ regime, and barely reaches 0.005% within the disk. We also tested the results for the case of an edge-on hot disk (Fig. B.1). In this case the polarization fraction remains the highest at 1.3 mm but consistently low ($\sim 1\%$).

Previous ALMA Band 6 polarization observations of IRAS 16293 B from Sadavoy et al. (2018) show an azimuthal E-vector pattern, with polarization fractions as high as $\sim 2 - 4\%$. The authors have associated this polarization emission to that produced by dust scattering from the dust thermal emission itself (i.e., self-scattering). To directly compare these models with IRAS 16293 B observations, we performed polarized synthetic observations at all three Stokes components, mimicking the corresponding observing setups presented in section 3.2, and the procedure described in sections 3.3.6. The resulting synthetic maps (in units of Jy/beam) are presented in Fig. 3.8 for both wavelengths and all three Stokes components. In this case, we have omitted the polarization fraction results from the layout because the polarized intensity is completely dominated by thermal noise. The resulting Stokes I fluxes are comparable to the original observations, confirming the analysis presented in section 3.4.1 but now with the inclusion of the polarized 1.3 mm data. However, the model Stokes Q and U fluxes are not detectable within the sensitivity levels achieved by these observing setups. We conclude from this analysis, that linear polarization produced by self-scattering from spherical grains in our model is not high enough to be consistent with the observations of IRAS16293B carried out at 1.3 and 7 mm by Sadavoy et al. (2018) and Liu et al. (2018b), respectively.

Our resulting polarization fractions are in-line with the predictions for IRAS 16293 B discussed by Yang et al. (2016) from analytical models of polarized scattering in optically thick media. The millimeter optical depth in IRAS 16293 B is extremely high ($\tau \gtrsim 100$), which reduces the degree of anisotropy in the radiation field and hence the percentage of polarized scattered light (Kataoka et al. 2015).

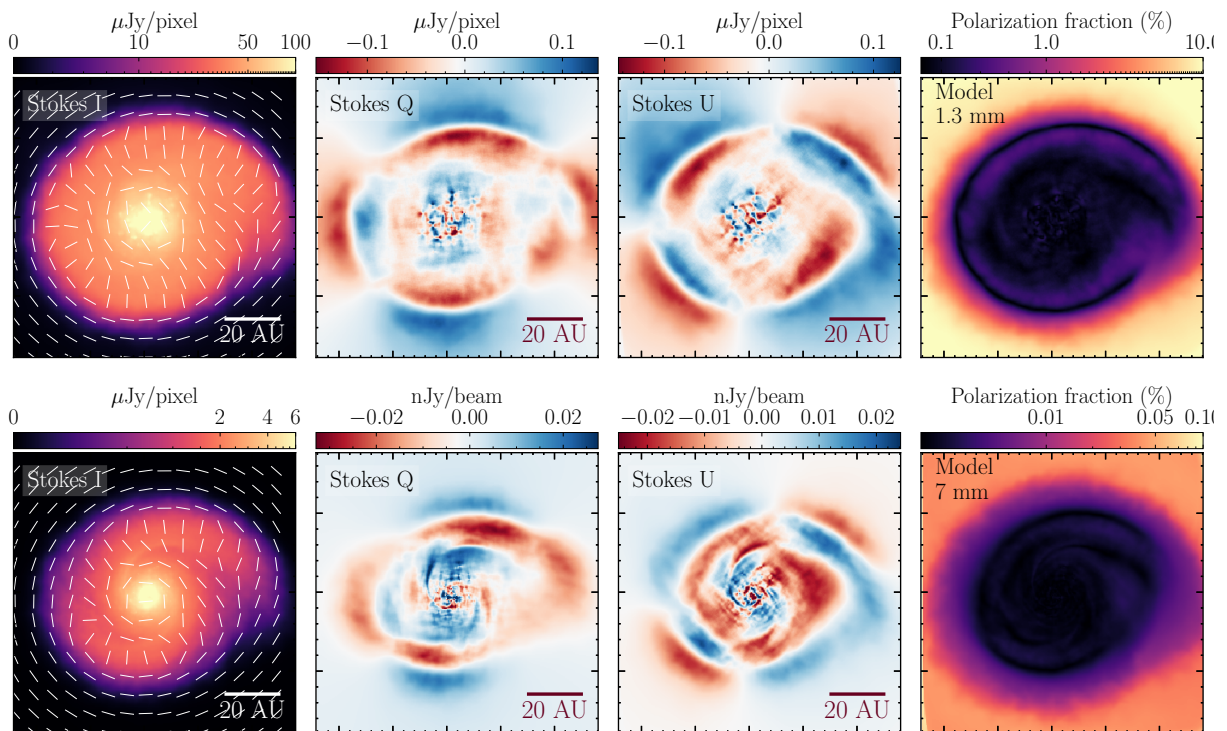


Figure 3.7: Radiative transfer models of self-scattering at 1.3 (top) and 7 mm (bottom) for $a_{\text{max}} = 100 \mu\text{m}$, shown in the upper and lower row, respectively. Panels illustrate the Stokes I, Q, U fluxes and polarization fraction (with constant-size polarization vectors overlaid) from left to right.

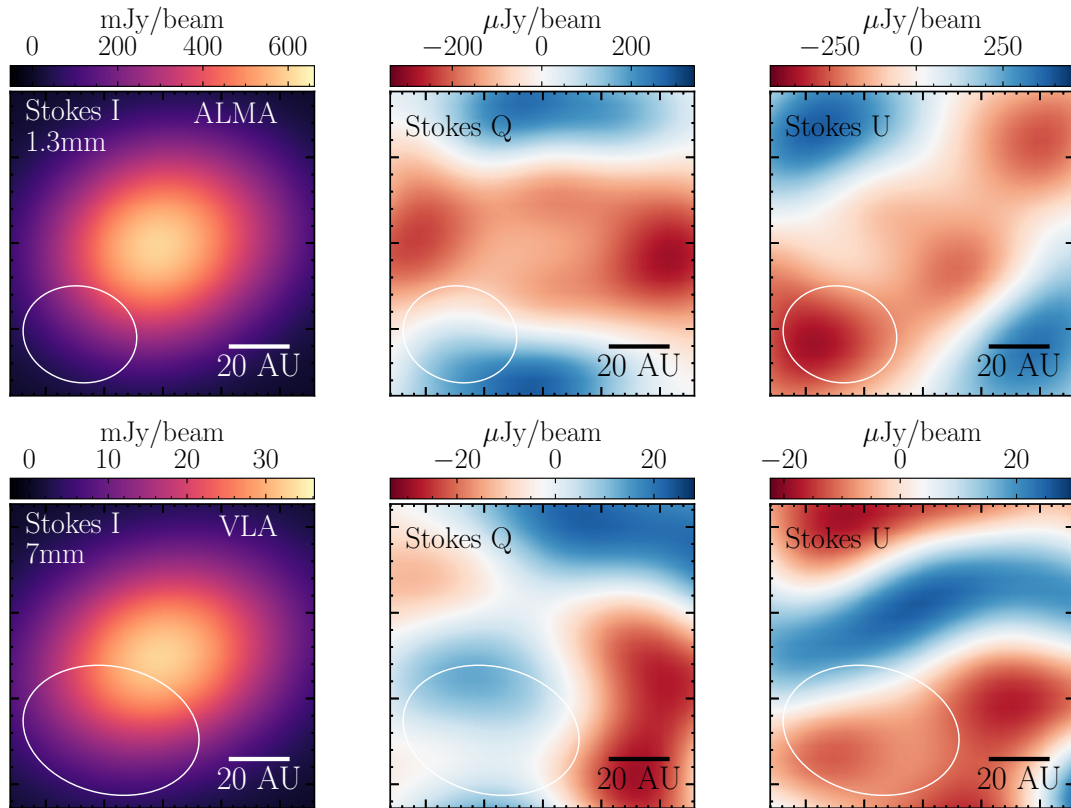


Figure 3.8: ALMA and VLA synthetic observations based on models of self-scattering from Fig. 3.7 (i.e., for $a_{\max} = 100 \mu\text{m}$). The polarization fraction panel is omitted since both Q and U components are dominated by thermal noise. The rms of the polarization components are $rms_Q \sim rms_U \sim 25 \mu\text{Jy beam}^{-1}$ and $\sim 12 \mu\text{Jy beam}^{-1}$, for the 1.3 mm and 7 mm maps, respectively.

3.5 Discussion

3.5.1 Grain growth in Class 0 disks

Grain growth in Class 0 protostars and their associated disks has been a subject of significant interest in recent years. Several recent studies, including Bate (2022), Kawasaki et al. (2022), and Koga et al. (2022), have provided compelling evidence suggesting the possibility of grain growth up to a few hundred microns in these environments. Bate (2022) conducted simulations of prestellar core collapse and followed them up to the formation of a rapidly rotating marginally gravitationally unstable first core. This represents a stage previous to the formation of well define protostellar disk, as the one in IRAS 16293 B, but shows similar physical properties. Bate (2022) demonstrated that the combination of enhanced collisional rates and efficient grain growth mechanisms can lead to the formation of substantial dust aggregates in Class 0 disks, growing up to $100\ \mu\text{m}$ in this first core stage. These results are in line with our possibility to have $100\ \mu\text{m}$ or even up to $1000\ \mu\text{m}$ sized particles in a Class 0 disk. Similarly, Kawasaki et al. (2022) evolved one-zone non-ideal MHD models of the collapse of dense cores up to densities comparable to those found in our disk model ($n_g \gtrsim 10^{12}\ \text{cm}^{-3}$). Their calculations focused on the evolution of the grain sizes along the collapse, including the effects of coagulation and fragmentation of silicate dust. Their models show that grains can coagulate up to a few 100 microns at the densities of our disk model, and therefore those expected in IRAS 16293 B, and even up to millimetric sizes within the very inner dense regions of the disk. These results seem to also be in line with our grain size estimations for the disk in IRAS 16293 B. The similar recent work conducted by Koga et al. (2022) simulated the formation of a protostellar disk with mass, radius and age similar to our disk model, i.e., representative of a Class 0 disk. In this simulations, they did not include dust coagulation but rather fixed grain sizes over the whole evolution. Their results indicate that only the big grains ($100\text{-}1000\ \mu\text{m}$) are tightly coupled to the gas within the disk, while small grains ($\lesssim 10\ \mu\text{m}$) are partly depleted or swept out form the disk. Older predictions for grain sizes in protostellar cores, such as those from Ormel et al. (2009), Hirashita & Yan (2009) and Hirashita & Li (2013), suggested that even isothermally collapsing dense cores can achieve coagulation up to $100\ \mu\text{m}$ but only if the cloud's dynamical support slows down the collapse beyond its free-fall time and let the grains grow. In the case of collapse faster than the free-fall time ($\lesssim 10^5\ \text{yrs}$), grains should coagulate up to a most a few $10\ \mu\text{m}$.

Observational constraints from dust emissivity indices do also suggest that grains in protostellar (Class 0) envelopes can grow up to 100 and $1000\ \mu\text{m}$ sizes (Kwon et al. 2009; Miotello et al. 2014; Bracco et al. 2017; Valdivia et al. 2019; Le Gouellec et al. 2019; Galametz et al. 2019; Hull et al. 2020).

It is also worth mentioning that a dust population with maximum grain sizes comparable to ISM values ($\lesssim 1\ \mu\text{m}$; Mathis et al. 1977) was not consistent with IRAS 16293 B based on model-observation comparison in Zamponi et al. (2021).

3.5.2 Grain growth within the soot-line

The recent VLA observation of FU Ori presented by Liu et al. (2021) showed that within the inner 10 au, where $T \gtrsim 400$ K, dust grains have grown to millimeter sizes. Since this region is hot enough for evaporation of the water icy mantles, this implies that grain growth was efficient in this "dry" conditions. This scenario of grain growth in the inner and hotter regions of protoplanetary disks is also supported by laboratory experiments (Kimura et al. 2020). They show that the stickiness of silicate and carbonaceous grains is enhanced after the removal of quasi-liquid layers of water. This process facilitates dust coagulation and supports the formation of planetesimals in dry environments (Pillich et al. 2021).

The possibility to have millimetric grains can potentially be explained by the high fragmentation velocity v_{frag} found for water-ice-free grains $\gtrsim 10$ m s⁻¹ (Kimura et al. 2015; Gundlach et al. 2018; Steinpilz et al. 2019; Pillich et al. 2021), larger than previously considered for rocky poorly-sticky grains of 1 m s⁻¹ (Blum & Wurm 2000). These results on the fragmentation velocity have also been independently found by Liu et al. (2021) and more recently by Yamamuro et al. (2023).

Motivated by these recent laboratory experimental results, we reproduced synthetic brightness profiles at 1.3 and 3 mm (similar to Fig. 3.4), accounting for sublimation and grain growth when the temperature is over 300 K. Outside of the sublimation zone the maximum grain size is 100 μm and a mixture of silicates, graphites and refractory organics (80% of the carbon budget). Inside of it, we have increased the grain size to 1000 μm . The results of this test are shown in Fig. 3.9 for two different sublimation temperatures, 300 and 500 K, at 1.3 and 3 mm. We present the synthetic ALMA Stokes I maps, at the resolution of the observations for comparison with IRAS 16293 B. The resulting brightness profiles show that the combination of the overestimation in the case of $a_{\text{max}} = 100 \mu\text{m}$ is mitigated by the reduction of flux in the center when $a_{\text{max}} = 1000 \mu\text{m}$ within the sootline. We present the results for two different sootlines, to explore the effects of considering the range of sublimation temperatures presented by Lin et al. (2021). The fluxes from models with a 500 K sootline are higher than with 300 K. This happens because with a sootline of 500 K the region traced by millimetric grains is more compact than the case with 300 K, this means that the region with higher opacity is smaller in the 500 K case. Another feature observed in Fig. 3.9 is the appearance of a gap in the model with sootline at 300 K observed at 3 mm. This is caused by the reduction of the opacity, and is not seen in the model with 500 K because the region with reduced opacity is more compact and less resolved by the observations. This shows that observations of such gaps for hot disks could then be the result of changes on the opacity.

Considering grain growth within the sootline results in a better match with the observations than the cases with homogeneous grain sizes. The comparison suggests that grain growth up to millimeter sizes could be enhanced within the sootline in this young Class 0 disk, provided the disk densities temperatures and densities in the model are close to the ones present in IRAS 16293B.

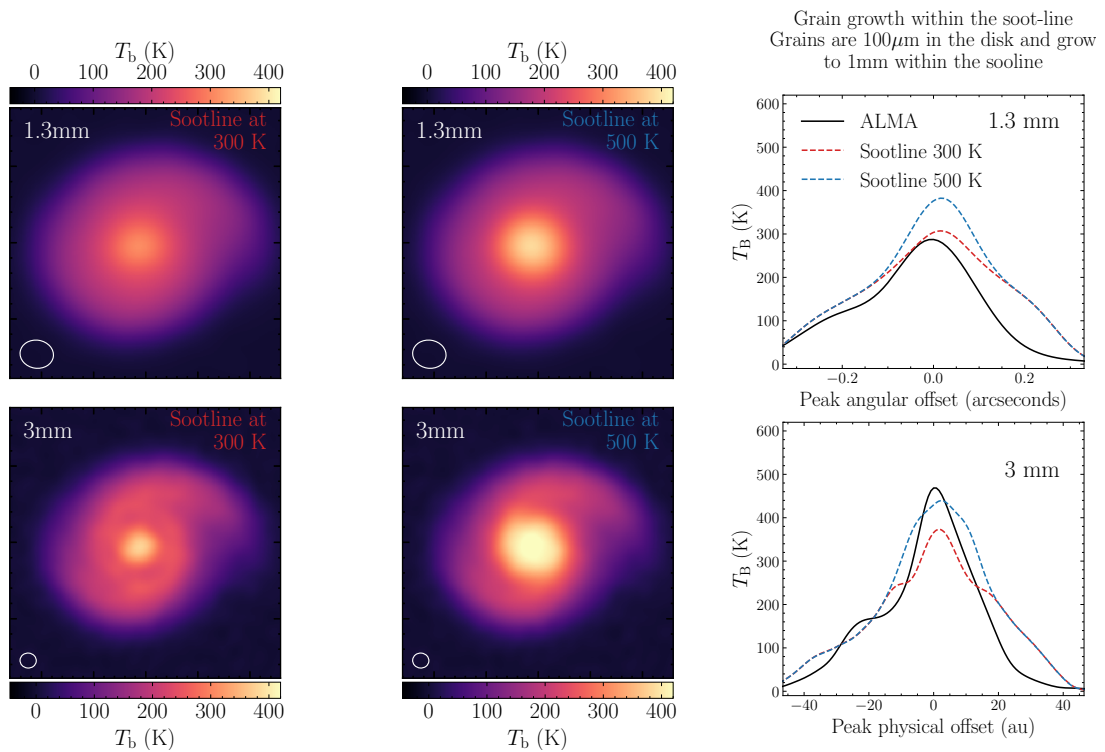


Figure 3.9: Models with grain growth within the sublimation zone. In these models, the maximum grain size is $100\mu\text{m}$ outside of the sublimation zone (i.e., in regions where $T > 300\text{ K}$ for the upper panels and $T > 500\text{ K}$ for the lower panels) and $1000\mu\text{m}$ within it, with a mixture of silicates, graphites and amorphous carbon (80% of the carbon).

3.5.3 If not self-scattering, what is the polarization mechanism in IRAS 16293B?

As we have shown in section 3.4.4, the emission from IRAS 16293B is too optically thick to produce detectable levels of polarization by self-scattering when considering spherical grains. This raises the question of what other mechanisms or grain properties can we consider to explain the observed patterns.

Polarization observations are commonly associated with the optically thin emission of magnetically aligned grains (Lazarian & Hoang 2007a; Andersson et al. 2015). However, the emission detected from young embedded disks is likely optically thick (Galván-Madrid et al. 2018; Lin et al. 2020; Zamponi et al. 2021). In the context of optically thick emission, the polarization observed might also come from magnetically aligned grains, but produced in the form of extinction (Ko et al. 2020; Liu 2021). In this case, the differential attenuation of the two orthogonal components of the light E-vectors, results in an excess of polarization along a given axis (Wood 1997). This is known as dichroic extinction and occurs when the grains are elongated and the background light is optically thick and almost unpolarized. In the context of optically thick embedded disks, this can be produced by foreground (e.g., envelope) elongated grains aligned with their minor axis parallel to the magnetic field lines, which absorb light preferentially along the grain's major axis and produce a net polarization parallel to the magnetic field lines, as opposed to the optically thin polarized emission. Such a polarization mechanism has actually been proposed and detected in a few other Class 0 sources and contradicts the current understanding of magnetic field structures within the optically thick inner regions of the disks (Liu 2021). Similarly, the multiwavelength polarization observations of NGC 1333 IRAS4A, presented by Ko et al. (2020), show a transition between E-vectors parallel to the magnetic field, traced at 0.87-1.3 mm, to E-vectors perpendicular to the magnetic field, traced at 6.9-14.1 mm. These results show evidence for a transition between extinction and emission of aligned grains which is determined by an optically thick to thin transition. Similarly, polarization by dichroic extinction has been detected within the inner 100 au of the Class 0 protostar OMC-3/MMS 6 (also known as HOPS-87) in Orion (Liu 2021), after comparing ALMA and VLA observations. Moreover, in the protostar HH212, the polarization observed at a resolution of 14 au, shows a possible combined contribution of both dichroic extinction and self-scattering (Lee et al. 2021). These studies support that dichroic extinction by aligned grains can be an important mechanism to explain the polarization pattern at or close to disks scales in several Class 0 protostars. As this mechanism requires that the region near disk scales is optically thick, it would be present preferentially in younger and more massive disks such as those in the Class 0 stage.

In the case of IRAS 16293 B, the 1.3 mm polarization observations from Sadavoy et al. (2018) show azimuthal E-vectors between 30-50 au and uniform vectors within 30 au (see Fig. 3.1). In Zamponi et al. (2021) and this work we have shown that the emission is optically thick and can reach optical depths well above 100 at 1.3 mm within the central 10 au. If the polarized emission is produced by dichroic extinction of magnetically aligned grains, this pattern would indicate a toroidal magnetic field. Alternatively, the polarization pattern could still be related to the direct emission of magnetically aligned grains close to the disk. The magnetic field morphology (traced by B-vectors) could be associated with a poloidal field in that scenario. Future modelling and

higher-resolution observations can help constraining the contribution of dichroic extinction as well as magnetic field configurations that can best explain the observations in Fig. 3.1.

Another possible scenario producing azimuthal E-vectors, as those in Fig. 3.1, is the polarization reversal effect, happening when millimetric elongated grains are present in the disk and observed in the Mie regime (i.e., millimetric wavelengths). This has been used by Guillet et al. (2020) to justify the azimuthal polarization pattern of [BHB 2007] 11 (the pretzel) in the Pipe nebula, where polarization E-vectors, and so B-vectors, could be aligned with the accretion streamers shown by Alves et al. (2019).

Another scenario is that the polarization can be produced by dust alignment, but not necessarily with the magnetic field only. Both emission and extinction of light from elongated particles lie on the assumption that dust grains are aligned with a given underlying field. This could be either the magnetic, the radiation or the velocity field (Gold 1952; Wood 1997; Lazarian 2007). The most commonly accepted mechanisms responsible for the alignment of grains (see Andersson et al. 2015 for a review) can be either associated to Radiative Torques (RAT) (Lazarian & Hoang 2007a) or to supersonic motions, namely, mechanical alignment (MET) (Gold 1952; Lazarian & Hoang 2007b; Kataoka et al. 2019; Reissl et al. 2022; Hoang et al. 2022). In the case of RAT, this can lead to alignment with the radiation field (k-RAT; Tazaki et al. 2017) instead of the magnetic field (B-RAT). In the case of mechanical alignment this could result in alignment with the B field (B-MET) or the velocity field (v-MET; Hoang et al. 2022). In the scenarios of alignment with the radiation (k-RAT) or the dust-gas drift velocity field (v-MET or MAT; Hoang et al. 2018), the resulting polarization pattern would be azimuthal, as long as the radiation field is assumed to be centrally concentrated and the disk to be Keplerian (e.g., around a protostar), respectively. The case of mechanical alignment depends strongly on the Stokes number, i.e., the degree of spatial coupling between the gas and the dust. Whether radiation or mechanical alignment are efficient in Class 0 disks requires further investigation.

3.6 Conclusions

In this work we have explored the effects of different maximum grain sizes and carbon sublimation in the millimeter continuum emission from a hot and optically thick Class 0 disk, generated from numerical simulations of prestellar core collapse. The disk model has successfully reproduced the fluxes of the nearby face on Class 0 disk IRAS 16293 B (Zamponi et al. 2021). Hence, we produced synthetic observations of the different cases to compare with multi-wavelength (1.3, 3, 9 and 18 mm) and high-resolution observations (6 to 44 au) of IRAS 16293 B, including polarization observations. In order to automate the generation of synthetic observations, we have developed a new publicly available tool called Synthesizer, that allows to generate synthetic models from numerical simulations directly from the command line. The conclusions of this work are summarized as follows:

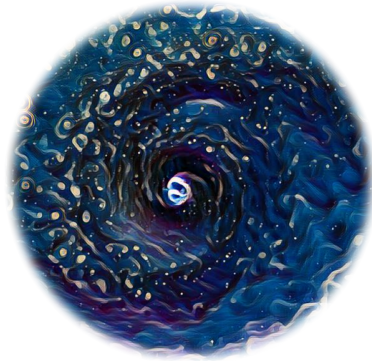
- For a dust mixture of silicates and graphites, we extended the results of Zamponi et al. (2021), that used maximum grain sizes a_{\max} of $1 \mu\text{m}$ and $10 \mu\text{m}$, and generated opacity tables for maximum grain sizes of up to $100 \mu\text{m}$ and $1000 \mu\text{m}$. Peak fluxes increase with

wavelength and decrease with a_{\max} , a feature of hot and optically thick disks. Optical depths range between 130 to 2 from 1.3 to 18 mm. The high optical depths and positive temperature gradient towards the center also results in extended regions in the disk with $\alpha < 2.5$ for all a_{\max} and even below 2 for $a_{\max} = 100 \mu\text{m}$ and $1000 \mu\text{m}$. Predictions from significant grain growth populations, including $a_{\max} = 1000 \mu\text{m}$ are comparable to the observations from IRAS 16293 B at all observed wavelengths. Hence, significant grain growth could be present in this young Class 0 disk.

- Motivated by the high brightness temperatures ($\gtrsim 400$ K) observed towards IRAS 16293 B, we explored the scenario of sublimation of solid amorphous refractory carbon at temperatures above 300 K, the so-called sootline. The sublimation results in a local decrease in the optical depth, due to both the reduction of graphite within the grain carbon budget and to the evaporated mass reduction. This decrease produce higher fluxes because the emission then traces deeper and hotter layers of the disk. The difference in the fluxes with and without sublimation are small ($< 10\%$).
- We also tested the hypothetical case of grain growth within the sootline, motivated by recent laboratory experiments suggesting that dry grains without ice mantles would enhance stickiness and coagulation. We modelled this scenario with an a_{\max} of $100 \mu\text{m}$ at all disk scales outside of the sootline, and with millimetric grains within it. Our results indicate that a combination of both grain sizes can help to provide a better match to the ALMA observations of IRAS 16293 B.
- We generated polarization models by self-scattering for three different maximum grain sizes, 10, 100 and $1000 \mu\text{m}$. The millimetric polarized intensity is highest for the case with $a_{\max} = 100 \mu\text{m}$ at 1.3 mm, thanks to the high albedo and not extremely high optical depth, as it happens for millimetric grains. However, the predicted polarization fraction produced by self-scattering are very low ($\sim 0.5\%$), both for edge-on and face-on disks. These low levels of polarization by self-scattering are too low to be consistent with those observed for IRAS 16293 B at both 1.3 mm and 7 mm (2 – 4%).

Since self-scattering is unlikely to be at the origin of the high-polarization fractions observed towards the Class 0 disk IRAS 16293 B, future modelling is needed to constraint the mechanism responsible for the observed polarization. Similar studies towards other embedded disks would be useful to see if this is a general result for other Class 0 disks. Higher-resolution molecular observations will also help to probe if there is enriched carbon chemistry in the inner regions of the disk.

Chapter 4



The Synthesizer

Synthetic observations from 3D numerical simulations

4.1 Introduction

4.1.1 What is a synthetic observation?

A synthetic observation is a theoretical construct created by combining observational setups and models. In other words, it is a simulation of what scientists would see if they were able to observe a physical system under particular conditions. It allows astronomers to investigate the impact of different observational setups before proposing and performing the real observations. Since astronomers have full control over the simulated setup, they can use it to find the most convenient observing setup when writing proposals or to directly compare models with already observed astronomical sources.

In order to properly compare simulations and observations, your observed models need to look as realistic as possible. This means, one needs to post-process the simulation output or analytical models by adding a series of instrument-related effects, such as resolution and sensitivity. All these values vary from telescope to telescope and must be as tailored as needed for every par-

ticular observation setup. According to Haworth et al. (2018), the most typical post-processing steps are:

1. **Spectral transmission:** Real telescopes do not have uniform sensitivity to all frequencies within a given bandwidth. As a result, it is necessary to use a filter that takes into account the spectral sensitivity of the detector. A box filter can provide a reasonable first-order approximation of such a filter.
2. **Beam convolution:** In single-dish telescopes, the response to the observed brightness distribution is determined by the antenna pattern or Point Spread Function (PSF), which can be reasonably approximated as a two-dimensional Gaussian beam. For interferometric arrays, the PSF is obtained through the Fourier transform of the sampled uv -plane. In order to properly compare simulations to observations, the physical resolution of the simulation needs to be downsampled to the telescope angular resolution and antenna efficiency.
3. **Finite pixel resolution:** The angular pixel size of a radiative transfer model needs to be at least same as small as the physical resolution of the simulation output, in order to catch all physical structures. However, the angular pixel size of an astronomical image is calculated such that it does not under- or over-sample the telescope's beam (Nyquist sampling) and is probably much bigger than the model's pixel size. Downsampling and flux rescaling of the radiative transfer output is therefore another necessary step.
4. **Addition of Noise:** The addition of noise is maybe the most important step during the image post-processing and should be based on the technical specifications of the simulated instrument. Various types of noise, including non-thermal noise such as mutual interference of wavefronts in speckle patterns seen in coronagraphic imaging, as well as noise added by side-lobes, and thermal noise, should be taken into consideration. Thermal noise is particularly relevant to consider as it plays a significant role in determining whether structures can be observed or not. If the level of noise exceeds the maximum signal, it can prevent the detection of structures that might be otherwise assumed to be detectable.

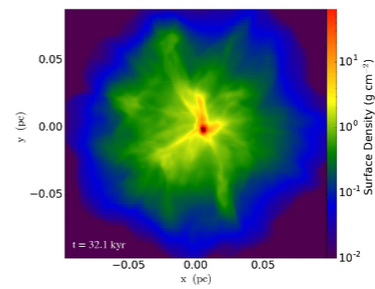
Post-processing simulation outputs with radiative transfer modelling and addition of instrument-related effects can soon become a tedious and repetitive task, specially when you need to do parameter space exploration. Since the order of each of these steps is usually the same, the whole post-processing pipeline can be easily automated, leaving the parameter controls all in one space. This is basically the motivation I had to create the Synthesizer, a tool that automates this pipeline without the need to learn and create input files for all the available different codes formats.

4.2 The code

The Synthesizer is a program used to calculate synthetic images from a numerical model directly from the command-line. It pipelines all the steps involved in a synthetic observation (see Fig. 4.1), from the generation of a physical model, either from an analytical prescription or from a 3D simulation output, to the generation of a realistic telescope observation. The program can be used

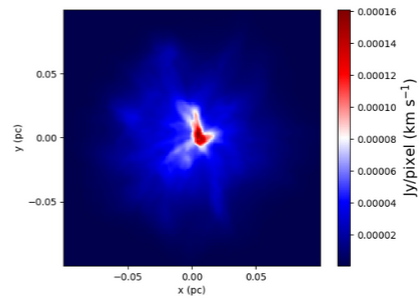
Physical
Model

MHD MODEL



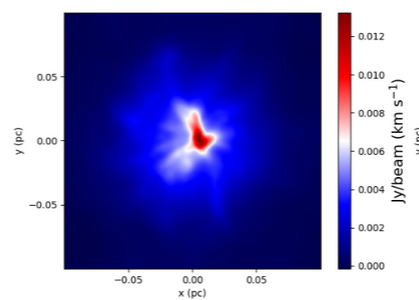
Radiative
Transfer

RADIATIVE TRANSFER



Synthetic
Observation

ALMA ($0.5''$)



APEX ($16.8''$)

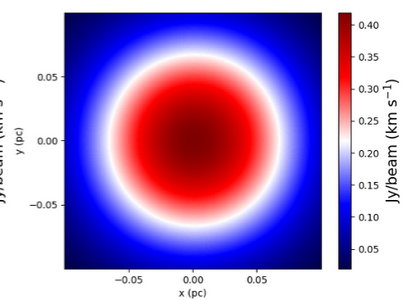


Figure 4.1: All the steps involved in the process of generating a synthetic observation, starting from the model, generating the flux via radiative transfer and finally convolving the image to a desired primary or synthesized beam, plus the addition of thermal receiver noise.

either in one or all of the modules available (see section 4.3). This means, you can use it to only calculate your model, and refine it, without the need to run all the extra steps (radiative transfer, opacity calculation, etc.), you can use it to post-process an independently prepared model or to investigate the effect of changing the physical properties of your model. The synthesizer comes also handy for users that might not be interested in modelling or generating synthetic observations, but in need of an easy to use data visualization tool. For instance, it allows for 2D and 3D visualization of your analytical models and simulation outputs, without the need to program your own plotting routines.

4.2.1 Requirements

The Synthesizer consists of four main modules (see section 4.3), out of which two are self-contained features fully written in Python. This means, that to use the `--grid` and `--opacity` options, no further installation is needed beyond the main package installation. For the other two `--raytrace` and `--synobs` options, two different softwares need to be separately installed. These are the commonly used parallelized radiative transfer code RADMC3D (Dullemond et al. 2012)¹ and the Common Astronomy Software Applications (CASA; McMullin et al. 2007)², needed for the raytrace and synobs modules, respectively. When attempting to use either of the two modules without the already-installed corresponding software, a warning and help message will be prompted by the Synthesizer. Installation of them both is quite easy and quick, but it needs to be done manually by the user.

4.2.2 Installation

The Synthesizer is fully written in Python 3 and is structured in the form of a Python package, publicly available through the Python Package Index³ and its public repository⁴. Installation of the latest stable version can be easily done via the `python-pip` command:

```
$ pip install astro-synthesizer
```

In order to catch up on more recent updates or to modify the code to your own needs, installation of a development version can also be done from source with the following commands:

```
$ git clone https://github.com/jzamponi/synthesizer
$ cd synthesizer
$ pip install -e .
```

The `-e` flag added to the last install command means the code will be installed in *editable* mode. This is optional and allows the user to have modifications to the source code taking immediate effect without the need to reinstall. This is particularly useful for users interested in modifying the predefined physical models. Once installed, an executable python file called `synthesizer` will be created in one of the folders added to your `PATH`. This is most likely `~/.local/bin`

¹<https://github.com/dullemond/radmc3d-2.0>

²casa.nrao.edu

³<https://pypi.org/project/astro-synthesizer>

⁴<https://github.com/jzamponi/synthesizer>

by default but it can be customized providing the `--prefix` flag (see `pip install --help` for further details). To make sure the program is now properly installed and callable, simply type `$ synthesizer` in your terminal and you should get the following output:

```
$ synthesizer
[synthesizer] Nothing to do. Main options: --grid, --opacity,
          --monte-carlo, --raytrace or --synobs
[synthesizer] Run synthesizer --help for details.
```

4.2.3 Running the code

Using the code is quite easy, that is its philosophy. All options and parameters can be provided directly from the command line without the need to create input files or learning new file formats. A list of all possible options and commands can be obtained by typing `$ synthesizer --help`. A copy of this output is provided in Table 4.1.

As a quick initial example, the following command will create a protoplanetary disk model (within a cartesian rectangular box) both in density (default) and temperature (optional):

```
$ synthesizer --grid --model ppdisk --temperature --opacity
--show-grid-2d --show-grid-3d --raytrace --synobs --show-rt --show-synobs
```

The code will first create the model grid. Once this is done it will show 2D midplane slices of the density and temperature in two different projections. You can close this window pressing `q`. It will then, open a Mayavi scene where the 3D density model is rendered and will dump a help message to the terminal. This figure is completely interactive and customized only to a minimum level. Once examined and closed, it will open a new scene rendering this time the dust temperature. After the figure is closed, the code will dump all the model information into text files ready to be fed to RADMC3D. These files are *amr_grid.inp*, *dust_density.inp* and (optional) *dust_temperature.dat*. The `--opacity` option tells the code to calculate a dust opacity table for bare silicate grains (by default) with a minimum and maximum grain size of $0.1\mu\text{m}$ and $10\mu\text{m}$, respectively (by default). This opacity is also written in a RADMC3D-compliant syntax to the file *dustkappa_s-10um.inp*. Given the `--raytrace` option, the Synthesizer will now call RADMC3D to run a monochromatic (1.3 mm by default) continuum radiative transfer calculation. Provided the `--show-rt` option, the resulting image will be opened and displayed once the calculation is done. The `--synobs` option represents the last step of the synthetic observation, as illustrated in Fig. 4.1, and consists on formatting the output from RADMC3D into a CASA-compliant format, i.e., to a header-customized FITS File containing all the relevant information for CASA. The Synthesizer then creates a template CASA script called *casa_script.py* with two main function calls, these are the two CASA tasks `simobserve` and `tclean`, plus some extra post-processing. `Simobserve` reads in a flux model, namely, the output from the radiative transfer calculation (called *radmc3d_I.fits*), and generates a measurement set (.ms) within a new folder called *synobs_data*. A measurement set is the CASA format for interferometric visibilities (by default). The visibilities are then provided to `tclean` and deconvolved to generate a final image. This image is saved in the new *synobs_I.fits* file. Provided the `--show-synobs` option, the final image will be opened and displayed. Once the full pipeline is finished, we encourage the

user to take a closer inspection to the standard output in order to get an idea of the parameters involved in the calculation.

4.3 Modules

4.3.1 Gridding (`--grid`)

The core functionality of the Synthesizer is to generate flux distributions from a physical model via radiative transfer calculations using the RADMC3D code. By design, RADMC3D does the raytracing and Monte-Carlo photon propagation on a spatial grid, as most common radiative transfer codes do. Because of this, all physical models, regardless of their numerical origin (analytical prescriptions or particle or grid-based simulations), must be constructed on a grid. In the following sections we describe how does the synthesizer generates such gridded models, even in the case of originally non grid-based simulations.

Using analytical models

One of the most common approaches to radiative transfer modelling is via analytical descriptions of a physical object. One of its main advantages is that it is quick to create them at a reasonable resolution. This facilitates the parameter space exploration and allows the further tailoring of the models to your own scientific case. The Synthesizer comes bundled with a few pre-defined models that can serve as a starting point for more sophisticated descriptions. Some of them are: a constant density box, a sphere with a power-law radial density profile, a filament, a prestellar core (see Fig. 4.2), and a protoplanetary disk (see Fig. 4.3). More models are to come in a future version of the program, such as bespoke profiles for most DSHARP disks (Andrews et al. 2018) and the textbook prestellar core L1544 (Chacón-Tanarro et al. 2019; Caselli et al. 2019).

The Synthesizer does also allow to calculate synthetic polarized fluxes produced by the alignment of elongated dust grains. To do this, the physical model needs to include information about the vector field along which grains will align. Vector fields can be directly converted from the realistic velocity or magnetic field of a 3D simulation by passing the `--alignment` option, as long as this information is available in the snapshots. If no vector field is available, they can be easily created by adding the `--vector-field` option, followed by a keyword indicating the name of the field. Available keywords are `x`, `y`, `z` (for uniform fields), `toroidal`, `hourglass`, `helical` (superposition of toroidal and hourglass), `dipole` and `quadrupole`. When a vector field is added to the model, the field streamlines are overplotted on top of the density colormaps, provided the `--show-grid-2d` option. An example of such images for some of the available vector fields is shown in Fig. 4.4.

Using grid-based hydro codes

The generation of models from grid-based hydrodynamical simulation outputs is in principle quite straightforward. In this gridding mode, the Synthesizer acts merely as a converter interface. For the radiative transfer to work, numerical limitations referring to the grid resolution, geometry

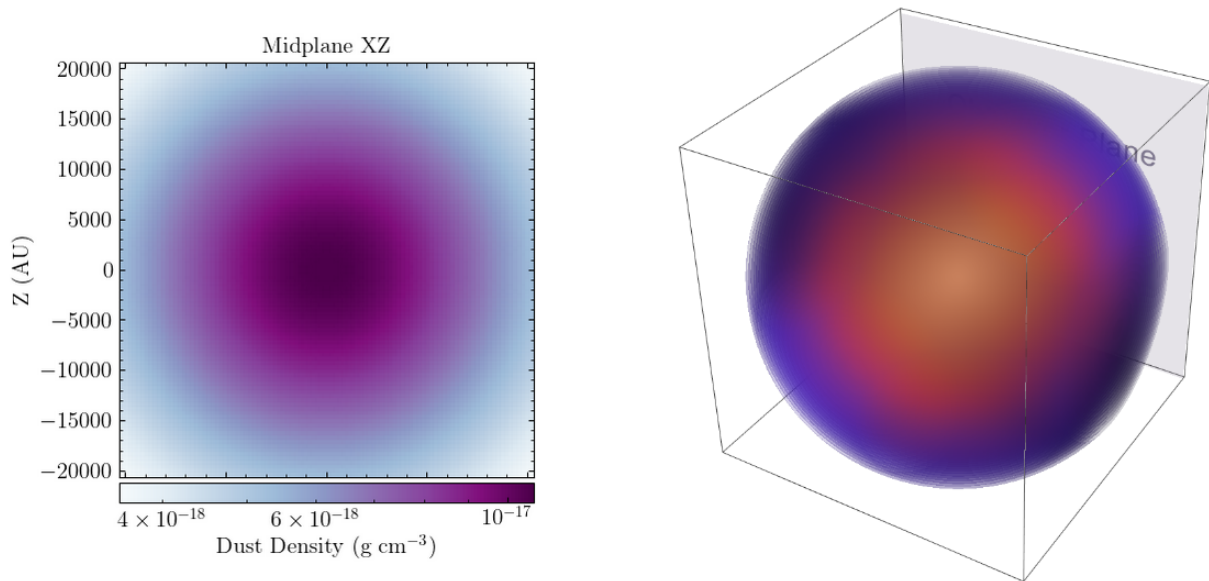


Figure 4.2: Analytical model a prestellar core, described as a Bonnor-Ebert sphere. Panels show a 2D midplane slice of the dust density and a 3D rendering of the same structure, from left to right.

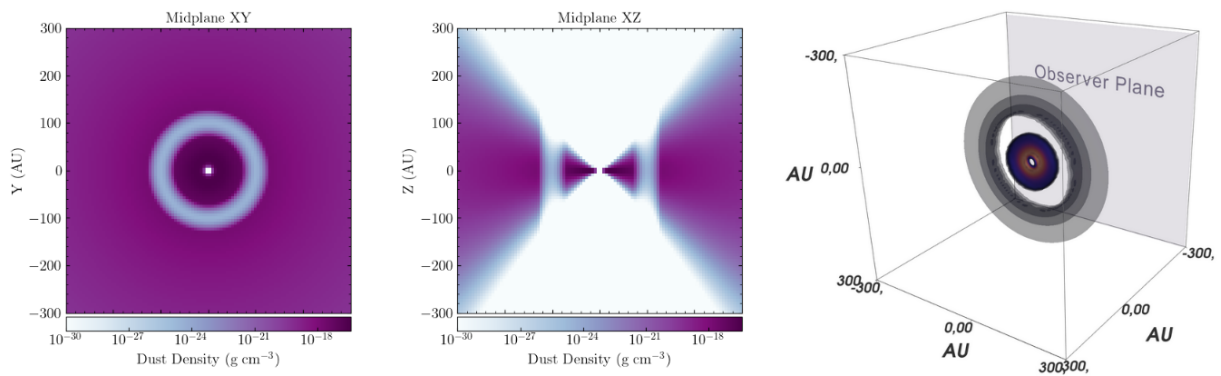


Figure 4.3: Analytical model of a protoplanetary disk with a gap. Left and middle panels show the 2D midplane slices of the model in face-on and edge-on projections. The right panel shows a 3D rendering of the disk density, indicating the plane of observation in gray.

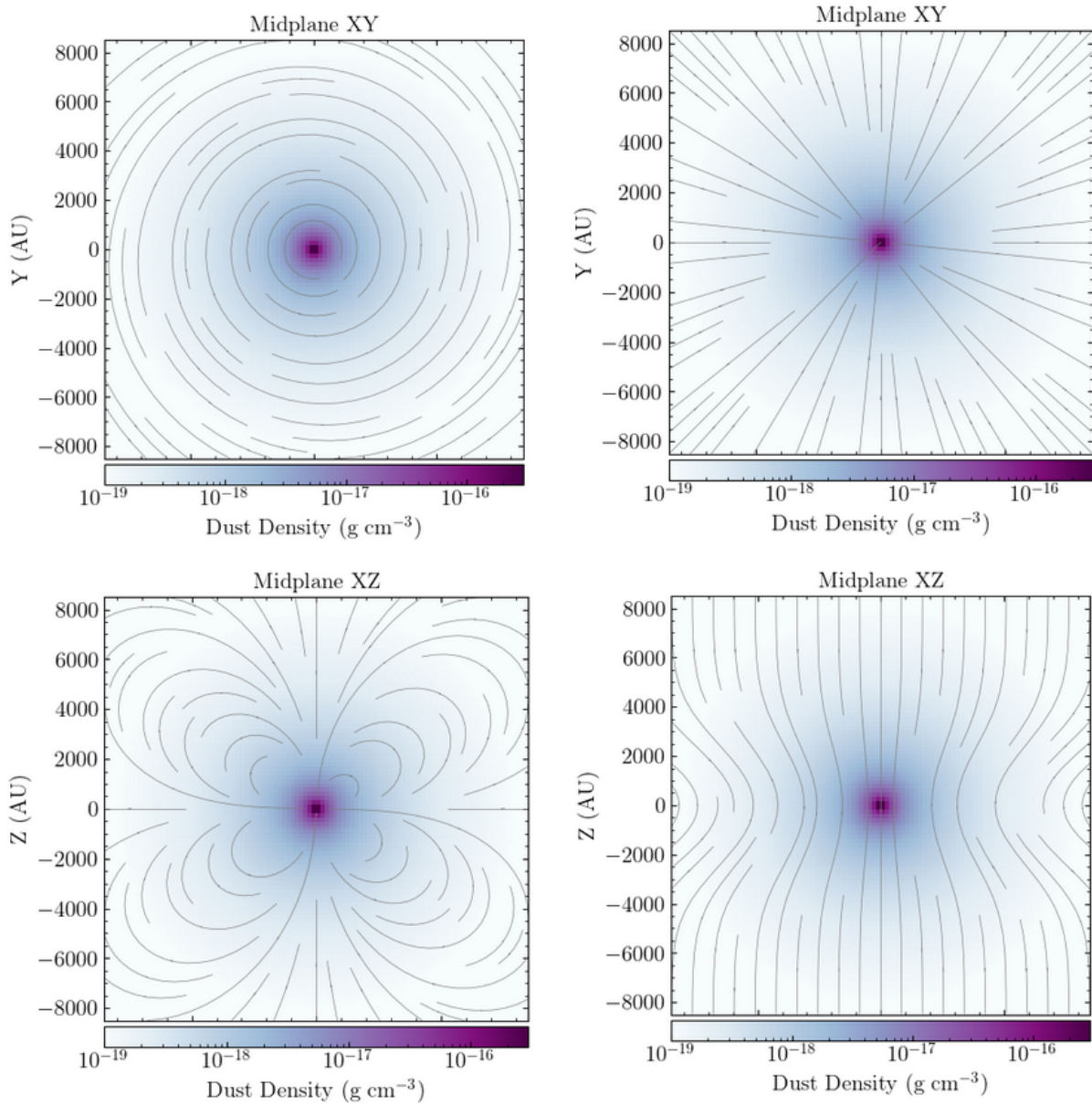


Figure 4.4: Some of the analytical vector fields available within the Synthesizer. The top row shows a toroidal and a radial vector field, from left to right, respectively. Bottom row shows a quadrupole and hourglass field morphology.

and memory size depend on what types of grids are supported by RADMC3D. In this regard, all the Synthesizer does is to read in all the grid and density information from the simulation output and translate it into the RADMC3D grid file format. Grid types currently supported by RADMC3D are regular cartesian and spherical grids, statically refined spherical grids and Oct-tree and layered cartesian grids (commonly generated by hydro codes with Adaptive Mesh Refinement; AMR). Beta versions of RADMC3D do offer support for unstructured grids such as Delaunay triangulations and Voronoi tessellations, however this not yet fully tested. The Synthesizer does not support conversion of unstructured meshes until it is fully supported by RADMC3D. The Synthesizer is very young and at the moment only snapshots from the grid-based MHD code ZeusTW (Krasnopolsky et al. 2010) are supported. Creating interfaces for new codes is easy to implement but it takes time. For AMR codes, initially only grid and density (and optionally temperature) information is needed to generate the input for RADMC3D. Future versions of the code will support conversion for some of the most commonly used hydro codes, such as Athena++ (Stone et al. 2020), FLASH (Fryxell et al. 2000), ENZO (Bryan et al. 2014) and RAMSES (Teyssier 2002) (see section 4.5). In order to use simulation outputs from grid-based codes, the `--source` and `--amrfile` options must be given. An example command would look like

```
$ synthesizer --grid --source athena --amrfile cbd.out1.00001.athdf ...
```

Using particle-based hydro codes

The core functionality of this module lies in its interpolation implementation for particle-based codes, namely Smoothed Particle Hydrodynamics (SPH) codes. The Synthesizer reads in 3D positions (in cartesian coordinates) and density values for an ensemble of particles. It then uses the *interpolate* module from the Python SciPy (Virtanen et al. 2020) library to generate a regularly-spaced 3D density cube by linearly (default) interpolating all the particle density values. The same is repeated for temperature values and vector field components when requested. In order to avoid interpolating low-density regions of low scientific interest, the options `--bbox` or `--rout` can be given, followed by a physical scale in au. These options reject particles outside of a given range. Both options act as a zoom-in implementation, where particles outside a given bounding-box (`rout`) or outter radius (`rout`) are excluded from the interpolation. This command can also be combined with the `--ncells` option to increase the resolution of a given region. This is particularly useful when using grids with a large spatial and physical dynamic range. An example of this implementation is shown in Fig. 4.5, for the case of an SPH protostellar disk formed out of the collapse of an initially spherical prestellar core. Because the interpolation of SPH particles needs only particle positions and physical quantities, there is not actual "conversion" involved in the generation of the grid. All the code needs is a way to read in one-dimensional data arrays containing the particle coordinates and values. This means that creating interfaces to more SPH codes is quite easy to implement. The most common approach is through HDF5 (Hierarchical Data Format 5) file readers, which is the de facto standard for large simulation outputs storage. The Synthesizer does currently offers compatibility with output files from SPHng (Bate et al. 1995), GIZMO (Hopkins 2015), GADGET-2 (Springel 2005) and AREPO (Springel 2010). In

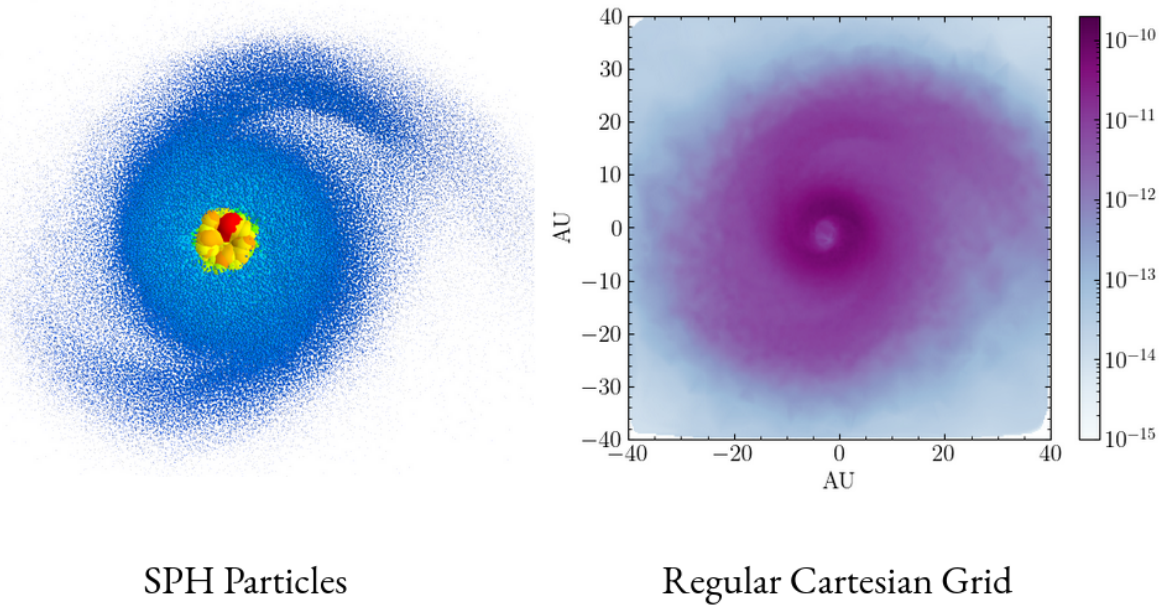


Figure 4.5: Interpolation of SPH particles onto a regular cartesian grid as done by the gridding module. This example shows the gridding of an SPH protostellar disk formed 18 kyr after the collapse of a Bonnor-Ebert sphere.

order to use simulation outputs from particle-based codes, the `--source` and `--sphfile` options must be given. An example command would look like this

```
$ synthesizer --grid --source arepo --sphfile snap_001.hdf5 ...
```

4.3.2 Dust Opacity (`--opacity`)

The second module available within the Synthesizer is in charge of creating dust opacity tables. This module is accessible via the `synthesizer --opacity` command.

How to calculate dust opacities

The simulated fluxes produced from a density model are the result of the radiative transfer equation, solved along a certain line-of-sight, plus the contribution of the emission scattered within the grid. The core quantity involved in the radiative transfer equation is the opacity of the radiating material. In the context of this thesis, dust continuum observations, the main contributor to the opacity is the dust opacity, which in turn depends on factors like the composition and the size of the grains. The Synthesizer includes a full module to calculate dust opacity tables for different mixtures and it is robust enough to receive its own name. This module is called `DUSTMIXER`, and it has been shortly introduced in Chapter 3, section B.1. The `DustMixer` is a full command-line driven tool as well, allowing to easily experiment with various dust models and the effects of polarization by scattering or grain alignment. In this section, we describe the process of calculating

dust opacity tables starting from laboratory measurements of specific material. These properties are represented as a complex number m , composed by two real and imaginary parts of the form

$$m(\lambda) = n(\lambda) - ik(\lambda). \quad (4.1)$$

They both receive the name of refractives indices, or also known as optical constants, and can be obtained from the literature (e.g., Draine & Lee 1984, Ossenkopf & Henning 1994, Weingartner & Draine 2001, Jager et al. 1998, Draine 2003a, Woitke et al. 2016 and Birnstiel et al. 2018) or from the nicely compiled repository of optical constants from the OPTOOL⁵ program. Optool (Dominik et al. 2021) is another publicly available command-line driven tool for calculating dust opacities with different mixtures. Optool is in fact the main motivation for the DustMixer to be created, as a tool easy to embed within the Synthesizer, and offers larger flexibility and customization for dust ensembles than the DustMixer does in its current version.

The DustMixer starts by reading in data tables of n and k values (see Fig. 4.6), for a specific material (e.g., silicates, graphites, molecular ices, etc), tabulated over a range of wavelengths. It then (see Fig. 4.6) uses the Bohren & Huffman (1983) algorithm BHMIE to convert optical constants into dust efficiencies Q , for a specific grain size, under the assumption that grains are spherical. Dust efficiencies represent the electromagnetic response of a medium (a spherical dust grain in this case) to an incident plane electromagnetic wave. The incident radiation causes the grain to radiate electromagnetic waves of itself. This is in principle an Electrodynamics problem, but the nature of this interaction can be modelled in simplified ways for cases when the grain size is either much larger or much smaller than the incident wavelength. The main quantity involved in this scattering event is the scattering efficiency Q_{sca} . For grain sizes much smaller than the incident wavelength ($a \ll \lambda$), this event is called *Rayleigh scattering*, and the scattering and absorption efficiencies can be obtained by

$$Q_{\text{sca}} = \frac{8}{3} \left(\frac{2\pi a}{\lambda} \right)^4 \left| \frac{m^2 - 1}{m^2 + 2} \right|^2 \quad Q_{\text{abs}} = 4 \left(\frac{2\pi a}{\lambda} \right) \text{Im} \left| \frac{m^2 - 1}{m^2 + 2} \right| \quad (4.2)$$

where a is the radius of the dust grain. On the other hand, if the particle is much larger than the incident wavelength ($a \gg \lambda$), the scattering can be treated as a geometric reflection and light can be propagated simply using raytracing. The middle case when the grain size is comparable to the incident wavelength ($a \sim \lambda$) is the most difficult to model and it was firstly introduced by Gustav Mie (Mie 1908; thereafter named Mie scattering), who described the sphere's response to light as a solution to Maxwell's equations. In the Mie regime, because the size of the grain is comparable to the wavelength, the incident electromagnetic wave arrives at different parts of the sphere's surface with different phases, and the net interaction must be modelled as an infinite sum of independently interacting dipoles. This way, the outgoing wave from the dielectric sphere is represented as the expansion of a scalar field using spherical harmonics but for a vector field. Similar to a scalar field, this involves numerically solving Legendre polynomials and Bessel functions, with expansion coefficients a_n and b_n , with n the expansion index going from $n = 1$ to $n \rightarrow \infty$, also known as scattering coefficients. This calculation requires to similarly decompose

⁵<https://github.com/cdominik/optool>

the incident wave into infinite spherical harmonics, with scattering coefficients c_n and d_n . By coupling the expressions for the incoming and outgoing radiation fields (see Bohren & Huffman 1983) and applying boundary conditions for a dielectric sphere, we can obtain the expressions for the outgoing scattering coefficients for a given n

$$a_n = \frac{m\psi_n(mx)\psi'_n(x) - \psi_n(x)\psi'_n(mx)}{m\psi_n(mx)\xi'_n(x) - \xi_n(x)\psi'_n(mx)} \quad (4.3)$$

$$b_n = \frac{\psi_n(mx)\psi'_n(x) - m\psi_n(x)\psi'_n(mx)}{\psi_n(mx)\xi'_n(x) - m\xi_n(x)\psi'_n(mx)} \quad (4.4)$$

where ψ and ξ are the Riccati-Bessel functions. With these two expressions we can write the scattering dust efficiencies from Mie theory as

$$Q_{\text{sca}} = \frac{2}{k^2 a^2} \sum_{n=1}^{\infty} (2n+1) (|a_n|^2 + |b_n|^2) \quad (4.5)$$

with $k = 2\pi/\lambda$ the wave number of the incident wave. A second product of Mie theory and the BHMIE algorithm is the dust extinction efficiency

$$Q_{\text{ext}} = \frac{2}{k^2 a^2} \sum_{n=1}^{\infty} (2n+1) \text{Re}(|a_n|^2 + |b_n|^2) \quad (4.6)$$

The final relevant quantity involved in the radiative transfer equation is the absorption dust efficiency. This can be obtained from the scattering and extinction efficiency as

$$Q_{\text{abs}} = Q_{\text{ext}} - Q_{\text{sca}}. \quad (4.7)$$

The BHMIE algorithm explicitly uses the theory of Mie scattering to obtain the scattering efficiencies regardless of the size of the grains, which in the context of small grains deliver the same results as the analytic expression for Rayleigh scattering (equation 4.2). It does also use Mie theory for grain sizes larger than the incident wavelength, without a geometric approximation. This makes the calculation of dust efficiencies highly computationally expensive for large grains (e.g., millimetric scattering on millimetric and centimetric dust grains as observed by ALMA and JVL A). The calculation of such sums (4.5 and 4.6) is computationally expensive, specially for larger grains. The bigger the grain size the more terms need to be included in the sum for it to converge. The computational expense is determined by the so called size parameter $x = 2\pi a/\lambda$. For $x \simeq 1$, $n \simeq x$ terms are needed. For larger size parameters $x \gg 1$, this might take much longer. In the Synthesizer, on sequential mode (i.e., single-thread calculation), calculating dust efficiencies for a $10\ \mu\text{m}$ sized grain takes no longer than 1 minute, and only a few seconds for even smaller grains. For 1 mm sized grains this can scale up to 20 or 40 minutes depending on the resolution of the wavelength grid (100 or 200 bins, respectively). In order to speed this up, the Synthesizer employs a multiprocess parallelization scheme to simultaneously calculate efficiencies for an ensemble of grain sizes. This however, still slows down on the bins corresponding to the largest grain sizes, and currently only works when no scattering matrices are needed, but

it does result in a faster calculation. To avoid re-calculating full opacity tables on every single synthetic observation, precomputed high-resolution dust opacity tables have been made available in a public repository⁶. This does not need to be manually downloaded by the user. If no explicit call to the DustMixer is made (via the `--opacity` option), the Synthesizer will first check whether an opacity table is already existent in the local directory, and if not, it will attempt to download the corresponding table from the public repository, as long as it exists.

The final step in the calculation of dust opacities is the conversion of dust efficiencies into mass-weighted dust opacities κ (see Fig. 4.6). This is maybe the quickest step to perform numerically, as it only involves the conversion of the adimensional dust efficiencies Q and cross sections $\sigma = 2\pi a^2$ (cm²) into opacities κ (cm²g⁻¹). For a single grain size, this is done as

$$\kappa_{\text{abs}} = 2\pi a^2 Q_{\text{abs}} \quad (4.8)$$

$$\kappa_{\text{sca}} = 2\pi a^2 Q_{\text{sca}} \quad (4.9)$$

$$\kappa_{\text{ext}} = 2\pi a^2 Q_{\text{ext}}. \quad (4.10)$$

If the DustMixer is called without customized by parameters, it will default to a power-law grain size distribution for 100 grains sizes between 0.1 μm and 10 μm . The results of this calculation are shown in Fig. 4.6. This default setup can be easily reproduced with the following command

```
$ synthesizer --opacity --show-nk --show-dust-eff --show-opac
```

The `--show-*` flags are completely optional and only serve as illustration. This command represents the default setup, which can be also explicitly expanded as

```
$ synthesizer --opacity --amin 0.1 --amax 10 --na 100 --q -3.5 --lmin 0.1 --lmax 1e5 --nlam 200 --material s
```

To explicitly calculate dust opacities for a single grain size, either the minimum and maximum grain size must be set equal or the number of grain size bins (`--na`) must be set to 1, as

```
$ synthesizer --opacity --amin 100 --amax 100 --na 1
```

Dust opacities for a range of grain sizes, as the default case, are obtained by calculating the dust efficiencies Q for each grain size and then integrating them over a size distribution. Currently, only power-law size distribution of the form $N(a) \propto a^q$ are implemented, with $q = -3.5$ the MRN (Mathis et al. 1977) interstellar size distribution slope as default. In such case, the size integrated dust opacity κ_λ is obtained as

$$\kappa_\lambda = \frac{1}{C} \int_{a_{\text{min}}}^{a_{\text{max}}} \pi a^2 Q_\lambda(a) \varphi(a) da \quad (4.11)$$

with $\varphi(a) = a^q$ and C a mass normalization constant of the form

$$C = \frac{4}{3} \pi \rho \int_{a_{\text{min}}}^{a_{\text{max}}} \varphi(a) a^3 da \quad (4.12)$$

where ρ is the density of the considered material (silicate by default).

⁶https://github.com/jzamponi/utills/tree/main/opacity_tables

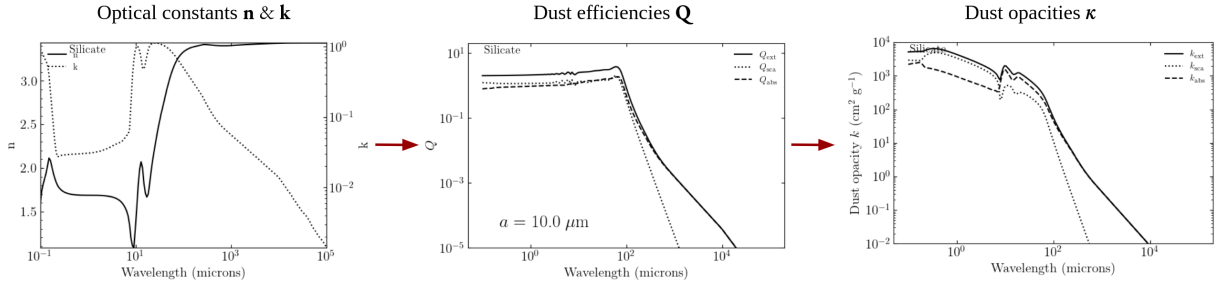


Figure 4.6: The process of calculating opacities. The first step (left) is to obtain laboratory optical constants of a given material. These are then converted into efficiencies (middle) for a given grain size and finally converted into mass-normalized dust opacities ($\text{cm}^2 \text{g}^{-1}$; right). The optical constants here shown represent silicate dust (Draine 2003b). The dust efficiencies are calculated for a single grain size of $10 \mu\text{m}$ and the dust opacities are obtained integrating the efficiencies for grains of $0.1 \mu\text{m}$ up to $10 \mu\text{m}$, using a power-law size distribution ($N(a) \propto a^{-3.5}$), for 100 size bins. This calculation takes 30 seconds to run.

The resultant thermal emission from a radiative transfer model is obtained by solving the radiative transfer equation along a given line of sight. The propagation of this flux is determined by the extinction opacity κ_{ext} . However, the total flux of a model should in principle consider the contributions from both the thermal and the scattered flux. Because following the direction of scattered rays in all directions (raytracing) would largely increase the computational time, one of most commonly employed numerical approaches is the use of Monte-Carlo calculations (Steinacker et al. 2013). In this way, scattering events are modelled by launching a finite amount of photons from a radiating source (either the protostar or the dust itself) and letting them enter the grid cells, depositing or removing a finite amount of energy, and being re-launched in a new random direction (Bjorkman & Wood 2001), until all photons have escaped the grid. Those photons reaching the observing plane are then counted towards the scattering flux. The direction of the outgoing photons after a scattering event is not isotropically distributed (isotropic scattering) in most astrophysical contexts. The most commonly used probability distribution function for the outgoing scattering angle θ is called the *Henye-Greenstein* phase function (Henyey & Greenstein 1941), and is fully parametrized by a single parameter g . This scattering phase function is the randomly-sampled (Monte-Carlo) distribution function and receives the form

$$p_g(\mu) = \frac{1}{2} \frac{1 - g^2}{(1 + g^2 - 2g\mu)^{3/2}} \quad (4.13)$$

where $\mu = \cos \theta$ represents the scattering angle. This approach is numerically convenient when modelling the final Stokes I-only flux or when generating temperature distributions by radiative heating. In reality, every single scattering angle should be sampled from the $p(\mu)$ function so that

$$\int_{-1}^{+1} p(\mu) d\mu = 1. \quad (4.14)$$

This is particularly important when dealing with polarization of light and the full Stokes representation of a light packet, since scattering tends to change the polarization status of the incident

photon. However, when only the Stokes I light information is needed, i.e., the net flux produced from a model, modelling scattering events using the Henyey-Greenstein approach is good enough to deliver accurate scientific results. This parameter g is another byproduct of the BHMIE algorithm previously mentioned and is also dumped by the DustMixer as an extra column in the opacity table.

How to include scattering matrices for polarization

In some cases, one might be interested in studying the final polarization status of light generated by a modelled. This could be important when studying the effects of dust self-scattering (see chapter 3) or the effect of alignment of elongated grains. In such cases, full information of the light Stokes parameters is needed at the end of the simulation. In the specific scenario of modelling polarization by scattering, the Henyey-Greenstein scattering phase function is not appropriate because it does not provide information about the Q , U , and V Stokes components, but only from the Stokes I intensity. In order for a radiative transfer code (as RADMC3D for the Synthesizer) to keep track of the polarization status of light during the Monte-Carlo modelling of scattering, it needs information about the *scattering matrix*. The scattering matrix Z_{ij} is the tensor that describes how will an incident photon $F = (F_I, F_Q, F_U, F_V)^T$ transform into an outgoing photon $W = (W_I, W_Q, W_U, W_V)^T$ after a scattering event. The outgoing wave W is a function of two scattering angles θ and ϕ and of the distance from the scattering particle, so its flux falls as $1/r^2$. This interaction can be described as

$$\begin{pmatrix} W_I \\ W_Q \\ W_U \\ W_V \end{pmatrix} = \frac{m_{\text{grain}}}{r^2} \begin{pmatrix} Z_{11} & Z_{12} & Z_{13} & Z_{14} \\ Z_{21} & Z_{22} & Z_{23} & Z_{24} \\ Z_{31} & Z_{32} & Z_{33} & Z_{34} \\ Z_{41} & Z_{42} & Z_{43} & Z_{44} \end{pmatrix} \begin{pmatrix} F_I \\ F_Q \\ F_U \\ F_V \end{pmatrix} \quad (4.15)$$

with m_{grain} the mass of a spherical grain of radius a . For spherical grains or similarly for randomly oriented non-spherical grains, symmetry arguments (Bohren & Huffman 1983) reduce the amount components of the scattering matrix needed to describe the scattering event to only six, Z_{11} , Z_{12} , Z_{22} , Z_{33} , Z_{34} and Z_{44} . In Mie theory, this even reduces to four relevant quantities because $Z_{22} = Z_{11}$ and $Z_{44} = Z_{33}$. These four components of the scattering matrix can be obtained by

$$Z_{11} = \frac{k^2 m_{\text{grain}}}{2} (|S_2|^2 + |S_1|^2) \quad (4.16)$$

$$Z_{12} = \frac{k^2 m_{\text{grain}}}{2} (|S_2|^2 - |S_1|^2) \quad (4.17)$$

$$Z_{33} = \frac{k^2 m_{\text{grain}}}{2} (S_2^* S_1 + S_2 S_1^*) \quad (4.18)$$

$$Z_{34} = \frac{k^2 m_{\text{grain}}}{2} (S_2^* S_1 - S_2 S_1^*) \quad (4.19)$$

where $k = 2\pi/\lambda$ and

$$S_1 = \sum_{n=1}^{\infty} \frac{2n+1}{n(n+1)} (a_n \pi_n + b_n \tau_n) \quad (4.20)$$

$$S_2 = \sum_{n=1}^{\infty} \frac{2n+1}{n(n+1)} (a_n \tau_n + b_n \pi_n) \quad (4.21)$$

$$(4.22)$$

with

$$\pi_n(\theta) = \frac{P_n^1(\theta)}{\sin \theta} \quad (4.23)$$

$$\tau_n(\theta) = \frac{dP_n^1(\theta)}{d\theta} \quad (4.24)$$

$$(4.25)$$

where $P_n^1(\theta)$ are the associated legendre polynomials. The S_1 and S_2 infinite sums are, as expected, another byproduct of the BHMIE algorithm along with the dust efficiencies and Henyey-Greenstein scattering parameter. They are similarly calculated for a specific grain size and then integrated over the size distribution. The phase function used in this case is

$$p(\mu) = k^2 m_{\text{grain}} \frac{Z_{11}(\cos \theta)}{\sigma_{\text{sca}}} \quad (4.26)$$

where

$$\sigma_{\text{sca}} = \int_0^{2\pi} Z_{11}(\theta, \phi) d\phi. \quad (4.27)$$

In the Synthesizer, adding the information about the scattering matrix to the dust opacity table is enabled with the `--polarization` option as

```
$ synthesizer --opacity --polarization
```

An additional parameter subject to customization is the number of angles used to sample the scattering matrix elements. This can be set with the option `--nang` and currently defaults to 181 angles. When calling RADMC3D for a polarized flux calculation, it will first make sure that the listed dust opacities κ_{sca} are consistent with the listed scattering matrix components Z_{11} . This test is passed when the difference between the angular integral of Z_{11} and the corresponding κ_{sca} , given by the condition

$$\kappa_{\text{sca}} \simeq 2\pi \int_{-1}^{+1} Z_{11}(\mu) d\mu, \quad (4.28)$$

is smaller than a predefined epsilon (1e-4).

4.3.3 Radiative Transfer (--raytrace)

The third module available within the Synthesizer is in charge of running the radiative transfer calculation for an already create density and dust model. This is accessed via the `--raytrace` option. The Synthesizer relies fully on RADMC3D to do the raytracing and Monte-Carlo and limits itself simply to the preparation of all the necessary input files and the post-processing of the results. Currently, only dust continuum radiative transfer is available within the Synthesizer. Future versions of the code will include support for molecular line modelling (see section 4.5).

In order to run a raytracing plus scattering monte-carlo calculation, one can simply use the default setup with the following command

```
$ synthesizer --raytrace
```

This example assumes that a `dust_temperature.dat` file has been created from the model via the `$ synthesizer ... --grid ... --temperature ...` command. If not dust temperature file is existent, RADMC3D will stop before starting the main calculations as it won't be able to create the initial radiation field. If dust temperature is not provided by the model's gas temperature, it can be easily created via Monte-Carlo radiative heating. In this mode, accessible simply by running

```
$ synthesizer --raytrace --monte-carlo
```

RADMC3D will first perform a thermal Monte-Carlo run by launching photon packets from a user-defined radiating source (central 4000 K protostar by default, customizable with the `--star` option) and heating the model until all photons are either absorbed or escape the grid. Once this temperature by radiation is created, it will proceed to do the raytracing. The Monte-Carlo heating step does not need to be repeated for every raytracing calculation. It is anyway recommended to test convergence of the Monte-Carlo heating by increasing the number of photons until no significant difference is seen in the temperature distribution. This distribution can be easily visualized on a new call with the command `$ synthesizer --temperature -show-grid-2d -show-grid-3d`.

Almost all RADMC3D parameters can be customized from the Synthesizer front-end (see Table 4.1 for details). For those parameters not explicitly defined, we provide an option called `--radmc`, meant to be followed by a sequence of command-line arguments to be passed to the standard RADMC3D call. In Fig. 4.7 is shown an example case of an SPH protostellar disk (the one shown in the gridding step in Fig. 4.5 but this time after the output of the radiative transfer step) observed at 1300 microns (default). This example show the disk's flux along with polarization vectors produced by dust alignment with the velocity field. Next to it is shown a map of optical depth also obtained using the Synthesizer. The optical depth map, obtained as $\tau = \int \rho_{\text{dust}} \kappa_{\text{ext}} dz$, with z the line-of-sight, used the extinction dust opacity κ_{ext} of an ensemble of grains grown up to $100 \mu\text{m}$, which leads to a highly optically thick emission. The explicitly expanded command used to generate such images goes as follows

```
$ synthesizer --raytrace --tau --lam 1300 --incl 0 --npix 300 --sizeau 50 --
  show-rt --alignment
```

In Fig. 4.7 the colorscale represents the Stokes I flux from the disk model. Polarization vectors are generated from the information about the polarized emission, which can be obtained

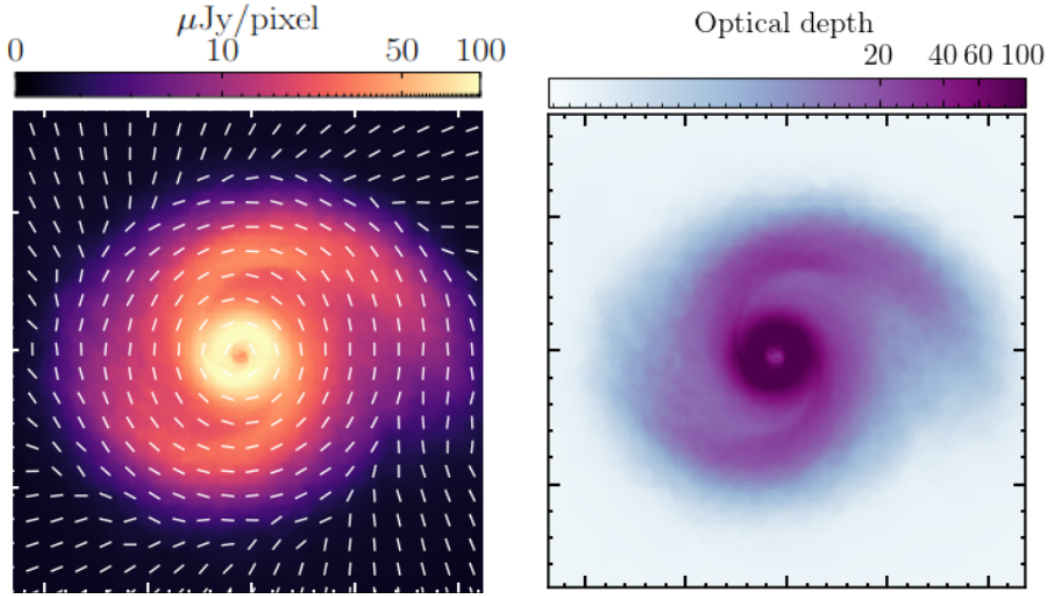


Figure 4.7: Example of results from the raytracing module within the Synthesizer. On the left is shown ideal synthetic flux map from a protostellar disk model, with polarization vectors overlaid, generated by dust alignment with the velocity field. On the right is shown a optical depth map for the same disk model, assuming grain sizes of up to $100\ \mu\text{m}$, which make the disk be extremely optically thick.

from the Q and U components as

$$P_1 = \sqrt{Q^2 + U^2}. \quad (4.29)$$

The vector angles are obtained from Q and U as well, as

$$P_{\text{angle}} = \frac{1}{2} \arctan\left(\frac{U}{Q}\right). \quad (4.30)$$

The length of the vectors is commonly scaled by the polarization fraction. This is obtained as the ratio of the polarized intensity P_1 over the total intensity $I \geq \sqrt{Q^2 + U^2 + V^2}$ as

$$P_{\text{frac}} = \frac{P_1}{I}. \quad (4.31)$$

In some cases, as in Fig. 4.7, when the polarization fraction spans a too large dynamic range within the image, it might be convenient to set all vectors to a constant length, in order to avoid empty and overcrowded regions. This is the default behaviour of the Synthesizer for the image displayed with the `--show-rt` option.

4.3.4 Synthetic Observation (`--synobs`)

The last module within the Synthesizer, and last step in the whole process of simulating observations (see Fig. 4.1) is the application of instrument and telescope-specific related effects.

Single-dish radio and optical/infrared observations

In the context of single-dish radio telescopes (e.g., APEX, IRAM 30-m, Green Bank Telescope, etc.) or single aperture optical/infrared telescopes (VLT, Herschel, Hubble, JWST, etc.), convolution with a beam and thermal noise addition are the two main effects needed to make a synthetic observation look as realistic as possible. The Synthesizer provides support for both of these techniques, however, only those applications for telescopes in the radio and sub-/millimeter range have been tested so far. The principle is basic and has been nicely detailed by Zamponi et al. (2022). As a first step, one can feed the Synthesizer the option `--resolution` followed by the size of a symmetric Gaussian beam in arcseconds. This will be used to convolve the map previously created with `--raytrace`. The convolution is done using the `convolve_fft` function from the Astropy Python Package (Astropy Collaboration et al. 2022). This function needs the standard deviation σ of a Gaussian profile to create a 2D Gaussian kernel, and performs the convolution in Fourier space in favour of speed for large images (≥ 50 pixels per side). This standard deviation can be obtained from the entered resolution θ as

$$\sigma = \frac{\theta}{\sqrt{8 \ln 2}}. \quad (4.32)$$

After convolution, the original flux F_{unconv} (in units of Jy/pixel, for radio observations) needs to be rescaled to a beam-dependent flux F_{conv} , multiplying by the ratio of the area of a Gaussian beam over the area of a square pixel as

$$\frac{F_{\text{conv}}}{\text{Jy pixel}^{-1}} = \frac{\pi}{4 \ln 2} \frac{\theta^2}{\text{arcseconds}} \left(\frac{\text{pixelsize}}{\text{arcsec}} \right)^{-2} \frac{F_{\text{unconv}}}{\text{Jy pixel}^{-1}}. \quad (4.33)$$

The second step is to add noise to our ideal images based on the telescope's receiver temperature. Within the Synthesizer this is currently only implemented for radio single-dish telescopes using the radiometer equation

$$T_{\text{rms}} = \frac{T_{\text{sys}}}{\Delta\nu t_{\text{int}}}, \quad (4.34)$$

where T_{rms} is the observation noise to be added to the new convolved image, in units of K, T_{sys} is the system temperature, $\Delta\nu$ is the spectral bandwidth to be considered (or channel resolution in case of line observations) and t_{int} is the time on source (provided to the Synthesizer via the `--obs-time` option). The system temperature T_{sys} for a single-dish measurement, is given by the following equation

$$T_{\text{sys}} = T_{\text{A}} + \left(T_{\text{rec}} + T_{\text{atm}} \left[1 - \exp\left(\frac{-\tau_0}{\sin(El)}\right) \right] \right) \exp\left(\frac{-\tau_0}{\sin(El)}\right), \quad (4.35)$$

where T_{A} is the antenna temperature, T_{rec} is the receiver temperature characterized by the Friis equation

$$T_{\text{rec}} = T_1 + \frac{T_2}{G_1} + \frac{T_3}{G_2 G_3} + \dots,$$

with $1, 2, \dots, n$ identifiers of the ordered electronic components in the receiver and G the gain of each of them, T_{atm} is the integrated physical atmospheric temperature, τ_0 is the atmospheric

zenith opacity and El is the elevation of the source. Because of T_{sys} being highly telescope specific, different radio telescopes offer their own system temperature calculators. Future versions of the Synthesizer will include either either core implementation of the system temperature calculation for most common telescope receivers or the option to provide such values as command line arguments.

Sub-/millimeter inteferometric observations

Simulating the antenna response and image reconstruction for a full interferometric array is a quite challenging task, both in terms of computational time and data manipulation. Luckily, this option is already provided by CASA. In CASA, inteferometric (and also single-dish) synthetic observations are split into two main steps: first, the generation of the complex visibilities for a specific sky model, and second, the deconvolution of the dirty image generated by the convolution of the real sky intensity distribution and the finite interferometric sampling (the visibilities). The first step is calculated using the CASA task `simobserve`. This function receives parameters related to the observing setup, such as, the sky coordinates of the synthetic model, the observing frequency and bandwidth, the time per scan and the time on source, the observing mode (interferometer or single-dish), the antenna configuration and customization of the parameters related to the generation of thermal noise, as in equation 4.35. An example call to the `simobserve` task goes as follows

```
simobserve(
    project = 'band6',
    skymodel = 'radmc3d_I.fits',
    incenter = '223GHz',
    inwidth = '0.12GHz',
    setpointings = True,
    integration = '2s',
    totaltime = '1.25h',
    indirection = 'J2000 16h32m22.63 -24d28m31.8',
    hourangle = 'transit',
    obsmode = 'int',
    antennalist = 'alma.cycle4.7.cfg',
    thermalnoise = 'tsys-manual',
    graphics = 'both',
    overwrite = True,
    verbose = True
)
```

When calling the Synthesizer with the `--synobs` option and no external script has been specified, it generates a minimal template CASA script called `casa_script.py`. This script serves as a starting point for the user to create a more customized version. This new version can then be feed to the Synthesizer on a new call via

```
$ synthesizer --synobs --lam 3000 --script my_new_script.py --show-synobs
```

for a 3000 microns observation example. Some parameters, such as the wavelength, need to be explicitly reentered since the Synthesizer does not trace history of previous calls. Otherwise it will always default to 1300 microns and will mismatch the already existing project, stored

in *synobs_data*. The Synthesizer includes also few more templates tailored to real ALMA and JVLA observations and previously used by Zamponi et al. (2021) and Zamponi et al. (Submitted), also available within the code distribution⁷. To use these scripts instead of the default minimal one, add the option `--use-template`. Given the `simobserve` argument `graphics = "file"` or `graphics = "both"`, `simobserve` will generate and optionally display two diagnostic plots during runtime. The first one, shown in the upper row of Fig. 4.8, shows what is the needed beam coverage of the observation given the size of the model and the telescope's field-of-view. In some cases only one pointing is needed, some other time a mosaic must be done. This is automatically detected and performed by `simobserve`. The second plot, upper right panel of Fig. 4.8, shows information about the source elevation (given the observing site and source celestial coordinates), the array configuration as seen by the source, the *uv*-coverage and the Point-Spread-Function (PSF). Once this step is done, the Synthesizer will create a folder called *synobs_data* where all these figures and the measurement set will be stored.

The second step is performed by calling the CASA task `tclean`. This function receives parameters related to the cleaning process of a dirty image, such as, the image size in pixels, the pixel size in arcseconds, the reference frequency (to match that from `simobserve`), the spectral mode (`mfs` for continuum, `cube` for line emission), the type of gridder used for the Fourier Transform of the visibilities, the type of deconvolver, type of visibility weighting and the cleaning threshold. An example call to `tclean` is included in the previously mentioned templates and reads as follows

```
tclean(
  vis = 'synobs_data/synobs_data.alma.cycle4.7.noisy.ms',
  imagename = 'synobs_data/clean_I',
  imsize = 400,
  cell = '0.008arcsec',
  reffreq = '223GHz',
  specmode = 'mfs',
  gridder = 'standard',
  deconvolver = 'multiscale',
  scales = [1, 8, 24],
  weighting = 'briggs',
  uvrange = '120~2670klambda',
  robust = 0.0,
  niter = 10000,
  threshold = '2.5e-4Jy',
  mask = 'synobs_data/synobs_data.alma.cycle4.7.skymodel',
  interactive = False,
  verbose = True
)
```

This step does not generate diagnostic plots on the run, but it does save several byproducts of the deconvolution to file. All these files are saved within the project folder *synobs_data*. Some of them are: the final cleaned image (shown in the lower left panel of Fig. 4.8) called *clean_I.image* and also saved to FITS file within the parent directory as *synobs_I.fits*, a residual map *clean_I.residual* (see lower right panel of Fig. 4.8), a file containing the cleaning mask

⁷<https://github.com/jzamponi/synthesizer/tree/main/synthesizer/synobs/templates>

used *clean_I.mask*, a file containing the telescope’s Primary Beam *clean_I.pb* and the primary beam corrected final image *clean_I.image_pbcor*. As mentioned, *synobs_I.fits* is the end result of the whole synthetic observation process illustrated in Fig. 4.1. This FITS image is the science ready model users can do for their own scientific purposes, being certain that it accounts for the proper resolution and sensitivity treatment when comparing high-resolution numerical simulations to real observations.

4.4 Science cases

This chapter would not be complete without a proper demonstration that the Synthesizer can deliver publication-ready results. The code started as a collection of previous slightly versatile scripts, highly specific for certain codes and setups. Earlier versions of such scripts have been used in previous works, such as Zamponi et al. (2021) and Zamponi et al. (2022), before coming into shape as a standalone Python package. The Synthesizer came to birth as the need to easily automate various tedious and isolated manual tasks and therefore its philosophy is to make the process of modelling observations more manageable for future users, letting them focus their time on the science and not on the file and code formatting. Below I list a couple of projects in which the Synthesizer has been used, regardless of their status as published, submitted, in preparation or future work. All the following figures and results are included here with full consent of the corresponding owners.

Polarization by self-scattering

The first and biggest scientific case for which the code has been used is that described in full in chapter 3 and Zamponi et al. (Submitted). Because of having a full chapter dedicated to this only, I refrain myself from elaborating on the details of the project and refer the reader to sections 3.3.2, 3.3.5 and 3.4 for further details. In summary, I have used the Synthesizer to model the polarized emission produced by dust self-scattering in the Class 0 protostellar disk IRAS 16293-2422 B, using a radiation-hydrodynamics simulation of protostellar disk formation as a physical model. The disk model is hot, with central (<10 au) temperatures above 400 K, and massive ($0.3 M_{\odot}$). Previous ALMA and JVLA observations (Sadavoy et al. 2018 and Liu et al. 2018a, respectively) have suggested that the observed azimuthal polarization pattern could be produced by the dust scattering of the dust thermal emission itself. If this is the case, being the polarization fraction (2-4%) similar between both 1.3 and 7 mm observed wavelengths, then dust grains must have grown to at least 200 or even up to 2000 microns in order to produce polarization by self-scattering detectable at both millimeter wavelengths. I employed the Synthesizer to automate the modelling of several parameters involved in the self-scattering polarization and to study their parameter space, aiming to assess the scenario of dust being grown to millimeter sizes in a Class 0 disk. The results of the modelling indicate that regardless of the dust composition and size, the disk model used (under the assumption that it properly represents the disk in IRAS 16293 B) is too massive and therefore too optically thick ($\tau > 100$) to produce polarization fractions by self-scattering of around 2-4% at both 1.3 and 7 mm. The maximum polarization fraction ob-

Simobserve

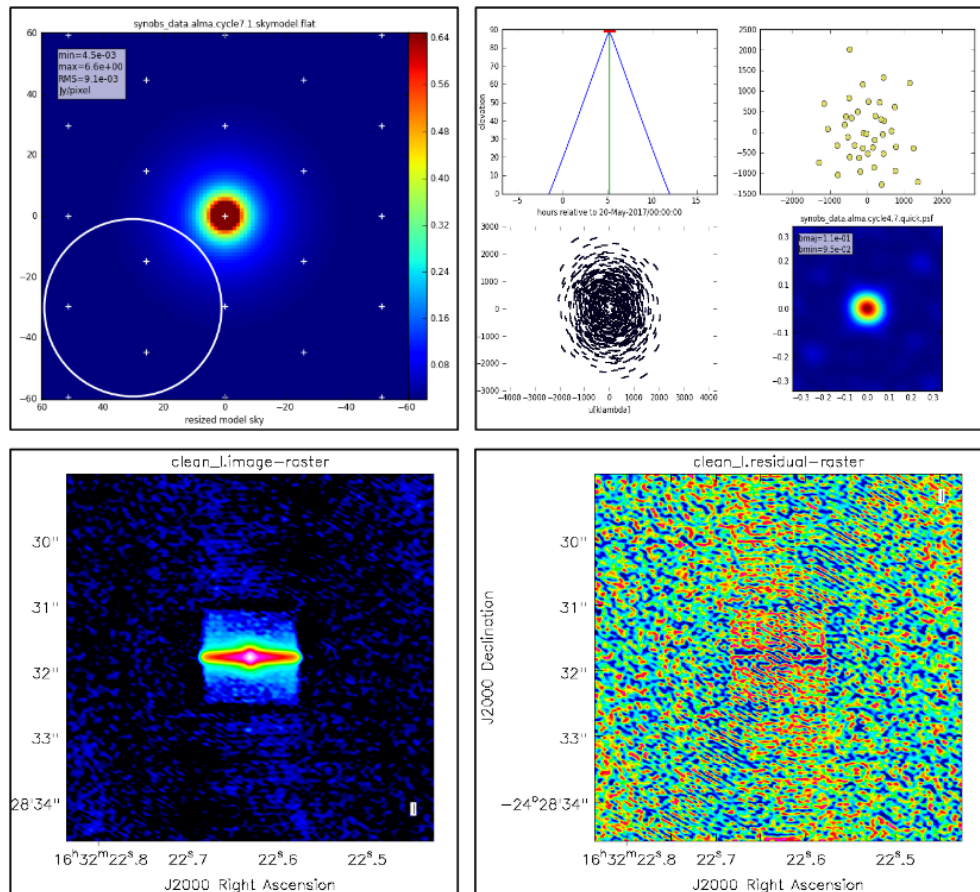


Figure 4.8: Diagnostic plots of the two main steps involved in an interferometric synthetic observation: simobserve (top row) and tclean (bottom row). The first (upper left) panel is displayed at the beginning of execution, to show what's the sky coverage needed given the model size and the field of view. Second panel (top right) show information about the source elevation, antenna array, uv -coverage and PSF. Third (bottom left) panel shows the end result of tclean, i.e., the cleaned map, using a default template cleaning mask. The fourth (bottom right) panel show the residuals of the cleaning process.

tained from the models comes from a dust population of $100\ \mu\text{m}$ sized silicate-graphite grains. However, this maximum fraction reaches values no larger than 0.2% from the output of the ideal intensity models (from the radiative transfer code). After feeding this model to the CASA synthetic observation module, mimicking the corresponding ALMA and JVLA observing setups, no polarized intensity is detected above the corresponding sensitivity levels. This means, that based on our results, self-scattering is unlikely to be the responsible mechanism for the observed polarization towards IRAS 16293 B. Future projects, see below, should focus on studying the polarization produced by dust alignment with either the underlying velocity, radiation or magnetic field in order to further characterize the polarization observed.

AREPO Protostellar Core

The Synthesizer has also been used to post-process magneto-hydrodynamic simulations of protostellar core formation, using the code AREPO. These simulations are performed by a PhD student at MPA, Alex Mayer, on the aim to test the newly-created interface between the Synthesizer and AREPO snapshots. The example shown serves more as a testing box, or a proof-of-concept than a science case. No further science related to the observability of modelled phenomena has been done with this simulation, however, this certainly opens a new window for AREPO users to easily couple their simulations with observations at no extra cost. All of these Synthesizer commands can be added at the end of the simulation post-processing scripts. This comes particularly handy when generating predictions for observational proposals. All intermediate results from the gridding of the particle/cell-center locations, the 2D plotting and 3D rendering, the raytracing and the final ALMA observations are shown in Fig. 4.9, and can be reproduced with the following command

```
$ synthesizer --grid --source arepo --sphfile snap_070.hdf5 --temperature --
  show-grid-2d --show-grid-3d
```

Magnetic field morphologies in the high-mass star-forming region G31.41

The Synthesizer is also currently being used to characterize the morphology of the magnetic field in the high-mass star forming clump G31.41+031 (see Fig. 4.10). This source is one of the first high-mass star forming regions suggested to be threaded by an hourglass magnetic field, shown by early SMA 0.89 mm observations (Girart et al. 2009). However, this observed hourglass field seem to be completely misaligned from the velocity axis, by approximately 90° (Cesaroni et al. 2011 and Moscadelli et al. 2013). More recent ALMA 1.3 mm observations (Beltran et al. 2019) support the same scenario but their vector angles mismatch those observed at 7 mm JVLA observations (Sia et al., priv. comm.). The magnetic field derived from the 7 mm polarization vectors is indeed parallel to the outflow orientation and has a much larger spatial coverage than the ALMA observation, where the vector angles remain almost uniform even up to 0.4 pc. The ALMA observations only cover the central 0.1 pc, where the vector flip occurs. The aim of the project is to understand why do polarization vectors flip within the central 0.1 pc when observed at 1.3 versus 7 mm. One possible scenario (Siu et al. in prep.) is that the central 0.1 pc, when targeted by ALMA, have a higher optical depth than the larger 0.4 pc scales observed at 7 mm,

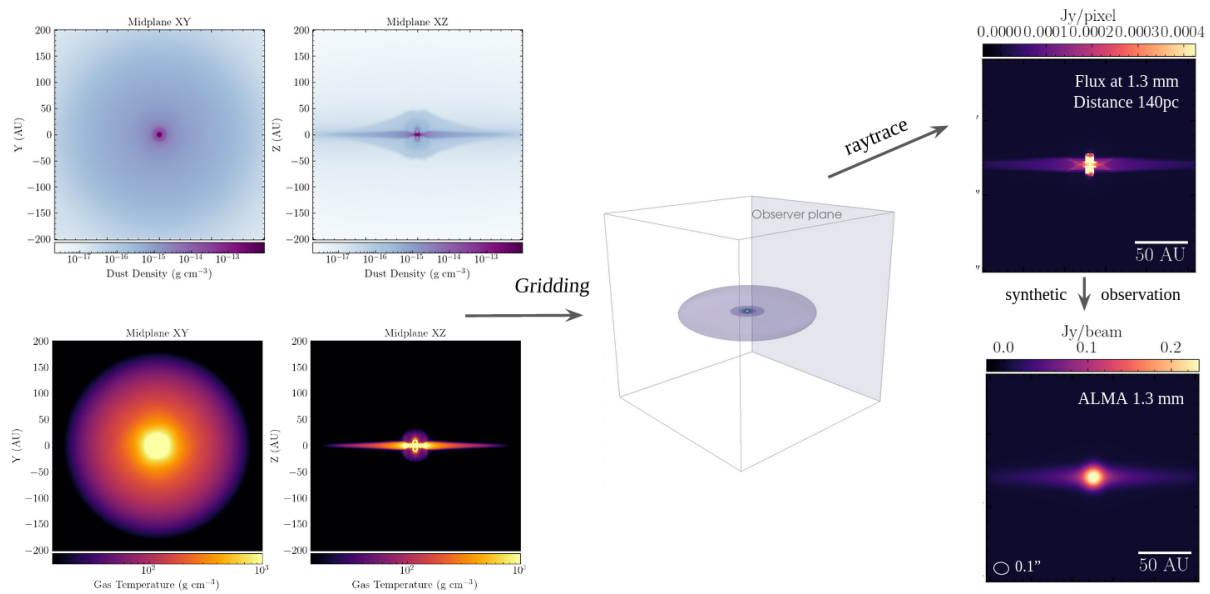


Figure 4.9: AREPO simulation of protostellar core formation post-processed using the Synthesizer. All the intermediate results included in the synthetic observations are shown here for illustration. The magneto-hydrodynamic simulations are performed by Alex Mayer (PhD student at MPA) using the code AREPO and reproduced here with permission from the author.

changing from optically thin to optically thick emission. The polarized emission coming from an optically thick medium can actually be produced by a different phenomenon than the commonly assumed case of emission from aligned grain. The latter assumes that elongated grains align their major axis perpendicular to the magnetic field and produce E-vectors perpendicular to the field lines. A 90° rotation is then assumed to derive the B-field vectors, but the picture changes if the polarization is produced in the form of absorption instead of emission. This can happen towards optically thick regions that reduce the net polarization of light and emit unpolarized light. This light is then absorbed by foreground envelope grains preferentially along the grain's long axis, letting polarized light pass through parallel to the field lines, and potentially explaining the central outflow-magnetic field misalignment. In order to test this scenario, Siu et al. (in prep.) is using the Synthesizer with a power-law density model and an hourglass field (both included in the code), to simulate the 1.3 and 7 mm observations (see Fig. 4.10).

4.4.1 Data visualization

For users not interested in generating synthetic observations, the Synthesizer can also be used as a standalone visualization tool. It relies on the Python libraries Matplotlib and Mayavi for the 2D and 3D plotting, respectively. It has already been mentioned how to tell the code to display intermediate plots between all the modules. Here, we describe how can the code be used without the need to run any of the of the main modules `--grid`, `--raytrace`, `--opacity` or `--synobs` again. If a model has been created, but no display option has been given, plotting options alone can

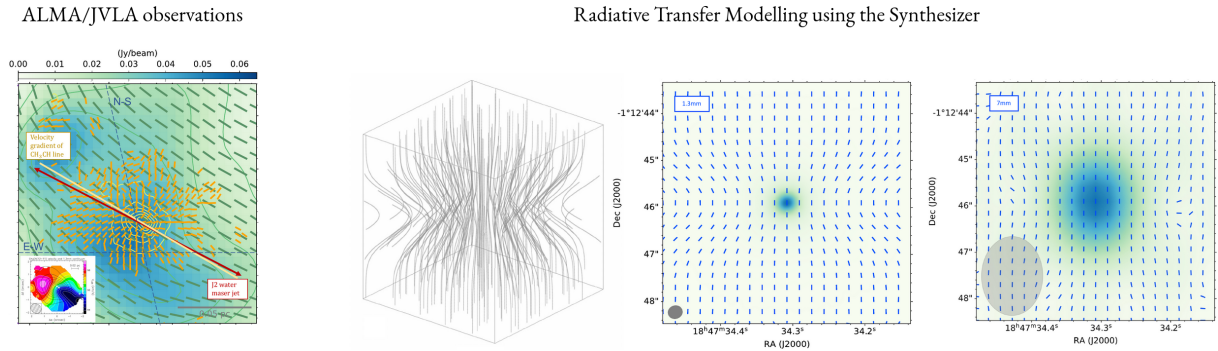


Figure 4.10: (left) ALMA/JVLA polarization observations of G31.41+031 at 1.3 and 7 mm. (right) Polarized radiative transfer modelling from analytical models using the Synthesizer. Reproduced with permission from Siu et al. (in prep.)

be provided in a new call and the Synthesizer will read from the lastly-created grid, FITS or datatable files. This applies for all `--show-*` options.

Midplane slices and 3D rendering of already existing models

All model grids, regardless of them being analytical prescriptions or full hydro simulations, can be visualized using the Synthesizer without the need to run all modules again. The visualization options allow to also open previously created grid files, such as, `dust_density.inp` and `dust_temperature.inp` without having to recalculate them, as

```
$ synthesizer --show-grid-2d --show-grid-3d
```

Optically thick $\tau = 1$ surface

The Synthesizer can also be used to visualize the optically thick $\tau = 1$ surface of your model, if it contains one. An example of this feature is shown in Fig. 4.11 for a massive SPH protostellar disk, as the one shown in Figs. 4.5 and 4.7. This is particularly useful when studying optically thick physical models that don't seem to show the embedded features we expect to see. When dealing with non-homogeneous optically thick models, it is important to understand the depth of the $\tau = 1$ surface along the line-of-sight because structures beyond this surface are in principle present but are not visible. Visualization of this surface can be done for any already created grid model, without the need to run any of the main modules, as

```
$ synthesizer --show-grid-3d --tau
```

4.5 Current and future code features

Below I summarize all the features currently implemented and tested in the code. I also provide a list of features currently implemented but in their beta status, i.e., lacking robust testing and

Optically thick surface at 1.3mm
Optically thick surface at 3mm

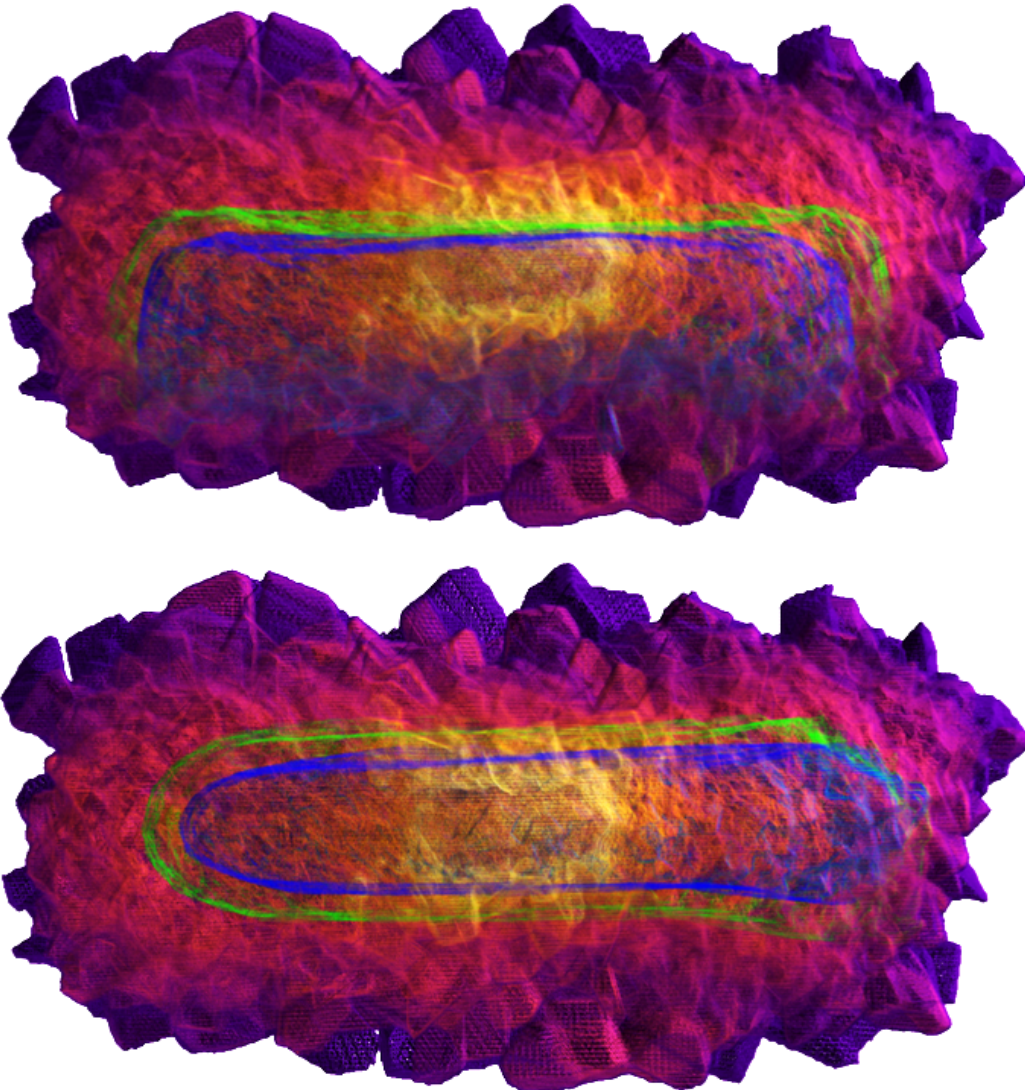


Figure 4.11: 3D rendering of the dust temperature and $\tau = 1$ surfaces along a face-on (top) and edge-on (bottom) projections for an SPH protostellar disk. This is one of the visualization modes obtained with the options `--tau` and `--show-grid-3d`.

problem catching. After that, I provide a list of features planned to be implemented in the future, that will make the code suitable for a wider range of science cases. At the end of this section, Table 4.1 lists all the possible command line arguments along with a short description, similar to what can be obtained with the command `$ synthesizer --help`.

Currently implemented features:

- Generation of monochromatic synthetic continuum images
- Generation of synthetic images with polarization by scattering
- Generation of synthetic images with polarization by dust alignment
- Gridding of particle locations and physical quantities onto a Cartesian regular gridding
- 2D plotting of the vector field stream lines from both analytical prescriptions and entered simulation vector fields
- 3D visualization of simulation outputs and analytical models
- Visualization of the $\tau = 1$ surface within the model, for optically thick models.
- Calculation of dust opacity tables for different grain sizes and materials, including full scattering matrices for polarization and alignment efficiencies.
- Support for realistic observations mimicking currently existing single-dish radio telescopes
- Support for realistic radio interferometric observations, with the option to vary antenna array configurations to achieve different angular resolutions

Current features in beta:

- Visualization of the vector field streamlines within the 3D rendered scene
- Creation of user-defined analytical models and vector fields
- Automatic detection of an appropriate antenna array configuration that would deliver a user-desired angular resolution
- Interfaces for simulation outputs from grid-based codes.
- Option to use spherical grids instead of the default regular cartesian grids.
- Mixing of optical constants (Bruggeman or Maxwell-Garnett Mixing).

Future implementations:

- Addition of new interfaces for different commonly-used hydro grid-based codes, such as, RAMSES, ENZO, ATHENA++, FLASH.

- Addition of new interfaces for different commonly-used hydro particle-based codes, such as, PHANTOM and GRADSPH.
- Addition of support for molecular line observations
- Addition of more tailored analytical models for most disks from the DSHARP survey along with PDS-70.
- Addition of toy analytical models used to test polarization, as those from Kataoka et al. (2015)
- Addition of ready-made common dust mixtures, such as DSHARP (Birnstiel et al. 2018) and DIANA (Woitke et al. 2016).
- Addition of support for telescopes outside of the sub-/millimeter range, such as, Herschel, Hubble, JWST and VLT instruments.

Option	Description
-h, --help	Show this help message and exit
-g, --grid	Create an input grid for the radiative transfer
--model MODEL	Keyword for a predefined density model.
--sphfile SPHFILE	Name of the input SPH file (snapshot from a particle-based code).
--amrfile AMRFILE	Name of the input AMR grid file (snapshot from a grid-based code).
--source CODENAME	Name of the code used to generate the input file.
--ncells NCELLS	Number of cells in every direction.
--bbox BBOX	Size of the half-length of a bounding box in au.
--rout ROUT	Size of the outer radial boundary in au (i.e., zoom in).
--g2d G2D	Set the gas-to-dust mass ratio.
--vector-field FIELD	Create a vector field for alignment of elongated grains.
--temperature	Write the dust temperature from the model.
--show-particles	Render the SPH particle positions weighted by density.
--show-grid-2d	Plot the midplane of the newly created grid.
--show-grid-3d	Render the new Cartesian grid in 3D.
--vtk	Call RADCM3D to create a VTK file of the newly created grid.
--render	Visualize the VTK file using ParaView.
-op, --opacity	Call dustmixer to generate a dust opacity table.
--material MATERIAL	Dust optical constants. Can be a predefined key, a path or a URL.
--amin AMIN	Minimum value for the grain size distribution.
--amax AMAX	Maximum value for the grain size distribution.
--na NA	Number of size bins for the logarithmic grain size distribution.
--q Q	Slope of the grain size distribution in logspace.
--nang NANG	Number of scattering angles used to sample the dust efficiencies.
--show-opacity	Plot the resulting dust opacities.
--show-nk	Plot the input dust optical constants.
--nopb	Disable printing of an opacity progress bar. Useful when logging to file.
-mc, --monte-carlo	Call RADMC3D to raytrace the new grid and plot an image.
--nphot NPHOT	Set the number of photons for scattering and thermal Monte Carlo.
--nthreads NTHREADS	Number of threads used.
-rt, --raytrace	Call RADMC3D to raytrace the new grid and plot an image
--lam LAM	Wavelength used to generate an image in units of micron
--lmin LMIN	Lower end of the wavelength grid in microns.
--lmax LMAX	Upper end of the wavelength grid in microns.
--nlam NLAM	Number of wavelengths to build a logarithmically spaced grid.
--npix NPIX	Number of pixels per side of new image
--incl INCL	Inclination angle of the grid in degrees
--phi PHI	Inclination angle over a second axis in degrees
--sizeau SIZEAU	Physical size of the image in AU

Table 4.1: List of all possible command line arguments to be passed to the synthesizer, along with a minimal description. This table is generated from the output of the command `$ synthesizer --help`.

--distance DISTANCE	Physical distance in pc, used to convert fluxes into Jy/pixel.
--star x y z Rstar Mstar Teff	6 parameters used to define a radiating star (values should be given in cgs)
--tau	Generate a 2D optical depth map.
--tau-surf tau	Generate a 3D surface at optical depth = tau.
--show-tau-surf	Render the 3D the optical depth = tau surface.
--polarization	Enable polarized RT and full scattering matrix opacity tables
--alignment	Enable polarized RT of thermal emission from aligned grains.
--noscat	Turn off the addition of scattered flux to the thermal flux
--sublimation SUBLIMATION	Percentage of refractory carbon that evaporates from the dust
--sootline SOOTLINE	Temperature at which carbon is supposed to sublimate
--dust-growth	Enable dust growth within the soot-line
--show-rt	Plot the intensity map generated by ray-tracing
--radmc3d [RADMC3D ...]	Additional commands to be passed to RADMC3D.
-so, --synobs	Call CASA to run a synthetic observation from the new image
--dont-observe	Skips CASA's Simobserve task.
--dont-clean	Skips CASA's tclean task to clean and image simobserve's output.
--dont-export	Don't export tclean's output as a fits image.
--obs-time OBS_TIME	Set the observing time in hours. Default is 1h.
--resolution RESOLUTION	Set a desired angular resolution in arcseconds.
--obsmode int,sd	Whether to observe with a radio interferometer or a single-dish.
--telescope {alma,aca,vla,sma, noema,atca,meerkat,vlba}	Radio telescope to use. Default: ALMA
--script SCRIPT	Name, path or url to a CASA script for the synthetic observations.
--use-template	Use one of the template CASA scripts contained within the synthesizer.
--show-synobs	Plot the ALMA/JVLA synthetic image generated by CASA.
-ow, --overwrite	Overwrite opacities, RADMC3D and CASA input files.
--quiet	Disable verbosity. Do not output anything.
--version	Show program's version number (v0.0.3) and exit.

Table 4.2: Continuation of Table 4.1.

Chapter 5

Summary and future

5.1 Work summary

In this thesis, I have studied the physical structure and dust population of the Class 0 protostar IRAS 16293-2422 B by comparing real and synthetic dust continuum and polarization observations.

In Chapter 2 I have used ALMA high-resolution continuum observations at 1.3 and 3 mm towards IRAS 16293 B. The protostellar disk has a radius of ~ 50 au and the resolution of both observations is 12 and 6.5 au, respectively. These are the two first observations that resolve the disk, revealing a deviation from a smooth Gaussian profile. They rather reveal a previously unseen brightness asymmetry with very high peak brightness temperatures of 290 and 470 K at 1.3 and 3 mm, respectively. The new millimetric observations presented in Chapter 2 also allow to resolve the spectral index distribution within the disk, showing values less than 2 (the optically thick limit) in the central ~ 20 au region. My aim was to understand the nature of these high brightness temperatures, the lopsided distribution and the low spectral index via radiative transfer modelling. I used two different disk models generated from the late stages of two different simulations of prestellar core collapse and disk formation. The first model, the MHD disk, included full non-ideal magnetohydrodynamic treatment of the gas and generates a marginally gravitationally unstable but smooth disk with a realistic magnetic field. The second model, the RHD disk, did not include magnetic fields but did include radiation transport along with the hydrodynamics. The final gas temperatures achieved by the RHD disk model ($\gtrsim 400$ K) were almost 5 times higher (see Figs. 2.2 and 2.3) than the MHD disk thanks to the more careful treatment of the thermodynamics. This included source terms from accretion heating, shock heating and dust cooling, whereas the MHD model derived its temperature from a barotropic equation of state, with gas temperatures peaking at around 200 K. When comparing both disk models to the observations, using different maximum dust grain sizes (1 and $10 \mu\text{m}$), different disk inclinations and different protostar luminosities, I found that only the high gas temperatures provided by the RHD model, regardless of the parameter combination, could reproduce the high brightness temperatures observed with ALMA. This suggests that simplified thermodynamical treatments of disk formation simulations might underestimate the disk true temperatures and

affect the comparison with observations. Similar results were simultaneously and independently found by Xu & Kunz (2021a) based on radiation-MHD simulations using Athena++. Different disk inclinations did not help to recreate the brightness asymmetry as I initially expected if due to self-obscuration. The simulated flux profiles for inclinations from 0 up to 40° did not show a significant shift of the peak compared to the observations. Finally, the observed low spectral index could be indeed reproduced by the two disk models given they are both optically thick and hotter towards the midplane. I was able to reproduce the spectral index purely by optically thick thermal emission, even without the need to account for scattering effects or millimetric grains. This was ensured by keeping the albedo negligible using a maximum grain size of 10 μm . Smaller grain sizes ($a_{\text{max}} = 1 \mu\text{m}$) were not able to reproduce the fluxes observed with ALMA, implying slight grain growth from MRN interstellar medium dust. The fact that only the massive (0.3 M_{\odot}) RHD disk could reproduce the high fluxes, suggested that we are in presence of a young hot and massive disk, massive enough to start to develop gravitational instabilities and substructures (e.g., spiral arms). The mechanical heating in the disk is sufficient and necessary to reproduce the observed high brightness temperatures. This heating dominated over the one produced by protostellar radiation alone.

In Chapter 3, I followed up on the work from Chapter 2 by increasing the data sample to more wavelengths (1.3, 3, 7, 9 & 18 mm) and including polarization data at 1.3 and 7 mm. In this project I studied the effects of using maximum grain sizes larger than 10 μm . I modelled the fluxes generated by grains grown up to 100 and 1000 μm and compared them against our expanded dataset. Models with 100 μm and 1000 μm do also reproduce the fluxes at all wavelengths. The observations lie between the models with $a_{\text{max}} = 100 \mu\text{m}$ and 1000 μm , with differences between the observations and models within a factor of up to 2 towards the center. This implies that significant grain growth could be present in IRAS 16293 B. The composition of the dust used in this modelling is a mixture of silicates and graphites. The large brightness temperatures observed in IRAS 16293 B overcome the recently proposed sootline temperature of 300 K, suggesting that carbon sublimation from the dust might be happening within this disk. To study this scenario, I also experimented with modifying the dust composition by replacing part of the graphite amorphous carbon and compare with the observations. The sublimation of refractory amorphous carbon within the sootline (<10 au) results in a local decrease of the optical depth, due to both a reduction of the grain's mass and the decrease of graphite within the carbon budget, since graphite's opacity is larger than that of amorphous carbon. The lower optical depth produces higher fluxes because the emission traced is originated by deeper and hotter layers of the disk. However, the differences of the cases with and without sublimation are small (<10%). I have additionally tested the combined scenario of carbon sublimation and grain growth within this sootline. This idea was motivated by recent laboratory experiments showing that dry grains without icy mantles would enhance their stickiness and coagulation. To test this, I generated models with maximum grain sizes of 100 μm and the fiducial composition of silicates and graphites all around the disk, except for within the sootline. Within this zone, I increase the grain size to 1000 μm and changed the composition, to have a carbon budget split between graphite (20%) and amorphous carbon (80%), and keeping the silicate fraction constant since its sublimation temperature is much higher (~2100 K). This combined picture of grain growth and carbon sublimation did indeed provide a closer match to the IRAS 16293 B observations,

suggesting that if grain growth is happening in this Class 0 disk, is possibly happening within the inner hot regions. I finally also studied the effects of polarization by self-scattering in the models, in order to assess if I can use it as an independent proxy of grain growth, as it has been previously suggested from ALMA/JVLA polarization observations. The results show that the polarized flux generated by scattering in such a massive and optically thick disk is one-order-of-magnitude lower than that observed. This means that the observed polarization is unlikely to be produced by dust self-scattering effects and therefore should be originated by a different phenomena (see sections 3.5.3 and 5.2), such as grain alignment with either the magnetic field, velocity field, radiation field or even the polarization reversal effect of large millimetric elongated grain. We note that it is also possible that others more ad-hoc dust compositions could potentially enhance the polarization by self-scattering from that obtained in this work. However, the predicted extremely high optical depths might prevent this. The results in this chapter highlight further the need to understand better the polarization mechanisms in young Class 0 disks, which might be certainly different from the mechanisms producing polarized continuum emission in the more evolved Class II disks.

In Chapter 4, I have described and detailed the numerical tool developed over the course of this thesis. This is called, Synthesizer, and allows to easily generate synthetic observations from the command line, without the need to manually compute analytical or simulated physical models. This code is created as a collection of all the scripts and tasks used throughout all these projects, put them together into one single package. This tool is now publicly available, easy to use and capable of delivering publication-ready results. In a nutshell, the Synthesizer pipelines the creation of a physical model up to the generation of realistic telescope observations. User can create models either from an analytical prescription or from full 3D MHD simulation outputs, regardless of them being grid- or particle-based. This can then be fed to RADMC3D for the radiative transfer modelling, both in Monte-Carlo and raytracing modes. The Synthesizer does also include a module called DustMixer, which serves as a command line tool to create complex dust opacity tables. Users can experiment with the effects of varying the dust composition and grain size and also include full scattering matrices to account for dust polarization. The code finally pipes the output from the radiative transfer modelling into a realistic interferometric observations simulator using CASA. This last step allows to do a one-to-one comparison of the simulated phenomena against real ALMA or JVLA observations. Additionally, the Synthesizer serves as a standalone data visualization tool for users not interested in generating synthetic observations. It uses the Matplotlib and Mayavi Python libraries to visualize 2D slices of the model or to even full render it interactively in 3D.

5.2 Future research

The projects carried out over the course of a PhD thesis are by no means case-closing projects. The more you finely study a subject the more questions arise, and is therefore important to recognize the newly open questions of the field. In this section I would like to briefly describe two major pathways that I consider interesting and important to follow after the conclusion of this thesis. The first project aims to further constrain the origin of the polarization observed towards

IRAS 16293 B, given that the results from Chapter 3 on polarization by self-scattering not being able to reproduce the observed levels of polarization. The second project focuses rather on the companion protostars IRAS 16293 A1 and A2, and attempts to explain the origin of recently observed multiple dust peaks around the two protostars.

5.2.1 Model ALMA dust polarization images with synthetic models of magnetic grain alignment

The results of the radiative transfer modelling of IRAS 16293 B, from Chapter 3, left an open window regarding the origin of the observed polarization. Self-scattering in such a massive and optically thick disk is unlikely to be the mechanism responsible for it. The natural question is, what is it then? what is producing comparable polarization fractions (2-4%) with similar vector pattern (azimuthal within <100 au) at both 1.3 and 7 mm wavelengths. As previously discussed in section 3.5.3, one possible wavelength-independent polarization phenomenon is the alignment of elongated grains with the magnetic field lines. This allows to recover the field morphology by rotating the polarization E-vectors by 90° , under the assumption that we observe the optically thin thermal emission of these grains. If this is indeed the case in IRAS 16293 B, the E-vector azimuthal pattern observed by ALMA/JVLA would represent a radial magnetic field. Radial components of the field, could be observed on the scales that connect the protostellar disk with the northern dust bridge (connecting B with A1 and A2) on its East and West site (Sadavoy et al. 2018). It could also represent infalling material along the line of sight, given that IRAS 16293 B is a close to face-on disk, but it would contradict the expected toroidal magnetic field of a magnetized keplerian rotating disk. One possible explanation to the observed azimuthal E-vectors is that these vectors are indeed tracing the magnetic field but in the form of polarized absorption, also known as dichroic extinction. This effect can naturally happen when the line-of-sight of this emission is optically thick (c.f., Ko et al. 2020). If this is the case, the central <100 au polarization would indeed trace a toroidal field, just without the need to rotate the vectors in order to infer the B-field. This idea can be fully tested making use of the Synthesizer to post-process MHD simulations of disk formation (Zhao et al. 2016, 2018). The current ALMA polarization data (Sadavoy et al. 2018) has an angular resolution of 25 au, which is more or less the region that our modelling suggest becomes highly optically thick ($\gtrsim 100$) at 1.3 mm. This means, that maybe the 100-50 au magnetic field is indeed radial and could flip to toroidal within even smaller scales ($\lesssim 30$ au). The vectors of the current ALMA data do become uniform within this central 30 au, but is likely to be the effect of limited resolution.

In Chapter 2, I presented MHD simulations that form a protostellar disk with such a magnetic field distribution (Zhao et al. 2018), which could be used as a starting point for the comparison with observations (see Fig. 5.1). On the observation side, I will potentially have PI Cycle 9 ALMA polarization observations (2022.1.00946.S; B grade) with higher resolution (~ 6 au) to resolve the inner 30 au region and find whether the polarization pattern remains toroidal or there are additional changes. On the radiative transfer side, I have already started to model the polarization maps of the MHD disk from Chapter 2 when observed from different angles and optical depths (see Fig. 5.1). Part of the calculations for this project are already done, which gives a good

starting point for this project.

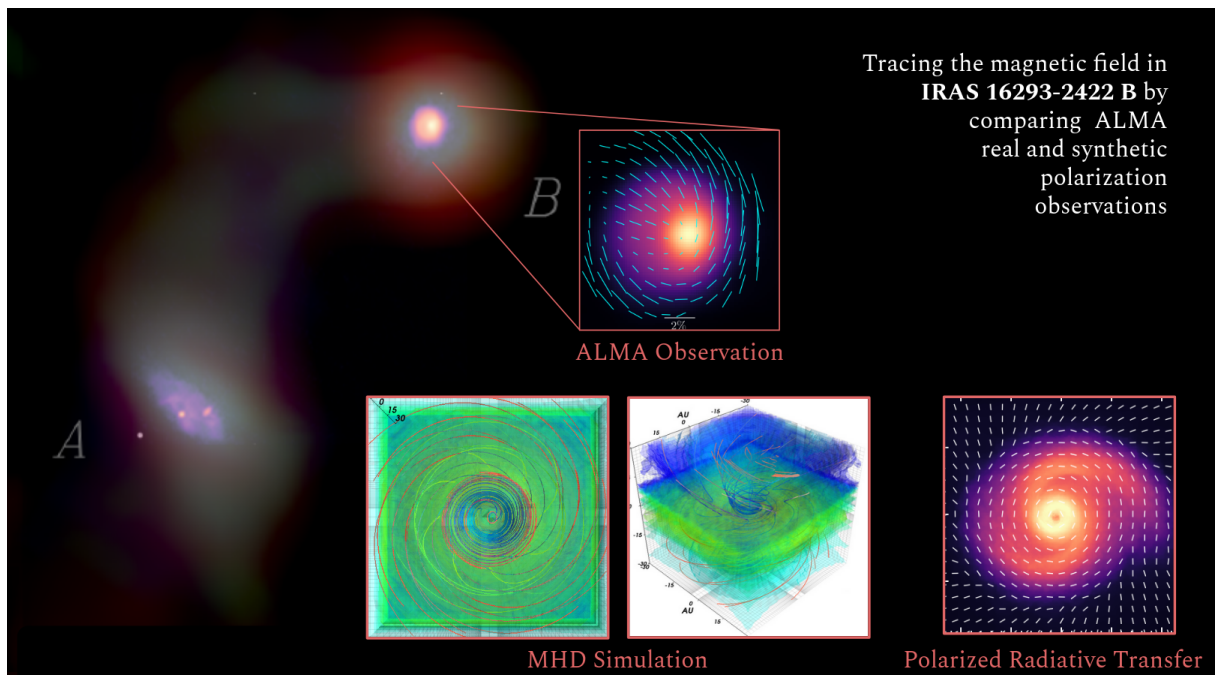


Figure 5.1: Science ideas for future research: Comparing my future high-resolution (~ 6 au) PI Cycle 9 polarization data from IRAS 16293 B with synthetic polarization maps from MHD simulations. The ALMA observations shown here represent polarization E-vectors as presented by Sadavoy et al. (2018). The MHD simulations from Zhao et al. (2018) reproduce realistic magnetic field morphologies during protostellar disk formation. The polarized radiative transfer example shown here, is generated using the RHD disk model from Chapter 2 and deriving the magnetic field direction from the velocity field, assuming flux-freezing.

5.2.2 Investigating the origin of hot dust spots in a young binary system

The Class 0 protostar I have studied during my thesis, IRAS 16293-2422 B, is actually part of a triple protostellar system, where the other two (A1 & A2) share a common circumbinary disk (Maureira et al. 2020). Recent high-resolution observations showed a couple of bright peaks around the two protostars (Figure 5.2), which have been suggested to represent a higher protostar multiplicity (Oya & Yamamoto 2020). The recent work from Maureira et al. (2022) showed that such hot spots are indeed temperature enhancements and not additional protostars. They suggest that a possible scenario to explain such temperature enhancements, is that A1 and A2 produce spiral arms within their circumbinary disk as they orbit each other (see right panel in Fig. 5.2) and then the rapidly compressed gas produce shock fronts along the arms. This idea can be tested with numerical simulations. As a starting point, I began working with the circumbinary disk setup developed by Moody et al. (2019) and used to study binary black hole formation. These simulations study the temporal evolution of the binary system and their common disk by

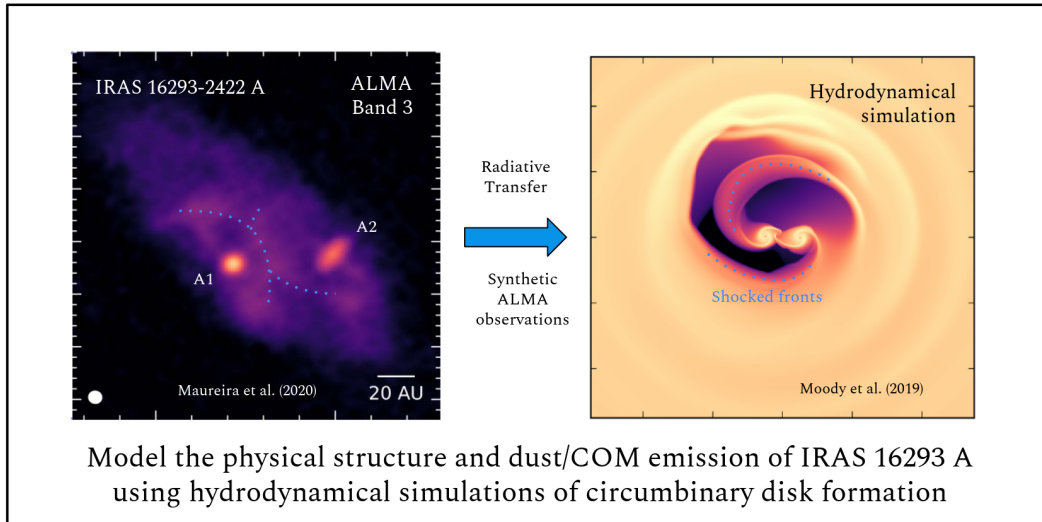


Figure 5.2: Science ideas for future research: Comparison of ALMA images (left) of the Class 0 protostellar system IRAS 16293-2422 A Maureira et al. (2020), to Hydrodynamical simulations (right) of circumbinary disk evolution from Moody et al. (2019). The goal is to understand the origin of the clumpy dust and molecular emission.

examining the different torques exerted on the system. After several orbits the interaction of the gas and the orbiting protostars give birth to two main spiral arms, whose wave fronts produce gas shocks that should locally raise the gas temperature. However, the simulations performed by Moody et al. (2019) are locally isothermal and are unable to provide a realistic temperature distribution. Future research should focus on the implementation of heating and cooling source terms within the numerical setup, using the MHD code Athena++, that would allow to follow the thermodynamical evolution of the system. The main sources to consider would be accretion and shock/compression heating, stellar radiation heating and dust thermal cooling. Future versions of the Synthesizer will support the post-processing of hydro simulation with Athena++. The coupling of a more detailed hydrodynamical setup with synthetic observations will allow to compare the simulations against the continuum and line (COMs) emission of IRAS 16293 A (Maureira et al. 2020; Oya & Yamamoto 2020). This could provide a possible scenario for the presence of clumped COMs emission originated by molecule desorption from locally heated grains (see Fig. 5.2). Once implemented the thermal source terms within the setup, I can compare the results to my ~ 6 au resolution PI VLA Band Ka observations and 6 au PI Cycle 9 ALMA Band 6 (and archival Band 3) observations, to constrain the nature of these hot spots through the eye of ALMA and VLA. If the comparison shows that shock heating is able to reproduce the hot spots in the binary we would have found another case in which mechanical heating needs to be taken into account at the early stages. Without considering this, realistic temperatures are not achieved, preventing a full description of the structure of young Class 0 disks and accurate determination of key parameters such as disk masses.

Appendix A

Complementary Material for Chapter 2

A.1 Spectral index

The slope of the spectral energy distribution (namely, the spectral index α) in logspace, between ν_1 and ν_2 (for $\nu_1 > \nu_2$), can be obtained as

$$\alpha = \frac{\log(I_1) - \log(I_2)}{\log(\nu_1) - \log(\nu_2)}, \quad (\text{A.1})$$

with I_1 and I_2 the specific intensities at frequencies ν_1 and ν_2 , respectively. In the Rayleigh-Jeans regime, the relation between the intensity and the brightness temperature T_b at frequency ν is given by

$$I_\nu = \frac{2k_B}{c^2} \nu^2 T_b, \quad (\text{A.2})$$

with k_B the Boltzmann constant. Since $I \propto \nu^2 T_b$, then equation A.1 can be expressed as

$$\alpha = \frac{\log(\nu_1^2 T_{b,1}) - \log(\nu_2^2 T_{b,2})}{\log(\nu_1) - \log(\nu_2)}, \quad (\text{A.3})$$

$$= \frac{2 \log\left(\frac{\nu_1}{\nu_2}\right) + \log\left(\frac{T_{b,1}}{T_{b,2}}\right)}{\log\left(\frac{\nu_1}{\nu_2}\right)}, \quad (\text{A.4})$$

$$= 2 + \frac{\log(T_{b,1}) - \log(T_{b,2})}{\log(\nu_1) - \log(\nu_2)}, \quad (\text{A.5})$$

thus,

$$T_{b,1} \begin{cases} \geq T_{b,2} & , \alpha \geq 2 \\ < T_{b,2} & , \alpha < 2 . \end{cases}$$

This last inequality tells us that a spectral index observed to be lower than 2 means that the brightness temperature at higher frequency is lower than at lower frequency, which is the opposite to what is expected for a black-body radiator at a single temperature. In our observations this

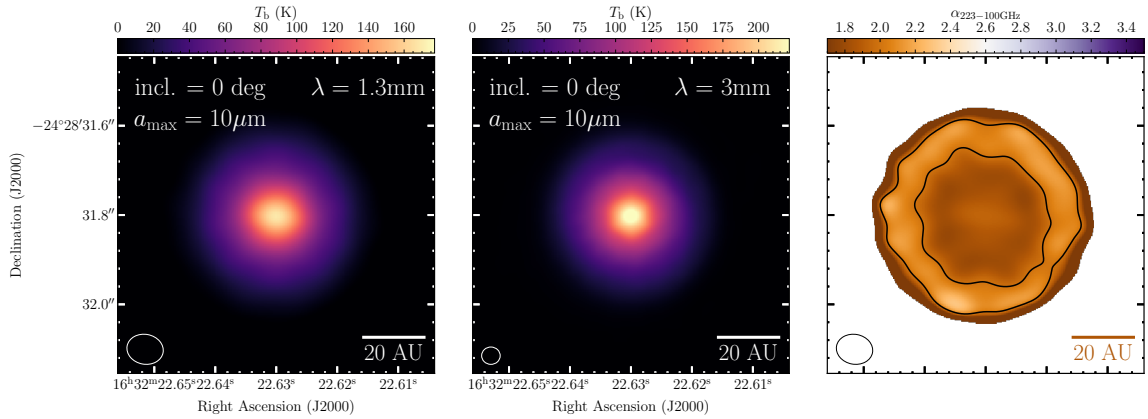


Figure A.1: Synthetic brightness temperature maps at 1.3 and 3 mm along with the spectral index for the MHD disk formation model from (Zhao et al. 2018), described in section 2.3.1. A similar behaviour is observed as compared to the RHD gravitationally unstable model, in which the spectral index (α) is observed to decrease toward the center of the disk. The contours in the rightmost panel indicate $\alpha = 1.7$ and 2, inside-out.

low value of α can be explained by the two wavelengths tracing optically thick ($T_b \lesssim T_{BB}$) layers at different temperatures. Moreover, since the opacity in the Rayleigh-Jeans regime decreases as a function of frequency ($\kappa \propto \nu^{\alpha-2}$), then the surface at $\tau = 1$ traced by the 3 mm observation lies deeper into the disk as compared to that traced at 1.3 mm. This is indicative of the inner regions of the disk being warmer than the outer regions.

A.2 Spectral index for the MHD disk model

To complement the analysis presented in section 2.5.2, we have also generated the 1.3 mm, 3 mm and spectral index maps for the MHD disk formation model described in section 2.3.1. The results are shown in Fig. A.1 in the same layout as Figs. 2.1 and 2.7. We observed a similar tendency as compared to the RHD model in which the spectral index falls to around 1.8 toward the densest parts of the model. This implies that both models considered in this study, are capable of reproducing the low values of α expected from early disks with a midplane at higher temperatures than the outer layers.

A.3 Toomre Q parameter for both disk models

In Fig. A.2 we show the Toomre parameter for the two disk models considered here, the RHD and MHD disk. Both disks are gravitationally unstable and susceptible to non-axisymmetric perturbations in the regions where $Q \lesssim 1.7$ (Durisen et al. 2007), which is between 7 and 20 au for the RHD disk and between 8 and 25 au for the MHD, with a small exception within a radius of

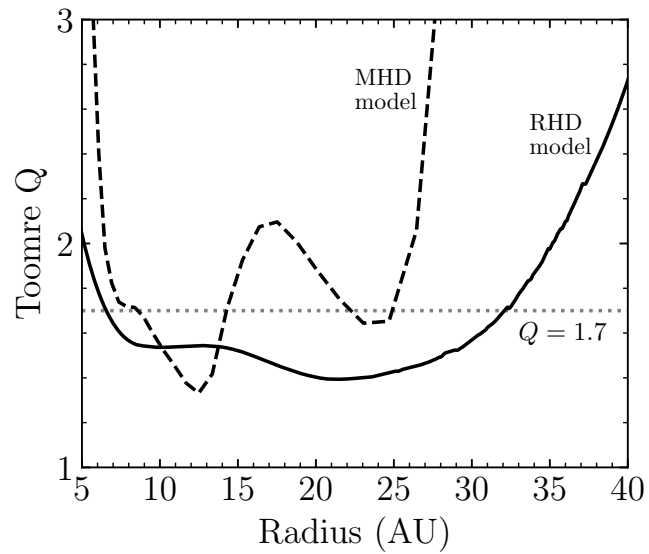


Figure A.2: Toomre Q parameter of both disk models. The RHD model has a $Q \lesssim 1.7$ at radii larger than 7 au, with a minimum value of 1.4 at 20 au. The MHD disk also reach values lower than 1.7 between 8 and 25 au. In spite of the spiral arms being prominent in only one of the two models (RHD), both disk are actually gravitationally unstable.

15 to 22 au, but still remaining under $Q=2$. In spite of the spiral arms being prominent in only one of the two models (RHD), both disk are actually gravitationally unstable.

Appendix B

Complementary Material for Chapter 3

B.1 The DustMixer: a command-line tool to generate dust opacities

The DUSTMIXER reads in tabulated optical constants n and k (also called refractive indices) for a given material. It interpolates the entered values over a user-defined wavelength grid and extrapolate if necessary. The extrapolations are done as a constant and a power-law for both the lower and upper wavelength bounds, respectively. Then, it uses the BHMIE algorithm (Bohren & Huffman 1983) to convert these constants into extinction and scattering dust efficiencies Q_{ext} and Q_{sca} , and also scattering matrix components, for all wavelengths and a single grain size. This algorithm calculates scattering efficiencies by assuming that re-emitted (scattered) photons can be modelled as the expansion of vector spherical harmonics. This calculation involves solving infinite Riccati-Bessel functions and is highly-computationally expensive. The larger the grain size compared to the wavelength, the more terms need to be added in the series and therefore the longer the calculation. The SYNTHESIZER employs a multiprocessing scheme to calculate this efficiencies within minutes, for a proper resolution (200 wavelengths and 200 grain sizes, see Fig. 3.3). To finally obtain dust opacities, all single grain size efficiencies are integrated over a power-law size distribution within a minimum a_{min} and maximum a_{max} grain size, for a given power-law slope q .

To combine different dust compositions several mixing methods exists in the literature. Some of them directly mix the refractive indices using mixing rules, such as the Bruggeman or Maxwell-Garnet rules (see e.g., Birnstiel et al. 2018), and create a new homogeneous sphere of mixed material to calculate the opacities. Other methods use effective medium theories and consider layered dust grains, composed of a core and a mantle (e.g., Ossenkopf 1991; Ossenkopf & Henning 1994) to calculate the opacities of grains with different core-mantle volume ratios. The DUSTMIXER provides support for both mixing techniques. However, in this work we calculated opacities per material and combined them as a sum weighted by their mass fractions (see section 3.3.4), meaning, different materials coexist within the grid cells and lead to a net opacity, rather than merging into an alloy. More details about this tool and its additional functionality can be found in its public repository.

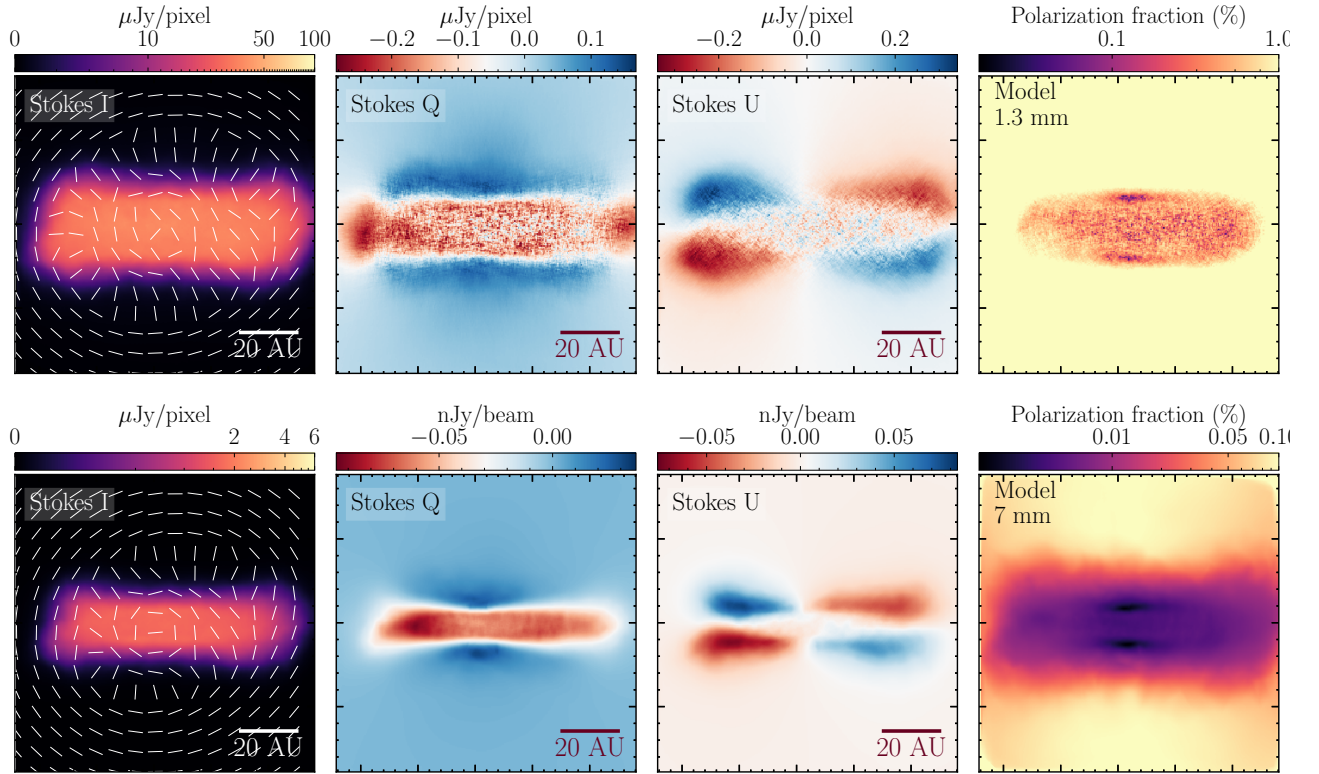


Figure B.1: Radiative transfer models of self-scattering at 1.3 (top) and 7 mm (bottom) for $a_{\max} = 100 \mu\text{m}$, shown in the upper and lower row, respectively. This figure is similar to Fig. 3.7 but for an edge-on projection of the same hot and massive disk model.

B.2 Polarization models by self-scattering for an edge-on hot disk

Here we present polarized radiative transfer models produced by self-scattering, similar to those presented in section 3.3.5 and shown in Fig. 3.7, but using a edge-on projection for the same disk model. Our aim is to provide more global predictions for self-scattering polarization in early embedded Class 0 disks than only the case of the nearly face-on disk on IRAS 16293 B. The results of this model are shown in Fig. B.1 for our fiducial dust population of silicates and graphites with $a_{\max} = 100 \mu\text{m}$, analogous to the case in Fig. 3.7. The polarization fraction of the edge-on models is slightly larger than for the face-on projection ($\lesssim 1\%$) but still low to match the ALMA and JVLA observations from Fig. 3.1.

Bibliography

- Agurto-Gangas, C., Pineda, J. E., Szűcs, L., et al. 2019, *A&A*, 623, A147
- Akiyama, E., Vorobyov, E. I., Baobabu Liu, H., et al. 2019, *AJ*, 157, 165
- Alves, F. O., Caselli, P., Girart, J. M., et al. 2019, *Science*, 366, 90
- Alves, F. O., Girart, J. M., Padovani, M., et al. 2018, *A&A*, 616, A56
- Alves, J. F., Lada, C. J., & Lada, E. A. 2001, *Nature*, 409, 159
- Andersson, B. G., Lazarian, A., & Vaillancourt, J. E. 2015, *ARA&A*, 53, 501
- Andre, P., Ward-Thompson, D., & Barsony, M. 1993, *ApJ*, 406, 122
- Andre, P., Ward-Thompson, D., & Barsony, M. 2000, in *Protostars and Planets IV*, ed. V. Mannings, A. P. Boss, & S. S. Russell, 59
- Andrews, S. M. 2020, *ARA&A*, 58, 483
- Andrews, S. M., Huang, J., Pérez, L. M., et al. 2018, *ApJ*, 869, L41
- Armitage, P. J. 2009, *Astrophysics of Planet Formation*
- Armitage, P. J. 2011, *ARA&A*, 49, 195
- Astropy Collaboration, Price-Whelan, A. M., Lim, P. L., et al. 2022, *apj*, 935, 167
- Avenhaus, H., Quanz, S. P., Garufi, A., et al. 2018, *ApJ*, 863, 44
- Bacciotti, F., Girart, J. M., Padovani, M., et al. 2018, *ApJ*, 865, L12
- Bacmann, A., André, P., Puget, J.-L., et al. 2000, *A&A*, 361, 555
- Ballering, N. P. & Eisner, J. A. 2019, *AJ*, 157, 144
- Barnard, E. E. 1907, *ApJ*, 25
- Bate, M. R. 2022, *MNRAS*, 514, 2145
- Bate, M. R., Bonnell, I. A., & Price, N. M. 1995, *MNRAS*, 277, 362

- Bergin, E. A. & Tafalla, M. 2007, *ARA&A*, 45, 339
- Bertoldi, F. & McKee, C. F. 1992, *ApJ*, 395, 140
- Birnstiel, T., Dullemond, C. P., Zhu, Z., et al. 2018, *ApJ*, 869, L45
- Bjorkman, J. E. & Wood, K. 2001, *ApJ*, 554, 615
- Blake, G. A., van Dishoeck, E. F., Jansen, D. J., Groesbeck, T. D., & Mundy, L. G. 1994, *ApJ*, 428, 680
- Blum, J. & Wurm, G. 2000, *Icarus*, 143, 138
- Bodenheimer, P., Yorke, H. W., Rozyczka, M., & Tohline, J. E. 1990, *ApJ*, 355, 651
- Bohren, C. F. & Huffman, D. R. 1983, *Absorption and scattering of light by small particles*
- Bolato, A. D., Wolfire, M., & Leroy, A. K. 2013, *ARA&A*, 51, 207
- Boley, A. C. & Durisen, R. H. 2008, *ApJ*, 685, 1193
- Boley, A. C., Mejía, A. C., Durisen, R. H., et al. 2006, *ApJ*, 651, 517
- Bonnor, W. B. 1956, *MNRAS*, 116, 351
- Boss, A. P. 2009, *ApJ*, 694, 107
- Bracco, A., Palmeirim, P., André, P., et al. 2017, *A&A*, 604, A52
- Brinch, C. & Hogerheijde, M. R. 2010, *A&A*, 523, A25
- Brunngräber, R. & Wolf, S. 2018, *A&A*, 611, A90
- Brunngräber, R. & Wolf, S. 2020, *A&A*, 640, A122
- Brunngräber, R. & Wolf, S. 2021, *A&A*, 648, A87
- Bryan, G. L., Norman, M. L., O'Shea, B. W., et al. 2014, *ApJS*, 211, 19
- Calcutt, H., Fiechter, M. R., Willis, E. R., et al. 2018a, *A&A*, 617, A95
- Calcutt, H., Jørgensen, J. K., Müller, H. S. P., et al. 2018b, *A&A*, 616, A90
- Caselli, P., Pineda, J. E., Zhao, B., et al. 2019, *ApJ*, 874, 89
- Cazaux, S., Tielens, A. G. G. M., Ceccarelli, C., et al. 2003, *ApJ*, 593, L51
- Ceccarelli, C., Castets, A., Loinard, L., Caux, E., & Tielens, A. G. G. M. 1998, *A&A*, 338, L43
- Ceccarelli, C., Loinard, L., Castets, A., Tielens, A. G. G. M., & Caux, E. 2000, *A&A*, 357, L9

- Chacón-Tanarro, A., Pineda, J. E., Caselli, P., et al. 2019, *A&A*, 623, A118
- Chandler, C. J., Brogan, C. L., Shirley, Y. L., & Loinard, L. 2005, *ApJ*, 632, 371
- Chen, H., Myers, P. C., Ladd, E. F., & Wood, D. O. S. 1995, *ApJ*, 445, 377
- Chiang, E. I. & Goldreich, P. 1997, *ApJ*, 490, 368
- Cieza, L. A., Casassus, S., Pérez, S., et al. 2017, *The Astrophysical Journal Letters*, 851, L23
- Cornwell, T. J. 2008, *IEEE Journal of Selected Topics in Signal Processing*, 2, 793
- Coutens, A., Commerçon, B., & Wakelam, V. 2020, *A&A*, 643, A108
- Cox, E. G., Harris, R. J., Looney, L. W., et al. 2018, *ApJ*, 855, 92
- Crimier, N., Ceccarelli, C., Maret, S., et al. 2010, *A&A*, 519, A65
- Dartois, E., Dutrey, A., & Guilloteau, S. 2003, *A&A*, 399, 773
- Das, H. K., Voshchinnikov, N. V., & Il'in, V. B. 2010, *MNRAS*, 404, 265
- Davis, Jr., L. & Greenstein, J. L. 1951, *ApJ*, 114, 206
- De Simone, M., Ceccarelli, C., Codella, C., et al. 2020, *ApJ*, 896, L3
- Dent, W. R. F., Pinte, C., Cortes, P. C., et al. 2019, *MNRAS*, 482, L29
- Devinat, M., Habart, É., Pantin, É., et al. 2022, *A&A*, 663, A151
- Dipierro, G., Lodato, G., Testi, L., & de Gregorio Monsalvo, I. 2014, *MNRAS*, 444, 1919
- Dolginov, A. Z. & Mitrofanov, I. G. 1976, *Ap&SS*, 43, 291
- Dominik, C., Min, M., & Tazaki, R. 2021, *OpTool: Command-line driven tool for creating complex dust opacities*, *Astrophysics Source Code Library*, record ascl:2104.010
- Dong, R., Vorobyov, E., Pavlyuchenkov, Y., Chiang, E., & Liu, H. B. 2016, *ApJ*, 823, 141
- Draine, B. T. 2003a, *ApJ*, 598, 1017
- Draine, B. T. 2003b, *ApJ*, 598, 1026
- Draine, B. T. 2011, *Physics of the Interstellar and Intergalactic Medium* (Princeton University Press)
- Draine, B. T. & Lee, H. M. 1984, *ApJ*, 285, 89
- Draine, B. T. & Malhotra, S. 1993, *ApJ*, 414, 632
- Draine, B. T. & Weingartner, J. C. 1997, *ApJ*, 480, 633

- Duan, H.-Y., Lai, S.-P., Hirano, N., & Thieme, T. J. 2023, *ApJ*, 947, 48
- Dullemond, C. P., Hollenbach, D., Kamp, I., & D'Alessio, P. 2007, in *Protostars and Planets V*, ed. B. Reipurth, D. Jewitt, & K. Keil, 555
- Dullemond, C. P., Juhasz, A., Pohl, A., et al. 2012, RADMC-3D: A multi-purpose radiative transfer tool, *Astrophysics Source Code Library*, record ascl:1202.015
- Dullemond, C. P., Küffmeier, M., Goicovic, F., et al. 2019, *A&A*, 628, A20
- Dunham, M. M., Stutz, A. M., Allen, L. E., et al. 2014, in *Protostars and Planets VI*, ed. H. Beuther, R. S. Klessen, C. P. Dullemond, & T. Henning, 195–218
- Durisen, R. H., Boss, A. P., Mayer, L., et al. 2007, in *Protostars and Planets V*, ed. B. Reipurth, D. Jewitt, & K. Keil, 607
- Dutrey, A., Guilloteau, S., Piétu, V., et al. 2017, *A&A*, 607, A130
- Dzib, S. A., Ortiz-León, G. N., Hernández-Gómez, A., et al. 2018, *A&A*, 614, A20
- Ebert, R. 1955, *ZAp*, 36, 222
- Elmegreen, B. G. 1989, *ApJ*, 344, 306
- Evans, M. G., Hartquist, T. W., Caselli, P., et al. 2019, *MNRAS*, 483, 1266
- Evans, M. G., Ilee, J. D., Boley, A. C., et al. 2015, *MNRAS*, 453, 1147
- Evans, M. G., Ilee, J. D., Hartquist, T. W., et al. 2017, *MNRAS*, 470, 1828
- Ferrer Asensio, J., Spezzano, S., Coudert, L. H., et al. 2023, *A&A*, 670, A177
- Forgan, D., Rice, K., Stamatellos, D., & Whitworth, A. 2009, *MNRAS*, 394, 882
- Fryxell, B., Olson, K., Ricker, P., et al. 2000, *ApJS*, 131, 273
- Galametz, M., Maury, A. J., Valdivia, V., et al. 2019, *A&A*, 632, A5
- Galván-Madrid, R., Liu, H. B., Izquierdo, A. F., et al. 2018, *ApJ*, 868, 39
- Garufi, A., Avenhaus, H., Pérez, S., et al. 2020, *A&A*, 633, A82
- Garufi, A., Benisty, M., Pinilla, P., et al. 2018, *A&A*, 620, A94
- Garufi, A., Podio, L., Bacciotti, F., et al. 2019, *A&A*, 628, A68
- Garufi, A., Podio, L., Codella, C., et al. 2022, *A&A*, 658, A104
- Gold, T. 1952, *MNRAS*, 112, 215

- Goldfarb, J. L. & Suuberg, E. M. 2008, *Journal of Chemical & Engineering Data*, 53, 670
- Greene, T. P., Wilking, B. A., Andre, P., Young, E. T., & Lada, C. J. 1994, *ApJ*, 434, 614
- Guillet, V., Girart, J. M., Maury, A. J., & Alves, F. O. 2020, *A&A*, 634, L15
- Guilloteau, S., Piétu, V., Chapillon, E., et al. 2016, *A&A*, 586, L1
- Gundlach, B., Schmidt, K. P., Kreuzig, C., et al. 2018, *MNRAS*, 479, 1273
- Habart, E., Boutéraon, T., Brauer, R., et al. 2021, *A&A*, 649, A84
- Hara, C., Kawabe, R., Nakamura, F., et al. 2021, *ApJ*, 912, 34
- Harries, T. J., Haworth, T. J., Acreman, D., Ali, A., & Douglas, T. 2019, *Astronomy and Computing*, 27, 63
- Harris, R. J., Cox, E. G., Looney, L. W., et al. 2018, *ApJ*, 861, 91
- Hartmann, L. 2002, *ApJ*, 578, 914
- Haworth, T. J., Glover, S. C. O., Koepferl, C. M., Bisbas, T. G., & Dale, J. E. 2018, *New A Rev.*, 82, 1
- Henning, T. & Stognienko, R. 1996, *A&A*, 311, 291
- Heney, L. G. & Greenstein, J. L. 1941, *ApJ*, 93, 70
- Hernández-Gómez, A., Loinard, L., Chandler, C. J., et al. 2019a, *ApJ*, 875, 94
- Hernández-Gómez, A., Sahnoun, E., Caux, E., et al. 2019b, *MNRAS*, 483, 2014
- Hildebrand, R. H. 1983, *QJRAS*, 24, 267
- Hirashita, H. & Li, Z. Y. 2013, *MNRAS*, 434, L70
- Hirashita, H. & Yan, H. 2009, *MNRAS*, 394, 1061
- Hoang, T., Cho, J., & Lazarian, A. 2018, *ApJ*, 852, 129
- Hoang, T., Tram, L. N., Phan, V. H. M., et al. 2022, *arXiv e-prints*, arXiv:2205.02334
- Hopkins, P. F. 2015, *MNRAS*, 450, 53
- Hsu, S.-Y., Liu, S.-Y., Liu, T., et al. 2020, *ApJ*, 898, 107
- Hull, C. L. H., Le Gouellec, V. J. M., Girart, J. M., Tobin, J. J., & Bourke, T. L. 2020, *ApJ*, 892, 152
- Hull, C. L. H., Plambeck, R. L., Bolatto, A. D., et al. 2013, *ApJ*, 768, 159

- Hull, C. L. H., Yang, H., Li, Z.-Y., et al. 2018, *ApJ*, 860, 82
- Ilee, J. D., Boley, A. C., Caselli, P., et al. 2011, *MNRAS*, 417, 2950
- Ilee, J. D., Forgan, D. H., Evans, M. G., et al. 2017, *MNRAS*, 472, 189
- Jacobsen, S. K., Jørgensen, J. K., van der Wiel, M. H. D., et al. 2018, *A&A*, 612, A72
- Jager, C., Mutschke, H., & Henning, T. 1998, *A&A*, 332, 291
- Jeans, J. H. 1902, *Philosophical Transactions of the Royal Society of London Series A*, 199, 1
- Jensen, S. S., Spezzano, S., Caselli, P., Grassi, T., & Haugbølle, T. 2023, arXiv e-prints, arXiv:2305.05932
- Jiao, W., Wang, K., Pillai, T. G. S., et al. 2023, *ApJ*, 945, 81
- Jørgensen, J. K., Bourke, T. L., Myers, P. C., et al. 2007, *ApJ*, 659, 479
- Jørgensen, J. K., Bourke, T. L., Nguyen Luong, Q., & Takakuwa, S. 2011, *A&A*, 534, A100
- Jørgensen, J. K., Favre, C., Bisschop, S. E., et al. 2012, *ApJ*, 757, L4
- Jørgensen, J. K., Müller, H. S. P., Calcutt, H., et al. 2018, *A&A*, 620, A170
- Jørgensen, J. K., van der Wiel, M. H. D., Coutens, A., et al. 2016, *A&A*, 595, A117
- Jørgensen, J. K., van Dishoeck, E. F., Visser, R., et al. 2009, *A&A*, 507, 861
- Kama, M., Min, M., & Dominik, C. 2009, *A&A*, 506, 1199
- Kataoka, A., Muto, T., Momose, M., Tsukagoshi, T., & Dullemond, C. P. 2016a, *ApJ*, 820, 54
- Kataoka, A., Muto, T., Momose, M., et al. 2015, *ApJ*, 809, 78
- Kataoka, A., Okuzumi, S., & Tazaki, R. 2019, *ApJ*, 874, L6
- Kataoka, A., Tsukagoshi, T., Momose, M., et al. 2016b, *ApJ*, 831, L12
- Kataoka, A., Tsukagoshi, T., Pohl, A., et al. 2017, *ApJ*, 844, L5
- Kawasaki, Y., Koga, S., & Machida, M. N. 2022, *MNRAS*, 515, 2072
- Kenyon, S. J. & Hartmann, L. 1987, *ApJ*, 323, 714
- Kimura, H., Wada, K., Kobayashi, H., et al. 2020, *MNRAS*, 498, 1801
- Kimura, H., Wada, K., Senshu, H., & Kobayashi, H. 2015, *ApJ*, 812, 67
- Ko, C.-L., Liu, H. B., Lai, S.-P., et al. 2020, *ApJ*, 889, 172

- Koga, S., Kawasaki, Y., & Machida, M. N. 2022, MNRAS, 515, 6073
- Körtgen, B., Bovino, S., Schleicher, D. R. G., et al. 2018, MNRAS, 478, 95
- Krasnopolsky, R., Li, Z.-Y., & Shang, H. 2010, ApJ, 716, 1541
- Kratter, K. & Lodato, G. 2016, ARA&A, 54, 271
- Kratter, K. M., Matzner, C. D., & Krumholz, M. R. 2008, ApJ, 681, 375
- Kraus, A. L., Ireland, M. J., Martinache, F., & Hillenbrand, L. A. 2011, ApJ, 731, 8
- Kress, M. E., Tielens, A. G. G. M., & Frenklach, M. 2010, Advances in Space Research, 46, 44
- Krumholz, M. R. 2015, arXiv e-prints, arXiv:1511.03457
- Kuffmeier, M., Dullemond, C. P., Reissl, S., & Goicovic, F. G. 2021, A&A, 656, A161
- Kuffmeier, M., Frimann, S., Jensen, S. S., & Haugbølle, T. 2018, MNRAS, 475, 2642
- Kuffmeier, M., Goicovic, F. G., & Dullemond, C. P. 2020a, A&A, 633, A3
- Kuffmeier, M., Reissl, S., Wolf, S., Stephens, I., & Calcutt, H. 2020b, A&A, 639, A137
- Kwon, W., Looney, L. W., Mundy, L. G., Chiang, H.-F., & Kemball, A. J. 2009, ApJ, 696, 841
- Körtgen, B., Bovino, S., Schleicher, D. R., Giannetti, A., & Banerjee, R. 2017, MNRAS, 469, 2602
- Labdon, A., Kraus, S., Davies, C. L., et al. 2021, A&A, 646, A102
- Lada, C. J. 1987, in Star Forming Regions, ed. M. Peimbert & J. Jugaku, Vol. 115, 1
- Laor, A. & Draine, B. T. 1993, ApJ, 402, 441
- Larson, R. B. 1969, MNRAS, 145, 271
- Lazarian, A. 1994, MNRAS, 268, 713
- Lazarian, A. 2003, Journal of Quantitative Spectroscopy and Radiative Transfer, 79-80, 881, electromagnetic and Light Scattering by Non-Spherical Particles
- Lazarian, A. 2007, J. Quant. Spectr. Rad. Transf., 106, 225
- Lazarian, A. & Hoang, T. 2007a, MNRAS, 378, 910
- Lazarian, A. & Hoang, T. 2007b, ApJ, 669, L77
- Le Gouellec, V. J. M., Andersson, B.-G., Soam, A., et al. 2023, arXiv e-prints, arXiv:2305.01908
- Le Gouellec, V. J. M., Hull, C. L. H., Maury, A. J., et al. 2019, ApJ, 885, 106

- Le Gouellec, V. J. M., Maury, A. J., Guillet, V., et al. 2020, *A&A*, 644, A11
- Lee, C.-F., Li, Z.-Y., Yang, H., et al. 2021, *ApJ*, 910, 75
- Lequeux, J. 2005, *The Interstellar Medium* (Springer)
- Li, J., Bergin, E. A., Blake, G. A., Ciesla, F. J., & Hirschmann, M. M. 2021, *Science Advances*, 7, eabd3632
- Li, J. I.-H., Liu, H. B., Hasegawa, Y., & Hirano, N. 2017, *ApJ*, 840, 72
- Lietzow, M. & Wolf, S. 2023, *A&A*, 671, A113
- Lin, Z.-Y. D., Lee, C.-F., Li, Z.-Y., Tobin, J. J., & Turner, N. J. 2021, *MNRAS*, 501, 1316
- Lin, Z.-Y. D., Li, Z.-Y., Yang, H., et al. 2020, *MNRAS*, 493, 4868
- Liu, H. B. 2019, *ApJ*, 877, L22
- Liu, H. B. 2021, *ApJ*, 914, 25
- Liu, H. B., Dunham, M. M., Pascucci, I., et al. 2018a, *A&A*, 612, A54
- Liu, H. B., Hasegawa, Y., Ching, T.-C., et al. 2018b, *A&A*, 617, A3
- Liu, H. B., Mérand, A., Green, J. D., et al. 2019, *ApJ*, 884, 97
- Liu, H. B., Tsai, A.-L., Chen, W. P., et al. 2021, *ApJ*, 923, 270
- Lizano, S., Tapia, C., Boehler, Y., & D'Alessio, P. 2016, *ApJ*, 817, 35
- Loinard, L., Chandler, C. J., Rodríguez, L. F., et al. 2007, *ApJ*, 670, 1353
- Loinard, L., Rodríguez, L. F., D'Alessio, P., Wilner, D. J., & Ho, P. T. P. 2002, *ApJ*, 581, L109
- Loren, R. B. 1989, *ApJ*, 338, 925
- Lucy, L. B. 1999, *A&A*, 344, 282
- Machida, M. N., Inutsuka, S.-i., & Matsumoto, T. 2011, *ApJ*, 729, 42
- Manigand, S., Coutens, A., Loison, J. C., et al. 2021, *A&A*, 645, A53
- Manigand, S., Jørgensen, J. K., Calcutt, H., et al. 2020, *A&A*, 635, A48
- Mathis, J. S., Rumpl, W., & Nordsieck, K. H. 1977, *ApJ*, 217, 425
- Mattila, K. 1970, *A&A*, 9, 53
- Maureira, M. J., Gong, M., Pineda, J. E., et al. 2022, *ApJ*, 941, L23

- Maureira, M. J., Pineda, J. E., Segura-Cox, D. M., et al. 2020, *ApJ*, 897, 59
- Maury, A. J., André, P., Testi, L., et al. 2019, *A&A*, 621, A76
- Maury, A. J., Girart, J. M., Zhang, Q., et al. 2018, *MNRAS*, 477, 2760
- McKee, C. F., Zweibel, E. G., Goodman, A. A., & Heiles, C. 1993, in *Protostars and Planets III*, ed. E. H. Levy & J. I. Lunine, 327
- McMullin, J. P., Waters, B., Schiebel, D., Young, W., & Golap, K. 2007, in *Astronomical Society of the Pacific Conference Series*, Vol. 376, *Astronomical Data Analysis Software and Systems XVI*, ed. R. A. Shaw, F. Hill, & D. J. Bell, 127
- Mie, G. 1908, *Annalen der Physik*, 330, 377
- Miotello, A., Testi, L., Lodato, G., et al. 2014, *A&A*, 567, A32
- Moody, M. S. L., Shi, J.-M., & Stone, J. M. 2019, *ApJ*, 875, 66
- Motte, F., Bontemps, S., & Louvet, F. 2018, *ARA&A*, 56, 41
- Mouschovias, T. C. 1974, *ApJ*, 192, 37
- Mushtaq, M., Ceverino, D., Klessen, R. S., Reissl, S., & Puttasiddappa, P. H. 2023, arXiv e-prints, arXiv:2304.10150
- Myers, A. T., McKee, C. F., Cunningham, A. J., Klein, R. I., & Krumholz, M. R. 2013, *ApJ*, 766, 97
- Myers, P. C. 2009, *ApJ*, 700, 1609
- Ohashi, N., Hayashi, M., Ho, P. T. P., & Momose, M. 1997, *ApJ*, 475, 211
- Ohashi, S., Kataoka, A., van der Marel, N., et al. 2020, *ApJ*, 900, 81
- Ormel, C. W., Paszun, D., Dominik, C., & Tielens, A. G. G. M. 2009, *A&A*, 502, 845
- Ossenkopf, V. 1991, *A&A*, 251, 210
- Ossenkopf, V. & Henning, T. 1994, *A&A*, 291, 943
- Oya, Y., Moriwaki, K., Onishi, S., et al. 2018, *ApJ*, 854, 96
- Oya, Y., Sakai, N., Lefloch, B., et al. 2015, *ApJ*, 812, 59
- Oya, Y., Sakai, N., López-Sepulcre, A., et al. 2016, *ApJ*, 824, 88
- Oya, Y. & Yamamoto, S. 2020, *ApJ*, 904, 185
- Padovani, M., Brinch, C., Girart, J. M., et al. 2012, *A&A*, 543, A16

- Paneque-Carreño, T., Pérez, L. M., Benisty, M., et al. 2021, *ApJ*, 914, 88
- Parker, E. N. 1966, *ApJ*, 145, 811
- Pillich, C., Bogdan, T., Landers, J., Wurm, G., & Wende, H. 2021, *A&A*, 652, A106
- Pineda, J. E., Arzoumanian, D., André, P., et al. 2022, arXiv e-prints, arXiv:2205.03935
- Pineda, J. E., Maury, A. J., Fuller, G. A., et al. 2012, *A&A*, 544, L7
- Pineda, J. E., Offner, S. S. R., Parker, R. J., et al. 2015, *Nature*, 518, 213
- Pineda, J. E., Segura-Cox, D., Caselli, P., et al. 2020, *Nature Astronomy*, 4, 1158
- Pinte, C., Ménard, F., Duchêne, G., & Bastien, P. 2006, *A&A*, 459, 797
- Planck Collaboration, Akrami, Y., Ashdown, M., et al. 2020, *A&A*, 641, A11
- Plunkett, A. L., Arce, H. G., Mardones, D., et al. 2015, *Nature*, 527, 70
- Pollack, J. B., Hollenbach, D., Beckwith, S., et al. 1994, *ApJ*, 421, 615
- Ponnada, S. B., Panopoulou, G. V., Butsky, I. S., et al. 2022, *MNRAS*, 516, 4417
- Purcell, E. M. 1979, *ApJ*, 231, 404
- Quénard, D., Ilee, J. D., Jiménez-Serra, I., et al. 2018, *ApJ*, 868, 9
- Rafikov, R. R. 2009, *ApJ*, 704, 281
- Rafikov, R. R. 2015, *ApJ*, 804, 62
- Rao, R., Girart, J. M., Lai, S.-P., & Marrone, D. P. 2014, *ApJ*, 780, L6
- Rao, R., Girart, J. M., Marrone, D. P., Lai, S.-P., & Schnee, S. 2009, *ApJ*, 707, 921
- Rau, U. & Cornwell, T. J. 2011, *A&A*, 532, A71
- Reipurth, B., Clarke, C. J., Boss, A. P., et al. 2014, *Protostars and Planets VI*, 267
- Reissl, S., Meehan, P., & Klessen, R. S. 2022, arXiv e-prints, arXiv:2201.03694
- Reissl, S., Wolf, S., & Brauer, R. 2016, *A&A*, 593, A87
- Roark, T., Roark, B., & Collins, II, G. W. 1974, *ApJ*, 190, 67
- Robitaille, T. P. 2011, *A&A*, 536, A79
- Rodríguez, L. F., Loinard, L., D'Alessio, P., Wilner, D. J., & Ho, P. T. P. 2005, *ApJ*, 621, L133
- Rybicki, G. B. & Lightman, A. P. 1979, *Radiative processes in astrophysics*

- Sadavoy, S. I., Myers, P. C., Stephens, I. W., et al. 2018, *ApJ*, 869, 115
- Sadavoy, S. I., Stephens, I. W., Myers, P. C., et al. 2019, *ApJS*, 245, 2
- Schöier, F. L., Jørgensen, J. K., van Dishoeck, E. F., & Blake, G. A. 2002, *A&A*, 390, 1001
- Scibelli, S., Shirley, Y., Schmiedeke, A., et al. 2023, *MNRAS*, 521, 4579
- Segura-Cox, D. in prep.
- Segura-Cox, D. M., Looney, L. W., Stephens, I. W., et al. 2015, *ApJ*, 798, L2
- Segura-Cox, D. M., Looney, L. W., Tobin, J. J., et al. 2018, *ApJ*, 866, 161
- Segura-Cox, D. M., Schmiedeke, A., Pineda, J. E., et al. 2020, *Nature*, 586, 228
- Seifried, D. & Walch, S. 2015, *MNRAS*, 452, 2410
- Sheehan, P. D. & Eisner, J. A. 2018, *ApJ*, 857, 18
- Siddiqi, M. A., Siddiqui, R. A., & Atakan, B. 2009, *Journal of Chemical & Engineering Data*, 54, 2795
- Sierra, A. & Lizano, S. 2020, *ApJ*, 892, 136
- Silsbee, K., Ivlev, A. V., Sipilä, O., Caselli, P., & Zhao, B. 2020, *A&A*, 641, A39
- Simmons, J. F. L. & Stewart, B. G. 1985, *A&A*, 142, 100
- Smith, I. W. M., Cockell, C. S., & Sydney, L. 2013, *Astrochemistry and Astrobiology* (Springer-Verlag Berlin Heidelberg)
- Snow, T. P. & McCall, B. J. 2006, *ARA&A*, 44, 367
- Springel, V. 2005, *MNRAS*, 364, 1105
- Springel, V. 2010, *Monthly Notices of the Royal Astronomical Society*, 401, 791
- Stahler, S. W. & Palla, F. 2004, *The Formation of Stars*
- Stamatellos, D., Whitworth, A. P., Bisbas, T., & Goodwin, S. 2007, *A&A*, 475, 37
- Stark, R., Sandell, G., Beck, S. C., et al. 2004, *ApJ*, 608, 341
- Steinacker, J., Baes, M., & Gordon, K. D. 2013, *ARA&A*, 51, 63
- Steinpilz, T., Teiser, J., & Wurm, G. 2019, *ApJ*, 874, 60
- Stephens, I. W., Looney, L. W., Kwon, W., et al. 2014, *Nature*, 514, 597
- Stephens, I. W., Looney, L. W., Kwon, W., et al. 2013, *ApJ*, 769, L15

- Stephens, I. W., Yang, H., Li, Z.-Y., et al. 2017, *ApJ*, 851, 55
- Stone, J. M., Tomida, K., White, C. J., & Felker, K. G. 2020, *ApJS*, 249, 4
- Takakuwa, S., Ohashi, N., Bourke, T. L., et al. 2007, *ApJ*, 662, 431
- Tapia, C. & Lizano, S. 2017, *ApJ*, 849, 136
- Tazaki, R., Lazarian, A., & Nomura, H. 2017, *ApJ*, 839, 56
- Testi, L., Birnstiel, T., Ricci, L., et al. 2014, in *Protostars and Planets VI*, ed. H. Beuther, R. S. Klessen, C. P. Dullemond, & T. Henning, 339–361
- Teyssier, R. 2002, *A&A*, 385, 337
- Tielens, A. G. G. M. 2010, *The Physics and Chemistry of the Interstellar Medium* (Cambridge University Press)
- Tobin, J. J., Hartmann, L., Calvet, N., & D’Alessio, P. 2008, *ApJ*, 679, 1364
- Tobin, J. J., Kratter, K. M., Persson, M. V., et al. 2016, *Nature*, 538, 483
- Tobin, J. J., Sheehan, P. D., Megeath, S. T., et al. 2020, *ApJ*, 890, 130
- Toomre, A. 1964, *ApJ*, 139, 1217
- Tsukamoto, Y., Maury, A., Commerçon, B., et al. 2022, arXiv e-prints, arXiv:2209.13765
- Tychoniec, Ł., Manara, C. F., Rosotti, G. P., et al. 2020, *A&A*, 640, A19
- Ueda, T., Okuzumi, S., Kataoka, A., & Flock, M. 2023, arXiv e-prints, arXiv:2305.12598
- Vaillancourt, J. E. 2006, *PASP*, 118, 1340
- Valdivia, V., Maury, A., Brauer, R., et al. 2019, *MNRAS*, 488, 4897
- Valdivia, V., Maury, A., & Hennebelle, P. 2022, arXiv e-prints, arXiv:2203.14505
- Valdivia-Mena, M. T., Pineda, J. E., Segura-Cox, D. M., et al. 2022, *A&A*, 667, A12
- van der Tak, F. F. S., Black, J. H., Schöier, F. L., Jansen, D. J., & van Dishoeck, E. F. 2007, *A&A*, 468, 627
- van der Wiel, M. H. D., Jacobsen, S. K., Jørgensen, J. K., et al. 2019, *A&A*, 626, A93
- van Dishoeck, E. F., Blake, G. A., Jansen, D. J., & Groesbeck, T. D. 1995, *ApJ*, 447, 760
- van ’t Hoff, M. L. R., Bergin, E. A., Jørgensen, J. K., & Blake, G. A. 2020a, *ApJ*, 897, L38
- van ’t Hoff, M. L. R., Tobin, J. J., Harsono, D., & van Dishoeck, E. F. 2018, *A&A*, 615, A83

- van 't Hoff, M. L. R., van Dishoeck, E. F., Jørgensen, J. K., & Calcutt, H. 2020b, *A&A*, 633, A7
- van't Hoff, M. L. R., Harsono, D., Tobin, J. J., et al. 2020, *ApJ*, 901, 166
- Veronesi, B., Paneque-Carreno, T., Lodato, G., et al. 2021, arXiv e-prints, arXiv:2104.09530
- Virtanen, P., Gommers, R., Oliphant, T. E., et al. 2020, *Nature Methods*, 17, 261
- Vorobyov, E. I. & Basu, S. 2010, *ApJ*, 714, L133
- Ward-Thompson, D., Motte, F., & Andre, P. 1999, *MNRAS*, 305, 143
- Weidenschilling, S. J. 1977, *MNRAS*, 180, 57
- Weingartner, J. C. & Draine, B. T. 2001, *ApJ*, 548, 296
- Whitehouse, S. C. & Bate, M. R. 2004, *MNRAS*, 353, 1078
- Whitehouse, S. C. & Bate, M. R. 2006, *MNRAS*, 367, 32
- Williams, J. P., Blitz, L., & McKee, C. F. 2000, *Protostars and Planets IV*, 97
- Woitke, P., Min, M., Pinte, C., et al. 2016, *A&A*, 586, A103
- Wolf, S. & Voshchinnikov, N. V. 2004, *Computer Physics Communications*, 162, 113
- Wood, K. 1997, *ApJ*, 477, L25
- Wootten, A. 1989, *ApJ*, 337, 858
- Xu, W. & Kunz, M. W. 2021a, *MNRAS*, 502, 4911
- Xu, W. & Kunz, M. W. 2021b, *MNRAS*, 508, 2142
- Yamamoto, S. 2017, *Introduction to Astrochemistry: Chemical Evolution from Interstellar Clouds to Star and Planet Formation*
- Yamamuro, R., Tanaka, K. E. I., & Okuzumi, S. 2023
- Yang, H. & Li, Z.-Y. 2020, *ApJ*, 889, 15
- Yang, H., Li, Z.-Y., Looney, L., & Stephens, I. 2016, *MNRAS*, 456, 2794
- Yang, H., Li, Z.-Y., Looney, L. W., Girart, J. M., & Stephens, I. W. 2017, *MNRAS*, 472, 373
- Zamponi, J., Giannetti, A., Bovino, S., et al. 2022, *Ap&SS*, 367, 65
- Zamponi, J., Maureira, M. J., Liu, H. B., et al. Submitted, *A&A*
- Zamponi, J., Maureira, M. J., Zhao, B., et al. 2021, *MNRAS*, 508, 2583

Zapata, L. A., Loinard, L., Rodríguez, L. F., et al. 2013, *ApJ*, 764, L14

Zhao, B., Caselli, P., Li, Z.-Y., & Krasnopolsky, R. 2018, *MNRAS*, 473, 4868

Zhao, B., Caselli, P., Li, Z.-Y., et al. 2016, *MNRAS*, 460, 2050

Zubko, V., Dwek, E., & Arendt, R. G. 2004, *ApJS*, 152, 211

Acknowledgements

Four years of journey have now come to an end, and all that is left for me to do is to thank all the beautiful people I have around.

To start, I wanna thank Paola, my professor, for the kindness and empathy I always felt when dealing with deadlines, reports and career advices. I've learned a lot from you and I very much appreciate that mental health was always for you as relevant of a concept as it is productivity. Second, I wanna thank Maria Jose (Cote), my direct supervisor and most importantly, my friend, for her scientific and human support. You've so much helped me grow as a scientist and as a person, despite my constant ranting and hate for academia.

I wanna thank my family in Germany: Jay, Simon, Yru, Monica, Davide, Lazaros, Stavroula, Marlin, Sam, Ale, Dani, Nahir et al. Every single one of you have been there for me in key moments. I can't thank that enough.

I'm also really grateful of the group I worked on, the CAS group. I guess not everyone can say they had a sweet, non-toxic and funny working environment for their phd plus a good coffee machine, specially in such a competitive institute. I guess I was just lucky :)

The biggest of all thanks goes to my true family back in Chile. My mom, my dad, my siblings, my grandpas. None of this would be possible without you. I miss you more than I say.

Last but not least, special thanks to the chamomille tee for helping my stomach somatize all the stress that meant writing this thesis. Thanks also to the Isar river for being so close to my place now that I had to write this during Summer.